Nonlinear Analysis of Rotors Supported by Air Foil Journal Bearings – Theory and Experiments

Larsen, Jon Steffen

Publication date:
2014

Document Version
Publisher's PDF, also known as Version of record

Nonlinear Analysis of Rotors Supported by Air Foil Journal Bearings - Theory & Experiments

PhD Thesis

$$(EIv'')'' = q - \rho A\ddot{v}$$

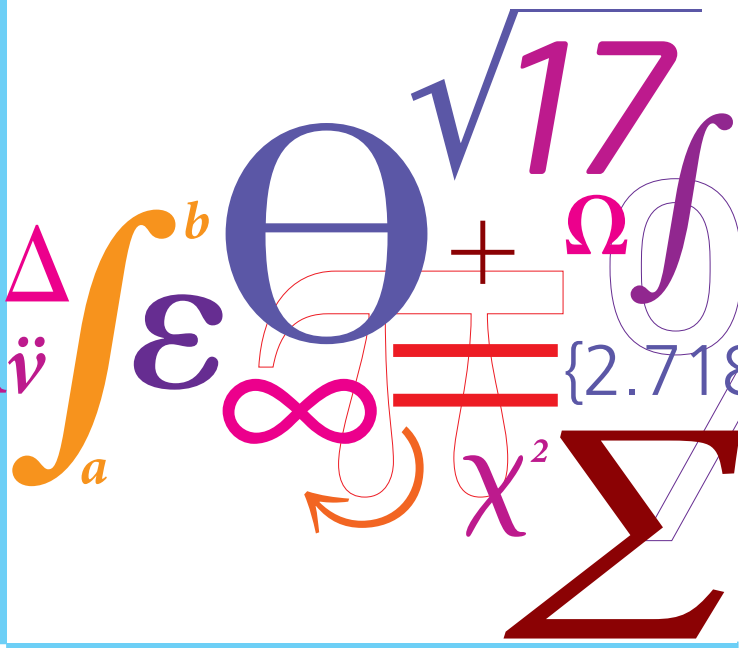

Jon Steffen Larsen
DCAMM Special Report No. S177
February 2015

DTU Mechanical Engineering
Department of Mechanical Engineering

Nonlinear Analysis of Rotors Supported by Air Foil Journal Bearings – Theory & Experiments

Jon Steffen Larsen

Kongens Lyngby 2014
DCAMM Special Report No. S177

PhD student:
Jon Steffen Larsen
josla@mek.dtu.dk

Principal supervisor:
Ilmar Ferreira Santos
ifs@mek.dtu.dk

Industrial supervisor:
Frans Pløger
fransploeger@gmail.com

Technical University of Denmark
Department of Mechanical Engineering, Section of Solid Mechanics
Building 404, DK-2800 Kongens Lyngby, Denmark
Phone +45 4525 4250, Fax +45 4593 1475
info.fam@mek.dtu.dk
www.mek.dtu.dk

MEK-PHD: ISBN 978-87-7475-402-2

Summary (English)

Direct driven compressors supported by air foil bearings (AFB) are gaining increasing popularity, for example within the waste water treatment industry where the demand for larger machines up to 250 kW is growing. In order to keep production costs low, the shaft and bearing design need to be simple and allow manufacturing using conventional materials and production facilities. As a consequence, the assembled rotor weight can be up to 50 kg. The compressors are operated at variable speed and load and are subjected to several starts and stops per day. Therefore, the rotor bearing design must be robust with a good margin of rotordynamical stable operation. To ensure this, good mathematical models, capable of accurately predicting the dynamic behaviour of the rotor-bearing system, are required at the design stage. This thesis focuses on developing and improving existing mathematical models for predicting the nonlinear dynamic behaviour of AFBs, both isolated and coupled with the rotor. Large emphasis is put on the experimental validation of the obtained theoretical results. Two experimental test rigs were designed and manufactured specifically for this purpose. With the first rig, the isolated nonlinear mechanical behaviour of the bump foils was carefully examined. A mathematical model capable of predicting this nonlinear behaviour was developed and compared to the experimental results with good agreement. With the second test rig, the overall nonlinear behaviour of the rotor-bearing system was investigated experimentally, and the linearised stiffness and damping coefficients of the bearings were identified. Results obtained theoretically were compared to these linearised coefficients with reasonably good agreement. Furthermore, the sensitivity to rotor unbalance and the nonlinear response were analysed experimentally and a coupled rotor-bearing mathematical model was compared to these results with very good agreement in terms of the nonlinear rotor unbalance response.

Resumé (Dansk)

Direkte drevne kompressorer med folielejer bliver stadig mere populære i f.eks. industrien for spildevandsrensning. Samtidig stiger efterspørgslen på større maskiner på op til 250 kW motoreffekt. Aksel og lejedesign skal være simpelt for at holde produktionsomkostninger nede. Et simpelt design muliggør fremstilling i standard materialer samt brug af standard produktionsapparater. Det simple design medfører rotorer med egenvægt på op til 50 kg. Kompressorerne opereres ved variabel last samt hastighed, og de er udsat for flere start og stop per døgn. Der stilles derfor krav til et robust design med en god margin til rotordynamisk ustabilitet. Dermed nødvendiggøres nøjagtige matematiske modeller, som i designstadiet kan forudsige rotor-leje systemets dynamiske opførsel. Denne afhandling omhandler arbejdet med udvikling og forbedring af eksisterende matematiske modeller til forudsigelse af den ikkelineære dynamiske opførsel af folielejer isoleret set, men også sammenkoblet med en rotor. Der er lagt vægt på den eksperimentelle validering af de teoretiske resultater. Således blev der designet og bygget to eksperimentelle teststande specifikt til formålet. Den isolerede ikkelineære opførsel af bølgefolierne blev grundigt undersøgt ved hjælp af den første teststand. Samtidig blev en matematisk model for disse bølgefolier udviklet for at forudsige deres ikkelineære opførsel, og resultaterne blev sammenholdt med målingerne med god overensstemmelse. Den overordnede ikkelineære opførsel af rotor-leje systemet blev eksperimentelt undersøgt ved hjælp af den anden teststand, og de lineariserede stivheds- og dæmpningskoefficienter blev identificeret. Teoretiske resultater for disse lineariserede koefficienter blev sammenlignet med de eksperimentelle med en relativ god overensstemmelse. Endvidere blev sensitiviteten til rotorubalance samt det ikkelineære transiente rotorrespons undersøgt eksperimentelt og sammenlignet med teoretiske resultater fra en koblet matematisk rotor-leje model med meget god overensstemmelse.

Preface

This thesis is submitted as a partial fulfilment of the requirements for obtaining the Danish PhD degree. The thesis consists of a summary report and a collection of six research papers written during the period 2011–2014, and elsewhere published. The work was founded by Siemens A/S, Aeration Competence Centre (Siemens-ACC) and the Danish Ministry of Research and Innovation and carried out from September 2011 to November 2014 at the Section of Solid Mechanics (FAM), Department of Mechanical Engineering (MEK), Technical University of Denmark (DTU). The project was supervised by the university-supervisor Professor, Dr.-Ing., Dr.techn. Ilmar Ferreira Santos and the industry-supervisor PhD Frans Pløger, to both I would express my sincere gratitude. I thank my industry-supervisor for establishing the infrastructure in Siemens-ACC and for allocating the resources necessary for me to focus entirely on the project work. A special thanks goes to my university-supervisor for his general support, guidance and the ever-inspiring weekly meetings, meetings that I will miss upon finalising this project. I also thank the managing director of Siemens-ACC, Mr. Jan Olsen, for his support during a hard transition period of our company. From Siemens-ACC, I also wish to thank Mr. Jørgen Lyquist and Mr. Asger Jørgen Thor Hansen for their help related to the design and construction of the experimental test facilities at Siemens. Regarding the test facilities at DTU, I owe a special thanks to Kristian Bjarklev, Niels Toftdahl Christensen and Peter Kjær Svendsen.

Thanks to my closest PhD student colleagues within the machinery dynamic research group at DTU, Alejandro V. Cerda, Andreas V. Jauernik, Emil Bureau, Bo B. Nielsen, Søren Enemark, Jorge A. G. Salazar, Fabián G. P. Vásquez, Jonas Lauridsen, Cesar Fonseca and Geraldo Rebouças for sharing countless hours at the office, and for exchanging ideas, opinions and knowledge. I also thank Mrs.

Mette Pihl Køster who spent her precious time proofreading most of this thesis.

Last but not least, I thank my family, in both Denmark and Norway, for their help, support and for their patience with me in some of the challenging periods of this project. But most of all I thank my dear and ever-understanding Hedvig Gjerstad, beyond any doubt my most important source of inspiration and support.

Kgs. Lyngby, 4 March 2015.

Jon Steffen Larsen

Appended publications

The following publications are part of this thesis:

[P1] J. S. Larsen, I. F. Santos, Compliant Foil Journal Bearings - Investigation of Dynamic Properties, in: Proceedings of 10th International Conference on Schwingungen in Rotierenden Maschinen (SIRM2013), Berlin, Germany, 25-27 February, 2013.

[P2] J. S. Larsen, A. C. Varela, I. F. Santos, Numerical and experimental investigation of bump foil mechanical behaviour, Tribology International, 74 (2014):46-56.

[P3] J. S. Larsen, I. F. Santos, Efficient solution of the non-linear Reynolds equation for compressible fluid using the finite element method, Journal of the Brazilian Society of Mechanical Sciences and Engineering, (published online 2014).

[P4] J. S. Larsen, J.-T. Hansen, I. F. Santos, Experimental and theoretical analysis of a rigid rotor supported by air foil bearings, Mechanics & Industry, 16 (1) 106 (2015).

[P5] J. S. Larsen, B. B. Nielsen, I. F. Santos, On the Numerical Simulation of Nonlinear Transient Behavior of Compliant Air Foil Bearings, in: Proceedings of 11th International Conference on Schwingungen in Rotierenden Maschinen (SIRM2015), Magdeburg, Germany, 23-25 February, 2015.

[P6] J. S. Larsen, I. F. Santos, On the nonlinear steady state response of rigid rotors supported by air foil bearings - theory and experiments, Submitted

September 2014 to the Journal of Sound and Vibration, ref. JSV-D-14-01395 (Accepted February 2015).

Nomenclature & abbreviations

Abbreviations

AFB	Air Foil Bearing
CFSM	Coupled Fluid Structure Model
CG	Centre of Gravity
DOF	Degrees of Freedom
DTU	Technical University of Denmark
FE	Finite Element
FFT	Fast Fourier Transform
NR	Newton-Raphson
ODE	Ordinary Differential Equation
RPM	Revolutions Per Minute
SEFM	Simple Elastic Foundation Model
VWP	Virtual Work Principle

Latin symbols

A	Area
$b, \tilde{b}$	Foil damping per unit area, $\tilde{b} = \frac{C}{p_a \omega} k$
C	Radial clearance

C_i	Coefficients, $i = 1, ..., 4$
D	Diffusion coefficient
$d_{\alpha\beta}$	Bearing damping coefficients, $\alpha = x, y$, $\beta = x, y$
E	Modulus of elasticity of foils
e	Element
$e_{x,y}$	Journal eccentricity components
e_{x_0,y_0}	Journal equilibrium position
f	Shaft force
F_μ	Friction force
F_n	Normal force
$F_{x,y}, \tilde{F}_{x,y}$	Bearing force components, $\tilde{F}_{x,y} = \frac{1}{p_a R^2} F_{x,y}$
$h, \tilde{h}$	Film height, $\tilde{h} = h/C$
h_0	Steady state film height
h_b	Bump foil height
$h_c, \tilde{h}_c$	Film height (compliant), $\tilde{h}_c = h_c/C$
$h_r, \tilde{h}_r$	Film height (rigid), $\tilde{h}_r = h_r/C$
h_s	Slope height
h_{c_0}	Steady state film height (compliant)
h_{r_0}	Steady state film height (rigid)
I	Area moment of inertia
K	Foil flexibility per unit area
$k, \tilde{k}$	Foil stiffness per unit area, $\tilde{k} = \frac{C}{p_a} k$
k^e	Nonlinear spring stiffness
K_c	Complex foil flexibility
$k_{\alpha\beta}$	Bearing stiffness coefficients, $\alpha = x, y$, $\beta = x, y$
k_{eq}	Equivalent bump stiffness
l	Length

$L, \tilde{L}$	Bearing length, $\tilde{L} = L/R$
l_0	Bump half length
L_0^e	Element initial length
L_1^e	Element deformed length
l_e	Top foil element length
$l_{1,2}$	Distance from CG to bearing (A, B)
M	Molar weight
m	Mass
N^e	Element force
N_i	Shape function
N_p	Number of pads
$p, \tilde{p}$	Film pressure, $\tilde{p} = p/p_a$
p_0	Steady state film pressure
p_a	Ambient pressure
$p_{x,y}$	Perturbed pressures
q	Shaft deflection
R	Bearing radius
R_u	Universal gas constant
S	Compressibility number, $S = \frac{6\mu\omega}{p_a}\left(\frac{R}{C}\right)^2$
S_b	Bump foil pitch
T	Temperature
t	Time
t_b	Thickness of bump foil
t_t	Thickness of top foil
U	Peak potential energy
u, v	Displacements in Cartesian coordinates
$u_{\mathrm{A,B}}$	Mass eccentricity

V	Volume
W	Load on bump foils
w_b	Width of foil specimen
$W_{x,y}$	Journal load components
$x, y, z, \tilde{z}$	Cartesian coordinates, $\tilde{z} = z/R$
x_r	Relative sliding

Greek symbols

ΔE	Energy loss per load cycle
$\Delta e_{x,y}$	Perturbation of journal equilibrium position
Δu	Spring total deformation, $u_j - u_i$
Δu_s	Shift
Δx	Spring undeformed length, $x_j - x_i$
δ	Variation
η	Structural loss factor
μ	Dynamic viscosity
μ_f	Coefficient of friction
ν	Poisson's ratio
ω	Journal angular speed
ω_s	Excitation/perturbation frequency of journal
ψ	Film state variable, $\psi = \tilde{p}\tilde{h}$
ρ	Density
σ	Stress
τ	Dimensionless time, $\tau = \omega t$
θ	Angular coordinate
θ_0	Bump half angle angular extend
θ_l	First pad leading edge angle
θ_s	Slope extend

θ_t	First pad trailing edge angle
$\tilde{\theta}$	Circumferential coordinate
ε	Dimensionless rotor displacement/strain
ε_s	Smoothing factor
ε_{ij}	Strain components
$\varepsilon_{x,y}$	Dimensionless rotor displacement, $\varepsilon_{x,y} = e_{x,y}/C$
φ	Angular displacement in Cartesian coordinates
ξ, ζ	Parametric coordinates

Vectors

$\{\Phi\}$	Body force vector
$\{\psi^e\}$	Film state element vector
$\{\psi\}$	Film state vector
$\{\sigma\}$	Stress vector
$\{\Theta\}$	Displacement derivatives vector
$\{\tilde{F}_{ub}\}$	Unbalance force vector
$\{\varepsilon_0\}$	Displacement independent strain
$\{\varepsilon_L\}$	Displacement dependent strain
$\{\varepsilon\}$	Strain or journal eccentricity vector
$\{d_f\}$	Top foil element nodal displacement vector
$\{D\}$	Global displacement vector
$\{d\}$	Element nodal displacement vector
$\{F_s\}$	Surface traction vector
$\{f\}$	Shaft nodal force vector
$\{F\}, \{\tilde{F}\}$	Air film force, $\{\tilde{F}\} = \frac{1}{p_a R^2}\{F\}$
$\{h_c\}, \{\tilde{h}_c\}$	Film height vector (compliant), $\{\tilde{h}_c\} = \frac{1}{C}\{h_c\}$
$\{h_{c_0}\}$	Film height vector (static compliant)
$\{h\}, \{\tilde{h}\}$	Film height vector, $\{\tilde{h}\} = \frac{1}{C}\{h\}$

$\{p^e\}$	Nodal load vector
$\{p_0\}$	Static fluid film pressure vector
$\{p_\gamma\}$	Dynamic pressure vector, $\gamma = x, y$
$\{P\}$	Global load vector
$\{p\}, \{\tilde{p}\}$	Fluid film pressure vector, $\{\tilde{p}\} = \frac{1}{p_a}\{p\}$
$\{q_\gamma\}$	Right hand side vector, $\gamma = x, y$
$\{q_{\mathrm{AB}}\}$	Shaft nodal displacement vector
$\{R^e\}$	Residual element vector
$\{R_{\mathrm{ext}}\}$	External residual vector
$\{R_{\mathrm{int}}\}$	Internal residual vector
$\{R\}$	Residual vector
$\{S\}$	Advection vector, $\{S\} = \{S,\ 0\}^T$
$\{U\}$	Speed, $\{U\} = \{\omega R/2,\ 0\}^T$
$\{u\}$	Displacement vector
$\{W\}, \{\tilde{W}\}$	Static bearing load, $\{\tilde{W}\} = \frac{1}{p_a R^2}\{W\}$
$\{y\}$	State vector
$\{z_1\}$	State vector, $\{z_1\} = \{\varepsilon\}$
$\{z_2\}$	State vector, $\{z_2\} = \{\dot{\varepsilon}\}$

Matrices

$\left[\bar{B}\right]$	Strain-displacement matrix
$\left[A^e_\psi\right]$	Fluidity element matrix
$[A_\psi]$	Fluidity matrix
$[A]$	Displacement derivatives matrix
$[B_0]$	Deformation independent strain-displacement matrix
$[B_L]$	Deformation dependent strain-displacement matrix
$[B]$	Shape function derivative matrix

$[C]$	Constitutive matrix
$[D_b]$	Bearing damping matrix
$[D_s]$	Shaft damping matrix including bearing coefficients
$[D]$	Shaft damping matrix
$[G]\,,[\tilde{G}]$	Shaft gyroscopic matrix
$[H^r_{AB}]^{-1}$	Dynamic stiffness matrix of the rotor
$[H_{AB}]$	FRF matrix related to A and B
$[H_{EP}]$	FRF matrix related to E and P
$[J]$	Jacobian matrix
$[k^e_t]$	Element tangential matrix
$[k^e_\sigma]$	Element stress stiffness matrix
$[K_b]$	Bearing stiffness matrix
$[K_f]$	Top foil stiffness matrix
$[k_f]$	Top foil element stiffness matrix
$[K_t]$	Tangential matrix
$[K_\gamma]$	Fluidity matrix, $\gamma = x, y$
$[K]$	Shaft stiffness matrix
$[M]$	Mass matrix
$[M]\,,[\tilde{M}]$	Shaft mass matrix
$[N]$	Shape function matrix
$[T_1]$, $[T_2]$	Transformation matrices

Functions

$\mathbf{g}$	Nonlinear vector function
$\mathbf{g}_{\dot{\psi}}$	Nonlinear vector function
$\mathbf{g}_{\dot{\bar{h}}_c}$	Nonlinear vector function

Mathematical notation

$(\ddot{})$	Time derivative, $\frac{d^2}{dt^2}$
$(\dot{})$	Time derivative, $\frac{d}{dt}$
$\nabla\cdot$	Divergence
∇	Gradient, $\nabla = \left\{ \frac{\partial}{\partial \tilde{\theta}},\ \frac{\partial}{\partial z} \right\}$

Contents

Chapter 1

Introduction

1.1 Background

Bearings are one of the fundamental machinery elements and dates as far back as to the invention of the wheel. Their purpose is to separate moving parts by reducing friction while transferring the reaction forces in predefined directions, that is in the constraint degrees of freedom. The ability to transfer reaction forces is linked to the load carrying capacity of the bearing, while the ability to separate the moving parts is associated with the internal frictional resistance. The load carrying capacity and the internal frictional resistance are two important attributes of a bearing. Another attribute is associated with the stiffness and damping characteristics of the bearing, the latter being important when dealing with bearings supporting fast rotating shafts, that is in turbo machinery applications. Today, several types of bearings are commonly applied in modern machinery; the main groups are: solid lubricated plain bearings, elastohydrodynamic lubricated bearings such as roller or ball bearings, hydrostatic lubricated bearings, hydrodynamic lubricated bearings and magnetic bearings. The bearings of each group are associated with different strengths and weaknesses, of both mechanical as well as economical nature.

Aerodynamic bearings belong to the main group of hydrodynamically lubricated bearings with the difference that the lubricant is air or other types of gas com-

positions. Unlike hydrostatic bearings that rely on external pressurisation of the lubricant, they are self-acting. The earliest aerodynamic journal bearings were of the rigid type, consisting of a journal rotating inside a rigid bearing bore. The rigid bearings rely on a very narrow clearance and they are extremely sensitive to shaft misalignment. Furthermore, they provide very low amounts of damping, which is generated in the fluid film only. A massive improvement to the aerodynamic journal bearings came with the invention of the Air Foil Bearing (AFB). The AFBs allow for a certain shaft misalignment and offer improved damping characteristics by introducing a compliant bearing surface. The deflections of the bearing surface, caused by shaft vibrations, generates energy dissipation due to dry friction. The most significant strengths of journal AFBs when compared to other types of bearings are:

1) Their frictional resistance is extremely low
2) The lubricant is ample, clean and operates well from low to extremely high temperatures
3) Their mechanical simplicity

On the other hand, some of the weaknesses are:

1) Load carrying capacity is low and shaft rotational speed must be high
2) Dimensions, clearances and shaft balancing must be extremely fine
3) Their rotordynamic stability characteristic is poor, which is linked to their stiffness and damping characteristics

In some industries like, for example the waste water treatment, fermentation and the medical industry, there is a demand for clean compressed air. For those applications, the AFBs are highly suitable, as they are oil-free. They completely eliminate the problem of oil leaking over the bearing seals into the compressor's aero parts and hence into the compressed process air. This makes the AFBs attractive from a process point of view, while the very low frictional resistance and the mechanical simplicity adds to the AFBs attractiveness from an engineering and economical point of view. Historically, compressors for the aforementioned industries were designed around a gearbox that served to increase the rotational speed from the input shaft, driven by a motor, to the output shaft, driving the compressor unit. As development of ever larger and less expensive Variable Frequency Drives (VFD) and associated electro-motors has progressed, the need for the gearbox, on the small- and medium-sized compressors, can be eliminated by driving the compressor directly. The direct drive in combination with a VFD

allows for optimal adjustment of the running speed during operation and hence increases the efficiency of the compressor. Furthermore, the elimination of the gears greatly reduces the bearing reaction forces, as the dominating gear forces are eliminated, leaving only the contribution from the mass of the rotor. Moreover, as the input drive shaft is eliminated, there is no longer any 'slow' rotating shafts and hence all requirements for successful utilisation of AFBs are fulfilled.

In 2007, Siemens-ACC launched the development of a new series of direct driven oil-free compressors with sizes ranging from 75 kW to 200 kW. The choice of bearings were carefully evaluated and the possibility of using active magnetic bearings were part of this evaluation. Mainly due to mechanical simplicity and cost savings, the choice was the AFB technology. With the AFB technology, the need of an electrical control unit and backup bearing systems could be eliminated, and bearings could generally be manufactured at a lower cost. In the development process of the rotor-bearing systems, a number of computer based design tools were employed. Besides an in-house rotordynamic code, a dedicated commercial state-of-the-art AFB code was used. Though all rotor-bearing systems were designed with a good margin to rotordynamical instability, actual prototype testing revealed severe stability problems with some of the designs. It turned out that the theoretical models were helpful as a rough guideline; however, the discrepancies between predictions and observations were simply unacceptable. However, at this point, a commercial potential were recognized by Siemens-ACC and it was decided to start up this research project in 2011. A research project with the goal of theoretically and experimentally investigate rotors supported by AFBs and develop the mathematical models and computer tools necessary to accurately predict their rotordynamical behaviour.

1.2 Literature study

Gas bearings have been intensively investigated, theoretically as well as experimentally, for nearly six decades [5, 14, 55, 66, 80–82] although some initial publications are dated back to the beginning of the last century [23]. Up until the mid-60s, only rigid surface bearings were investigated. Before 1960, existing applications were restricted to two specialized areas: gyroscopes for inertial navigation and gas circulators in nuclear reactors [66]. Later, they were widely employed in the manufacturing industry, in small scale grinding machines, drilling machines and hand tools, and in a wide range of medical and scientific instruments. A common application were in dental-drills in which two rigid surface air bearings support a small turbine, driven by pressurised air, operating at a velocity of up to 500,000 RPM. After 1960, the compliant surface gas bearings (that is the AFBs) were matured. Garrett AiResearch were the pioneers within

the AFB development and built several laboratory and prototype machines in the mid-60s. Their first production air cycle machine (ACM) using AFBs was developed for the environmental control system (ECS) of the DC-10 jet airliner in 1969 [1]. Other examples are the ACM of the F-16 aircraft that switched from roller bearings to AFBs in 1982, and today, all modern jet airliners utilise AFBs for their ACM. The introduction of AFBs into commercial aircrafts from 1969 up until the middle of the 1980s was a clear indicator of a mature technology. As a consequence, compliant foil bearings found their way into an increasing number of industrial applications within high-speed rotating machinery over the next three decades. The current tendency is that the technology is progressing from small high-speed rotating machinery, like micro turbines and aforementioned equipment related to the aeronautical industries, towards larger mass-produced industrial compressors and turbines [28, 85]. In such industrial compressors, widely available today, the assembled rotor weight is often above 50 kg and the rated power up to 200 kW. The advantages of these compressors compared to conventional oil lubricated compressors are low mechanical power loss, clean non-contaminating operation and the fundamental simplicity of the mechanical design. The main disadvantages of AFBs are related to low load-carrying capacity, though greatly improved within the recent decade [19]; wear during starts and stops due to breakdown of the air lubrication film at low journal speeds; and finally, their limited mechanical damping. To limit the wear during starts and stops, PTFE coatings are commonly utilised but other types of coatings for instance PS304 has been investigated, in particular for higher temperature applications [17, 68]. As a consequence of the limited mechanical damping, the risk of rotordynamic instability is a fundamental issue. Though AFBs generally offer significantly better stability characteristics compared to rigid gas bearings, the stability of the AFB supported rotors are still a major concern, seen from an engineering perspective. As a result, much experimental and theoretical work has been conducted through the past three decades to achieve accurate mathematical models of the AFB dynamics. However, mathematical modelling of AFBs are still associated with significant uncertainties which makes the design of rotor-bearing systems challenging and sometimes very costly. In the following summary of published literature, a rough categorisation is made due to the multi-physical nature of the problem.

1.2.1 Simple elastic foundation model

Although mathematical modelling of the air film itself with the Reynolds equation has proven very accurate compared to experiments [33, 60, 66] and thermal effects are found to be negligible [58, 60, 77], the accurate prediction of the AFB static and dynamic behaviour has proven to be non-trivial. Their behaviour is determined by not only the fluid film but also the flexible element underneath

the bearing surface, altering it compliant. Several configurations are possible to obtain compliance; one of the most widely used is the usage of corrugated bump foils. The addition of these compliant elements to the design enables the introduction of additional damping to the one generated in the fluid film. The increase of damping is caused by hysteric energy dissipation due to the sliding friction forces, generated as the bearing surface deforms and induces displacements between the mating foil layers.

Heshmat [30, 31] was among the pioneers within mathematical modelling of AFBs with corrugated foils. He originally included the flexibility of the foil structure in the Reynolds equation by introducing a linear elastic displacement as function of the fluid film pressure, $h_c = K(p - p_a)$. The foil flexibility was based on the analytical expressions given by Walowit and Anno [84]. This model is commonly referred to as the simple elastic foundation model (SEFM). The SEFM was extended by several authors, for example [40, 41, 61, 63] to include a structural loss factor η for the compliant foil and a perturbation method, originally suggested by Lund [55], to obtain equations for the linearised stiffness and damping coefficients of the bearing. San Andrés and Kim [77] further extended the model to include thermohydrodynamic effects (THD).

Due to the simplistic nature of the SEFM, in which the entire structure of the flexible foils are represented by a linear stiffness and loss factor, it is associated with a number of assumptions and limitations; it assumes the foil stiffness to be linear and neglects the stiffening effect generated by friction forces in the sliding contact points; the foil deformation in any given point is assumed completely independent of the deformation in its neighbouring points; and finally, it does not take into account the top foil sagging between bumps. Depending on the particular foil configuration, for example the bump geometry and top foil thickness, and the amplitude of the deformation, these assumptions may lead to significant errors. However, Iordanoff [38] developed a more detailed analytical mathematical model for the bump foil stiffness which took into account the attachment of the first bump.

1.2.2 Foil structure and coupled fluid-structure models

As mentioned, the compliant surfaces of an AFB introduces additional damping to the one generated in the fluid film. The mechanism behind this additional damping is friction, which is highly nonlinear and introduces significant complexities when considering the accurate prediction of the behaviour of the foil structures. The challenges related to this accurate prediction have generated a significant number of publications, dealing with the theoretical modelling and experimental testing of foil bearings. The mathematical models of the foil struc-

tures can be divided into two main categories:

1) Simplified equivalent and analytical models in which the foil structure is represented by simple springs approximately equivalent to the actual structural members
2) Detailed models in which the foil structure is accurately mathematically modelled by means of, for example the principle of virtual work (VWP) and later discretised by finite element (FE) or finite difference (FD) methods

In the following presentation of literature, the terms *stiffness* and *damping* may refer to:

1) The structural stiffness and damping, that is the stiffness and damping of the foil structures alone without the contribution of the fluid film
2) The bearing stiffness and damping, which is the stiffness and damping coefficients provided by the entire bearing between the housing and the rotor while including the fluid film contribution

The main category of equivalent and analytical models include the work of Ku and Heshmat [44, 47, 48] who presented an analytical mathematical bump foil model based on the work of Walowit [84]. The model considered a circular bearing and took into account the effect of the pad location. The model provided predictions for structural stiffness, hysteresis and equivalent viscous damping. Nonlinear structural stiffness behaviour was attributed to the geometrical effects of having a circular journal loading the foils. They predicted that the dynamic bearing coefficients were anisotropic and highly nonlinear and that the stiffness and damping was dependent on the pad angle. Bump stiffness under different load distributions along the bump strip was also investigated [44] and the theoretical prediction followed the trend of earlier experimental data that indicated a higher structural stiffness of the bumps located close to the fixed end of the bump strip compared to those closer to the free end. Lower friction coefficients were found to decrease the structural stiffness, whereas an increment in friction increased the stiffness and could result in pinned bump ends for the bumps close to the fixed end. Experimental results of hysteresis curves for bump strips deformed between two straight surfaces were presented in [45]. One of the surfaces featured a pivot to enable tilting motion in order to obtain different load distributions over the foils. The effect of pivot location and different surface coatings were investigated and the bump deflections were recorded using an optical tracking system. 'Local' stiffness and damping were identified and found to be dependent on amplitude and load.

Peng and Carpino [61] were among the first ones to couple the bump structure with the fluid film in a mathematical model. Coulomb friction forces and bump flexibility were included by means of an equivalent continuous friction force and a spring constant. Stiffness and damping coefficients were calculated using the coupled model. No isolated validation of the foil structural model was included in this work. Meanwhile, Ku and Heshmat [29, 46] performed an experimental investigation of the dynamic behaviour of a compliant foil bearing and compared the results to the mathematical model presented in [44, 47, 48]. Agreement between the theoretical and experimental results was reasonably good. The results showed that the structural cross-coupled stiffness and damping coefficients are negligible and that the direct terms decrease with increasing dynamic amplitude. An increase of the excitation frequency was found to decrease the equivalent viscous structural damping and to increase the structural stiffness. Similar experiments were later performed by Rubio and San Andres [69, 70]. These authors compared the experimental results to the ones obtained using a simplified mathematical model, in which the bump foil contribution was represented by simple elastic springs. The stiffness of these springs were calculated by the analytical expression of Iordanoff [38]. Furthermore, the equivalent structural damping was, for a given bump geometry, determined experimentally by assuming a one DOF system to which the experimental data was fitted [70, 72]. This method is based on the assumption of harmonic oscillations which can be difficult to obtain in an experimental set-up. Temperature effects were also investigated [70] and found to be negligible. The dry friction coefficient was found to be nearly constant with the excitation frequency but dependent on the load amplitudes. The obtained friction coefficient values varied between 0.05 to 0.2.

A unique equivalent bump foil model including the effect of Coulomb friction was presented by Le Lez and Arghir [50, 51]. The foil structural model was composed of simple spring elements with elementary stiffness given by analytical expressions. The results were compared to a detailed FE model based on a commercial software as well as experimental data [50] with good agreement. Furthermore, the calculated structural stiffness was compared to the simple foil flexibility given by Walowit [84] and implemented in the simple elastic foundation model by Heshmat [30, 31]. The updated results indicated a significantly higher bearing stiffness compared to the reference, which can be explained by the stiffening effect caused by the dry friction. Peng and Carpino [12] also presented an equivalent foil structure model which they coupled to the fluid and presented linearised stiffness and damping coefficients based on a predefined circular rotor orbit. Finally, Le Lez *et al.* [50, 51] developed equivalent structural models taking into account the Coulomb friction in the contact zones. The theoretical models were compared to experimental results with good agreement and underlined the importance of taking into account the bump interactions and their individual state (stick-slip). Feng and Kaneko [21] developed a sim-

ilar equivalent foil model coupled with the fluid film equations and compared calculated film heights with experimental data [71].

In the abovementioned literature, the bump foil structure is mainly modelled by means of analytical or equivalent simplified models. Work based on detailed structural models derived by for example the principle of virtual work, following a discritization by for example FE or FD methods, includes among others the work presented by Carpino *et al.* [11] who developed a structural FE model of the bump and top foils. Simultaneously, Peng and Carpino [62] investigated the effects of Coulumb friction on the linearised bearing coefficients by means of an equivalent viscous damping coefficient. Their joint effort resulted in the first fully coupled mathematical model [63] with a detailed foil FE formulation and an equivalent viscous damping for the friction. Their model included the stiffening effect of the foil layers caused by the friction in the contact points. However, their work was purely theoretical. Lee *et al.* [54] coupled a detailed three-dimensional structural model with the steady-state solution of the Reynolds equation but did not include friction. They later suggested a mathematical model [53] incorporating both the fluid film pressure field described by the Reynolds equation and the structural dynamics of the foil. The solution was based on the FE method, and it was performed using a time domain integration routine. An algorithm to deal with the stick-slip phenomenon related to friction forces was incorporated as well. A parametric study was performed and hysteresis loops were presented for the bearings running under steady-state conditions. The dissipated energy for the individual bumps were calculated at a given unbalance. The study indicated that optimum values of bump stiffness and friction coefficients exist with regard to minimising the resonance vibration response of a rotor mounted on foil bearings.

Zywica [89, 90] simulated the top foil structure using commercial FE programs and compared the results to previously published results in [69]. The structural model was applied in a complex model [42] taking into account the fluid film pressure by solving the Reynolds equation. The study was of purely theoretical nature. San Andrés and Kim [74, 76] integrated FE models of the top foil structure into the steady-state solution and compared this result to experimental values [71]. The bump foils were modelled using the analytical mathematical expressions developed by Iordanoff [38]. However, their model did not take into account the stiffening effect caused by the friction forces in the sliding points. Heshmat [27] coupled the structural deformations obtained with a commercial FE program with the solution of the Reynolds equation for a thrust bearing. A study on different foil geometries and their effect on the steady state and dynamic linearised coefficients was performed by Hoffman *et al.* [33] using a coupled FE model but friction was neglected.

1.2.3 Time domain simulations

In most of the literature presented so far, the focus has been on static or steady-state frequency domain analysis. In this subsection, a collection of articles dealing with the time domain analysis of the compressible Reynolds equation, either coupled with structural models or alone, is presented. Historically, the rotor-bearing dynamic analysis in time domain has been based on the linear damping and stiffness coefficients obtained by different perturbation methods [55]. However, the rapid development of computer science and increasing computer power has enabled the solution of the mathematical models in time, allowing for the inclusion of gas compressibility and foil compliance in the models. Although almost a century has passed since the first publications about gas bearings, the accurate time simulation of gas bearings with compliant surfaces is still a challenging and very time-consuming task. Here, a selection of different articles dealing with the solution of the compressible Reynolds equation in time is presented.

Wang and Chen [86] used FD for the spatial and temporal dimensions when solving the Reynolds equation. They simulated the steady-state response of a perfectly balanced rigid rotor supported by two identical bearings. The spatial discretisation was performed with a central-difference scheme, while the temporal discretisation was performed with an implicit-backward-difference scheme. Furthermore, Successive Over Relaxation (SOR) was used in order to reduce the number of unknowns in the iteration step. Their solution took advantage of the bearings being rigid, hence only the rotor movement contributed to the temporal terms of the Reynolds equation. This made an explicit solution of the transient compressible Reynolds equation possible since a movement of the rotor resulted in a change in the gap and then a change in pressure, which then again affected the rotor. Arghir *et al.* [3] presented a finite volume solution where the pressure was implicitly integrated for a prescribed gap perturbation to calculate linear stiffness and damping coefficients dependent on the perturbation amplitude. In the procedure, the rotor was stationary in one direction, while in the other it was perturbed by a sinusoidal displacement. At each time step, the reaction forces from the air film was calculated, including the temporal terms of the Reynolds equation, and based on the displacement/velocity and reaction force pairs, the least square method was used to calculate the linear stiffness and damping for a given amplitude. This enabled the inclusion of the nonlinearities related to the rotor vibration amplitude in the analysis. The method is well suited for calculating the linear coefficients of a bearing with gap discontinuities. A common method to solve the compressible Reynolds equation in time is to substitute the temporal terms dp/dt and dh/dt by backward difference approximations, for example Song and Daejong [79] and Lee *et al.* [53]. In this case, these time derivatives will be lagging behind in time, and the time

steps needs to be very small in order to preserve the accuracy of the solution. Le Lez *et al.* [52] presented a similar method too [79]. The same method was also used in [88] to solve the transient Reynolds equation but with four-node planar FE for the spatial discretisation of the Reynolds equation and for a rigid gas journal bearing. As previously mentioned, Lee *et al.* [53] also used a four-node FE to solve the compressible Reynolds equation in time and space and a backward-difference iterative procedure to solve the pressure in time. This solution was used in conjunction with an FE model of the bump foil, affected by Coulomb friction at the bump foils contact points, to investigate the performance of a rigid rotor symmetrically supported by two bearings under different bearing configurations. In order to accelerate the time simulations, several authors have been consistently and diligently working on improving the numerical methods and developing new numerical strategies. A simplified method for evaluating the nonlinear fluid forces in air bearings was recently proposed by Hassini and Arghir [24–26]. The fundamental idea was based on approximating the frequency dependent linearised dynamic coefficients at several eccentricities by second-order rational functions in Laplace domain. By applying the inverse of Laplace transform to the rational functions, a new set of Ordinary Differential Equations (ODE) was obtained, leading to an original way of linking the fluid forces components to the rotor displacements. The numerical results showed good agreement with the results obtained by solving the full nonlinear transient Reynolds equation coupled to the equation of motion of a point mass rotor. By ensuring the continuity of the values of the fluid forces and their first derivatives and imposing the same set of stable poles to the rational functions, simplified expressions of the fluid forces were found, avoiding the introduction of false poles into the rotor-bearing system. In [26], the authors showed that the new formulation may be applied to compute the nonlinear response of systems with multiple degrees of freedom such as a flexible rotor supported by two air bearings. On the other hand, Bonello and Pham [9, 65] solved the nonlinear Reynolds equation by using an alternative state variable $\psi = ph$. Using this alternative state variable, it was possible to set up a set of ODEs and solve the Reynolds equation with all state variables calculated simultaneously at each time step, that is with the finite-difference state equations of the air films, the state equations of the foil structures and the state equations of the rotor model. In [10] they accelerated the time simulations by obtaining the state Jacobian matrix using symbolic computing followed by solving the ODEs using a readily available implicit integrator and a predictor-corrector approach.

1.2.4 Experimental work

Overall experimental investigations of AFBs were performed by several authors for example Ku and Heshmat [29, 46] who as previously mentioned performed

an experimental investigation of the foil structural behaviour of a compliant foil bearing and compared the results to the mathematical model presented in [44, 47, 48]. Rubio and San Andrés [69, 70] performed similar experiments, and San Andrés *et al.* [78] compared predicted unbalance response and critical speeds to experimental results. Dellacorte and Valco [19] experimentally investigated the load carrying capacity of foil bearings and derived a rule of thumb, and Howard [35] investigated the effect of misalignment on the bearing performance. However, the number of authors dealing with the experimental identification of the linearised dynamic stiffness and damping coefficients are limited. Howard *et al.* [34, 36] experimentally identified the dynamic coefficients of a foil journal bearing and investigated the temperature dependency. Matta *et al.* [56] identified the bearing coefficients of a rigid journal gas bearing. Ertas *et al.* [20] developed a floating bearing test rig for the identification of foil journal bearing coefficients and presented experimental results; San Andrés [73] identified the dynamic coefficients for a hybrid flexural tilting pad gas bearing.

More recently, Balducchi *et al.* [7] performed experimental tests of a thrust AFB. They presented experimentally obtained structural stiffness and equivalent damping of the foils as well as linearised bearing coefficients. Their results indicated that the linearised stiffness increased with increasing load frequency while the equivalent damping decreased. Balducchi *et al.* [6] also obtained the experimental unbalance responses of two slightly different rigid rotors, supported by two identical aerodynamic foil bearings, at rotation speeds comprised between 50 kRPM and 100 kRPM. The displacements in the two foil bearings were also measured during coast-down and presented in waterfall plots. They showed a nonlinear behaviour with sub-synchronous vibrations accompanying the synchronous component. The sub-synchronous components bifurcate at typical rotation speeds. The nonlinear behaviour was found dependent on the unbalance. The experimental results were compared with a simple theoretical model, built under the assumption that the air film in the two bearings is infinitely stiff compared to the foil structure. Many of the theoretical results could not be reproduced by the authors' simplified model.

1.3 Objectives and original contributions of this research project

Without accurate mathematical models for the prediction of the complex dynamic behaviour of AFBs, the technology will continue being associated with a limited amount of applications and its true potential will not be explored. The objective of this thesis is to contribute to bringing the technology out of the shadow by means of experimental and theoretical studies, adding to the general

understanding of the AFB dynamics and in particular the dynamics of a rigid rotor supported by two identical AFBs. This thesis is a summary of the work presented in the papers [P1-P6]. In the following, the original contribution of each of these papers is highlighted.

In [P1], a foil bearing is analysed using the SEFM and the mathematical model is perturbed using a complex notation. This allows for the introduction of a complex stiffness and a loss factor for the foils. The solution is based on the FE method and the structural stiffness is approximated using the analytical expression given by Walowit and Anno [84]. The fluid film model is validated against experimental pressure profiles from the literature [66], by simulating a rigid bearing. Good agreement is found between the pressure profiles obtained experimentally and theoretically. The main original contribution of [P1] is the detailed comparison of the minimum static film heights and attitude angles obtained theoretically against experimental values from the literature [71], when two sets of boundary conditions are used. These boundary conditions deal with the problem of zero foil deflection on the edges subjected to ambient pressure. It is concluded that the correct choice of boundary condition depends on the foil configuration of the specific bearing under investigation.

The paper [P2] focuses on the isolated dynamical behaviour of a bump foil strip. A quasi-static mathematical model of a bump foil strip, in which the sliding friction is modelled using an original approach, is presented. The theoretically obtained deflections, stiffness and hysteresis loops are compared to original results obtained experimentally. The experiments are performed using a dedicated test rig in which a foil strip is compressed between two flat surfaces, both statically and dynamically, while simultaneously measuring the compression force and the compression movement between the plates. Good agreement is found for the static results; however, discrepancies appear for the dynamic ones. The paper clearly illustrates how the stiffness approximated by simple analytical expressions, without taking into account the stiffening effect provided by the Coulomb friction, is underestimated by almost one order of magnitude. It also highlights how a 'local' oscillation upon a static loading will result in an even higher stiffness. Finally, a 'flattening' tendency of the hysteresis loops at higher frequencies is found. Though this tendency was confirmed in later experiments [15], it was found to be less prevalent.

In [P3], an original and efficient method for solving the nonlinear Reynolds equation for compressible fluids is presented. It is based on an implicit Newton-Raphson (NR) method and applied on the perturbed SEFM [P1] with the addition of a correction term for the foil stiffness formulation, allowing for top foil sagging between bumps. The FE formulation and implementation is thoroughly explained and the method is compared to the Successive Under Relaxation (SUR) method, which is commonly used. The NR based method is found

to be superior in terms of computational efficiency.

As mentioned, there is a lack of publications dealing with the experimental identification of the linearised stiffness and damping coefficients of AFBs. In [P4], experimental and theoretical analysis of a rigid rotor supported by AFBs is presented including experimental identification of the stiffness and damping coefficients. The experimental identification is performed by means of a dedicated rotor test rig, and the coefficients are compared to the theoretically predicted ones. The theoretical model is based on the perturbed model in [P3] but with a 2D-plate implemented for the top foils. The perturbed first-order equations are based on the SEFM. The main original contribution of the paper is related to the linearised bearing coefficients, experimentally obtained, and the unique idea of distinguishing between a static and a dynamic bump foil stiffness for the zero- and first-order equations respectively. Good agreement between the experimental and theoretical results were found.

The paper [P5] presents numerical time domain simulations of a rigid rotor supported by two identical AFBs. The rotor and bearings are similar to the test rig treated in [P4]. The original contribution is related to the implementation of a technique for time domain analysis from Bonello and Pham [9, 65]. The method is extended by coupling the rotor and AFBs state-equations and solving for the coupled rotor-bearing response to unbalance. Furthermore, the discretisation of the fluid film, that is the Reynolds equation, is performed by means of the FE method contrary to the FD methods originally described. The implications this has on the boundary conditions are thoroughly explained. Finally, it is highlighted how a rotor unbalance can drive an otherwise stable rotor-bearing system into a nonlinear regime in which subsynchronous vibration components appear.

The time domain simulations described in [P5] is further treated in the paper [P6]. Here, the mathematical modelling of the test rig rotor and AFBs are refined by more accurate approximations for the foil structural stiffness and loss factor. Specifically, the stiffness and loss factor of the bump foils are now based on the results of the foil structural model presented in [P2]. Simulations of the rotor unbalance response at a variety of different rotor speeds are compared to results experimentally obtained from a free rotor coast down. At a certain unbalance level, these experiments clearly show how the subsynchronous vibration components, described in [P5], appear and disappear. The main original contribution of the paper is tied to the unique experimental data presented and the demonstration of a numerical method capable of predicting the nonlinear rotor unbalance response, including the appearance and disappearance of the subsynchronous vibrations, to a very high degree of accuracy.

1.4 Outline of the thesis

At DTU, a PhD thesis can be presented either by submitting a monograph or a paper-based thesis. The paper-based thesis is a composition of a summary of papers conducted during the PhD project period. The included papers form the basis of the research work accompanied by a summary thesis. The thesis includes a comprehensive introduction to the research field, explains the theoretical methods employed in the work and highlights the original contributions. This thesis is submitted as a paper-based thesis and summarises the work carried out during the PhD study; it is divided into six chapters and gives an overview of the results presented in the six publications [P1-P6].

Chapter 2 gives an introduction to AFBs in general and the Siemens-ACC AFB in particular. Basic design and dimensioning are explained and the importance of solid lubrication is highlighted. Furthermore, the adjustment of the clearance, the importance of the bump foil geometry and some basic details on the manufacturing of AFBs are explained.

Chapter 3 describes the basic mathematical models used for the theoretical analysis and, to some extent, in the experimental identification of bearing coefficients. The chapter separates the mathematical modelling into three subdomains: mathematical modelling of the bearing foil structure, mathematical modelling of the lubricating air film, and finally, the modelling of the rigid shaft. For the shaft and the foil structure, discretised FE equations are derived readily. For the air film however, the discretisation of the mathematical model is reserved for Chap. 4 because this will be dependent on the specific type of analysis to be performed.

Chapter 4 introduces a perturbation of the SEFM to enable the calculation of the linearised stiffness and damping coefficients. A discretised solution based on the FE method is given. In order to improve the SEFM, a modified model is introduced. This model is referred to as the CFSM and incorporates a slightly more complex foil model for the static solution. Finally, a nonlinear transient solution of the SEFM in the time domain is introduced. This solution is coupled in order to simulate a rigid rotor supported by two identical AFBs.

Chapter 5 presents the experimental approaches followed in this PhD work. These are related to the development and instrumentation of two different test rigs: one for characterising the bump foil structures, and one for experimentally identifying the linearised bearing coefficients and investigating the rotor response to unbalance. The test rigs are thoroughly described and all relevant dimensions, enabling reproduction of the experiments, are given. Finally, the identification procedures are described and measurement uncertainties are dis-

cussed.

Chapter 6 highlights some of the main results obtained and published in the publications [P1-P6]. Only the main results and findings are presented, that is the results related to validation of methods and computer codes are left out. It is however, still recommended to study the appended publications. The chapter presents: hysteresis curves of the bump foil strips, linear bearing coefficients, and rotor response to unbalance, all obtained both theoretically as well as experimentally. Finally, the stability of the assembled rotor-bearing system is investigated using both linear and nonlinear methods.

Chapter 2

AFB fundamentals

Until this point of the thesis, the AFBs have been described as having an elastic layer under the bearing surface altering the bearing compliance. In this chapter, different types of radial AFBs, basic AFB dimensioning, measurement and adjustment of the bearing clearance, and basic manufacturing techniques will be discussed.

2.1 Siemens-ACC AFBs

The compliances of the bearing surface in a radial AFB can be achieved by means of a number of different designs [13, 18]. A search on patents and patent applications related to compliant bearings reveals a large amount of different methods to achieve the compliance of the bearing surface. These methods involve, for example the addition of an array of simple helical springs or leaf springs under the bearing surface or even a layer of wire mesh. However, the two most common designs are based on either a pattern of leaf foils as illustrated in Fig. 2.1a or a layer of corrugated foils, that is bump foils as illustrated in Fig. 2.1b. The leaf pad AFB, Fig. 2.1a, offers compliance due to deflection of the individual leaf foils and, at the same time, sliding friction occurs in the contact points leading to energy dissipation. In addition to energy dissipation caused by friction, this type of bearing offers additional viscous damping due

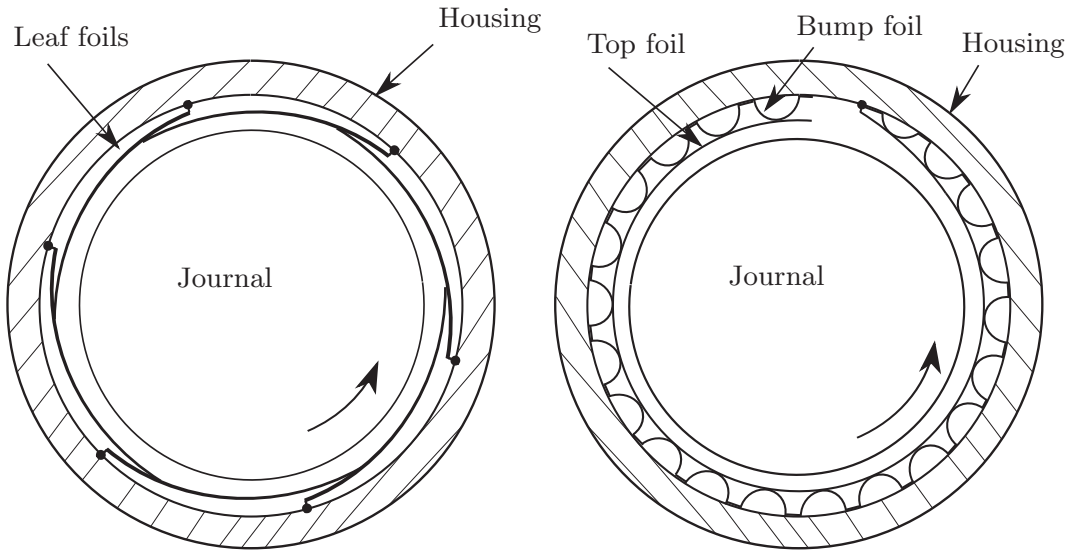

(a) Leaf spring bearing. (b) Bump foil bearing.

Figure 2.1: Schematics of two types of common journal AFBs; (a) leaf foil bearing, (b) bump foil bearing.

to the opening and closing of small gaps between each leaf foil, resulting in a pumping or squeeze film effect. These small gaps are associated with the overlapping of one leaf foil over the next leaf foil leaving a small gap that can open and close dependent on the loading on the foils. The film pressure profile of a lightly loaded leaf foil bearing consists of several local pressure peaks, one for each leaf foil. This is a consequence of the converging gaps formed between the journal and the pattern of leaf foils. Though the bearing illustrated in Fig. 2.1a only features six leaf foils, it is not uncommon to have up to 20 leafs in a bearing. The leaf foil AFB is used by Siemens-ACC in its smallest compressor (75 kW). It is proved to offer great stability characteristics and the compressor operates with extremely low external vibration levels, that is when measured on the motor casing. However, the load carrying capacity of the leaf foil bearing is low compared to the bump foil AFB as illustrated in Fig. 2.1b.

The bump foil AFB offers compliance by adding one or more layers of flexible bumps between the housing and the top foil. When the bump foils deform, energy is dissipated in the contact points between bump foils and housing and bump foils and top foils. Since the number of pads are usually below six, the bearing offers a larger supporting area for the film pressure to build up upon and hence a higher load carrying capacity compared to the leaf foil bearing. The bump foil bearing can be configured in a variety of different ways for example with a different number of pads or a different number of foil layers and combinations [1]. The bearing illustrated in Fig. 2.1b is the most simple configuration

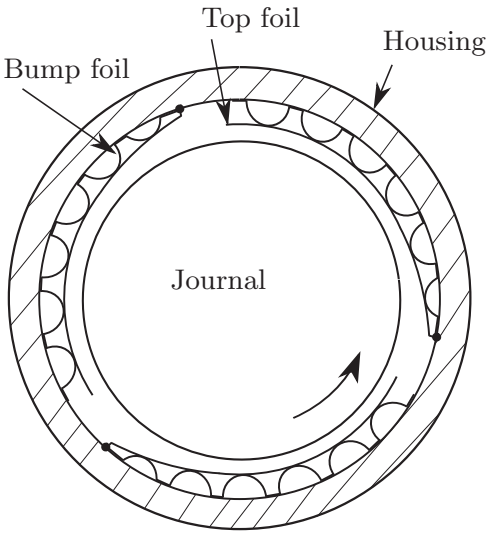

(a) 3-pad segmented bump foil bearing.

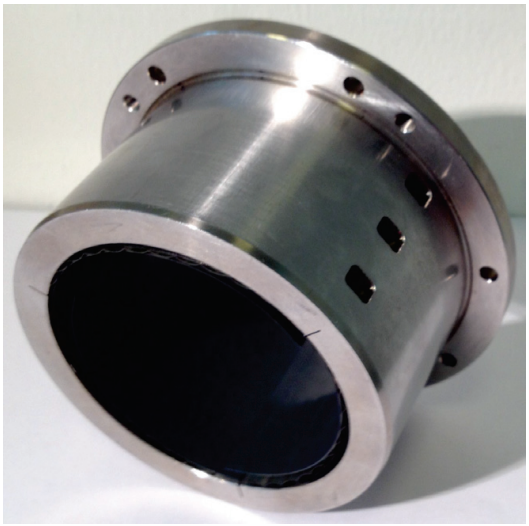

(b) 3-pad segmented bump foil bearing (R = 33.5 mm).

Figure 2.2: Schematics and photo of a Siemens-ACC 3-pad segmented AFB with bump foils.

and is commonly referred to as a first generation AFB [19]. Note the direction of rotation compared to the top foil attachment point. For a single pad foil bearing, the direction of rotation is always from the free end of the pad towards the attachment point to prevent the pad being ripped off by capstan/Eytelwein winch forces. For bearings with more than one pad, the direction of rotation can be both ways compared to the pad attachment points. The AFB of the larger Siemens-ACC compressors (up to 200 kW) can be categorised as being a second generation bearing as it incorporates bump foil layer, sliced-up in the circumferential direction which enables slightly offset bumps between each slice (see. Fig. 2.3). This offset provides an improved support of the top foils. A third generation bearing is defined as having a varying stiffness, that is a varying bump foil geometry along the circumferential direction, which the Siemens-ACC bearings do not have [19]. This thesis focuses on the second generation Siemens-ACC bump foil AFB, which is illustrated in Fig. 2.2. As seen from Fig. 2.2a, the bearing is designed in such a way that the journal rotates from the attachment points towards the free ends of the pads. The direction of rotation combined with a slight retraction of the pads, towards the bearing housing at the attachment points, generates a converging gap between the top foil and the journal which has proven to increase the stability characteristics in the Siemens-ACC compressors. The retraction also eliminates the risk of having rotor-pad contact in the attachment points, which are less compliant compared to the rest of the pad surface.

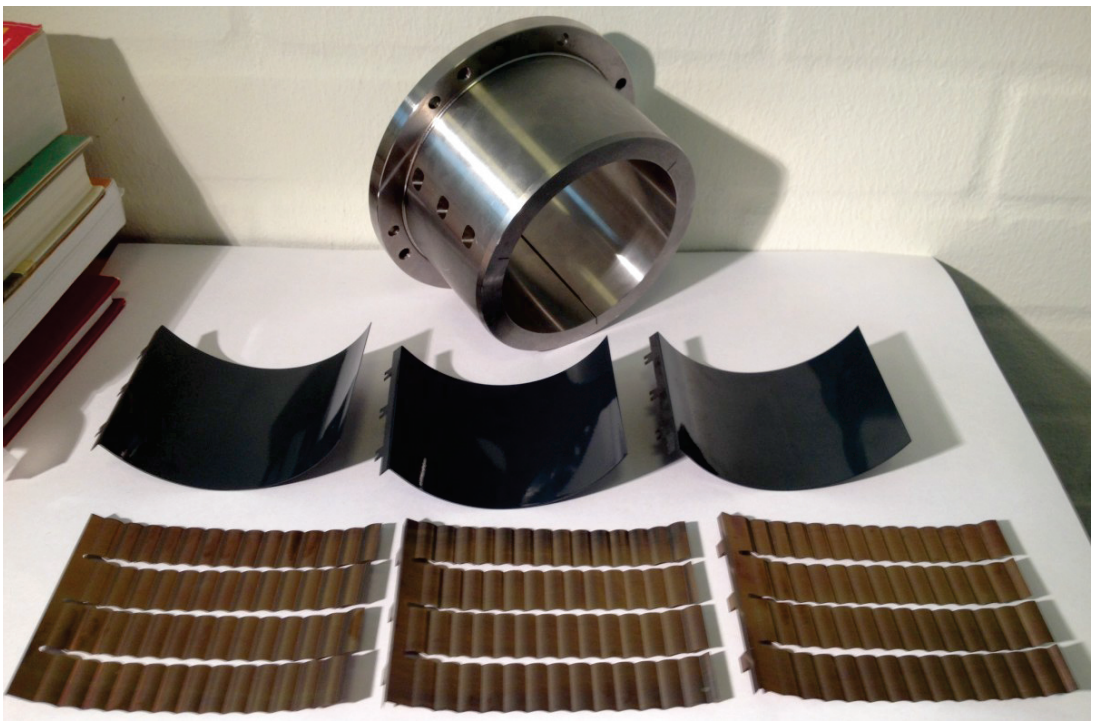

Figure 2.3: Siemens-ACC AFB broken down in parts. First row (from the top): the bearing housing with through holes for foil attachment. Second row: the top foils after heat treatment and coating with PTFE. Third row: the sliced and offset bump foils after heat treatment.

A Siemens-ACC bump foil bearing, broken down in its parts, is illustrated in Fig. 2.3. It is clearly seen from the picture that the AFB is extremely simple compared to other types of bearings. It consists of three different parts only: the housing, the top foils and the bump foils. The foils depicted are heat treated and coated and ready to be mounted inside the housing. The attachment of the foils in the housing[1] is based on a simple technique in which flaps on the foils are put through three holes in the bearing housing and bent while carefully adjusting the height of the foil in the attachment point, that is the retraction of the foil. This adjustment is performed by first mounting all foils loosely in the housing without the flaps being bent. Next, the bearing with these loose foils is installed on a dummy journal. Shims with predefined heights h_s are then pressed in between the journal and the three pads in the attachment points, such that the pads are retracted the distance h_s before the flaps are finally bent and the pads and foils are securely fixed in their current positions.

[1]Pat. pend. No. EP2706245 A1

2.2 Dimensioning

As previously mentioned, AFBs offer a low load carrying capacity compared to oil lubricated bearings, and therefore, they need higher operating speeds to form a lubricating film and separate the journal from the pads. Consequently, wear will occur during starts and stops, that is before the film is built up when starting and after the film breaks down when stopping, respectively.

With regard to machines which are anticipated to be operated with a high number of starts and stops within the machine lifetime, it is necessary to consider wear at the design stage. Solid lubricants like, for example PTFE coatings on the top foils are commonly used to reduce the wear. Though these coatings eventually will wear down after a certain number of starts and stops, they serve to increase the bearing life significantly. To estimate the maximum load that can be carried by an AFB before the lubrication film breaks down, a general rule of thumb was given by Dellacorte and Valco [19] as:

$$W_m = L_c L D^2 \omega \tag{2.1}$$

where L_c is the load coefficient, L is the bearing length, D is the bearing diameter, ω is the journal rotational speed and W_m is the maximum load the bearing is capable of supporting before the lubrication film breaks down. Regarding the Siemens-ACC AFB, the load coefficient is experimentally found to be $L_c \approx 1.5 \cdot 10^3$ kg/(m^{2}s). It is an approximate number that generally depends on the bearing design, for example generation one, two or three [19]. By knowing the load coefficient L_c, a new AFB can be dimensioned from (2.1). With regards to machines anticipated to have a high number of starts and stops, the length L and diameter D are chosen to obtain a low value of ω, that is the speed at which the lubrication film is formed should be low. How low depends on: a) the wear properties of the solid lubricant; b) the journal load; c) the polar moment of inertia of the rotor and d) the design criteria, that is how many starts and stops. All are known quantities except for the propagating wear of the solid lubricant. Therefore, start-stop experiments needs to be performed in order to accurately determine the start-stop capacity of each individual machine. Experiments conducted by Siemens-ACC show that by choosing bearing dimensions so that $\omega \approx 2,500$ RPM, a start-stop capacity of more than 20,000 start-stop cycles can be anticipated with a standard PTFE coating and a journal surface roughness of 0.1 μm [R$_a$].

Regarding shafts supported by two AFBs subjected to unequal loads $W_{m1} \neq W_{m2}$, it is important to dimension the bearings to have the same film breakdown speed ω. If the film in one of the bearings breaks down at a higher speed during coast down, this bearing will wear down quickly and limit the lifetime of the machine. This is because the bearing effectively acts as a brake when the

lubricating film disappears and hence, if the film breaks down in one bearing before the other, this first bearing will have to take up most of the braking energy leading to excessive wear. With regards to bearings having a similar length to diameter ratio, for example $L/D = 0.8$, the ratio between the diameters should be

$$\frac{D_1}{D_2} = \sqrt[3]{\frac{W_{m1}}{W_{m2}}} \tag{2.2}$$

to make sure that both bearings experience approximately the same amount of wear and the lifetime of the machine is maximised.

Another concern regarding the basic dimensioning of the AFBs is related to the power loss generated in the bearing. The relation between the bearing dimensions, the operating speed and the power loss generated can be approximated by Petrov's equation

$$P_b = \frac{2\pi\mu R^3 L\omega^2}{C} = C_1 R^3 L\omega^2 \tag{2.3}$$

in which the coefficient C_1 can be experimentally obtained, for example by free coast down tests. From such tests with rotors of different sizes, the loss coefficient is found to be $C_1 \approx 10$ kg/(m^{2}s) for the Siemens-ACC AFB. Like the load coefficient L_c, it is an approximate number that generally depends on the bearing design, for example generation one, two or three [19]. Thus, for the bearings primarily investigated in this thesis ($D = 67$ mm and $L = 53$ mm), the power loss is $P_b \approx 170$ W per bearing at 28,000 RPM.

2.3 Clearance

The clearance of an AFB is not as well defined in contrast to the clearance of a rigid oil lubricated journal bearing. In fact, due to its compliant nature, there is no clearance between the journal and the bearing pads at standstill. However, the stiffness of the bearing surface is very low until a certain deflection is reached; this is because the compliant foil layers need to settle before actual deformation of the bumps occur.

The deformation at which the foil layers are settled is defined as the clearance C of the bearing [67]. A schematics illustrating the definition of the bearing clearance is given in Fig. 2.4c and a device for measuring this clearance is illustrated in Fig. 2.4a and 2.4b. Here, a mass of 10 kg can pull the bearing up or down towards a dummy journal while simultaneously measuring the position of the bearing housing. The mass is chosen to consistently settle the bearing surfaces and allow for accurate clearance measurements. The bearing surfaces

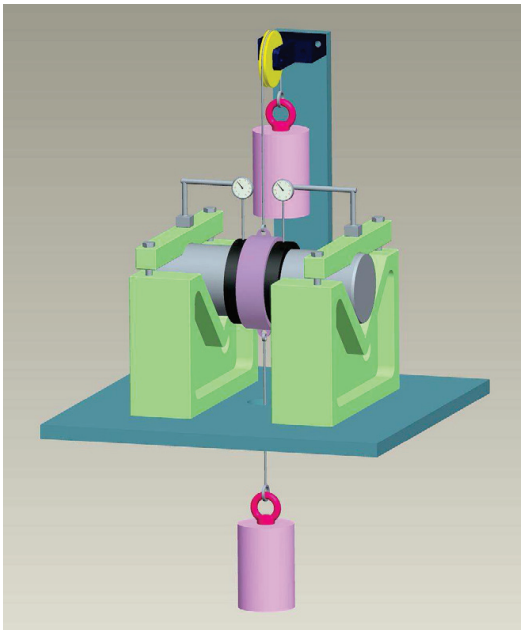

(a) Schematics of test stand for measuring bearing clearance of a Siemens-ACC AFB.

(b) Photo of test stand for measuring bearing clearance of a Siemens-ACC AFB.

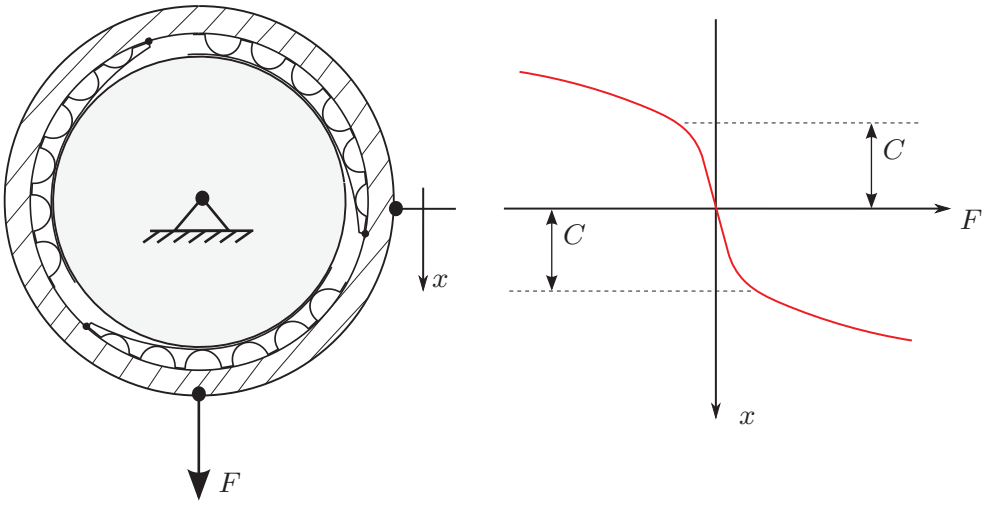

(c) Schematics illustrating the definition of the bearing clearance C.

Figure 2.4: a,b) Test stand for measuring bearing clearance of a Siemens-ACC AFB. c) Schematics illustrating the definition of the bearing clearance C.

are considered settled when the force-displacement curve flattens out, as seen in Fig. 2.4c. The clearance is measured at three angular positions and the mean value is calculated. In case the clearance needs adjustment, thin layers of metal film are placed between the bump foils and the housing, and the clearance

measurement is repeated.

2.4 Bump foil geometry

One of the most critical parts of the AFB design is the bump foil geometry. The geometry of the bump foil layers basically determines the stiffness supporting the bearing pads or in other words the compliance of the bearing. If the bump foil is too stiff, the compliance will be low and the bearing will be more sensitive to misalignment and other imperfections. A bump foil layer that is too stiff might also offer less structural damping compared to a softer one because movement in the contact points, with dry friction, will be reduced. On the other hand, if the foils are too soft, the yield stress of the foil material may be exceeded during operation with failure as the result. A poorly designed foil geometry might result in dominating normal forces in the contact points, leading to lock-up of the contacts and thus a very high stiffness and no hysteresis damping at all. Optimizing the bump foil geometry to provide maximum hysteresis damping and compliance with a sufficient margin of plastic deformations is certainly not straightforward. To accomplish this, the load or consequently the lubrication film pressure, needs to be known and an accurate mathematical model of the foil structure, including friction effects, is required. This thesis does not give a final recipe on bump foil optimisation, though an accurate mathematical bump foil model is described in [P2]. However, it is important to highlight that a well-designed bump foil layer is often the difference between a well-functioning bearing offering good damping characteristics and a poorly performing bearing leading to instabilities and failures.

2.5 Manufacturing

In this section, some fundamental manufacturing methods are discussed. However, some specific manufacturing details associated with the Siemens-ACC bearings, such as tolerances coating technique etc., are classified and will not be mentioned. Regarding the Siemens-ACC AFB, the housing is manufactured in AISI 316L, a standard stainless steel, but the choice of housing material is not critical. The material of the foils; however, needs to possess certain properties. Both the top foils and the bump foils are manufactured in Inconel X750 nickel-chromium-based super alloy, which is precipitation hardenable and commonly used for gas turbines, aircraft structures, etc. This material has a very low initial yield stress that allows it to be accurately shaped in a die press, as illustrated

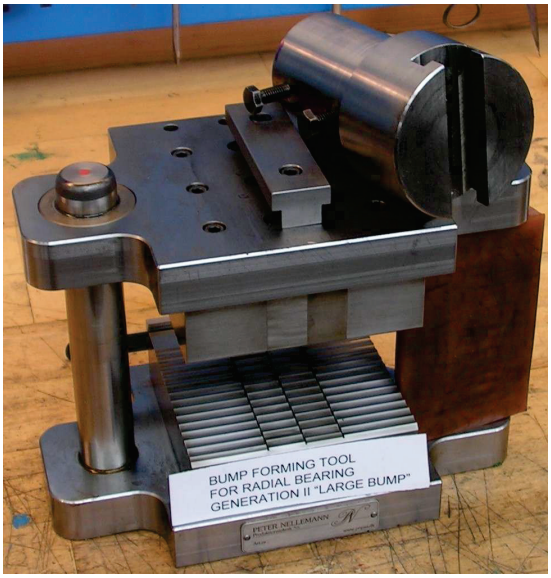

(a) Die press tool for pressing the bump foils.

(b) Heat treatment form to be used in connection with heat treatment of top foils.

Figure 2.5: Tools for manufacturing the bump and top foils; (a) Bump foil press tool. (b) Heat treatment form for the top foil.

in Fig. 2.5a, before the yield stress is significantly increased by a heat treatment procedure. After the heat treatment, a yield stress of more than 1,000 MPa is obtained, which, for the bump foils in particular, is necessary to avoid plastic deformations during operation. Both the bump foils and the top foils are heat treated. To ensure conformity to the journal, the latter can be heat treated in a die, as illustrated in Fig. 2.5b. However, Siemens-ACC has recently introduced pre-bent top foils using a dedicated roller and thus eliminated the need for the heat treatment dies. After heat treatment, the top foils are coated with a layer of PTFE and the foils can be mounted in the housings, adjusted to achieve the right inlet slope and fixed (see Fig. 2.3).

2.6 Summary on AFB fundamentals

In this chapter, the fundamental design and manufacturing methods related to AFBs was briefly described. As initially pointed out, the chapter does not serve as a complete design and manufacturing recipe, but rather as a basic introduction to the technology. Furthermore, the definition of the bearing clearance C and the method used for measuring it was thoroughly explained. As men-

tioned, the bearing clearance C is a fundamental parameter of and AFB and it is repeatedly referred to through out this thesis. For more information on the manufacturing, adjustment and testing of AFBs, Chen *et al.* [13] and Dellacorte *et al.* [18] both give a good introduction.

Chapter 3

Mathematical modelling

One of the main objectives of this thesis is to obtain an accurate mathematical model, enabling the accurate prediction of the dynamic behaviour of rigid rotors supported by AFBs. The dynamical behaviour of such systems are determined by the behaviour of the spinning rotor and its interaction with the bearings in which the lubricating air film interacts with the bump and top foils. In short, a structural, aero-dynamical interaction is occurring in the rotor-bearing system during operation. Hence, the theoretical analysis of rotors supported by AFBs is a coupled fluid-structure problem. Because such a problem often depends on more than one governing equation, one for each domain, it tends to be significantly more complex compared to a decoupled problem. It is therefore advantageous to model the two domains, fluid and structure respectively, in their simplest possible way. More specifically, this is done by discarding all insignificant effects/phenomena associated with each domain while preserving the fundamental original behaviour. The result of an oversimplification is an insufficient mathematical model unable to accurately predict the dynamical behaviour of the rotor-bearing system. Special attention is thus given to each domain of the AFB, which are separately modelled and later coupled together, solved and compared to experimentally obtained results. In this chapter, the mathematical modelling of the fluid and structure domains, associated with the AFB, are introduced as well as a simple structural model of the rigid rotor.

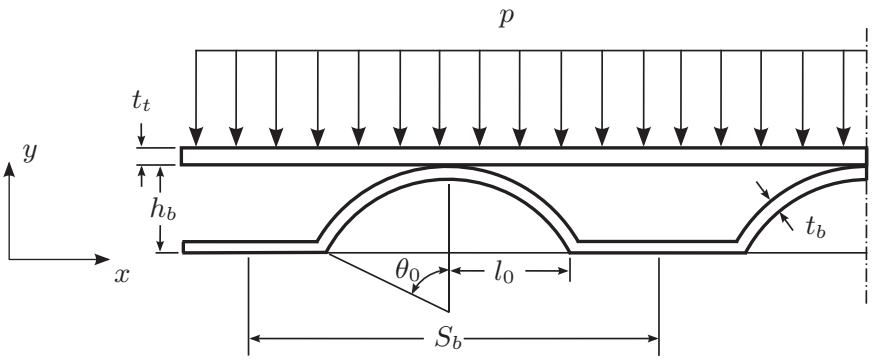

Figure 3.1: Schematics of 3/2 period of the bump and top foil geometry, subjected to a uniform pressure, with the associated nomenclature.

3.1 Foil structure models

As mentioned in Chapter 2, the structural compliance of the AFBs investigated in this thesis, is mainly generated in the bump foil layer under the bearing pads/top foils. A section of the bump and top foil structure is illustrated in Fig. 3.1. In this section, two mathematical models for the foil structure are presented. The first is the well known [30, 31] and highly simplified SEFM and the second is a detailed complex FE based model.

3.1.1 SEFM

The simplest mathematical model for the foil structure is given by Walowit and Anno [84] as

$$h_c = K(p - p_a) \tag{3.1}$$

where h_c is the deformation in the foils and the flexibility is given as

$$K = \frac{2S_b}{E}\left(\frac{l_0}{t_b}\right)(1-\nu^2). \tag{3.2}$$

This structural model is commonly referred to as the SEFM and it only takes the deformation of the bump foils into account. However, an extension can be made [P3], which adds the flexibility of the top foils to (3.2) so that

$$K = \frac{S_b^4(1-\nu^2)}{Et_t^3}\left(\frac{1}{60} - \frac{3}{2\pi^4}\cos\left(\frac{2\pi\tilde{\theta}}{S_b}\right)\right) + \frac{2S_b}{E}\left(\frac{l_0}{t_b}\right)(1-\nu^2). \tag{3.3}$$

Due to the obvious simplicity of the SEFM, it is relatively easy to couple to a mathematical model of the lubricating fluid film. However, it introduces some

fundamental assumptions such as: 1) the stiffness of the foil structure is linear, 2) the stiffness is constant over the length and angular extension of the pads, 3) the deformation of one point of the pad is completely independent of the deformation of any neighbouring points. But most important: 4) the effect of friction force in the sliding contact points between the top foil, the bump foil and the housing is discarded. Other equivalent and simplified models exist, for example [38], and some of them include frictional effects, for example [50, 51]. However, the SEFM as given by Walowit and Anno [84] still seems to be the most common and is widely used.

In order to investigate the validity of the assumptions and limitations associated to the SEFM, especially the assumption that the friction force does not affect the bump foil stiffness, it was decided to develop a refined mathematical model of the foil structure based on FE methods.

3.1.2 FE formulation - structure

A mathematical model of the foils is developed with the goal of accurately describing the mechanical behaviour of the bump foils, enabling the investigation of geometrical nonlinearity and the nonlinear friction forces and their effect on the overall stiffness and energy dissipation of the foils. The reason for investigating the effect of geometrical nonlinearities, or large deflections, is related to the shape and support of the bumps. When compressing a bump, its two supports, that is the bump ends, will move away from each other causing an increased span which could lead to a softening effect. By including the ability to take into account the geometrical nonlinearities, the significance of this softening can be investigated. On the other hand, the friction forces in the contact points, that is the bump ends may lock or restrict the movement of these ends so that a stiffening effect may arise. By including the friction forces, the significance of this effect can be investigated as well.

The model introduced in the following text has previously been presented in the publication [P2]. In this publication though, some details regarding the structural finite element formulation were left out. For the sake of completeness, the mathematical model is expanded in this chapter and derived from the VWP and discretized by use of a nonlinear FE procedure based on an implicit NR method. The FE formulation is based on an isoparametric four-node bilinear quadrilateral plane finite element, which is illustrated in Fig. 3.2. The formulation of the element, its shape functions N_i, Jacobian matrix $[J]$, strain-displacement matrix $[B_0]$, etc. can be found in most books on linear FE, for example Cook [16], Sec. 6.2. Therefore, the linear part of this isoparametric element formulation is omitted here and the focus is set on the nonlinear part of the theory with

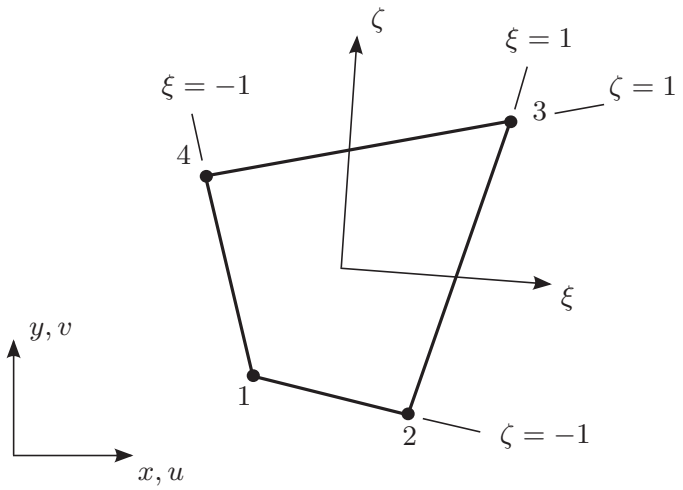

Figure 3.2: Schematics of a four-node isoparametric plane element in physical space with ξ, ζ coordinates applied on it.

the goal of obtaining the residual vector $\{R\}$ and tangential stiffness matrix $[K_t]$ which, in combination with an implicit incremental NR solution scheme, are used to obtain the solution of the nonlinear structural problem. The NR scheme is explained in App. B.

Green-Lagrange strain-displacement measures

In order to model the bump foil structure using large displacement theory, it is convenient to use the Green-Lagrange strain measure instead of the more commonly used Cauchy strain measure. The Green-Lagrange strain measure can be written as

$$\begin{aligned}
\varepsilon_{11} &= \frac{\partial u}{\partial x} + \frac{1}{2}\left[\left(\frac{\partial u}{\partial x}\right)^2 + \left(\frac{\partial v}{\partial x}\right)^2\right] \\
\varepsilon_{22} &= \frac{\partial v}{\partial x} + \frac{1}{2}\left[\left(\frac{\partial u}{\partial y}\right)^2 + \left(\frac{\partial v}{\partial y}\right)^2\right] \\
\varepsilon_{12} &= \frac{1}{2}\left[\frac{\partial u}{\partial y} + \frac{\partial v}{\partial x}\right] + \frac{1}{2}\left[\frac{\partial u}{\partial x}\frac{\partial u}{\partial y} + \frac{\partial v}{\partial x}\frac{\partial v}{\partial y}\right]
\end{aligned} \tag{3.4}$$

or in vector form as:

$$\{\varepsilon\} = \{\varepsilon_0\} + \{\varepsilon_L\} = \begin{Bmatrix} \frac{\partial u}{\partial x} \\ \frac{\partial v}{\partial y} \\ \frac{\partial u}{\partial y} + \frac{\partial v}{\partial x} \end{Bmatrix} + \frac{1}{2}[A]\{\Theta\} \tag{3.5}$$

where $\{\Theta\}^T = \{\{\Theta_x\}^T \ \{\Theta_y\}^T\}$ and the matrix $[A]$ is defined as

$$[A] = \begin{bmatrix} \{\Theta_x\}^T & \{0\} \\ \{0\} & \{\Theta_y\}^T \\ \{\Theta_y\}^T & \{\Theta_x\}^T \end{bmatrix}, \quad \{\Theta_x\} = \begin{Bmatrix} \frac{\partial u}{\partial x} \\ \frac{\partial v}{\partial x} \end{Bmatrix}, \quad \{\Theta_y\} = \begin{Bmatrix} \frac{\partial u}{\partial y} \\ \frac{\partial v}{\partial y} \end{Bmatrix} \tag{3.6}$$

and the vector

$$\{\Theta\} = \begin{Bmatrix} \{\Theta_x\} \\ \{\Theta_y\} \end{Bmatrix} = \begin{Bmatrix} \sum_i N_{i,x} u_i \\ \sum_i N_{i,x} v_i \\ \sum_i N_{i,y} u_i \\ \sum_i N_{i,y} v_i \end{Bmatrix} = [[g_1]\,[g_2]\,[g_3]\,[g_4]] = [G]\,\{d\} \tag{3.7}$$

in which the components of $[G]$ is

$$[g_i] = \begin{bmatrix} N_{i,x} & 0 \\ 0 & N_{i,x} \\ N_{i,y} & 0 \\ 0 & N_{i,y} \end{bmatrix}. \tag{3.8}$$

The shape functions N_i and the Jacobian matrix $[J]$ are as mentioned given by Cook in [16], Sec. 6.2. The relation between the shape function derivatives with respect to the Cartesian coordinates x, y and the reference coordinates ξ, ζ are

$$\begin{Bmatrix} N_{i,x} \\ N_{i,y} \end{Bmatrix} = [J]^{-1} \begin{Bmatrix} N_{i,\xi} \\ N_{i,\zeta} \end{Bmatrix}. \tag{3.9}$$

The relation between the strain and displacement variations is defined as

$$\{\delta\varepsilon\} = \left[\bar{B}\right]\{\delta d\}. \tag{3.10}$$

It can then be shown that the deformation dependent strain-displacement matrix is

$$\left[\bar{B}\right] = [B_0] + [B_L], \quad [B_L] = [A(\{d\})]\,[G] \tag{3.11}$$

and finally, the strain-displacement relationship can be written as:

$$\{\varepsilon\} = \{\varepsilon_0\} + \{\varepsilon_L\} = [B_0]\,\{d\} + \frac{1}{2}\,[A]\,[G]\,\{d\} = \left([B_0] + \frac{1}{2}\,[B_L]\right)\{d\}. \tag{3.12}$$

Stress-strain relationship

The bump foil is modelled in two dimensions x, y and the width of the foil structure is defined in the z direction, see. Fig. 3.1. Therefore, the plane strain assumption is appropriate and the stress-strain relation becomes

$$\begin{Bmatrix} \sigma_{11} \\ \sigma_{22} \\ \sigma_{12} \end{Bmatrix} = \frac{E(1-\nu)}{(1+\nu)(1-2\nu)} \begin{bmatrix} 1 & \frac{\nu}{1-\nu} & 0 \\ \frac{\nu}{1-\nu} & 1 & 0 \\ 0 & 0 & \frac{1-2\nu}{2(1-\nu)} \end{bmatrix} \begin{Bmatrix} \varepsilon_{11} \\ \varepsilon_{22} \\ \varepsilon_{12} \end{Bmatrix} \tag{3.13}$$

or

$$\{\sigma\} = [C]\,\{\varepsilon\} \tag{3.14}$$

where $[C]$ is the constitutive matrix.

Residual vector and tangential stiffness matrix

In order to derive the residual vector $\{R\}$ and the tangential stiffness matrix $[K_t]$, for use with the implicit NR solution approach, the VWP is used. For a general elastic body, the VWP can be written as [16, 43]:

$$\int_V \{\delta\varepsilon\}^T\{\sigma\}dV = \int_A \{\delta\mathbf{u}\}^T\{F_s\}dA + \int_V \{\delta\mathbf{u}\}^T\{\Phi\}dV + \sum_i \{\delta\mathbf{u}\}_i^T\{p^e\}_i \tag{3.15}$$

where $\{\Phi\}$ is the body forces, for example gravity, and $\{F_s\}$ is the surface forces. By assuming the external forces to be applied in nodes only, that is $\{\Phi\} = \{F_s\} = 0$, and given the nodal force vector $\{P\}$ including the concentrated nodal loads $\{p^e\}_i$, the VWP reduces to

$$\sum_e \int_{V^e} \{\delta\varepsilon\}^T\{\sigma\}dV = \{\delta D\}^T\{P\} \tag{3.16}$$

where $\{D\}$ is the global displacement vector containing the element nodal displacements $\{d\}$. In order to account for large deformations, the strain displacement matrix $\left[\bar{B}\right]$ is dependent on the deflections as stated in (3.11). Inserting the virtual strain (3.10) into (3.16), we get

$$\{\delta D\}^T\left(\sum_e \int_{V^e} \left[\bar{B}\right]^T\{\sigma\}dV - \{P\}\right) = \{0\} \tag{3.17}$$

where $\{\delta D\}$ is written outside the integral as it is not a function of the coordinates. (3.17) must be true for any admissible virtual displacement $\{\delta D\}$ and therefore, the residual becomes

$$\{R\} = \{R_{\text{int}}\} + \{R_{\text{ext}}\} = \sum_e \int_{V^e} \left[\bar{B}\right]^T\{\sigma\}dV - \{P\} = \{0\} \tag{3.18}$$

and the tangential stiffness matrix is defined as the derivative of the internal residual with respect to the deflections

$$[K_t] \equiv \frac{\partial\{R_{\text{int}}\}}{\partial\{D\}}. \tag{3.19}$$

By keeping in mind that $\{\sigma\} = [C]\left[\bar{B}\right]\{d\}$, the tangential matrix given in (3.19) can be derived on element basis

$$[k_t^e] = [k_\sigma^e] + \int_{V^e} \left[\bar{B}\right]^T [C]\left[\bar{B}\right] dV \tag{3.20}$$

where the element stress stiffness matrix is

$$[k_\sigma^e] = \int_{V^e} [G]^T [M_\sigma(\{\sigma\})][G]\, dV \tag{3.21}$$

in which the stress dependent matrix $[M]$ is given as

$$[M_\sigma] = \begin{bmatrix} \sigma_{11}[I_2] & \sigma_{12}[I_2] \\ \sigma_{12}[I_2] & \sigma_{22}[I_2] \end{bmatrix} \tag{3.22}$$

and $[I_2]$ is the 2 by 2 identity matrix. The element matrices are expanded to structure size by the usual element summation:

$$[K_t] = \sum_e [k_t^e] \tag{3.23}$$

where the volume integrals are numerically integrated using a quadrature rule [16]. Note that full integration should be employed, that is in the corresponding 2 by 2 Gauss points.

3.1.3 FE formulation - friction

The above FE formulation will allow modelling of the bump foil structure and take into account large deflections. However, in order to take the Coulomb dry friction occurring in the sliding contact points into account an additional element is needed. Including the dry friction in the FE model can be done in several different ways. One of the commonly used methods is to add nodal forces in the points of the sliding contacts. Here however, an original method is described which, in combination with the nonlinear FE formulation of the foil structure, as described above, simplifies the analysis. The derivation of the method was presented in [P2]; however, for completeness and consistency regarding the nomenclature, it is repeated here. First, the reaction forces acting on the sliding bodies is reviewed.

The reaction force between two contacting bodies can be decomposed in two forces: the normal force F_n and the friction force F_μ. If Coulomb friction law is assumed and the static and dynamic friction coefficients are equal, the friction force F_μ can be written as:

$$F_\mu = \begin{cases} F_n\mu_f, & \text{if } \dot{x}_r < 0 \\ -F_n\mu_f, & \text{if } \dot{x}_r > 0 \end{cases} \tag{3.24}$$

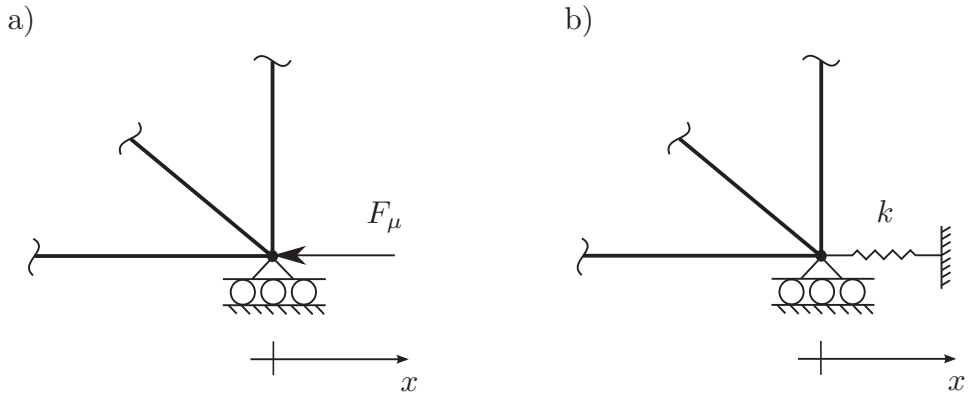

Figure 3.3: (a) Modelling friction with a nodal load F_μ. (b) Modelling friction by use of a nonlinear spring $k(\varepsilon)$.

and

$$-F_n\mu_f \leq F_\mu \leq F_n\mu_f, \quad \text{if} \quad \dot{x}_r = 0 \tag{3.25}$$

where $\dot{x}_r$ is the relative sliding velocity in the contact point and μ_f is the coefficient of friction. Consequently, the friction force F_μ is a function of the sliding velocity $\dot{x}_r$ and is continuous but nonlinear. It could be included in the FE model as a nodal load, illustrated in Fig. 3.3a; in which case, the magnitude and sign of the force would be unknown, unless an iterative procedure with checks for sliding direction, that is the sign of $\dot{x}_r$, and updates of the nodal reaction force F_n were introduced. An alternative method is to add a spring in the point of contact as illustrated in Fig. 3.3b. The first thing to note when considering this method is that the problem of determining the sign of the force F_μ is eliminated because the reaction force of the spring k will automatically be in the opposite direction of the motion $\dot{x}_r$. The magnitude of the reaction force would not be constant if the spring k is linear though. Then, it would increase linearly with the movement of the contact point, which is obviously wrong. However, by choosing the stiffness k to be nonlinear and softening, the reaction force versus deflection can be made constant and fulfilling (3.24). Choosing a proper stiffness function for k can even eliminate the problem of determining the magnitude of the friction force F_μ when there is no motion $\dot{x}_r = 0$ corresponding to (3.25).

Nonlinear spring element

The objective is to derive a nonlinear spring element to be used in the implicit incremental NR scheme that will mimic the behaviour of a friction force. The

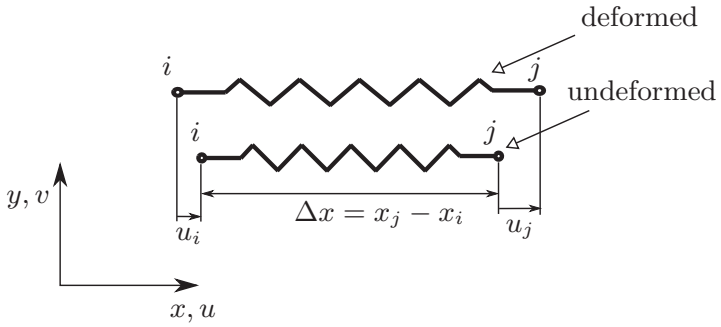

Figure 3.4: Deformed and undeformed one dimensional spring.

schematics and nomenclature of the spring are illustrated in Fig. 3.4. Again, the derivation is based on the VWP as given in (3.15) and, by assuming body forces are negligible and writing the internal work as a summation over the elements and assuming the external forces are only applied in nodes (i.e. $\{\Phi\} = \{0\}$ and $\{F_s\} = \{0\}$) and given by the global force vector $\{P\}$, the VWP (3.15) can be reduced to

$$\sum_e \int_{V_e} \delta\varepsilon\sigma dV = \{\delta D\}^T \{P\} \tag{3.26}$$

where displacements are described by the element nodal displacement vector $\{d\}$ or the global displacement vector $\{D\}$. Assuming the stress and strains are constant in each spring element, the integral on the left hand side of (3.26) can be evaluated as

$$\sum_e \delta\varepsilon N^e L_0^e = \{\delta D\}^T \{P\} \tag{3.27}$$

where the element forces are defined as $N^e = \varepsilon L_0^e k^e$, in which $k^e(\varepsilon)$ is a general nonlinear stiffness dependent on the strain and L_0^e is the initial length of the element e. The strain variations for each element are related to the displacement variations by

$$\delta\varepsilon = \{\bar{B}\}^T \{\delta d\} \tag{3.28}$$

where $\{\bar{B}\}$ is the strain-displacement vector. The strain-displacement vector can now be found by using the Cauchy strain assumption $\varepsilon = (L_1^e - L_0^e)/L_0^e$. If the vertical and horizontal displacements of the two nodes, i and j, (see Fig. 3.4) are described by the vector

$$\{d\} = \{u_i \quad v_i \quad u_j \quad v_j\}^T, \tag{3.29}$$

then the strain in the spring element can be written as

$$\varepsilon = \frac{L_1^e - L_0^e}{L_0^e} = \frac{(x_j - u_j) - (x_i - u_i) - (x_j - x_i)}{(x_j - x_i)} = \frac{\Delta u}{\Delta x} \tag{3.30}$$

where $\Delta u = u_j - u_i$. Using (3.29) and (3.30), the strain can now be written as

$$\varepsilon = \{d\}^T \frac{1}{L_0^e} \{-1 \quad 0 \quad 1 \quad 0\}^T = \{d\}^T \{B_0\} \tag{3.31}$$

where the strain displacement vector $\{B_0\}$ is independent of the displacements and hence it is given the zero subscript. The variation in strain (3.28) then becomes $\delta\varepsilon = \{\delta d\}^T \{B_0\}$, which inserted into (3.27) gives

$$\sum_e \{\delta d\}^T \{B_0\} N^e L_0^e = \{\delta D\}^T \{P\}. \tag{3.32}$$

The VWP should hold for any virtual displacements meaning that (3.32) reduces to

$$\sum_e \{B_0\} N^e L_0^e = \{P\} \tag{3.33}$$

which can be put on residual form as

$$\{R\} = \{R_{\text{int}}\} - \{R_{\text{ext}}\} = \sum_e \{B_0\} N^e L_0^e - \{P\} = \{0\} \tag{3.34}$$

and from the definition of the tangent stiffness matrix, we have

$$[K_t] = \frac{\partial \{R_{\text{int}}\}}{\partial \{D\}} = \sum_e \{B_0\} \frac{\partial N^e}{\partial \varepsilon} \frac{d\varepsilon}{\partial \{D\}} L_0^e = \sum_e \{B_0\} \{B_0\}^T L_0^e \frac{\partial N^e}{\partial \varepsilon} \tag{3.35}$$

where $\partial N^e / \partial \varepsilon = L_0^e k^e(\varepsilon)$. Finally, the tangent stiffness matrix becomes

$$[K_t] = \sum_e \{B_0\} \{B_0\}^T L_0^{e\,2} k^e(\varepsilon). \tag{3.36}$$

Nonlinear spring stiffness function

From the definition of the strain-displacement vector (3.31), it is seen that the length of the spring L_0^e cancels out from the tangent matrix (3.36). Therefore, it is convenient to redefine the nonlinear element stiffness k^e to be dependent on the displacement rather than the strain so that the length L_0^e is eliminated in the element definition. A suitable element stiffness function is:

$$k^e(\Delta u) = \frac{F_n \mu_f}{|\Delta u| + \varepsilon_s} \tag{3.37}$$

where ε_s is introduced to avoid zero division and to obtain a smoothing element force curve. The element stiffness and force curves are illustrated in Fig. 3.5. Examining the element force curve, $N^e(\Delta u)$, in Fig. 3.5, it is clear that the

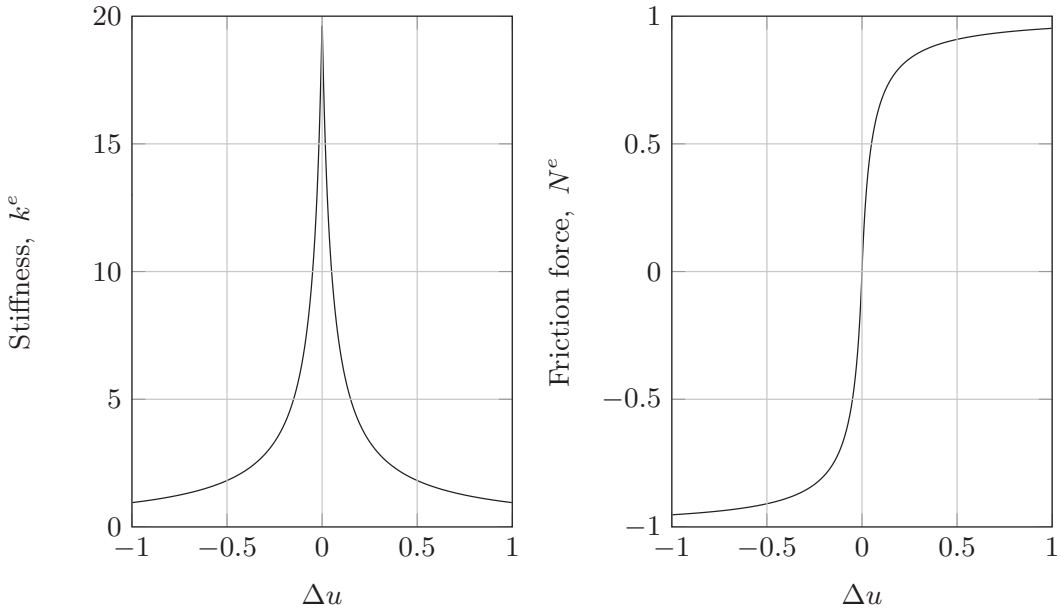

Figure 3.5: Element stiffness and force curves for $F_n\mu_f = 1$ and $\varepsilon_s = 0.05$.

stiffness function (3.37) is a good choice as it produces a force curve very similar to that of a friction force. The optimal value of ε_s depends on the amount of movement in the sliding contact. For small movements, ε_s should be chosen to be small. Choosing too small values, the convergence of the incremental solver will be affected negatively and choosing too large values will affect the accuracy of the solution. A good choice (according to Fig. 3.5) is: $\varepsilon_s \approx \Delta u_{max}/100$.

The theory presented will enable the modelling of sliding friction for several contact points in an FE model. Independent of the sliding direction in each point, the resulting friction force will have the correct sign when starting the analysis from $\Delta u = 0$. However, if the sliding direction changes at $\Delta u \neq 0$, for example due to cyclic loading, the resulting friction force will have the wrong sign. To assure the correct sign of the friction force, a 'shift' is introduced so that the nonlinear spring is relaxed when ever the sliding directions changes at $\Delta u \neq 0$. By introducing the 'shift' in (3.37) a modified stiffness function is obtained

$$k^e(\Delta u - \Delta u_s) = \frac{F_n\mu_f}{|\Delta u - \Delta u_s| + \varepsilon_s} \tag{3.38}$$

where Δu_s is set to Δu in the event of changing the sliding direction. This means that for cyclic loading, the sliding direction in the contact point needs to be monitored.

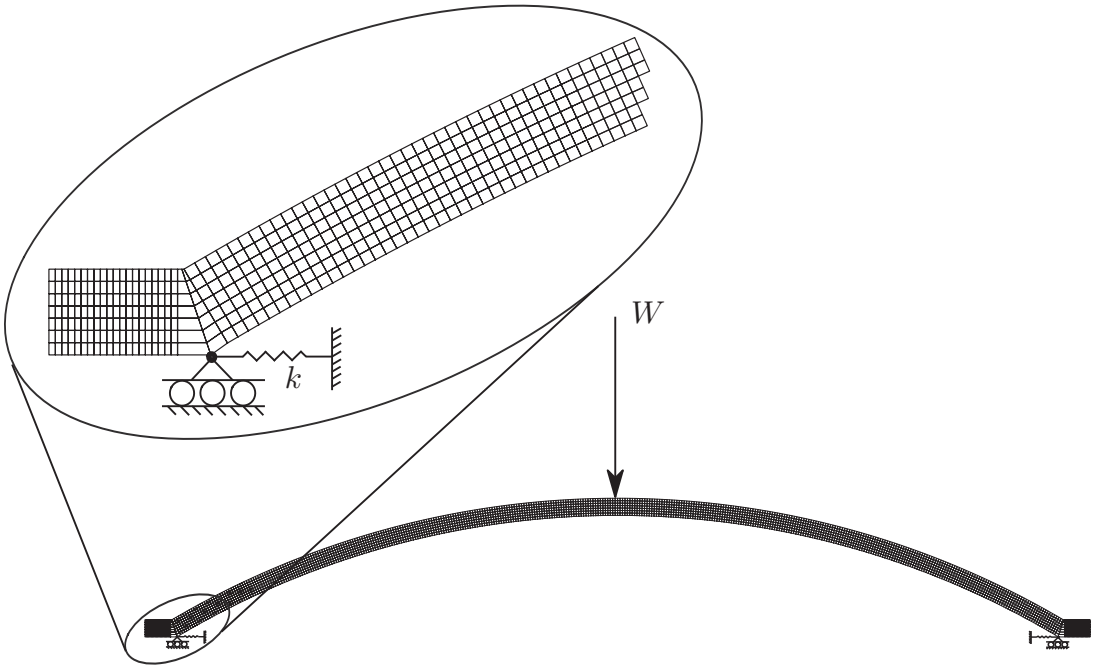

Figure 3.6: FE model of a single bump, of a bump foil, composed of nonlinear structural elements and friction elements in the sliding contact points.

3.1.4 Foil FE model

In Sec. 3.1.2 and 3.1.3, two FE elements were derived. One for modelling the solid structure of the foils and one for modelling the friction in the sliding contact points. A model of the foil structure can now be established using these two elements, an example is illustrated in Fig. 3.6. Here, a single bump is modelled using the actual geometry and dimensions from a Siemens-ACC bearing. As seen, the mesh is relatively fine and corresponds with the actual mesh used in the later analysis, which is based on a mesh convergence study. In Fig. 3.7, a typical bump foil composed of several bumps is illustrated. As seen, the friction elements are imposed at both the top and the bottom of the foil in order to take into account the sliding friction occurring between, top foil and bump foil, as well as between the bump foil and housing. The thickness of the foil in this figure is exaggerated and the number of elements reduced for illustration purpose. Note the positions of the friction elements between the bump foil and housing. It is assumed that the contact will mainly occur in the outer most nodes, as illustrated in the magnified section of Fig. 3.7; this is an assumption based on the resulting moments in the foils on the two neighbouring bumps that during a compression of the bumps, will lift the middle node away from the housing.

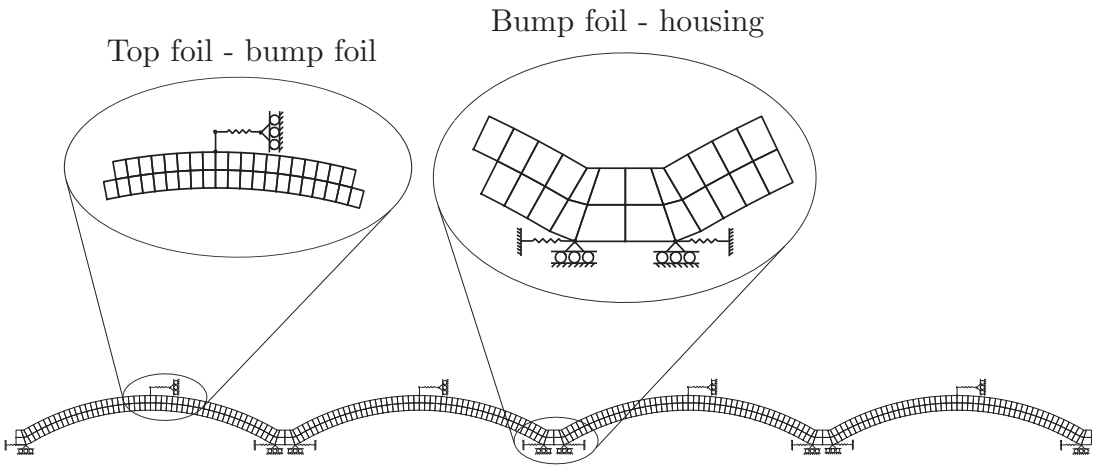

Figure 3.7: FE model of four interconnected bumps of a bump foil including friction elements in the sliding contact points. Note, the thickness is exaggerated for illustration purpose.

With the FE model presented above, quasi-static simulations of the isolated foil structure can be performed. The model will take into account the nonlinearities associated with large deflections and Coulomb friction in the contact points. However, the model is a 2D model limiting the analysis to the case of uniform deflections along the length L of the foil structure, that is in the z-direction. Furthermore, the friction elements are based on simple nonlinear springs under the fundamental assumption that all contact points are always in contact, meaning there is no foil separation from the housing. In fact, the nodes in which the friction elements are applied are restricted from moving in the normal direction.

3.2 Fluid film model

Previously, in Sec. 3.1, a model of the foil structure in the AFB was presented. As mentioned, the foil structure alters the bearing surface compliant and allows for imperfections, such as journal misalignment, etc., and at the same time, accommodates for additional damping in the bearing. The top foils and the journal are separated by a thin film of air during operation. The separation is a result of a pressure field developed in the air film when the journal is rotating, that is the air film is separating the stationary and moving parts of the bearing while providing the load carrying capabilities. However, it also contributes to the overall stiffness and damping characteristics of the bearing. Hence an accurate model of the air film is necessary in order to analyse AFBs.

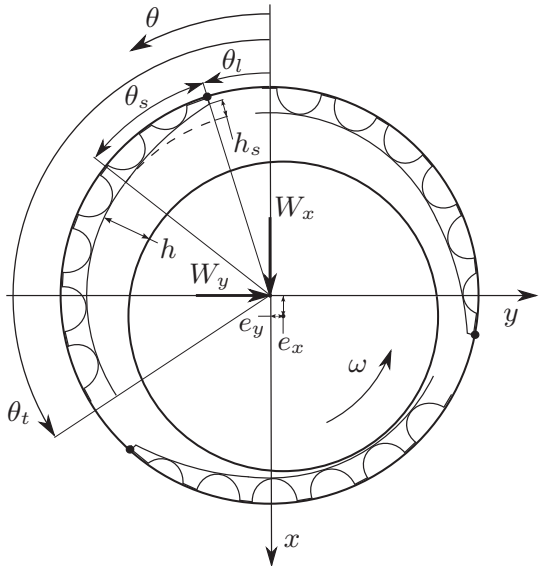

(a) Detailed geometry of the Siemens-ACC AFB with associated nomenclature.

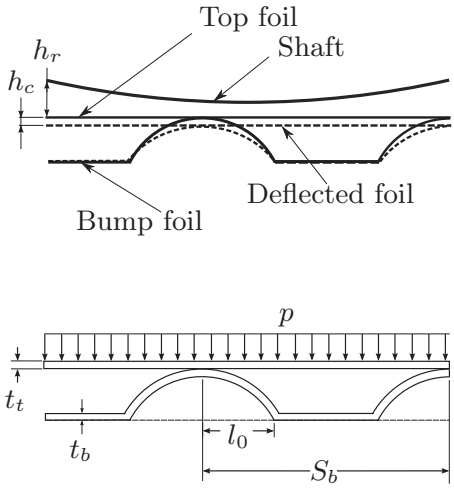

(b) Deformed and undeformed bump foil geometry and the associated nomenclature.

Figure 3.8: a) Detailed geometry of the Siemens-ACC AFB with associated nomenclature. b) Definition of the deformed and undeformed heights, h_r and h_c respectively.

The formation of the air film pressure is dependent on the journal speed, the air viscosity, and the bearing geometry, or more specifically, the shape of the gap between the journal and the pads. The geometry of the Siemens-ACC AFB is illustrated in Fig. 3.8 together with the nomenclature used for the mathematical modelling of the bearing. The mathematical model generally used for describing the pressure field in hydrodynamically lubricated bearings is known as the Reynolds equation. It is derived from a subset of the Navier-Stokes equations and the continuity equation under the assumptions of laminar, Newtonian, inertia-less, thin-film flows. A comprehensive derivation of the Reynolds equation can be found in for example Hamrock [22], Sec. 7.2 and, for a journal bearing in Cartesian coordinates, it can be written as:

$$\frac{\partial}{\partial\tilde{\theta}}\left(\frac{\rho h^3}{12\mu}\frac{\partial p}{\partial\tilde{\theta}}\right)+\frac{\partial}{\partial z}\left(\frac{\rho h^3}{12\mu}\frac{\partial p}{\partial z}\right)=\frac{\omega R}{2}\frac{\partial(\rho h)}{\partial\tilde{\theta}}+\frac{\partial(\rho h)}{\partial t} \tag{3.39}$$

where $\tilde{\theta}=\theta R$ is the circumferential coordinate and R is the radius of the bearing. The density ρ of the air can be calculated by the ideal gas law, expressed as a function of temperature and pressure

$$\rho=\frac{pM}{R_u T}. \tag{3.40}$$

As previously mentioned, the power loss of air bearings is very low leading

to the assumption of near iso-thermal operation (T is constant). Thus, all terms, except the pressure p, in (3.40) are constant and by inserting (3.40) into (3.39), the Reynolds equation for compressible fluids under the assumption of iso-thermal operation becomes

$$\frac{\partial}{\partial\tilde{\theta}}\left(\frac{ph^3}{12\mu}\frac{\partial p}{\partial\tilde{\theta}}\right)+\frac{\partial}{\partial z}\left(\frac{ph^3}{12\mu}\frac{\partial p}{\partial z}\right)=\frac{\omega R}{2}\frac{\partial(ph)}{\partial\tilde{\theta}}+\frac{\partial(ph)}{\partial t} \tag{3.41}$$

which is a nonlinear parabolic partial differential equation for the pressure p. It is convenient, especially when utilizing the FE method later on, to rewrite the compressible Reynolds equation into vector form as:

$$\nabla\cdot\left(\frac{ph^3}{12\mu}\nabla p\right)=\nabla\cdot(ph)\{U\}+\frac{\partial}{\partial t}(ph). \tag{3.42}$$

With the compressible Reynolds equation for a journal bearing defined, the next step in order to complete the mathematical model of the journal bearing, as illustrated in Fig. 3.8, is to establish a mathematical expression for the air film height. The height consists of two terms

$$h=h_r+h_c \tag{3.43}$$

where h_r is the undeformed height

$$h_r=\begin{cases}C+e_x\cos(\theta)+e_y\sin(\theta)-h_s\frac{\theta-\theta_i}{\theta_s}, & \theta_{li}\le\theta\le\theta_i\\ C+e_x\cos(\theta)+e_y\sin(\theta), & \theta_i<\theta\le\theta_{ti}\end{cases} \tag{3.44}$$

and

$$\begin{aligned}\theta_i&=\theta_s+\theta_l+\frac{2\pi}{N_p}(i-1)\\ \theta_{li}&=\theta_l+\frac{2\pi}{N_p}(i-1)\\ \theta_{ti}&=\theta_t+\frac{2\pi}{N_p}(i-1)\end{aligned} \tag{3.45}$$

where i is the bearing pad number. The deformed height $h_c(p)$ is a function of the pressure field p acting on the pads and can be calculated from a structural model of the foils, for example as described in Sec. 3.1. The equations (3.42) through (3.45) together with the appropriate boundary conditions and the foil structure model constitute the mathematical model of the AFB. Solving this model for the air film pressure p enables the calculation of the reaction forces acting on the bearing journal as

$$\begin{Bmatrix}W_x\\ W_y\end{Bmatrix}=-\int_0^L\int_0^{2\pi}(p-p_a)\begin{Bmatrix}\cos(\theta)\\ \sin(\theta)\end{Bmatrix}Rd\theta dz. \tag{3.46}$$

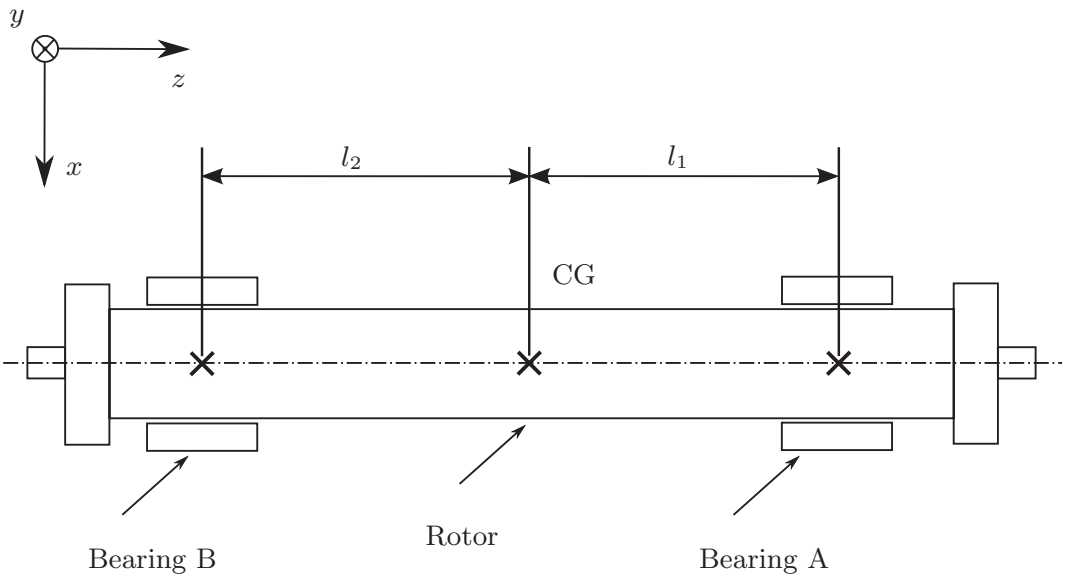

Figure 3.9: Schematics and nomenclature of the rigid shaft and its supporting bearings.

The model is a coupled fluid-structure model and the coupling is related to the pressure dependent modification of the film height quantified as h_c. Setting the modification $h_c = 0$, the model is decoupled and describing the fluid film behaviour only. This can be used for validating the fluid film model against experimentally obtained results and it was done in the publication [P1] with very good agreement. In this work, the model above is solved and analysed in mainly two different ways: perturbed steady-state analysis [P1, P3, P4] and time-domain analysis [P5, P6]. Both the SEFM, as represented by (3.1) and (3.2), as well as more detailed and accurate methods are employed for these solutions. Further description and discussion of the the different solutions and methods are given in Chap. 4.

3.3 Rigid shaft model

In this section, a mathematical model of a rigid shaft is presented. This model is used when simulating a complete coupled rotor-bearing system but also for the experimental parameter identification presented later in Sec. 5.2.2. The model is derived with focus on mathematical simplicity. A schematics of the rigid shaft model including bearings and nomenclature is illustrated in Fig. 3.9. Assuming the shaft to be rigid and rotations around x and y to be small, the equations of

motion can be derived, using the Newton-Euler equations, to be

$$[M]\{\ddot{q}\} + (-\omega[G] + [D])\{\dot{q}\} + [K]\{q\} = \{f\} \tag{3.47}$$

where the nodal loading and displacement vectors are defined as

$$\{q\} = \begin{Bmatrix} q_{\mathrm{Ax}} \\ q_{\mathrm{Ay}} \\ q_{\mathrm{Bx}} \\ q_{\mathrm{By}} \end{Bmatrix}, \quad \{f\} = \begin{Bmatrix} f_{\mathrm{Ax}} \\ f_{\mathrm{Ay}} \\ f_{\mathrm{Bx}} \\ f_{\mathrm{By}} \end{Bmatrix} \tag{3.48}$$

and the system matrices $[M_{\mathrm{AB}}]$, $[G_{\mathrm{AB}}]$, $[D_{\mathrm{AB}}]$ and $[K_{\mathrm{AB}}]$ are given in App. A.1, (A.35) along with a comprehensive derivation of the model.

3.4 On the coupling of the domains

With the three domains, foil structure, air film and shaft structure mathematically modelled, it is possible to establish a complete coupled model. In fact, several models can be established depending on the type of analysis to be performed, for example a steady-state or nonlinear transient analysis. The coupling of the domains is a mathematically challenging task that requires a great amount of effort. However, it does not make sense to perform this task without first having verified that each model accurately predicts the behaviour of its respective domain. There is only one way to perform this verification and it is through physical experiments. Experimental validation is, like the mathematical coupling of the domains, a very challenging task. However, it is a task that is regarded necessary and very important since the current literature contains very limited amount of detailed experimental work considering each domain separately. As a consequence, a great deal of effort within the frame of this PhD work was put in the experimental validation with a special focus on the bump foil structure.

The foil structural model presented in this chapter is relatively complex in the sense that it is an FE model having a high number of DOFs. Furthermore, it is nonlinear meaning that an iterative solution procedure is necessary. This particular model would not perform well in a coupled fluid structure system as it is computationally heavy. As initially mentioned, the target when developing this foil model was not set on efficiency but rather accuracy compared to the physical system. A mathematical foil model that can be successfully coupled with the other two domains would need to be computationally efficient and, at the same time, it should accurately capture the essential behaviour of the physical foil structure. Such a model could be equivalent, for example constructed of

simple springs with a minimum of DOFs and perhaps incorporating the simple friction element described in Sec. 3.1.3. Several authors have presented equivalent bump foil models for example Ku and Heshmat [44, 47, 48] who compared the model against experimental results but obtained only limited agreement. Later, Le Lez and Arghir [50, 51] presented models which, however, were not fully experimentally validated on an isolated basis.

Basically, the path towards a simplified equivalent foil structural model capturing the essential behaviour of the physical foil structure goes through experimental and theoretical investigations, that is investigations highlighting the actual foil behaviour. Having accurately mapped the actual foil behaviour, the equivalent model can be verified and calibrated accordingly. Before this task is completed, it does not make sense to use the equivalent model in a full mathematical model that couples all the individual domains. In this light, the focus of this thesis was set on increasing the understanding of the foil structural behaviour, but at the same time, to investigate how it affects the overall statical and dynamical behaviour of the shaft and bearing system. This is largely achieved by improving the estimation of the foil flexibility K and the loss factor η in the SEFM according to experimentally and theoretically obtained values. However, investigations involving a slightly more complex coupled model (CFSM) in which the top foils are modelled by use of 2D plates are also performed.

Chapter 4

Numerical solution

Previously, in Chap. 3, individual mathematical models for the flexible foils, the air film and the rigid rotor were established. The models for the foil structure and the rigid shaft were readily derived as discretised mathematical models, suited for numerical solution procedures. However, the mathematical model describing the pressure in the air film was left in analytical form. It is a partial nonlinear differential equation that cannot be solved analytically; hence, it needs to be discretised using for example the FE method. The reason for omitting this discretisation in the previous chapter is related to the later analysis. The mathematical model of the air film is central for the combined or mathematically coupled model of the rotor-bearing system. Therefore, the discretisation depends on how the individual models are combined or mathematically coupled and the type of analysis performed, for example steady-state or transient analysis. In this chapter, the different types of analysis and their solution are treated in individual sections. The solutions can be divided in two categories: 1) traditional steady-state solutions based on the calculation of the linearised stiffness and damping coefficients of the bearings, using a perturbation technique. The calculated coefficients are then used with frequency domain analysis of the shaft, for example for unbalance response and stability analysis and, 2) nonlinear transient analysis in the time domain in which the state equations for the foil structure, the air film and the shaft are solved simultaneously.

4.1 Perturbed steady-state solution – SEFM

With regard to rotors supported by oil lubricated bearings, the method of introducing linearised stiffness and damping coefficients for the bearings has historically proven to be very useful. The method enables the decoupling of the shaft and bearing calculations and is therefore computationally effective. At the same time, accurate prediction of the steady-state rotor response as well as evaluation of the stability is possible based on accurate linearised stiffness and damping coefficients. This is because the stiffness and damping coefficients of oil lubricated bearings are indeed relatively linear within their normal operational range. Based on the good and accurate results obtained with linearised bearing coefficients within hydrodynamical lubrication, it is natural to transfer these methods to the analysis of aerodynamically-lubricated bearings more or less directly. That is, we assume the bearing stiffness and damping coefficients close to linear in the normal operating range of the bearings. The validity of this assumption will be investigated experimentally in Chap. 6.

In this section, a method for calculating the linearised coefficients, based on an FE solution of the perturbed SEFM, is presented. In [P1], this method was validated according to static results, for example the pressure profiles and eccentricity ratios as well as dynamical results, for example the frequency dependent stiffness and damping coefficients obtained from the literature. The efficient FE formulation and solution were thoroughly described in [P3] and compared to less efficient methods. Here, the method is described briefly.

4.1.1 Perturbed equations

To obtain the linearised bearing coefficients from the SEFM as constituted by (3.1), (3.2) and (3.42) through (3.45), a harmonic perturbation method is employed. The method, which was first introduced by Lund [55], is a commonly used and widely accepted method. Assuming that the shaft exhibits small harmonic oscillations around its equilibrium position in the bearing (e_{x_0}, e_{y_0}), the shaft motion is given by

$$e_x = e_{x_0} + \Delta e_x e^{i\omega_s t} \quad \text{and} \quad e_y = e_{y_0} + \Delta e_y e^{i\omega_s t}. \tag{4.1}$$

Assuming the amplitudes to be small $\Delta e_x \ll C$ and $\Delta e_y \ll C$, a first-order Taylor expansion of the pressure can be written as

$$p = p_0 + (\Delta e_x p_x + \Delta e_y p_y) e^{i\omega_s t}. \tag{4.2}$$

According to (4.2), the pressure p is a harmonic oscillating field. This enables the introduction of a frequency dependent mobility in the film height function

rather than a static flexibility K as given in (3.2) or (3.3). The mobility can be written as

$$K_c = \frac{K}{1 + i\eta} \tag{4.3}$$

where $\eta = \omega_s b_{foil} K$ is the mechanical energy loss factor related to the foils [37]. Implementing the mobility K_c, the film height becomes

$$h = h_r + h_c = h_r + K_c(p - p_a) \tag{4.4}$$

where the rigid height h_r is given by (3.44) and (3.45). Substituting (4.1), (4.2), (4.3) into (3.42) and (4.4), discarding second- and higher-order terms yields, upon separation of variables, the zero- and first-order equations are:

Zero-order:

$$\nabla \cdot \left(\frac{p_0 h_0^3}{12\mu} \nabla p_0 \right) - \nabla \cdot (p_0 h_0)\{U\} = \{0\} \tag{4.5}$$

First-order:

$$\begin{aligned} &\nabla \cdot \left(\frac{p_0 h_0^3}{12\mu} \nabla p_\gamma \right) + \nabla \cdot \left(\frac{h_0^3 + 3h_0^2 p_0 K_c}{12\mu} \nabla p_0 p_\gamma \right) - \nabla \cdot ((h_0 + p_0 K_c) p_\gamma)\,\{U\} \\ &- i\omega_s (h_0 + p_0 K_c) p_\gamma = -\nabla \cdot \left(\frac{p_0 h_0^2 \mathrm{f}_\gamma}{4\mu} \nabla p_0 \right) + \nabla \cdot (p_0 \mathrm{f}_\gamma)\{U\} + i\omega_s (p_0 \mathrm{f}_\gamma) \end{aligned} \tag{4.6}$$

where

$$h_0 = h_{r_0} + K_c(p_0 - p_a) \tag{4.7}$$

and $\gamma = x, y$ and $\mathrm{f_x} = \cos(\theta)$ and $\mathrm{f_y} = \sin(\theta)$. Furthermore, the rigid height h_{r_0} is defined as the height at static equilibrium, that is at (e_{x_0}, e_{y_0}). Solving the zero-order equation (4.5) for an eccentricity (e_{x_0}, e_{y_0}) and $\eta = 0$, yields the static film pressure p_0. This pressure is then used when solving the first-order equation (4.6) to obtain the dynamic pressures p_x and p_y. The bearing reaction forces are found by integration of the static pressure p_0 over the bearing surface

$$\begin{Bmatrix} W_x \\ W_y \end{Bmatrix} = -\int_0^L \int_0^{2\pi} (p_0 - p_a) \begin{Bmatrix} \cos(\theta) \\ \sin(\theta) \end{Bmatrix} R d\theta dz \tag{4.8}$$

and a similar integration of the dynamic pressures (p_x, p_y) determines the dynamic stiffness and damping coefficients as

$$\begin{bmatrix} k_{xx} & k_{xy} \\ k_{yx} & k_{yy} \end{bmatrix} + i\omega_s \begin{bmatrix} d_{xx} & d_{xy} \\ d_{yx} & d_{yy} \end{bmatrix} = \int_0^L \int_0^{2\pi} \begin{bmatrix} p_x \cos(\theta) & p_y \cos(\theta) \\ p_x \sin(\theta) & p_y \sin(\theta) \end{bmatrix} R d\theta dz. \tag{4.9}$$

4.1.2 FE formulation and solution

The FE formulation consists of two parts. The first part is dealing with the zero-order nonlinear parabolic partial differential equation (4.5) for the static pressure p_0, which needs to be solved iteratively. The second part deals with the first-order linear complex differential equation (4.6) for the dynamic pressures p_γ, which can be solved directly. While the first-order equation is easily solved, the solution of the zero-order equation is more complicated. Here, an FE formulation for the zero-order equation that can be combined with the iterative Newton-Raphson solution scheme is sought. The solution given here can be seen as the equivalent to solving structural problems including material nonlinearities [16, 43] as was the case in Secs. 3.1.2 and 3.1.3 where the numerical models are quantified by a tangent matrix and residual vector and solved using an implicit incremental NR scheme as given in App. B.

Zero-order solution

As mentioned, the derivation of the tangent matrix and residual vector is thoroughly described in [P3]. The residual vector can be written as

$$\{R^e\} = \{R^e_{\text{ext}}\} - \{R^e_{\text{int}}\} = \{0\} - \int_{V^e} [B]^T D\,[B]\,\{p^e_0\}\; dV + \int_{V^e} [B]^T \{U\} h\,[N]\,\{p^e_0\}\; dV \tag{4.10}$$

and the tangent matrix becomes

$$[K^e_t] = \frac{\partial\{R^e_{\text{int}}\}}{\partial\{p^e_0\}} = \int_{V^e} [B]^T D\,[B]\; dV - \int_{V^e} [N]^T \{U\}^T h\,[B]\; dV \tag{4.11}$$

where the diffusion coefficient $D(p_0) = \frac{p_0 h^3}{12\mu}$ is a scalar and real field (only the real part of the foil mobility is used in the zero-order equation). The element vectors and matrices are expanded to structure size by the usual element summation:

$$[K_t] = \sum_e [K^e_t]; \quad \{R\} = \sum_e \{R^e\}; \quad \{p\} = \sum_e \{p^e\} \tag{4.12}$$

where the volume integrals are numerically integrated using a quadrature rule [16]. The scalar field quantities p_0, h, K_c in D are calculated in the respective Gauss points (ξ_i, ζ_j) using the interpolation functions $[N]$. Full integration must be employed which, in case of linear four node quadrilateral elements (Q4), means that 2 by 2 Gauss points are used.

First-order solution

The first-order equation (4.6) is a linear complex differential equation. Following the same Bubnov-Galerkin FE procedure as for the zero-order equation leads to a linear set of complex algebraic equations

$$[K_\gamma]\,\{p_\gamma\} = \{q_\gamma\} \tag{4.13}$$

that can be solved by factorisation for the dynamic pressures. The coefficient matrix $\left[K_\gamma^e\right]$ and right hand side $\{q_\gamma^e\}$ on the element level are given by

$$\begin{aligned}\left[K_\gamma^e\right] = \int_{V^e} \Big(&[B]^T C_1 [B] + [B]^T C_2 [B] \{p_0\} [N] + [B]^T C_4 \{U\} [N] \\ &- [N]^T i\omega_s C_4 [N] \Big)\, dV\end{aligned} \tag{4.14}$$

$$\{q_\gamma^e\} = \int_{V^e} \left([B]^T C_3 \mathrm{f}_\gamma [B] \{p_0\} + [B]^T p_0 \mathrm{f}_\gamma \{U\} - i\omega_s p_0 \mathrm{f}_\gamma [N]^T \right)\, dV$$

where the coefficients are

$$\begin{aligned} C_1 &= \frac{p_0 h_0^3}{12\mu} \\ C_2 &= \frac{h_0^3 + 3h_0^2 p_0 K_c}{12\mu} \\ C_3 &= -\frac{p_0 h_0^2}{4\mu} \\ C_4 &= -(h_0 + p_0 K_c). \end{aligned} \tag{4.15}$$

Again, during the numerical integration procedure of the coefficient matrix and right hand side vector (4.14), all field quantities are calculated in the Gauss points using of the shape functions. Once again, the element vectors and matrices are expanded to structure size by the usual element summation:

$$[K_\gamma] = \sum_e \left[K_\gamma^e\right]; \quad \{q_\gamma\} = \sum_e \{q_\gamma^e\}; \quad \{p_\gamma\} = \sum_e \{p_\gamma^e\}. \tag{4.16}$$

Boundary conditions

The boundary conditions for the zero- and first-order systems (4.10), (4.11), (4.13) are applied following common methods. For a bearing as depicted in

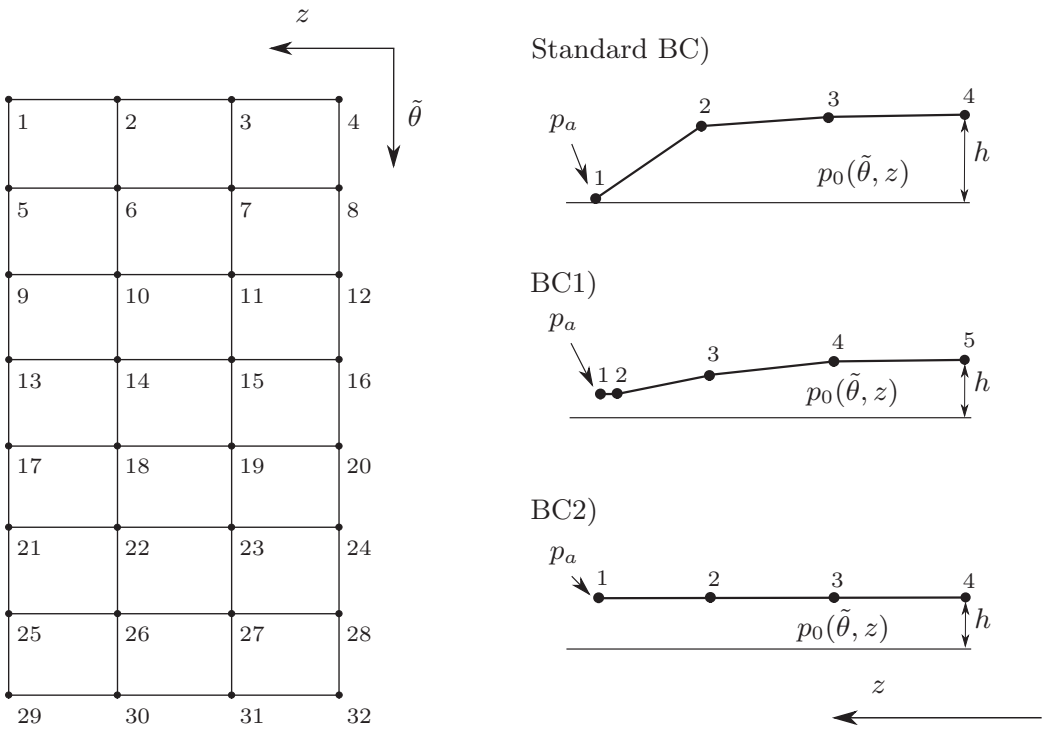

(a) FE mesh of a single pad.

(b) Film height and pad deflection along axial direction.

Figure 4.1: a) Schematics of FE mesh for a single pad. b) Three different edge boundary conditions and their effect on the pad deflection.

Fig. 3.8, the boundary conditions for each bearing pad are

$$p_0 : \begin{cases} p_0(\theta_l, z) = p_0(\theta_t, z) = p_a \\ p_0(\theta, L/2) = p_0(\theta, -L/2) = p_a \end{cases} \quad p_\gamma : \begin{cases} p_\gamma(\theta_l, z) = p_\gamma(\theta_t, z) = 0 \\ p_\gamma(\theta, L/2) = p_\gamma(\theta, -L/2) = 0. \end{cases} \tag{4.17}$$

Note that the boundary condition for the zero-order equation should only be applied for the first iteration of the NR solution algorithm. A detailed explanation and a pseudo code is given in [P3]. As illustrated in Fig. 4.1, the prescribed boundary conditions (4.17) will pose a problem for large journal eccentricities. The foil deflection $h_c(p_0) = K_c(p_0 - p_a)$ becomes zero in the nodes where $p_0 = p_a$. This is the case at the pad edges. If the bearing pad mesh in Fig. 4.1a is subjected to ambient pressure p_a on its left edge and the bearing eccentricity ratio is approaching 1, the resulting film height h and the deflected pad profile will take a form as illustrated in Fig. 4.1b (Standard BC). This is obviously incorrect since the radial deflection of the top foil along the axial direction z should be smooth. In the situation illustrated with zero film height $h = 0$ on the edge, the air leakage will become zero with an elevated pressure along the edge as a consequence. This is a problem specifically related to the SEFM. To correct it,

one has to assure that the foils take on realistic deflections on the pad edges. This can be achieved by meshing with a narrow band of elements that have the width of $L/50$ or less along the bearing edges subjected to ambient pressure and letting the foil deflection $h_c(p)$ in the outermost nodes of these elements (on the bearing edge) adopt the deflection values of the innermost nodes (away from the bearing edge) on that element. This situation is shown in Fig. 4.1b (BC1). Regarding foil configurations where the top foil is stiffer than the bump foil, the top foil deflection can be regarded as constant along the axial direction of the bearing [64]. In these cases, the deflection $h_c(p_m)$ can be used where the pressure p_m is taken as the arithmetic mean pressure along the axial direction for a given angle θ. This situation is illustrated in Fig. 4.1b (BC2).

In gas bearings, where the fluid is compressible, significant sub-ambient pressures may arise. These sub-ambient pressures will cause the top foil to separate from the bumps into a position in which the pressure on both sides of the pad are equalized. Heshmat [31] introduced a set of boundary conditions accounting for this separation effect. However, in this work, a simple Gümbel [22] boundary condition is imposed, meaning that sub-ambient pressures are discarded when integrating the pressure to obtain the bearing force components (W_x, W_y). This means that the parts of the bearing having sub-ambient pressures are inactivated and hence these areas need prescribed boundary conditions, $p_\gamma = 0$ where $p_0 < p_a$, when solving the first-order equation.

4.1.3 Assumptions and limitations

As already mentioned, the SEFM is based on a number of assumptions:

1) The foil stiffness is assumed to be linear

2) Depending on the choice of K, that is (3.2) or (3.3), the foil stiffness is assumed constant over the length and angular extension of the pads

3) The deformation in one point of the pad is assumed completely independent on the deformation in any neighbouring points

Furthermore, in the numerical solution, as presented above, additional assumptions are made:

4) Depending on the choice of boundary condition, that is BC1 or BC2, the foil deflection is assumed constant along the length of the pads

5) The energy dissipation occurring in the foil structure is regarded as being evenly distributed over a period of vibration, that is a linear damping is assumed

Common for the assumptions 1-5 is their relation to the simplified structural foil model (3.1). If the static foil deflection and the dynamic foil deflection amplitudes are sufficiently small, these assumptions are valid. This is either the case for a lightly loaded bearing subjected to small vibrations around its equilibrium position (e_{x_0}, e_{y_0}) or a medium to heavily loaded bearing having a relatively stiff foil structure. On the other hand, it is not the case for a heavily loaded bearing subjected to large vibration amplitudes or a bearing with very low foil stiffness. In other words, the validity of the assumptions 1-5 is limited by the foil geometry and the operation conditions of the bearing.

There is one more very important and fundamental assumption in the SEFM. It is related to the definition of the bump foil flexibility used with the method, for example defined by (3.2), (3.3) or similar formulations. These formulations assume:

6) The friction force in the contact points contribute to the generation of hysteresis damping only and not to the total foil stiffness

This is a consequence of neglecting the friction force in the stiffness calculation and only account for it through the loss factor η in the complex flexibility formulation. This assumption differs from the assumptions 1-5 as its validity is not limited by foil geometry and operating conditions but rather by the friction coefficient μ_f between the foils and the housing. Seen from that perspective, any significant influence on the foil stiffness that the friction forces might have will render this fundamental assumption invalid, regardless of the operation conditions or geometry. In fact, as will be shown in Sec. 6.1, the friction forces do significantly alter the bump foil stiffness. It does so by introducing a stiffening effect of the bump foil layer. Discarding this stiffening effect may lead to significant overestimation of the foil flexibility and inaccurate static and dynamic results obtained with the SEFM.

4.2 Perturbed steady-state solution – CFSM

In Sec. 4.1, a perturbed steady-state solution based on the SEFM was presented. Problems related to the pad-edge boundary conditions were highlighted and

alternative boundary conditions were proposed. Furthermore, the assumptions and limitations related to the simple foil deflection model and the proposed boundary conditions were discussed.

In this section, a modified model based on the perturbed solution, as given in Sec. 4.1, is presented. It is developed in order to deal with the problems and limitations highlighted with the perturbed steady-state solution of the SEFM. The modified model presented here is covered in [P4] in which the results obtained theoretically were compared to results obtained experimentally. It is thus recommended that this section is read as a supplement to [P4]. The modification includes a top foil structure that is modelled using 2D linear FE elements and a bump foil structure that is modelled by equivalent springs k^i_{eq}. This 'complex' foil structure model is then coupled to the zero-order equation (4.5) and solved. In the following, it is referred to as the Coupled Fluid Structure Model (CFSM). The objective with this modified model is to obtain a static solution, that is the static pressure p_0, foil deflection h_{c_0} and journal eccentricity (e_{x_0}, e_{y_0}), with improved accuracy.

The improved static solution is later used when solving the first-order equation (4.6) to obtain the linearised bearing coefficients. It is important to highlight that the CFSM is only related to the solution of the zero-order equation (4.5), not the solution of the first-order equation (4.6) which is still based on the SEFM. In Fig. 4.2a, a nonlinear foil FE model based on the theory presented in Sec. 3.1.4 is illustrated for a single foil segment. As will be shown in Sec. 6.1.1, this model behaves almost linearly when subjected to distributed monotonic loading. It is therefore possible to linearise the model by introducing the aforementioned equivalent springs k^i_{eq}. A linearised model based on equivalent springs is illustrated in Fig. 4.2b. The stiffness of each of these springs k^i_{eq} is based on a bump foil calculation using the detailed bump foil model presented in Sec. 3.1.4, and the top foil is modelled using a basic linear 2D FE element with a local stiffness matrix defined as:

$$[k_f] = \frac{EI}{l_e^3}\begin{bmatrix} 12 & 6l_e & -12 & 6l_e \\ 6l_e & 4l_e^2 & -6l_e & 2l_e^2 \\ -12 & -6l_e & 12 & -6l_e \\ 6l_e & 2l_e^2 & -6l_e & 4l_e^2 \end{bmatrix}, \quad \{d_f\} = \begin{Bmatrix} v_1 \\ \varphi_1 \\ v_2 \\ \varphi_2 \end{Bmatrix}. \tag{4.18}$$

Since the load distribution, that is the pressure profile acting on each pad, is initially unknown, the calculation of the equivalent spring stiffness k^i_{eq} is updated during the solution. A flow chart of the CFSM based solution of the zero-order equation is illustrated in Fig. 4.3. As it is seen, the foil deflection h_c is updated at each NR iteration over the pressure, and the vector containing the equivalent stiffness for each bump $\{k_{eq}\}$ is updated at each eccentricity iteration until force equilibrium is obtained. Having obtained a static solution with the CFSM of higher accuracy, the first-order perturbed equation (4.6)

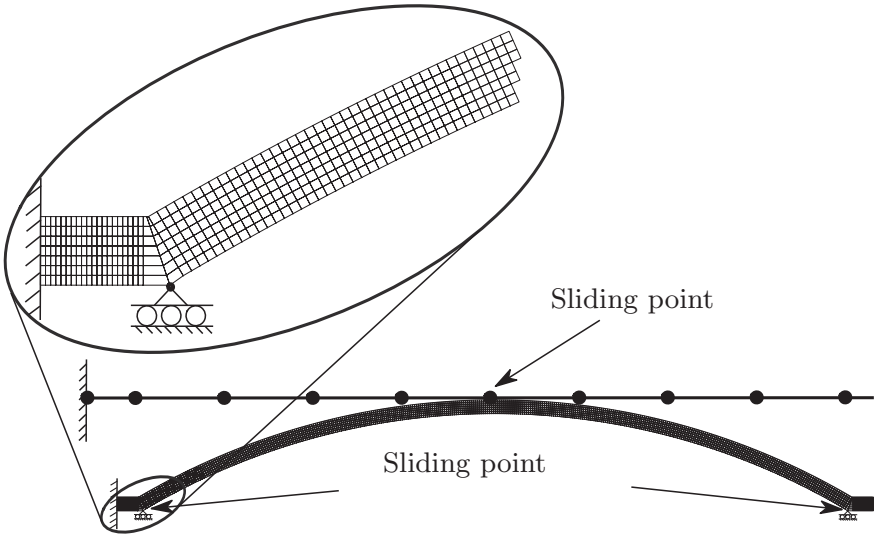

(a) Nonlinear FE model of the initial segment of the foil structure (leading edge on the left side).

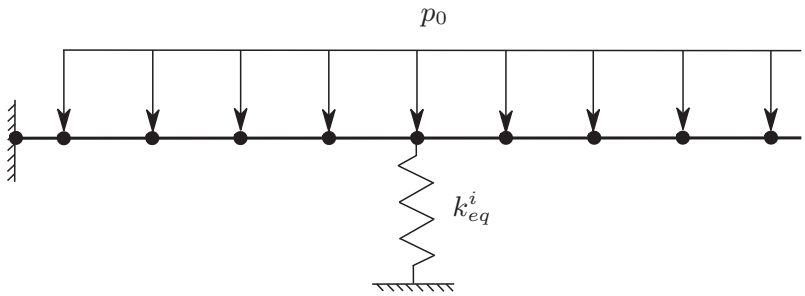

(b) Linear equivalent FE model of the initial segment of the foil structure (leading edge on the left side). The bump foil support stiffness is modelled using equivalent linear springs.

Figure 4.2: a) Schematics of FE mesh for a single bump modelled using the nonlinear FE model. b) Schematics of equivalent linearised model for a single bump.

for the stiffness and damping coefficients can be solved. Experimental and theoretical results presented in [P2] and Sec. 6.1.1, highlights the importance of distinguishing between the static and dynamic foil stiffness. Hence for the first-order solution, the dynamic stiffness should be used. This stiffness can be found by examining local hysteresis loops obtained theoretically with the detailed foil structure model as presented in Sec. 3.1.4.

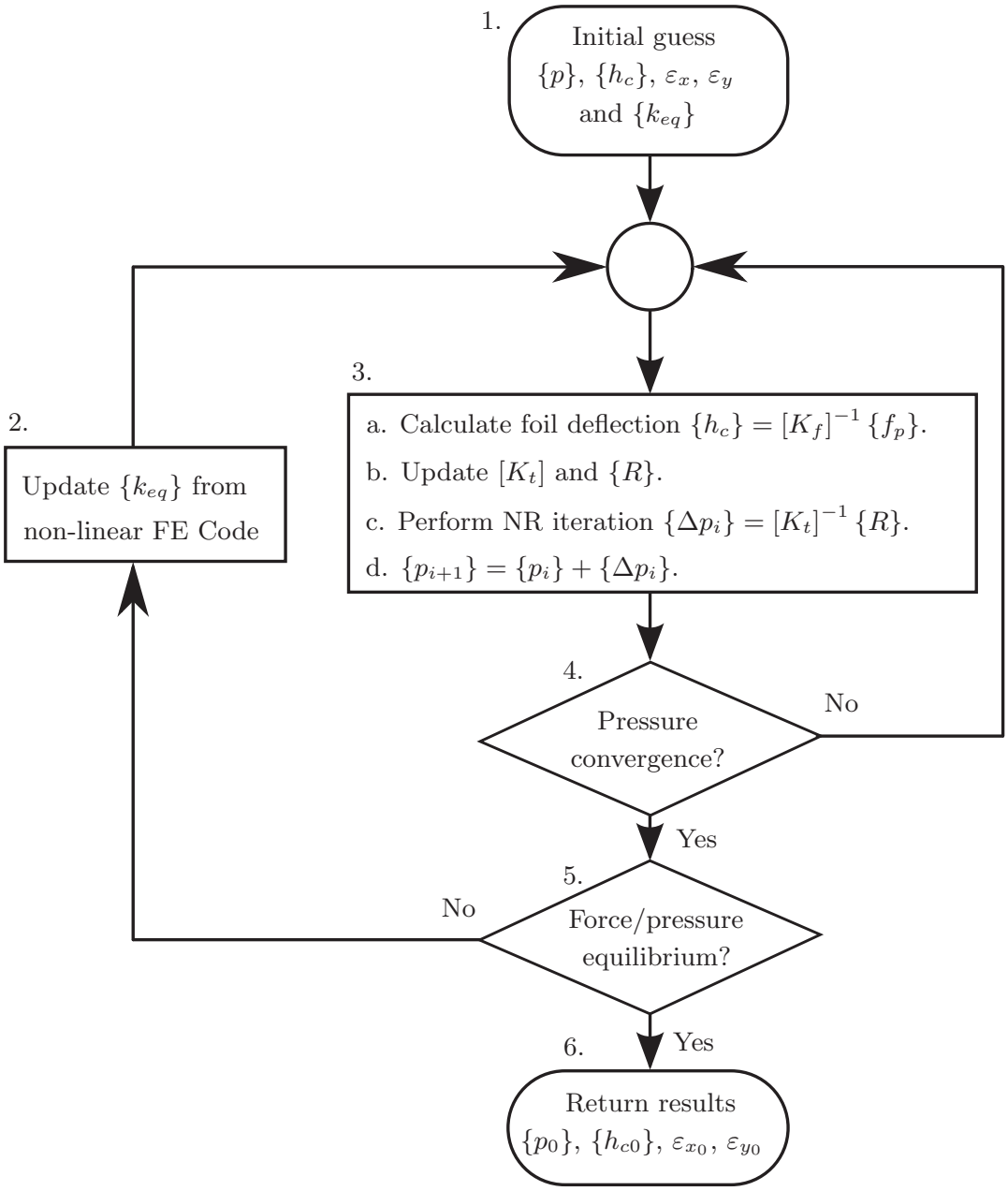

Figure 4.3: Flow chart illustrating the CFSM solution.

4.2.1 Assumptions and limitations

Keeping in mind the assumptions 1-5 related to the SEFM discussed in Sec. 4.1.3, the CFSM eliminates 2 and 3. That is the foil stiffness is no longer assumed constant over the length of the pads, and the deformations in one point is no

longer independent of the deformations in the neighbouring points. However, the foil stiffness is still regarded linear and since the foil model is 2D, the deflection along the length of the bearing is still regarded as constant and based on the average film pressure along the z-direction. However, due to the elimination of 2 and 3 and the introduction of the equivalent bump foil stiffness based on the detailed model, it is fair to assume an improvement in accuracy of the static solution over the SEFM. Assuming that an accurate static solution is available, the first-order equation, which is based on the SEFM and the assumptions 1-5, would likely be valid as the dynamic deflections imposed in this perturbed solution is per definition small. Furthermore, by applying a dynamic stiffness that takes the stiffening effect caused by the friction force in the contact points into account, the first-order solution would no longer make use of assumption 6 that is discussed in Sec. 4.1.3. This is the assumption that friction forces do not significantly alter the foil stiffness.

4.3 Time domain nonlinear transient solution

In Secs. 4.1 and 4.2, two steady-state perturbed solutions were presented and they both yield the static journal eccentricity, foil deflection as well as linearised stiffness and damping coefficients. The stiffness and damping coefficients that are generally frequency dependent for gas bearings can be used together with the shaft model (3.47) to perform steady-state analysis, such as unbalance response and complex eigenfrequency- and stability-analysis. The linearised stiffness and damping coefficients can also be used in combination with the shaft model to simulate the shaft in the time domain. However, such a simulation would not capture any transient, nonlinear dynamics related to the bearings. In this section, a nonlinear transient solution of the shaft and bearing system as illustrated in Fig. 3.9 is presented. The solution is thoroughly described in [P5] and results obtained theoretically are compared to results obtained experimentally in [P6]. The solution includes the nonlinear behaviour of the bearings by solving the Reynolds equation in the time domain, and hence discarding the linearisation previously introduced. Several methods for simulating this kind of systems exist and they will be discussed briefly. The time domain solution given here uses the mathematical models for the foil structure, shaft and air film presented in Chap. 3. Though the steady-state solutions presented were in dimensional form, it is generally a good idea to non-dimensionalise or scale the equations of the mathematical models when performing numerical simulations, both in order to reduce the amount of variables in the numerical solution, but also to keep the numerical values of each variable close to unity in order to minimise rounding errors and convergence problems.

4.3.1 Mathematical model - dimensionless form

Omitting the damping and stiffness matrices related to the the linearised bearing coefficients, the mathematical model for a rigid rotor, as illustrated in Fig 3.9 and given by (3.47), can be written in dimensionless form as:

$$[\tilde{M}]\{\ddot{\varepsilon}\} - [\tilde{G}]\{\dot{\varepsilon}\} = \{\tilde{W}\} - \{\tilde{F}\} + \{\tilde{F}_{ub}\} \tag{4.19}$$

with the bearing eccentricities defined as $\{\varepsilon\} = \{\varepsilon_{\mathrm{A}x}, \varepsilon_{\mathrm{A}y}, \varepsilon_{\mathrm{B}x}, \varepsilon_{\mathrm{B}y}\}^T$ and the non-dimensional form of the mass and gyroscopic matrices and the mass unbalance force vector are given by:

$$[\tilde{G}] = \frac{\omega^2 C}{p_a R^2}[G], \quad [\tilde{M}] = \frac{\omega^2 C}{p_a R^2}[M], \quad \{\tilde{F}_{ub}\} = \left\{ \begin{matrix} \frac{u_{\mathrm{A}}\omega^2}{p_a R^2} \begin{Bmatrix} \cos(\tau) \\ \sin(\tau) \end{Bmatrix} \\ \frac{u_{\mathrm{B}}\omega^2}{p_a R^2} \begin{Bmatrix} \cos(\tau) \\ \sin(\tau) \end{Bmatrix} \end{matrix} \right\}. \tag{4.20}$$

Furthermore, $\{\tilde{W}\}$ is the static load vector and $\{\tilde{F}\}^T = \{\{\tilde{F}_{\mathrm{A}}\}^T,\ \{\tilde{F}_{\mathrm{B}}\}^T\}^T$ is the reaction force vector stemming from the bearings. It is composed by the reactions from the bearings A and B that are determined by integrating the fluid film pressure for each particular bearing as

$$\{\tilde{F}_\gamma\} = \begin{Bmatrix} \tilde{F}_x \\ \tilde{F}_y \end{Bmatrix} = \int_0^{\tilde{L}} \int_0^{2\pi} (\tilde{p} - 1) \begin{Bmatrix} \cos(\theta) \\ \sin(\theta) \end{Bmatrix} d\theta d\tilde{z} \tag{4.21}$$

where $\gamma = \mathrm{A}, \mathrm{B}$. The equation of motion for the foil structure can be written in dimensionless form as:

$$\tilde{p} - 1 = \tilde{k}\tilde{h}_c + \tilde{b}\dot{\tilde{h}}_c \quad \text{or} \quad \tilde{h}_c(\tilde{p}, \dot{\tilde{h}}_c) = \frac{\tilde{p} - 1 - \tilde{b}\dot{\tilde{h}}_c}{\tilde{k}} \tag{4.22}$$

which is basically a rewritten form of the SEFM as given by (3.1). Finally, the mathematical model for the air film, as given by the equations (3.42) through (3.45), can be written in dimensionless form as:

$$\nabla \cdot \left(\tilde{p}\tilde{h}^3 \nabla \tilde{p}\right) - \nabla \cdot \left(\tilde{p}\tilde{h}\right)\{S\} - 2S\frac{\partial \tilde{p}\tilde{h}}{\partial \tau} = 0 \tag{4.23}$$

where the dimensionless rigid film height can be written as:

$$\tilde{h}_r = \begin{cases} 1 + \varepsilon_x \cos(\theta) + \varepsilon_y \sin(\theta) - \tilde{h}_s \frac{\theta - \theta_i}{\theta_s}, & \theta_{li} \le \theta \le \theta_i \\ 1 + \varepsilon_x \cos(\theta) + \varepsilon_y \sin(\theta), & \theta_i < \theta \le \theta_{ti} \end{cases} \tag{4.24}$$

and

$$\begin{aligned}\theta_i &= \theta_s + \theta_l + \frac{2\pi}{N_p}(i-1)\\ \theta_{li} &= \theta_l + \frac{2\pi}{N_p}(i-1)\\ \theta_{ti} &= \theta_t + \frac{2\pi}{N_p}(i-1).\end{aligned} \tag{4.25}$$

Now, the mathematical model for a rigid shaft supported by AFBs can be represented by the non-dimensional equations (4.19) through (4.25).

4.3.2 Solution strategy

In order to simulate the nonlinear rotor response, a commonly used strategy is to rewrite (4.19) to a system of ODEs to be integrated while the bearing forces $\{\tilde{F}\}$ are updated at each time step. The bearing forces relate to the pressure through (4.21) and the pressure is obtained by solving (4.23). This can be accomplished by discretising the air film PDE (4.23) and substituting the time dependent terms by backward difference approximations as:

$$\frac{\partial\{\tilde{p}\}}{\partial\tau} \approx \frac{\{\tilde{p}\}_n - \{\tilde{p}\}_{n-1}}{\Delta\tau}, \quad \frac{\partial\{\tilde{h}\}}{\partial\tau} \approx \frac{\{\tilde{h}\}_n - \{\tilde{h}\}_{n-1}}{\Delta\tau} \tag{4.26}$$

where n is the current time step. The pressure can then be found by iteratively solving a set of nonlinear algebraic equations. Following this strategy, the time dependent terms are lagging behind in time since they are based on the previous time step in the integration of the rotor ODEs. As pointed out by Bonello and Pham [9, 65], this method does not preserve the true simultaneously coupled nature of the state variables, $\varepsilon, \tilde{p}, \tilde{h}_c$, of the system. This means that very small time steps are necessary in order to ensure an accurate solution. It makes the solution slow, and being strictly rigorous, each simulation should be accompanied by a convergence study on the time step size to ensure an accurate solution. Another problem with the solution strategy described above is numerical stability. This is particularly related to the term $\partial\{\tilde{p}\}/\partial\tau$, which tends to become dominant and sensitive to the accuracy of $\{\tilde{p}\}_n - \{\tilde{p}\}_{n-1}$ due to the division by the very small number $\Delta\tau$. Assuming the term negligible is not an option, simulations performed by Olsen [59] clearly showed that discarding this term leads to significant errors. Bonello and Pham [9, 65] introduced a basic strategy to regard all the state variables simultaneously and an efficient solution method based on a Galerkin reduction method to significantly limit the number of state variables. Here, only the basic strategy is followed and it implies setting up one coupled system of nonlinear ODEs of the state variables $\varepsilon, \psi, \tilde{h}_c$, where $\psi = \tilde{p}\tilde{h}$.

4.3.3 The Reynolds equation - discretisation

First, a partial substitution with ψ is performed to obtain a PDE of only one temporal variable

$$\nabla \cdot \left(\tilde{p}\tilde{h}^3 \nabla \tilde{p}\right) - \nabla \cdot \left(\tilde{p}\tilde{h}\right)\{S\} - 2S\frac{\partial \psi}{\partial \tau} = 0. \tag{4.27}$$

Next, following a standard Bubnov-Galerkin FE discretisation procedure as described in [P5], a system of nonlinear equations on the element level can be obtained as:

$$\left[A_{\psi}^{e}\right]\{\dot{\psi}^{e}\} = \{R^{e}\} \tag{4.28}$$

where

$$\begin{aligned} \left[A_{\psi}^{e}\right] &= 2S\int_{V^e}[N]^T[N]dV \\ \{R^e\} &= -\int_{V^e}[B]^T\tilde{p}\tilde{h}^3[B]dV\{\tilde{p}^e\} + \int_{V^e}[B]^T\{S\}\tilde{h}[N]dV\{\tilde{p}^e\}. \end{aligned} \tag{4.29}$$

The element vectors and matrices are expanded to structure size by the usual element summation:

$$\{R\} = \sum_e \{R^e\}; \quad \{\tilde{p}\} = \sum_e \{\tilde{p}^e\}; \quad \{\dot{\psi}\} = \sum_e \{\dot{\psi}^e\}; \quad [A_\psi] = \sum_e \left[A_{\psi}^{e}\right] \tag{4.30}$$

where the volume integrals are numerically integrated using a quadrature rule [16]. The scalar field quantities $\tilde{p}$, $\tilde{h}$ are calculated in the respective Gauss points (ξ_i, ζ_j) using the interpolation functions as:

$$q(\xi_i, \zeta_j) = [N(\xi_i, \zeta_j)]\{q^e\} \tag{4.31}$$

where q and $\{q^e\}$ are the scalar field quantities and nodal vectors respectively. Note that the right hand side of (4.28) is denoted $\{R^e\}$. In fact, $\{R^e\}$ is the residual that needs to be minimised in order to find the static equilibrium of the journal and it is basically similar to (4.10), only here in non-dimensional form. When performing simulations in the time domain, it is very handy to start the simulations from this static equilibrium position that can be found by the method described in Sec. 4.1.2 and [P3].

4.3.4 Coupled state-space equations

With the film PDE discretised, the mathematical model can be written as a system of ODEs, in the form $\{\dot{y}\} = \mathbf{g}(\tau, \{y\})$, and solved for all state variables simultaneously. The state-vector is defined as

$$\{y\}^T = \{\{\psi_{\mathrm{A}}\}^T,\ \{\psi_{\mathrm{B}}\}^T,\ \{\tilde{h}_{c\mathrm{A}}\}^T,\ \{\tilde{h}_{c\mathrm{B}}\}^T,\ \{z_1\}^T,\ \{z_2\}^T\}^T \tag{4.32}$$

with $\{z_1\} = \{\varepsilon\}$, $\{z_2\} = \{\dot{\varepsilon}\}$ and the A and B sub-indices referring to the bearing locations as illustrated in Fig. 3.9. For the particular case of a rigid rotor supported by two bearings, the system dimension of the coupled ODEs is $4N + 8$ with N being the number of nodes in the fluid film finite element model of each individual bearing. The system of ODEs takes the form:

$$\begin{Bmatrix} \{\dot{\psi}_\mathrm{A}\} \\ \{\dot{\psi}_\mathrm{B}\} \\ \{\dot{\tilde{h}}_{c\mathrm{A}}\} \\ \{\dot{\tilde{h}}_{c\mathrm{B}}\} \\ \{\dot{z}_1\} \\ \{\dot{z}_2\} \end{Bmatrix} = \begin{bmatrix} [0] & \cdots & [0] & [0] \\ \vdots & \ddots & \vdots & \vdots \\ & & & [0] \\ [0] & \cdots & [0] & [I] \\ [0] & \cdots & [0] & [\tilde{M}]^{-1}[\tilde{G}] \end{bmatrix} \begin{Bmatrix} \{\psi_\mathrm{A}\} \\ \{\psi_\mathrm{B}\} \\ \{\tilde{h}_{c\mathrm{A}}\} \\ \{\tilde{h}_{c\mathrm{B}}\} \\ \{z_1\} \\ \{z_2\} \end{Bmatrix} + \begin{Bmatrix} \mathbf{g}_{\dot{\psi}\mathrm{A}}(\{\psi_\mathrm{A}\}, \{z_1\}, \{z_2\}, \{\tilde{h}_{c\mathrm{A}}\}, \{\dot{\tilde{h}}_{c\mathrm{A}}\}) \\ \mathbf{g}_{\dot{\psi}\mathrm{B}}(\{\psi_\mathrm{B}\}, \{z_1\}, \{z_2\}, \{\tilde{h}_{c\mathrm{B}}\}, \{\dot{\tilde{h}}_{c\mathrm{B}}\}) \\ \mathbf{g}_{\dot{\tilde{h}}_{c\mathrm{A}}}(\{\psi_\mathrm{A}\}, \{z_1\}, \{z_2\}, \{\tilde{h}_{c\mathrm{A}}\}) \\ \mathbf{g}_{\dot{\tilde{h}}_{c\mathrm{B}}}(\{\psi_\mathrm{B}\}, \{z_1\}, \{z_2\}, \{\tilde{h}_{c\mathrm{B}}\}) \\ \{0\} \\ [\tilde{M}]^{-1}(\{\tilde{W}\} - \{\tilde{F}\} + \{\tilde{F}_{ub}\}) \end{Bmatrix}. \tag{4.33}$$

The the nonlinear functions on the right hand side are defined as:

$$\mathbf{g}_{\dot{\psi}\gamma}(\{\psi_\gamma\}, \{z_1\}, \{z_2\}, \{\tilde{h}_{c\gamma}\}, \{\dot{\tilde{h}}_{c\gamma}\}) = [A_{\psi\gamma}]^{-1} \{R_\gamma\} \tag{4.34}$$

and by introducing the loss factor $\eta = \tilde{b}\omega_s/(\tilde{k}\omega)$ and vectorising the pad deflection given in (4.22):

$$\mathbf{g}_{\dot{\tilde{h}}_{c\gamma}}(\{\psi_\gamma\}, \{z_1\}, \{z_2\}, \{\tilde{h}_{c\gamma}\}) = \left(\frac{\{\tilde{p}_\gamma\} - 1}{\tilde{k}_\gamma} - \{\tilde{h}_{c\gamma}\} \right) \frac{1}{\eta_\gamma} \tag{4.35}$$

where $\gamma = \mathrm{A}, \mathrm{B}$ denotes the individual bearings. In this work, the system of ODEs is solved using the 'lsoda' solver from the Fortran library ODEPACK [32]. This solver has an automatic time step control and switches between dedicated solvers for stiff- and non-stiff systems. To efficiently solve the ODEs, a program for the discretisation and solution of (4.34) is implemented in C using the sparse solver DGBESV from the LaPack library [2]. However, the solution is still time consuming, and it should be highlighted that Bonello and Pham [9, 10, 65] significantly improved the speed of the solution by implementing a Galerkin reduction method or by symbolically computing the Jacobian matrix to be used with a readily available implicit integrator and a predictor-corrector approach.

4.3.5 Boundary conditions

In dimensionless form, the edge-boundary conditions for the bearings, as depicted in Fig. 3.8, are:

$$\begin{aligned} \tilde{p}(\theta_l, \tilde{z}) = \tilde{p}(\theta_t, \tilde{z}) = 1 \\ \tilde{p}(\theta, \tilde{L}/2) = \tilde{p}(\theta, -\tilde{L}/2) = 1. \end{aligned} \tag{4.36}$$

To obey these conditions, it is necessary to evaluate the film state variable $\dot{\psi} = \dot{\tilde{p}}h + \dot{\tilde{h}}p$. On the pad edges, it is known that $\tilde{p} = 1$ and it is constant so $\dot{\tilde{p}} = 0$. This means that when solving (4.34) in order to obtain the film state variable, the following boundary conditions must be imposed:

$$\begin{aligned} \dot{\psi}(\theta_l, \tilde{z}) = \dot{\psi}(\theta_t, \tilde{z}) = \dot{\tilde{h}}(\dot{\varepsilon}_x, \dot{\varepsilon}_y, \dot{\tilde{h}}_c) \\ \dot{\psi}(\theta, \tilde{L}/2) = \dot{\psi}(\theta, -\tilde{L}/2) = \dot{\tilde{h}}(\dot{\varepsilon}_x, \dot{\varepsilon}_y, \dot{\tilde{h}}_c) \end{aligned} \tag{4.37}$$

which is achieved by using the standard FE procedure. Symmetry conditions can be achieved by neglecting (4.37) on one side, for example on $(\theta, \tilde{L}/2)$. In this case, the reaction forces need to be multiplied by two. A commonly used boundary condition is to assume that the bearing foils deform evenly over the length $\tilde{L}$ of the bearing. This condition is implemented by replacing $\{\tilde{p}_\gamma\}$ in (4.35) with $\{\tilde{p}_{\gamma m}\}$, where $\{\tilde{p}_{\gamma m}\}$ is the arithmetic mean pressure over the length $\tilde{L}$. As mentioned in Sec. 4.1.2, significant sub-ambient pressures may arise in gas bearings, again a simple Gümbel [22] boundary condition is imposed, meaning that sub-ambient pressures are discarded when integrating the pressure (4.21) to obtain the bearing force components $(\tilde{F}_x, \tilde{F}_y)$, essentially leaving the sub-ambient regions ineffective.

4.3.6 Assumptions and limitations

The method described above for transient nonlinear analysis of a rigid rotor supported by AFBs are based on the SEFM. Consequently, the method depends on all assumptions related to the SEFM. As will be seen in Sec. 6.3.2, good results can be obtained by carefully estimating the foil stiffness and damping properties based on the hysteresis curves obtained experimentally using the complex foil model presented in Sec. 3.1.4.

Chapter 5

Experimental approaches

In the previous two chapters, the mathematical models and different solutions related to the AFB and the rigid shaft were presented. Parallel to the work developing these mathematical models and their numerical implementation, extensive work related to the development of two experimental test rigs followed by their instrumentation and the experimental testing were carried out. Though the description of this work does not occupy many pages in this thesis, the amount of time spent on this part of the work is still quite substantial. As mentioned, two experimental test rigs were designed, built and used for the experimental validation of the mathematical models. Not only did the experimental results serve as validation, they also served as inspiration and a source for obtaining an increased understanding of the dynamical behaviour of the bump foils as well as the complete rotor-bearing system. As an example, it was initially unclear how the rotor-bearing system would react to increasing levels of unbalance, so this was investigated experimentally. In this chapter, the experimental test rigs are introduced and their purpose explained. Most details about the two test rigs can be found in the publications [P2] and [P4]. Here, further details about the instrumentation, measurement methods and identification procedures are given.

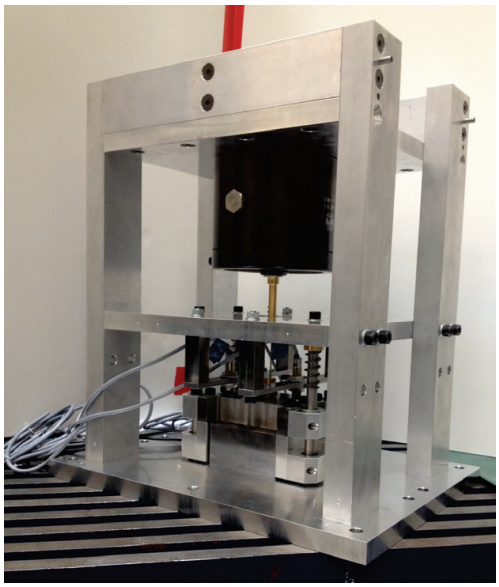

(a) Foil test rig full view.

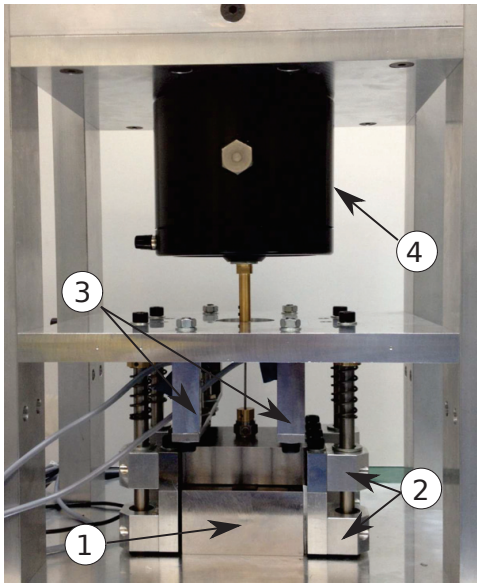

(b) Foil test rig detailed view.

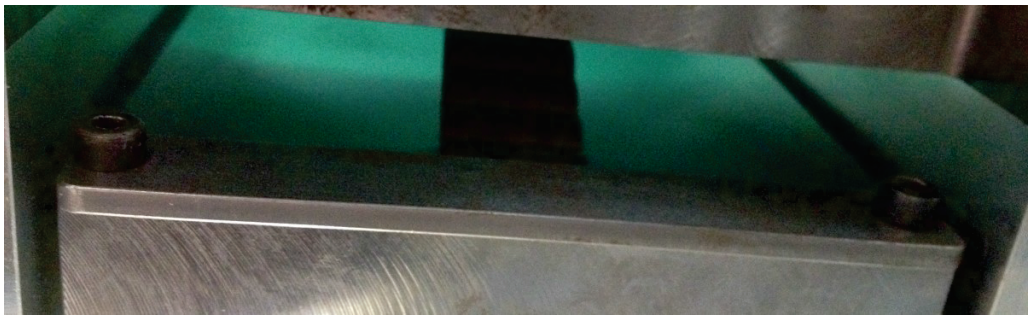

(c) Fixture of the foil specimen at the lower block.

Figure 5.1: Foil test rig including instrumentation. 1) steel blocks for compressing the bump foil. 2) vertical guides. 3) fixture for proximity probes. 4) electromagnetic shaker.

5.1 Foil test rig

In order to characterise the static and dynamic behaviour of the bump foils, a test rig as illustrated in Fig. 5.1 was designed. The fundamental idea behind the test rig is to evenly compress a bump foil strip while simultaneously measuring the force required and the deflection produced at a high level of accuracy. The core of the test rig is the two steel blocks (FE 510D, ISO 630), labelled 1 in Fig. 5.1b. The upper block features linear guides in each corner that allow a vertical movement. These guides are composed of two high-precision linear ball bearings in each corner and are labelled 2 in the figure. The foil specimen is

Table 5.1: Probes and sensors used in the bump foil test rig setup.

Probe	Make	Type	Sensitivity	Range
Prox1	Pulsotronic	KJ4-M12MN50-ANU	0.5050 mm/V	0-400 Hz
Prox2	Pulsotronic	KJ4-M12MN50-ANU	0.4338 mm/V	0-400 Hz
Prox3	Pulsotronic	KJ4-M12MN50-ANU	0.4738 mm/V	0-400 Hz
Acc1	B&K	4384 (charge)	1.7925 $m/s^2/V$	0.1-12.6 kHz
Force	B&K	8200 (IEPE)	11.09 N/V	0.1-5 kHz

placed between the two parallel mating blocks with one end fixed by a clamp attached in the lower block as illustrated in Fig. 5.1c. This ensures that the foil specimen is not moving around during testing and it simulates the actual configuration of the bearing, in which the bump foils are clamped at their leading edge. The arrangement enables the direct determination of the relation between the vertical displacement of the upper block and the deflections of the bumps of the foil strip. The displacements are measured using three displacement probes looking at the upper surface of the moving block, see number 3 in Fig. 5.1b. The sensors are located in a 'triangle' arrangement to detect if any undesired swash or tilting motion occurs during the experimental tests. The upper block can be statically or dynamically loaded in order to induce deflections of the foil strip placed underneath. Static load is applied by means of calibrated weights, whereas dynamic load is obtained by using an electromagnetic shaker, a steel stinger with a diameter of 2 mm and a piezoelectric load cell, see number 4 in Fig. 5.1b. Since the load cell is mounted on the top of the upper block, it does not directly measure the dynamic load on the foils as there is a mass in between. Therefore, an accelerometer is mounted on the upper block so that a compensation can be carried out for the dynamic results. The entire arrangement is mounted in a rigid aluminium frame. The rubber sealing in the bearings are removed and the grease washed out and replaced by thin oil in order to ensure that the damping contribution from the linear bearings are kept at a minimum. The instrumentation of the test rig consists of five probes: Three proximity probes, one accelerometer and a force transducer. The make, type and sensitivity of each of the probes are given in Tab. 5.1. The sensitivities listed in the table are calibrated sensitivities obtained in the DTU laboratory. All signals are simultaneously picked up, sampled and digitally recorded using a dSpace acquisition system with a sample rate of 2,000 Hz.

5.1.1 Bump foil specimen dimensions

The bump foil specimen are taken from the actual AFB being investigated both theoretically and experimentally in this thesis. As mentioned in Sec. 2.1 and

Table 5.2: Geometry and material properties of the bump foil specimen.

Parameters	Values
Bump foil thickness, t_b	0.127 mm
Bump foil height, h_0	0.9 mm
Bump foil pitch, S_b	7.00 mm
Bump half length, l_0	3.30 mm
Bump foil width, w_b	18 mm
Young's modulus of bump foil, E	2.07×10^{11} Pa
Poisson's ratio of bump foil, ν	0.3
Coefficient of friction, μ	0.20

illustrated in Fig. 2.3, the bump foils are sliced in the circumferential direction. One such slice is 18 mm in width and constitutes the tested bump foil specimen. By shortening the specimen, the number of bumps can be reduced. The geometry and nomenclature of the bump foils are given in Fig. 3.1 and the associated dimensions are listed in Tab. 5.2. The foil is manufactured using Inconel X750 hardened for maximum yield stress.

5.1.2 Foil test rig characterisation

During testing, the bump foil specimen is subjected to deflections in the range $0 - 250$ μm for the static measurements and $10 - 50$ μm for the dynamic ones. These are small deflections, especially for the dynamic case. Hence, it is very important that the test rig is free from eigenfrequencies in the frequency range of the measurements, which is defined as $0 - 100$ Hz. To ensure this, a test rig characterisation was thoroughly performed. It involved, among other tests, a modal analysis with a coil spring between the two steel blocks. Vibrating the upper steel block, that is compressing the spring, at frequencies swept from $0 - 100$ Hz while measuring the force and the acceleration of the block, using an accelerometer for the latter, enabled the performance of a modal analysis of the system under the assumption that the system behaved as a single DOF system. The test showed a completely flat frequency response except for the single resonance frequency at 18.6 Hz, related to the mass of the upper block, which is 3.99 kg, and the coil spring which has a stiffness of approximately 54.6 kN/m. Consequently, it was concluded that the system did, as expected, behave as a single DOF system with no unwanted test rig resonances in the frequency range of interest. The test also allowed the identification of the damping generated in the linear guiding bearings. This damping was identified by fitting the measured response to a single DOF system using the least squares method, and it was found to be approximately 100 Ns/m. This is considered a negligible

damping contribution compared to the amount of damping generated in the bump foil specimens which is between one and two orders of magnitudes higher. The beams holding the proximity-probes (number 3 in Fig. 5.1b.) were also investigated and no natural frequencies in the range of interest were identified. Finally, using bump foil specimens with a different number of bumps, the movement of the upper block was carefully investigated using the three proximity probes oriented in a triangular pattern. No swash movement of the pressure plate was identified and the three proximity probes all had readings within 5% of each other, indicating a close to parallel movement.

5.1.3 Uncertainty analysis

For the uncertainty analysis of the static results, the relationship between applied static load (calibrated weights) and resulting deflection of the bump foil was examined. A foil specimen originally consisting of 10 bumps was progressively shortened down to 8, 6, 4 and 2 bumps. For each configuration, five full load cycles (loading and unloading) were performed. The standard deviation of the measured deflections was calculated in order to check the influence of random errors over the results. The largest uncertainty interval obtained is 8 μm and the lowest one is 2 μm. This uncertainty interval is much larger than the uncertainty contribution from the measurement chain, and hence this part is neglected. With respect to the uncertainty analysis of the dynamic results, the applied force on the foil specimen was determined as the summation of the preload, the value measured by the piezoelectric load cell associated with the shaker stinger plus the inertia force coming from the upper steel block, quantified using a piezoelectric accelerometer. The deflections were measured using the displacement probes. The reported hysteresis curves were composed by averaging the loading cycles obtained over a one minute long test. Repeatability was checked by repeating the test five times, with different foil specimens, obtaining similar results. Variability of the results was on the same order of magnitude as the one registered for the static testing, that is 2-8 μm.

5.2 Rotor-bearing test rig

A rotor-bearing test rig consisting of a rigid shaft supported by two AFBs in a similar arrangement of a Siemens direct driven compressor was built with two specific goals:

1) Identifying the linearised stiffness and damping coefficients of AFBs ex-

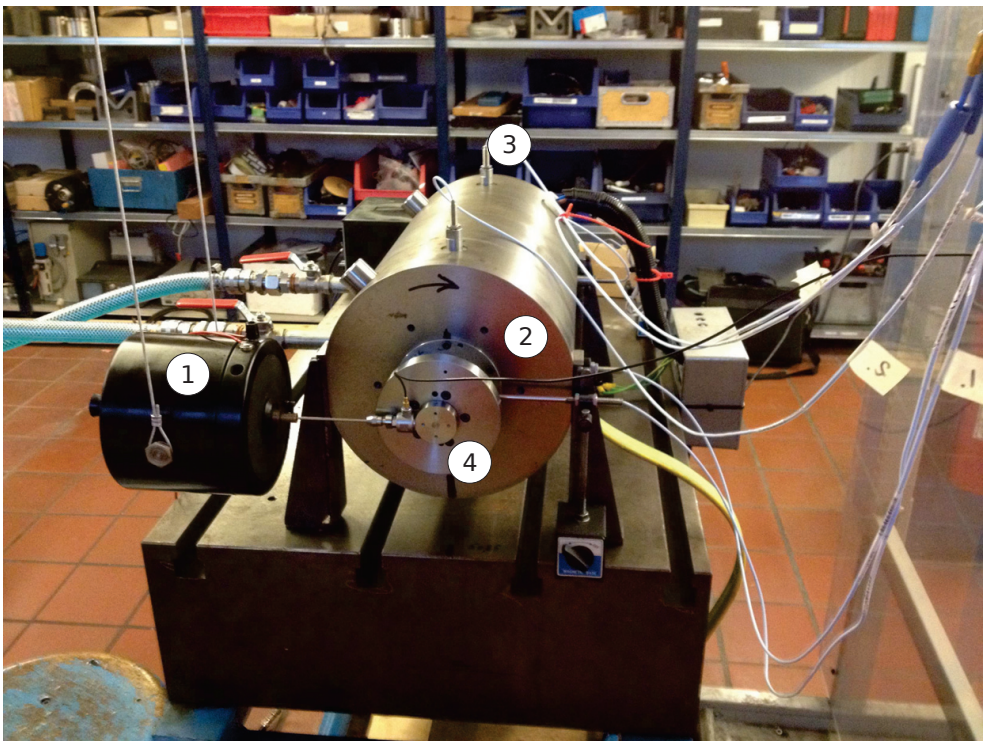

Figure 5.2: Experimental test rig for identification of bearing coefficients. 1) Electro magnetic shaker. 2) Stator housing. 3) Proximity probe. 4) Rotor disk with stator inner part.

perimentally under realistic loading and operation conditions

2) Investigating the rotor response to unbalance

A photo of the test rig is illustrated in Fig. 5.2 and a drawing highlighting all the major parts is illustrated in Fig. 5.3. As previously mentioned, it consists of a rigid, near symmetric hollow rotor supported by two identical AFBs. A set of permanent magnets are press-fit in the centre of the rotor, and together with a set of stator windings, this arrangement constitutes the electrical drive motor for spinning the rotor. There is no axial bearing, that is the shaft is held axially in place only by the magnetic forces. The shaft is equipped with a disk-mounting-flange at each end. Plane disks or disks with a stationary inner part can be mounted at these flanges. With regard to rotor unbalance tests, the plane disks can be used and specified unbalance can be added by calibrating the weights of the bolts holding the disks in place. For identifying the linearised stiffness and damping coefficients of the AFBs, the disks having the stationary inner part, numbered 4 in Fig. 5.2, are used. An electromagnetic shaker, numbered 1, is connected to the stationary inner part of the disks through a stinger and a force transducer enabling the excitation of the spinning rotor while simultaneously

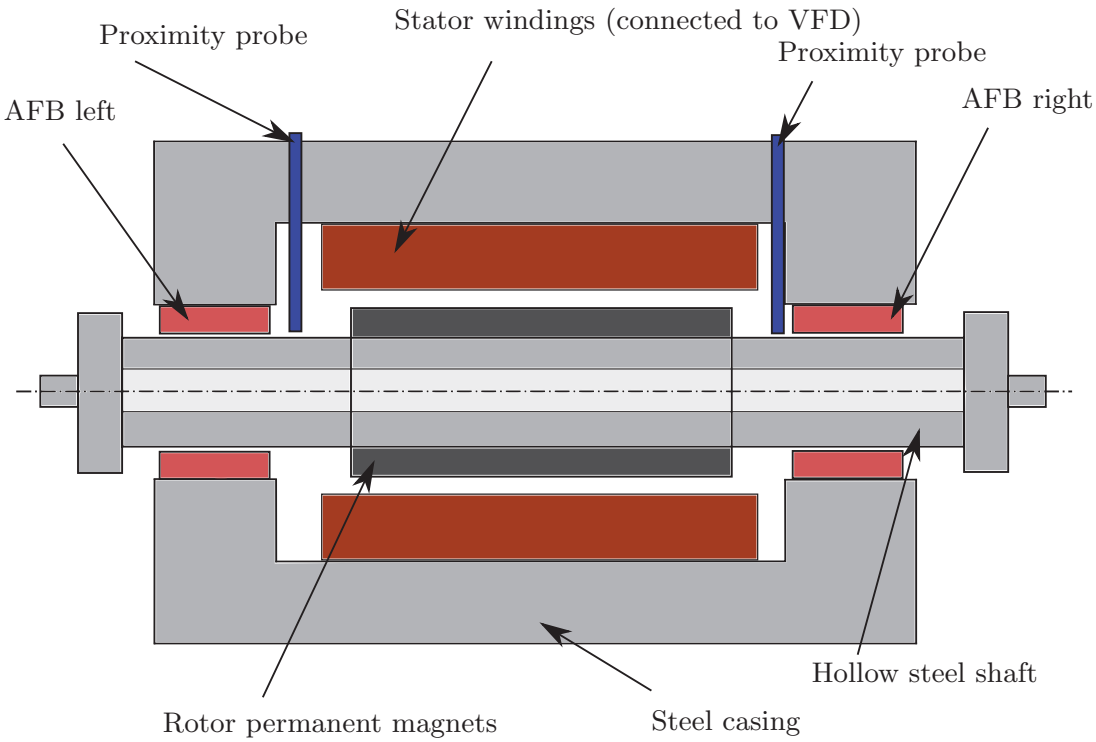

Figure 5.3: Schematic of the assembled rotor-bearing test rig. It consists of a rigid steel housing accommodating the stator windings (which are electrically connected to a VFD) and the AFBs which supports the hollow steel rotor. The permanent magnets are press fit on the hollow steel rotor. Proximity probes are located close to each bearing in vertical and horizontal directions.

measuring the excitation force. The rotor vibrations are picked up using four proximity probes close to the bearing locations in the x- and y-direction; these are numbered 3 in the figure. The mass of the assembled rotor is 21 kg and the operational speed range is 15 to 30 kRPM. The first free-free eigenfrequency is theoretically calculated and experimentally measured to be approximately 1050 Hz, which is more than twice the 1X excitation frequency at maximum speed, that is the rotor can be treated as being rigid. The entire rotor assembly is balanced to below ISO G2.5. A detailed schematic of the rotor assembly with important reference positions is given in Fig. 5.4. The positions are: B, BE and BP that are related to the left bearing, exciter and proximity sensor respectively. Similar to the right side: A, AE and AP are the right bearing, exciter and proximity sensor reference positions respectively. The sensors used for instrumenting the test rig are listed in Tab. 5.3. All sensor signals are picked up, sampled and digitally recorded using a National Instrument CompaqDAQ system with NI9239 and NI9234 high resolution (24 bit) modules capable of sample frequencies up to 50 kHz with integrated anti-aliasing filters. For this setup, a sample frequency of 1,706 Hz is used.

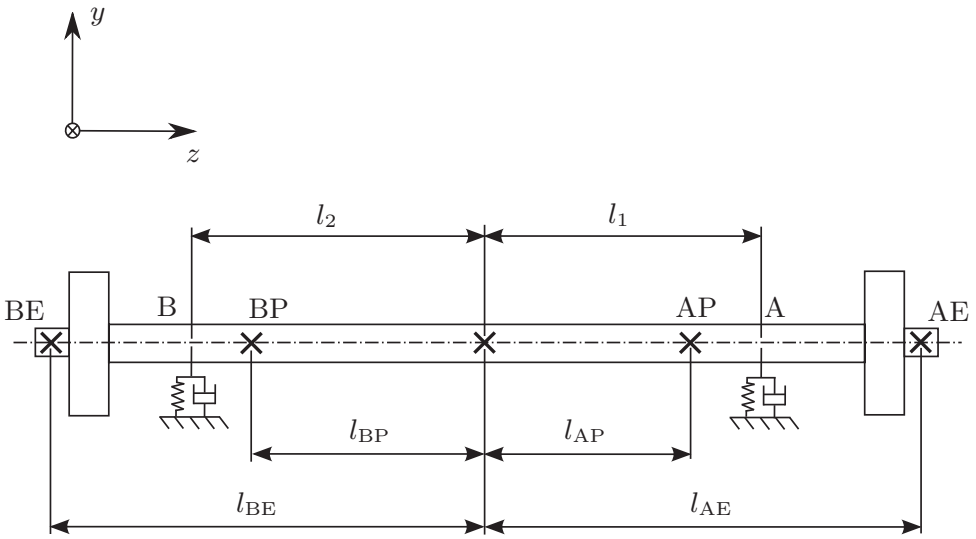

Figure 5.4: Schematic and positions nomenclature of the assembled rotor.

Table 5.3: Probes and sensors used in the rotor-bearing test rig setup.

Probe	Make	Type	Sensitivity	Range
Prox1	Bently Nevada	3300 5mm	0.1272 mm/V	0-10 kHz
Prox2	Bently Nevada	3300 5mm	0.1323 mm/V	0-10 kHz
Prox3	Bently Nevada	3300 5mm	0.1284 mm/V	0-10 kHz
Prox3	Bently Nevada	3300 5mm	0.1284 mm/V	0-10 kHz
Force	B&K	8230 (IEPE)	42.64 N/V	0.1-5 kHz
Exc1	B&K	4384	-	-

5.2.1 Dimensions

In Tab. 5.4, all dimensions, material properties and operating conditions related to the test rig AFB are listed. The dimensions essential for the analysis of the rigid test rig rotor are listed in Tab. 5.5. All experimental and theoretical analyses related to the test rig are based on these data.

5.2.2 Identification procedure

The identification of the linearised bearing coefficients of the two bearings A and B is achieved using frequency domain techniques combined with the method of a structural joint parameter identification procedure [4, 87]. Harmonic forcing excitation is applied to the individual excitation points AE, BE of the rotor, while simultaneously measuring the vibrations, using the position sensors at AP, BP

Table 5.4: Geometry, material properties and operating conditions of the Siemens air foil bearing.

Parameters	Values
Bearing radius, R	33.50 mm
Bearing length, L	53.00 mm
Bearing radial clearance, C	40 μm
Number of pads, N_p	3
First pad leading edge, θ_l	30 deg.
First pad trailing edge, θ_t	145 deg.
Slope extend, θ_s	30 deg.
Slope, h_s	50 μm
Bump foil thickness, t_b	0.127 mm
Top foil thickness, t_t	0.254 mm
Bump foil pitch, S_b	7.00 mm
Bump foil half length, l_0	3.30 mm
Bump foil height, h_b	0.9 mm
Bump foil extend, θ_0	30 deg.
Young's modulus of bump foil, E	2.07×10^{11} Pa
Poisson's ratio of bump foil, ν	0.3
Foil friction coefficient, μ_f	0.2
Ambient pressure, p_a	1×10^5 Pa
Air viscosity, μ	1.95×10^{-5} Pa·s

Table 5.5: Dimensions for the test rig rotor.

Parameters	Values
l_1	201.1 mm
l_2	197.9 mm
l_{AP}	163.1 mm
l_{BP}	158.4 mm
l_{AE}	287.2 mm
l_{BE}	304.0 mm
$m = m_x = m_y$	21.1166 kg
$I_{xx} = I_{yy}$	$525.166 \cdot 10^{-3}$ kgm^2
I_{zz}	$30.079 \cdot 10^{-3}$ kgm^2

as illustrated in Fig. 5.4. Values of all relevant parameters for the identification are as mentioned listed in Tab. 5.5. The relation between excitation forcing and the mechanical vibrations are

$$[H_{\mathrm{EP}}]\,\{f_{\mathrm{E}}\} = \{q_{\mathrm{P}}\}, \tag{5.1}$$

where $[H_{\mathrm{EP}}]$ is the FRF matrix experimentally obtained [P4] and $\{f_{\mathrm{E}}\} = \{f_{\mathrm{AE}x}, f_{\mathrm{AE}y}, f_{\mathrm{BE}x}, f_{\mathrm{BE}y}\}^T$ and $\{q_{\mathrm{P}}\} = \{q_{\mathrm{AP}x}, q_{\mathrm{AP}y}, q_{\mathrm{BP}x}, q_{\mathrm{BP}y}\}^T$ are the complex force and deflection vectors respectively. The FRF matrix (5.1) can be transformed to relate the forcing and mechanical vibrations to the bearing locations A and B

$$[H_{\mathrm{AB}}]\{f\} = \{q\} \tag{5.2}$$

where

$$\begin{aligned} [H_{\mathrm{AB}}] &= [T_1]\,[H_{\mathrm{EP}}]\,[T_2]^{-1} \\ \{f\} &= \{f_{\mathrm{A}x}, f_{\mathrm{A}y}, f_{\mathrm{B}x}, f_{\mathrm{B}y}\}^T \\ \{q\} &= \{q_{\mathrm{A}x}, q_{\mathrm{A}y}, q_{\mathrm{B}x}, q_{\mathrm{B}y}\}^T. \end{aligned} \tag{5.3}$$

The transformation matrices $[T_1]$ and $[T_2]$ are given in [P4]. The equation of motion of the rotor-bearing system can be written as

$$[M]\{\ddot{q}\} + (-\omega\,[G] + [D] + [D_b])\{\dot{q}\} + ([K] + [K_b])\{q\} = \{f\} \tag{5.4}$$

where $[M]$, $[K]$, $[G]$ and $[D]$ are the mass, stiffness, gyroscopic and damping matrices of the rotor alone, and $[D_b]$ and $[K_b]$ are the damping and stiffness contributions from the bearings. The dynamic stiffness of the rotor-bearing system can then be stated as

$$[H_{\mathrm{AB}}]^{-1} = -\omega_s^2\,[M] + i\omega_s(-\omega\,[G] + [D] + [D_b]) + ([K] + [K_b]). \tag{5.5}$$

Since $[H_{\mathrm{AB}}]$ is obtained experimentally, the stiffness and damping of the bearings can be obtained as

$$[K_b] + i\omega_s\,[D_b] = [H_{\mathrm{AB}}]^{-1} - [H^r_{\mathrm{AB}}]^{-1} \tag{5.6}$$

where $[H^r_{\mathrm{AB}}]^{-1}$ is the dynamic stiffness matrix of the rotor without bearings. For a rigid rotor $[D] = [0]$, hence it can be obtained theoretically as

$$[H^r_{\mathrm{AB}}]^{-1} = -\omega_s^2\,[M] - i\omega_s\omega\,[G]\,. \tag{5.7}$$

5.2.3 Uncertainty analysis

If the exact values of the matrices $[H_{\mathrm{AB}}]$ and $[H^r_{\mathrm{AB}}]$ are known, then from (5.6) the bearing coefficients can be exactly identified too, since no approximations have been introduced. However, both matrices are associated with uncertainties. The matrix $[H_{\mathrm{AB}}]$ is associated with measurement uncertainties and the matrix $[H^r_{\mathrm{AB}}]$ is associated with modelling uncertainties. The systematic uncertainties of both have been evaluated using standard statistical methods as described in [8, 57]. Specifically, a computerised uncertainty analysis is imposed where the

Table 5.6: Uncertainty intervals in percent for all relevant probes and parameters used in the experimental identification procedure.

Probe	Uncertainty in percent	Note
Prox1	$[+0.5\% : -0.5\%]$	experimentally obtained
Prox2	$[+0.5\% : -0.5\%]$	experimentally obtained
Prox3	$[+0.5\% : -0.5\%]$	experimentally obtained
Prox3	$[+0.5\% : -0.5\%]$	experimentally obtained
Force	$[+1\% : -1\%]$	manufacture data
Mass	$[+5\% : -5\%]$	guess
Inertia	$[+5\% : -5\%]$	guess
lengths (l_1, l_2, etc)	$[+5\% : -5\%]$	guess

uncertainty of all variables, that is the measurement transducers and geometrical properties like mass, inertia and lengths associated with the identification procedure is taken into account by varying all recorded data in the identification procedure up and down by its individual uncertainty and storing the result for each of these variations. The overall uncertainty can then be calculated as the root-sum-square of each of these results. The uncertainty variations used for each sensor and parameter of the identification procedure are listed in Tab. 5.6. As can be seen in Sec. 6.2, the identified uncertainties are relatively small. It should be kept in mind though that this is under the assumption that the dynamics of the test rig can be precisely described by the mathematical model given in Sec. 3.3, that is the higher order (non-modelled) dynamics do not play a role in the frequency range of interest. Any mechanical effects not described by the mathematical model may result in significant uncertainties, higher than what has been estimated. To minimise the random errors, each of the FRFs in $[H_{\mathrm{AB}}]$ are obtained as an average of 50 measured chirps from 5-300 Hz with a chirp duration of 9.5 s.

Chapter 6

Theoretical & experimental results

The main theoretical and experimental results obtained during this PhD work are summarised in this final chapter. Most of these results were already published in the collection of papers composing the main body of this paper-based PhD thesis. Some results that are left out of this chapter, especially concern: the static verification of the air film model which is presented in [P1], verification of the bump foil model against analytical results and detailed analysis of the friction forces on a foil strip subjected to a load cycle [P2], performance study on the steady-state solution of the Reynolds equation, as well as the impact of foil sagging with respect to the dynamic coefficients [P3], and finally, the verification of the nonlinear transient time domain analysis presented in [P5]. In order to highlight the main findings of the PhD work, the theoretical and experimental results are compared and presented in a direct and progressive fashion, that is by leaving the abovementioned results out of the presentation. However, it is recommended to read [P1-P6] as a supplement to this chapter. Where nothing else is mentioned, all theoretical analyses and experimental results presented in this chapter are based on the geometries and operation conditions listed in Tabs. 5.4 and 5.5.

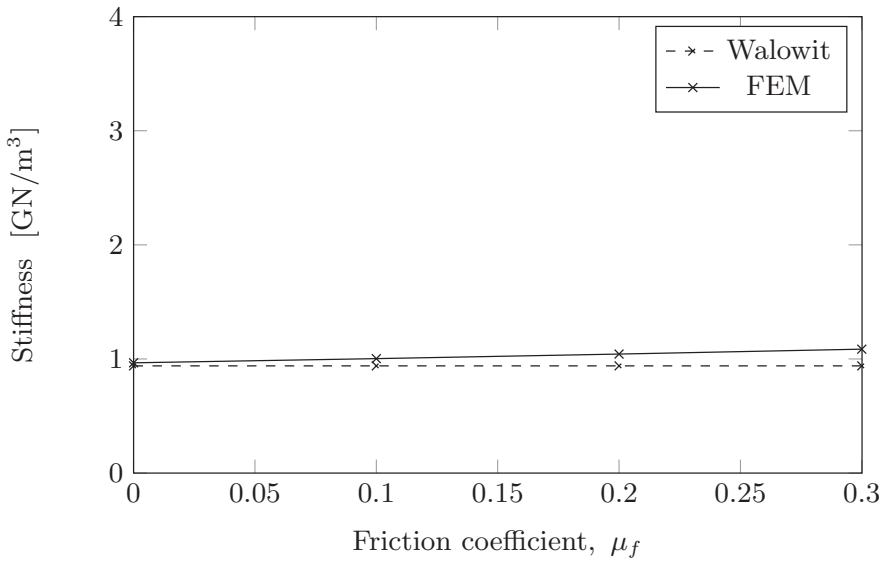

Figure 6.1: Stiffness of a single bump numerically calculated as function of varying coefficients of friction - comparison to analytical results of Walowit and Anno [84].

6.1 Bump foil analysis

As discussed in Chap. 2, the bump foil is the flexible element that alters the AFB compliance. An accurate model for predicting the behaviour of the bump foils is therefore important in order to predict the overall dynamical behaviour of an AFB. A model based on the FE method was proposed in Sec. 3.1.4 and in Fig. 6.1; the stiffness obtained from this model is compared to the stiffness obtained using the analytical model (3.2) given by Walowit and Anno [84]. Their model is based on a single bump that is only constrained in the vertical direction at its ends, that is no rotational constraints are prescribed. They show that the angular extend of the bump θ_0 cancels out when the coefficient of friction is small $\mu_f \approx 0$. Hence by assuming the friction $\mu_f = 0$, they obtain the stiffness given by (3.2). The angular extend can be found from:

$$\theta_0 = \arctan\left(\frac{2h_b l_0}{l_0^2 - h_b^2}\right). \tag{6.1}$$

Furthermore, they show that for small angular extends, $\theta_0 \leq 30$ degrees, the effect of the friction forces on the bump stiffness is small for coefficients of friction $\mu_f < 0.25$. This is confirmed by the FE results as illustrated in Fig. 6.1. The calculated stiffness is nearly unchanged for coefficients of friction in the range $\mu_f = [0; 0.3]$. In fact, a very good agreement between the analytical results [84] and the results obtained by the FE method is found. However, for higher

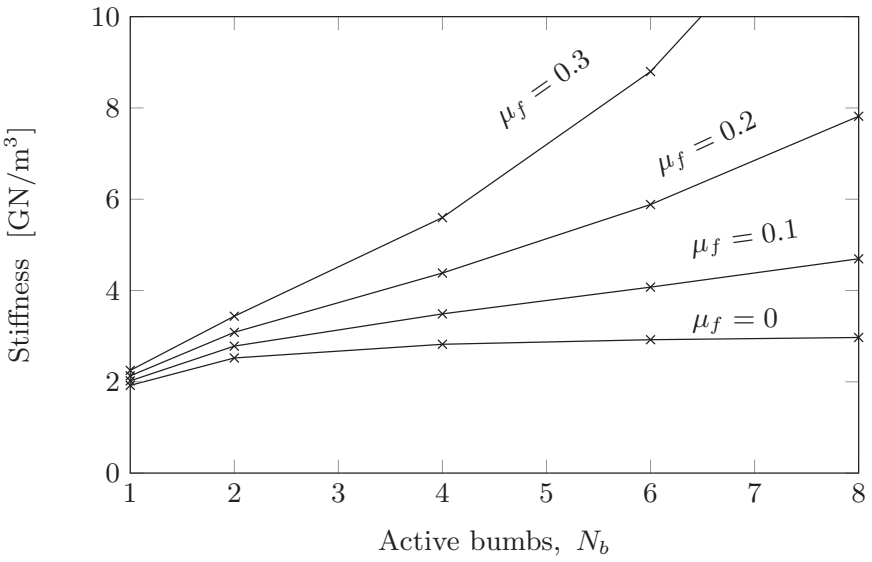

Figure 6.2: Bump stiffness calculated numerically - varying coefficients of friction and number of bumps in the foil strip.

angular extends, $\theta_0 > 30$ degrees, and higher coefficients of friction, the bump foil stiffness is significantly altered. This is shown by Walowit and Anno [84] and lately confirmed by Iordanoff *et al.* [39] who present analytical expressions for the stiffness of a single bump subjected to a similar set of boundary conditions. They investigate the bump stiffness for different coefficients of friction and report increasing bump stiffness at increasing coefficients of friction. It is noted, that their bump geometry is characterised by a slightly larger bump extend, $\theta_0 > 30$ degrees, compared to the Siemens geometry.

In Sec. 4.1.3, six assumptions related to the SEFM were discussed. Assumption number six was highlighted as being fundamental because it states that the friction forces in the sliding contact points do not alter the overall stiffness of the bump foils. According to the analytical expression given by Walowit and Anno and the FE results presented here, this turns out to be true for the given configuration, that is a single bump having small angular extend θ_0 and low coefficient of friction μ_f and only constrained in vertical direction at each end. However, regarding the case where the first bump is clamped at one end and attached to several other bumps, this assumption is challenged, as seen in Fig. 6.2. Here, the results are based on an equal compression of a bump foil strip from zero deflection. As mentioned, the first bump is now clamped at one side and the total number of bumps and the the coefficient of friction are varied. It is clear that both parameters significantly alters the overall stiffness (per area) of the foil, and consequently, assumption number six becomes invalid. Basically, the analytical expression underestimates the stiffness if more than one bump is

loaded and the coefficient of friction is different from zero, $\mu_f \neq 0$. This finding is supported by several authors, for example [30, 31, 39, 44, 45, 51, 53].

6.1.1 Static hysteresis curves

The stiffness, predicted by the numerical procedure, is unequal for loading and unloading when $\mu_f \neq 0$. As mentioned, Figs. 6.1 and 6.2 are based on the loading process. In Fig. 6.3, the difference between loading and unloading is clearly illustrated. The figure illustrates load-displacement diagrams for $\mu_f = 0.1$ and $\mu_f = 0.2$ for a foil strip with four bumps ($w_b = 22$ mm). All bumps are given a gradual compression to approximately 25 μm with small oscillations of 1.5 μm amplitude occurring at approximately 5, 10, 15 and 20 μm during the loading process. The particular bump foil geometry is designed for a journal bearing having a clearance of 50 μm, meaning that a compression of 25 μm would result in a bearing eccentricity ratio of approximately 1.5. The stiffness related to the small 'local' hysteresis loops contained in the large 'global' hysteresis loop is referred to as the local stiffness. It is found to be nonlinear and significantly higher than the global. This is in good agreement with previous experimental studies performed by Ku and Heshmat [45]. The hysteresis loops cause the bump foil strip to provide Coulomb damping proportional to its confined area. The size of the confined area is dependent on where at the global hysteresis curve the deflection oscillation is taking place (5, 10, 15 or 20 μm). If the deflection is sufficiently large, the load versus displacement will track the global hysteresis curve during the unloading process. This situation is seen in Fig. 6.3a for the oscillation around 5 μm. In this case, the confined area grows significantly leading to more Coulomb damping, and the stiffness becomes highly nonlinear as it changes significantly at the points where the local load-displacement coincides with the global hysteresis loop. Tracking the global hysteresis curve corresponds to the situation where all contact points are sliding.

In order to verify the results of the FE model, the test rig, as described in Sec. 5.1, was used to obtain experimental static hysteresis loops for a bump foil strip. The results obtained experimentally and theoretically are illustrated in Fig. 6.4. As mentioned, the uncertainty is between 2-8 μm. The results obtained with strips of two and four bumps are illustrated in Fig. 6.4a and the results of a strip with six bumps is illustrated in Fig. 6.4b. Good agreement between the experimental and theoretical results are found when using a coefficient of friction $\mu = 0.2$ for the simulations. This value corresponds well with common values, which is typical in the range $0.1 < \mu < 0.5$ for steel against steel (0.5 in vacuum), and also with the results obtained by e.g [45, 70]. With regards to strips with a higher number of bumps, higher global stiffness and larger discrepancies with theoretical results are observed. The results obtained for a

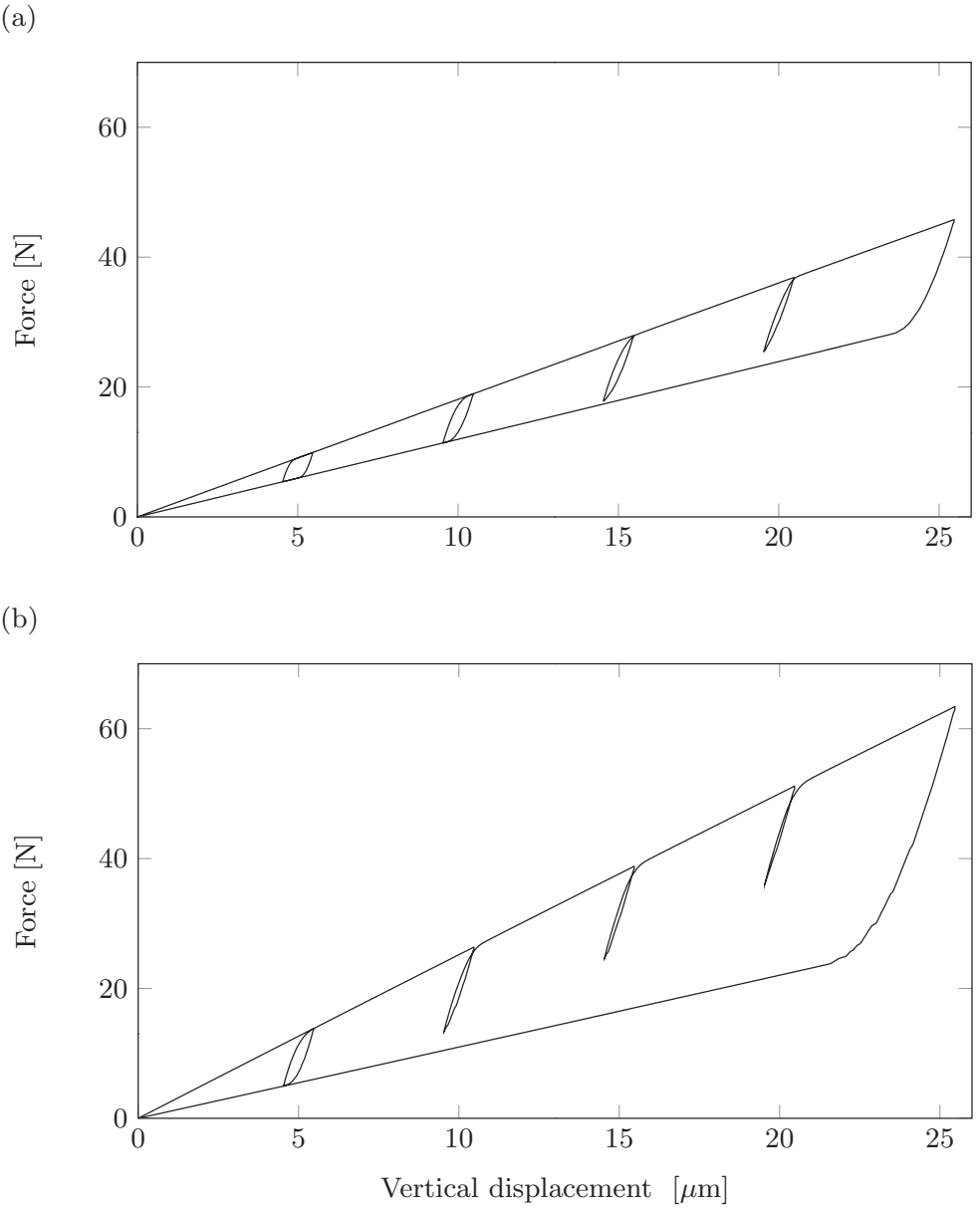

Figure 6.3: Theoretical results of a bump strip given a global compression of approximately 25 μm with local oscillations of 1.5 μm amplitude occurring at 5, 10, 15 and 20 μm during the loading process. (a) Using a coefficient of friction $\mu_f = 0.1$ (b) Using a coefficient of friction $\mu_f = 0.2$

strip with six bumps, see Fig. 6.4b, portray these trends. The discrepancies can be attributed to geometrical imperfections of the foils, specifically different bump heights entailing that not all bumps are in contact with the mating surface from the beginning of the loading cycle. This effect becomes more prevailed for

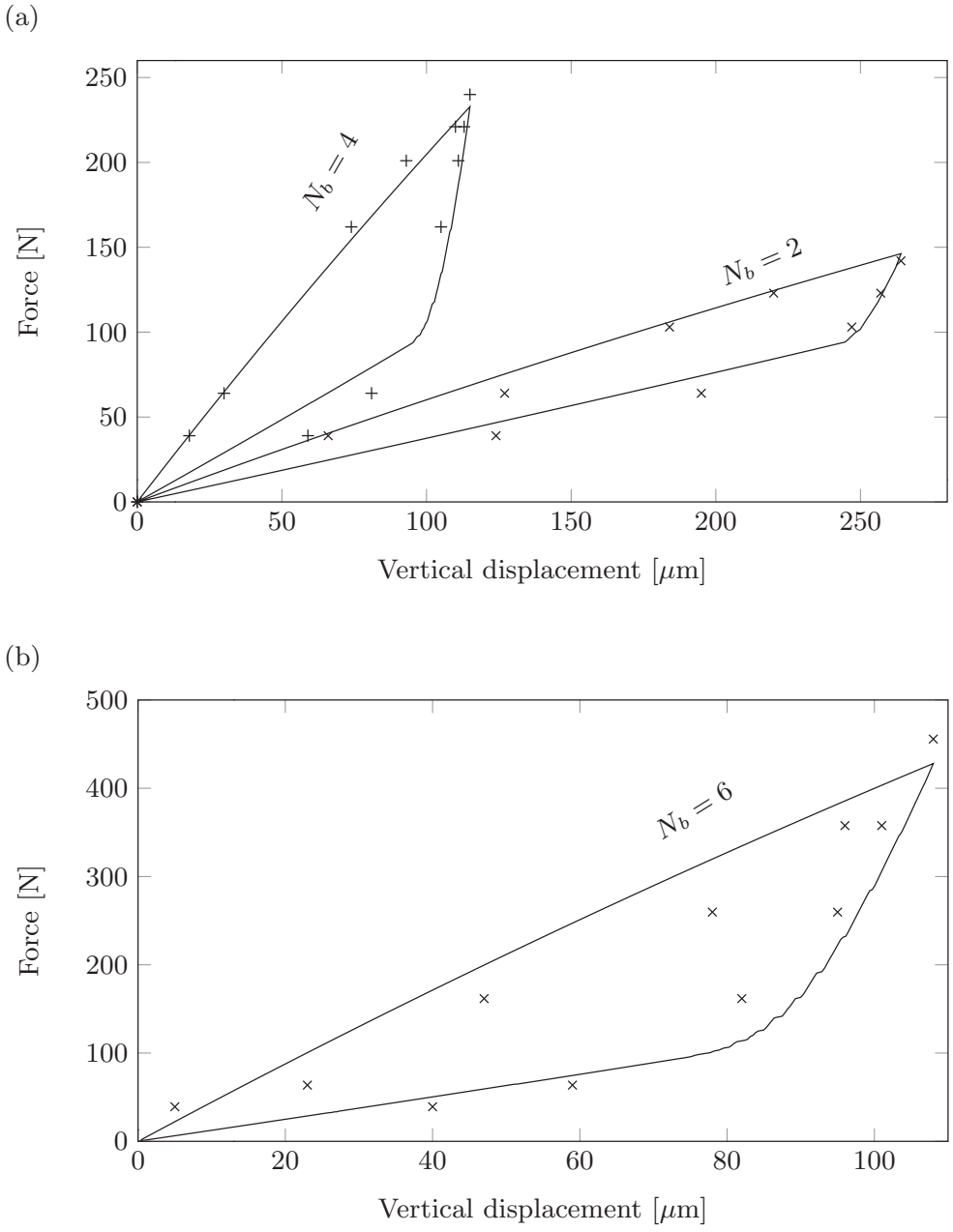

Figure 6.4: (a) Hysteresis loops for two and four bump strips; numerical results using $\mu_f = 0.2$ (full lines), experimental results (markers). (b) Hysteresis loops for a six bump strip; numerical results using $\mu_f = 0.2$ (full lines), experimental results (markers).

higher number of bumps. Similar trends are observed when testing strips of eight and ten bumps.

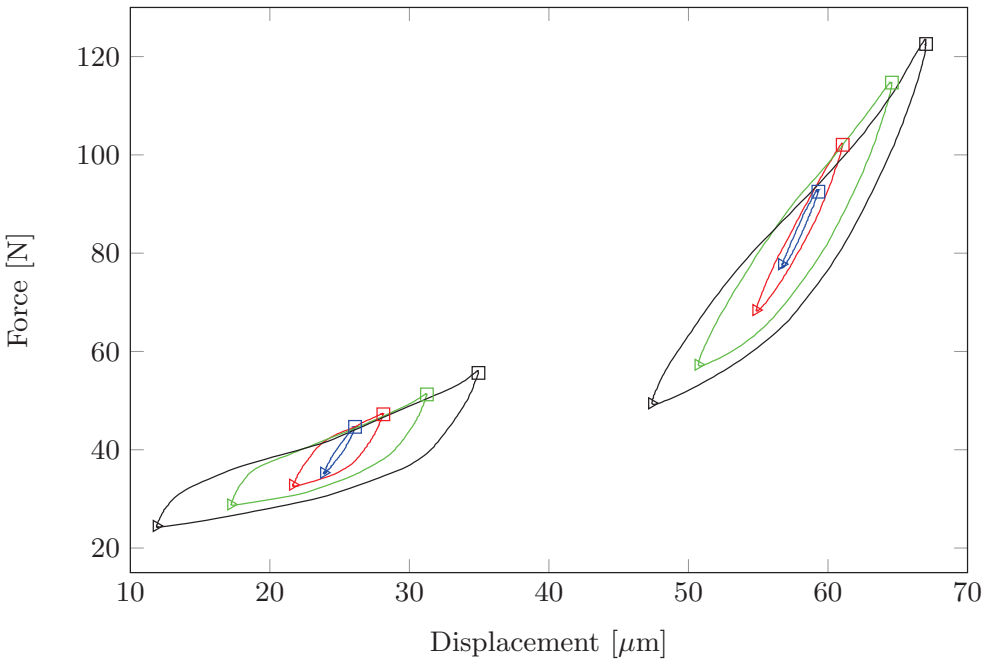

Figure 6.5: Results of the dynamic testing for different displacement amplitudes (2 (blue), 4 (red), 8 (green), 12 (black) μm). The applied load frequency is 1 Hz. The preloads are 40 N and 90 N. The foil strip consists of three bumps.

6.1.2 Dynamic hysteresis curves

In the previous section, the static results of the foil FE model were compared to static results obtained experimentally. In this section, it is investigated whether a dynamic loading will have any effect on the results, that is if a frequency dependency exists. As mentioned, the FE based program is limited to perform steady-state analysis. Hence, the results presented in this section, most of which was previously published in [P2], will be of purely experimental nature.

Experimentally obtained hysteresis curves for a foil specimen with three bumps are illustrated in Fig. 6.5 through Fig. 6.8. They are based on load frequencies of 1, 10, 20 and 40 Hz respectively. Common for all experiments is that a static preload and a dynamic load are simultaneously applied on the foil strip. The preload is adjusted to 40 N and 90 N respectively in order to study the effect of this parameter. The dynamic load is generated by supplying a sine wave of fixed voltage amplitude and frequency to the electromagnetic shaker in order to induce the foil deflections. The amplitude of the dynamic load is tuned to obtain different displacement amplitudes for the hysteresis cycles. Hence, results for 2 (blue), 4 (red), 8 (green) and 12 (black) μm of displacement amplitude are obtained.

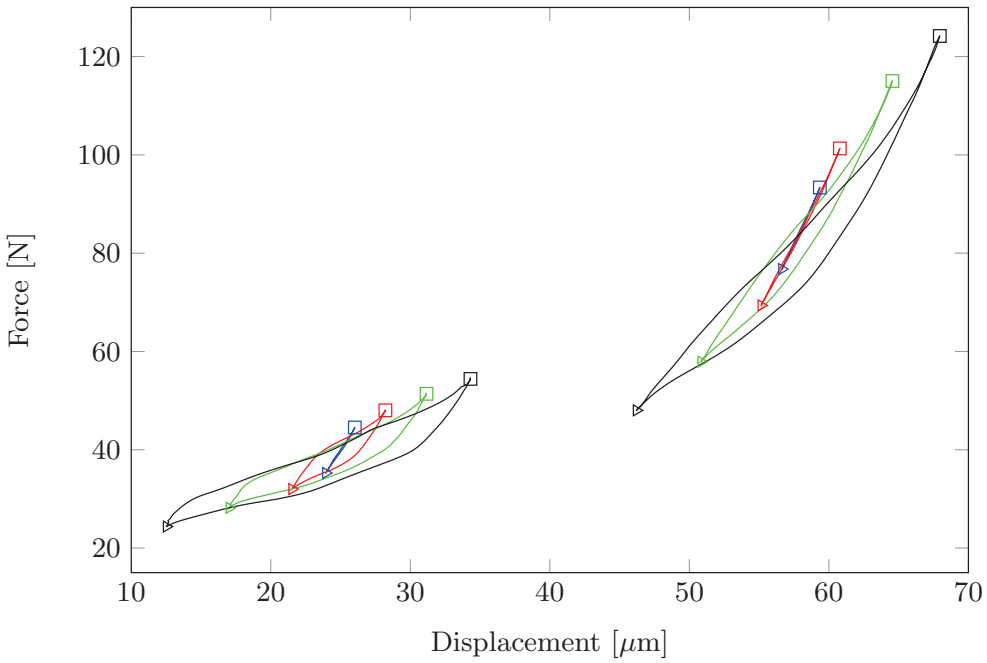

Figure 6.6: Results of the dynamic testing for different displacement amplitudes (2 (blue), 4 (red), 8 (green), 12 (black) μm). The applied load frequency is 10 Hz. The preloads are 40 N and 90 N. The foil strip consists of three bumps.

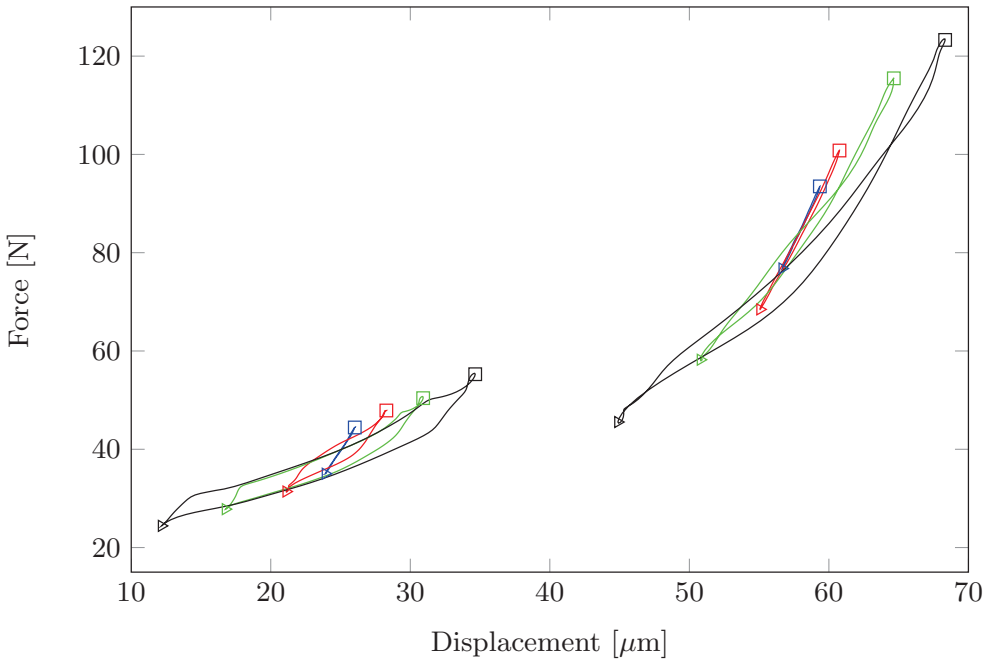

Figure 6.7: Results of the dynamic testing for different displacement amplitudes (2 (blue), 4 (red), 8 (green), 12 (black) μm). The applied load frequency is 20 Hz. The preloads are 40 N and 90 N. The foil strip consists of three bumps.

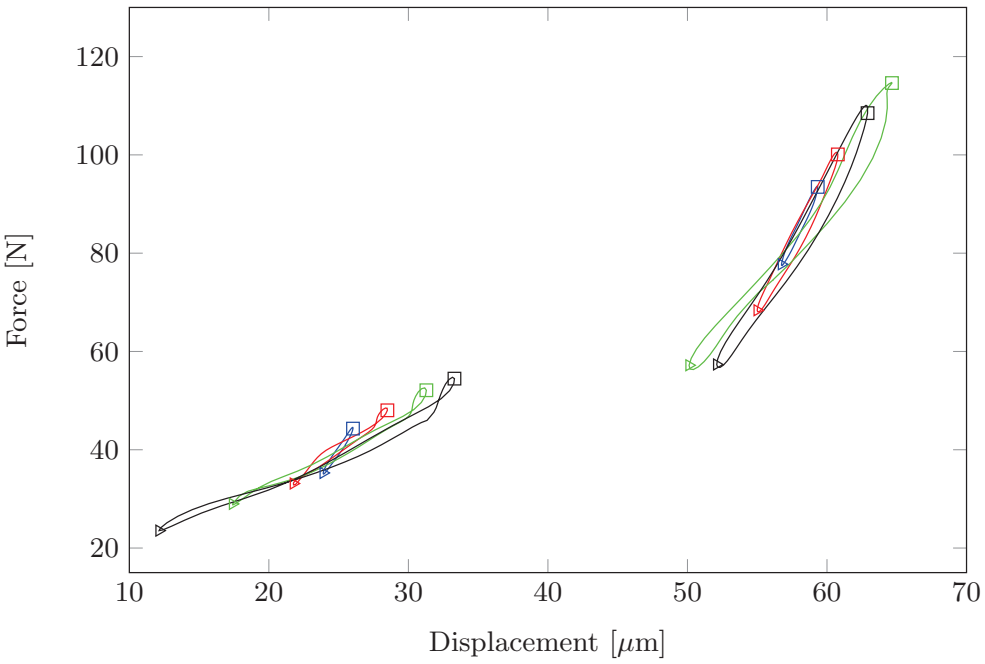

Figure 6.8: Results of the dynamic testing for different displacement amplitudes (2 (blue), 4 (red), 8 (green), 12 (black) μm). The applied load frequency is 40 Hz. The preloads are 40 N and 90 N. The foil strip consists of three bumps.

The loading frequencies tested here are well below the first resonant frequency of the experimental setup. Although the studied frequency range might seem limited when compared to the broad frequency range in which an AFB is normally operated, a distinctive modification in the overall behaviour of the hysteresis loops is already observed within the studied range. The maximum loading frequency that can be achieved with the test rig is limited by the natural frequency of the current setup, which depends on the foil specimen in place. Regarding a specimen having three bumps, this is found to be approximately 100 Hz. The results obtained for a loading frequency of 1 Hz (see Fig. 6.5) coincide with the static results. By increasing the loading frequency, significant changes in the hysteresis behaviour are observed. This is especially true at the larger displacement amplitudes, as it can be seen in Fig. 6.6 through Fig. 6.8. With regard to higher loading frequencies, the area enclosed by the local hysteresis curves tends to become smaller, and they are not tracing the global static anymore. A closer inspection reveals that the 'high slope' behaviour observed for the low frequency results tends to diminish or disappear for excitations with a higher frequency. Following the reasoning established before, this could be attributed to the fact that all the bumps exhibit a sliding motion without switching to a sticking phase when the direction of the displacement is inverted.

Basically, the dynamic results illustrated in Fig. 6.5 through Fig. 6.8 indicate

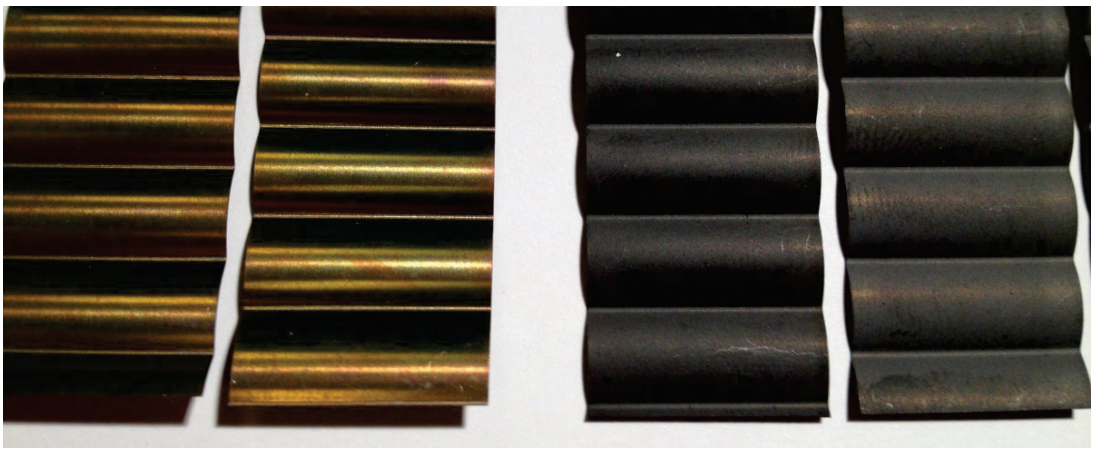

Figure 6.9: Bump foils subjected to different heat treatments. Left: the new heat treatment resulting in a brown colour. Right: the old heat treatment resulting in a black colour caused by an oxide-like layer.

that the hysteresis loops are strongly load frequency dependent, and consequently, the stiffness and damping properties of the foil structure will be load frequency dependent as well. These results were published in [P2], but the investigations were continued with the goal of clarifying what caused the hysteresis loops to be so strongly frequency dependent. The metal blocks in the test rig were refurbished to the original surface roughness, Ra = 0.4, and readjusted. New foil specimens were prepared and probes and sensors were recalibrated, and finally, all experiments were performed again [15]. At this point, it is important to mention that the heat treatment procedure of the bump foils was changed at some point within the duration of this PhD work. This changed the colour of the foils from matte black to a metal-shine brown. The black colour on the foils exposed to the old heat treatment is assumed to be caused by some kind of oxide layer and it clearly results in a higher surface roughness on the foils. The new heat treatment results in a metal-shine finish with lower surface roughness and slightly brownish glow. The two differently coloured specimens are illustrated in Fig. 6.9. The first set of experiments were conducted with the black foil specimens and the second using both the black and the brown [15]. In the latter, the experimental results based on the black foils turned out to be inconsistent and hysteresis loops with clear distinction between the sticking and sliding regions, as presented earlier, could not be reproduced. The hysteresis curves took the shape of what would be expected for an equivalent viscous system. On the other hand, the experimental results related to the brown specimens produced consistent hysteresis curves with well-defined regions (sticking and slipping). A selected set of results for the brown specimen consisting of four bumps is illustrated in Fig. 6.10 and Fig. 6.11 for 5 and 10 μm displacement amplitude respectively. The slopes (foil stiffness) of the hysteresis curves correspond well

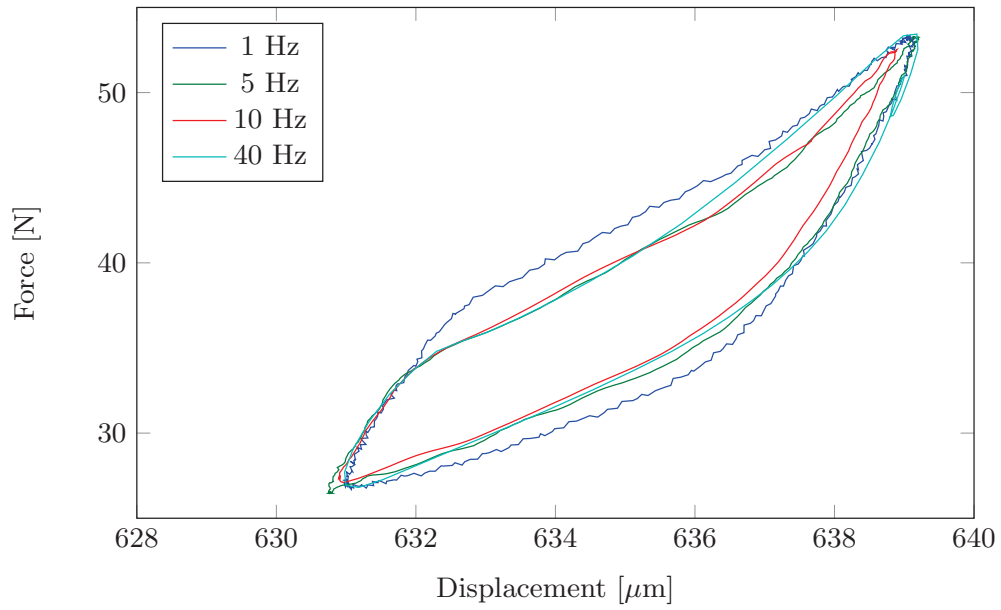

Figure 6.10: Results of the dynamic testing for different frequencies with an amplitude of approximately 5 μm. The preload is 40 N. The foil strip consists of four brown bumps.

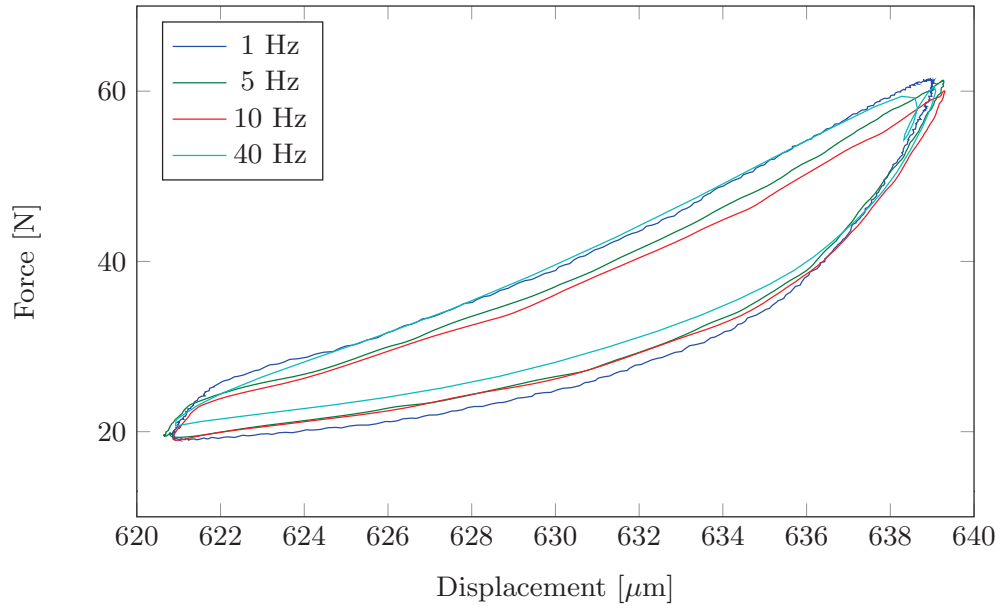

Figure 6.11: Results of the dynamic testing for different frequencies with an amplitude of approximately 10 μm. The preload is 40 N. The foil strip consists of four brown bumps.

with the static results illustrated in Fig. 6.4a. However, the significant frequency dependency identified in the first set of experiments, which were based on the black bump specimen, is not reproduced in this second set of experiments. A slight reduction of the area enclosed by the hysteresis loop is seen between the results obtained at 1 Hz and higher at frequencies. But between the results obtained at 10 and 40 Hz, there is no difference.

6.1.3 Summary of bump foil analysis

The main findings from the theoretical and experimental results related to the bump foil structure, which is presented in this chapter and in [P2], can be summarised by the following six points:

1) The bump foil stiffness is dependent on the number of bumps and the coefficient of friction between the foils and the housing.

2) The bump foil stiffness is close to linear for monotonic loading from zero deflection.

3) The bump foil stiffness predicted by analytical expressions that does not take into account the stiffening effect of the friction forces, like for example (3.2) and (3.3), will considerably under-predict the bump foil stiffness.

4) For oscillating loads on a preloaded bump foil, the stiffness is many times higher than what is predicted by (3.2), and depending on the load amplitude, the stiffness can become highly nonlinear.

5) The FE model, presented in Sec. 3.1.4, predicts the hysteresis loops of the bump foils accurately when compared to experiments.

6) The shape and size of the hysteresis loops are found to be load frequency dependent.

However, an important note should be tied to point 6 in the findings list above. Whereas the first set of dynamic experiments indicated a significant load frequency dependency, the second set indicated an insignificant dependency. These results are contradictory, and since no errors related to the experiments could be identified, none of the results can be excluded at this point. As mentioned, the results of the first set of experiments were based on the black foil specimen. The static part of these results were not reproducible in the second test using the black specimen, only when using the brown ones. Based on this, one could assume that the frequency dependency found in the first set of experiments are

related to the black oxide-like coating, and hence, that the frequency dependency is negligible if the foils are not subjected to this coating. However, not enough evidence is available to conclude this at the time of writing.

6.2 Perturbation analysis

In this section, the SEFM and CFSM for obtaining the linearised bearing coefficients are compared to each other as well as to results obtained experimentally with the rotor-bearing test rig. The test rig was previously presented in Sec. 5.2. Due to the experimental comparison, all theoretical results presented in this section are based on the dimensions and operating conditions of the actual rotor-bearing test rig. The two theoretical methods, SEFM and CFSM, are presented in Sec. 4.1 and Sec. 4.2 respectively. The first method is based on the analytical foil model given by Walowit and Anno [84], and the latter is based on a foil FE model. Results of the FE model was presented and thoroughly discussed in the previous section. Before presenting the results obtained with the SEFM and CFSM, once again, it is important to highlight the differences in the predicted foil stiffness related to the two models. In Fig. 6.12, an example of load displacement curves obtained using the FE foil model and the analytical model are presented in the same diagram. From this, it is seen that the slope,

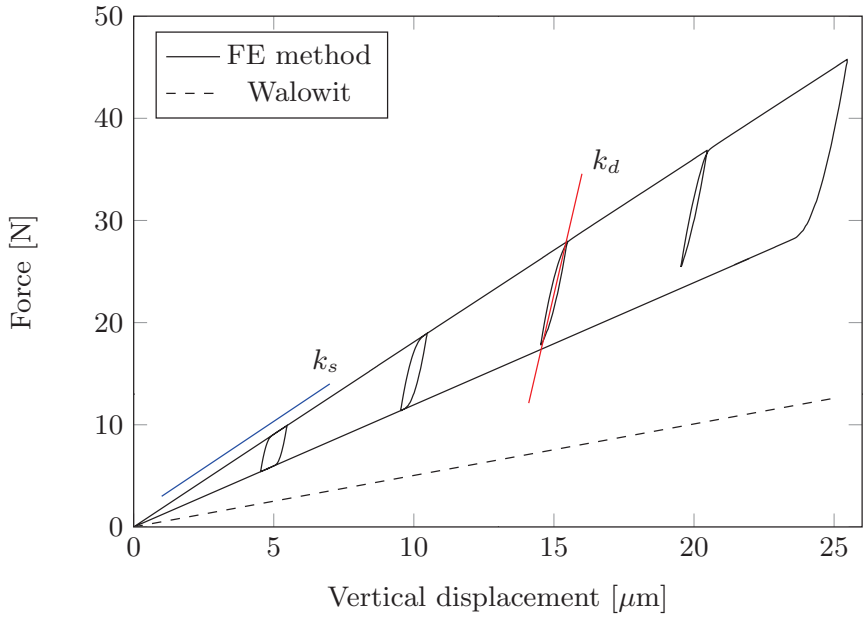

Figure 6.12: Load displacement diagrams obtained using nonlinear finite element model and the analytical expression of Walowit and Anno [84].

which is equivalent to the stiffness, given by the analytical model is significantly lower than the stiffness given by the FE model. Moreover, the hysteresis loop calculated by the FE model indicates the need of distinguishing between a static and a dynamic stiffness, k_s and k_d respectively. When the bearing is initially loaded, the foils have a stiffness as indicated by the blue line in the figure (monotonic loading from zero deflection). Whereas for the loaded bearing subjected to perturbations around an equilibrium position, the foil stiffness will be significantly higher as indicated by the red line (preloaded foils subjected to load oscillations). Consequently, the static stiffness, k_s, should be used when solving the zero-order equation for the static equilibrium position and pressure, and the dynamic stiffness should be used when solving the first-order perturbed equation for obtaining the linearised bearing coefficients. Distinguishing between the static and the dynamic foil stiffness is accomplished by the CFSM as opposed to the SEFM, which uses the same low stiffness for both the zero- and first-order equations.

By solving the perturbed SEFM, as given by (4.3) to (4.9), with a foil flexibility based on the analytical expression (3.2) and with an operating speed of $\omega = 20,000$ RPM, the bearing coefficients can be obtained at a range of journal excitation frequencies ω_s. The results are illustrated in Fig. 6.13, in which the sub-figures contain: (a) the stiffness coefficients and (c) the damping coefficients. Similar results based on the CFSM are illustrated in the sub-figures (b) and (d) respectively. Comparing the stiffness and damping coefficients obtained by the two different theoretical methods reveals large discrepancies. The coefficients obtained by the CFSM are generally much higher compared to the ones obtained by the SEFM. As highlighted a number of times throughout this thesis, foil deflection models excluding the effect of the friction stiffening will generally underestimate the foil stiffness. This was the initial motivation for modifying the SEFM and developing the CFSM. However, as described in [P4], the CFSM did not perform as intended due to unanticipated behaviour related to the steady-state equilibrium of the journal position and the foil deflections. Specifically, by solving for a steady-state solution using the CFSM with a coefficient of friction $\mu_f \neq 0$, several solutions might appear depending on the initial conditions, that is the journal eccentricity guess. To overcome the problem of multiple solutions, the coefficient of friction is set to zero when solving for the steady-state. This will result in a load displacement curve between the global loading and unloading, that is a slightly lower stiffness than k_s as illustrated in Fig. 6.12. Having determined the steady-state solution of the foil structure, the coefficient of friction is then changed back to $\mu_f = 0.2$, and a foil stiffness is obtained with the foil FE model following a numerical perturbation. This foil stiffness is then used when solving the first-order equation to obtain the linearised coefficients. Using this approach, the friction stiffening is neglected in the steady-state solution, but it is included in the first-order solution. However, as indicated in Tab. 6.1, a significant difference between the steady-state

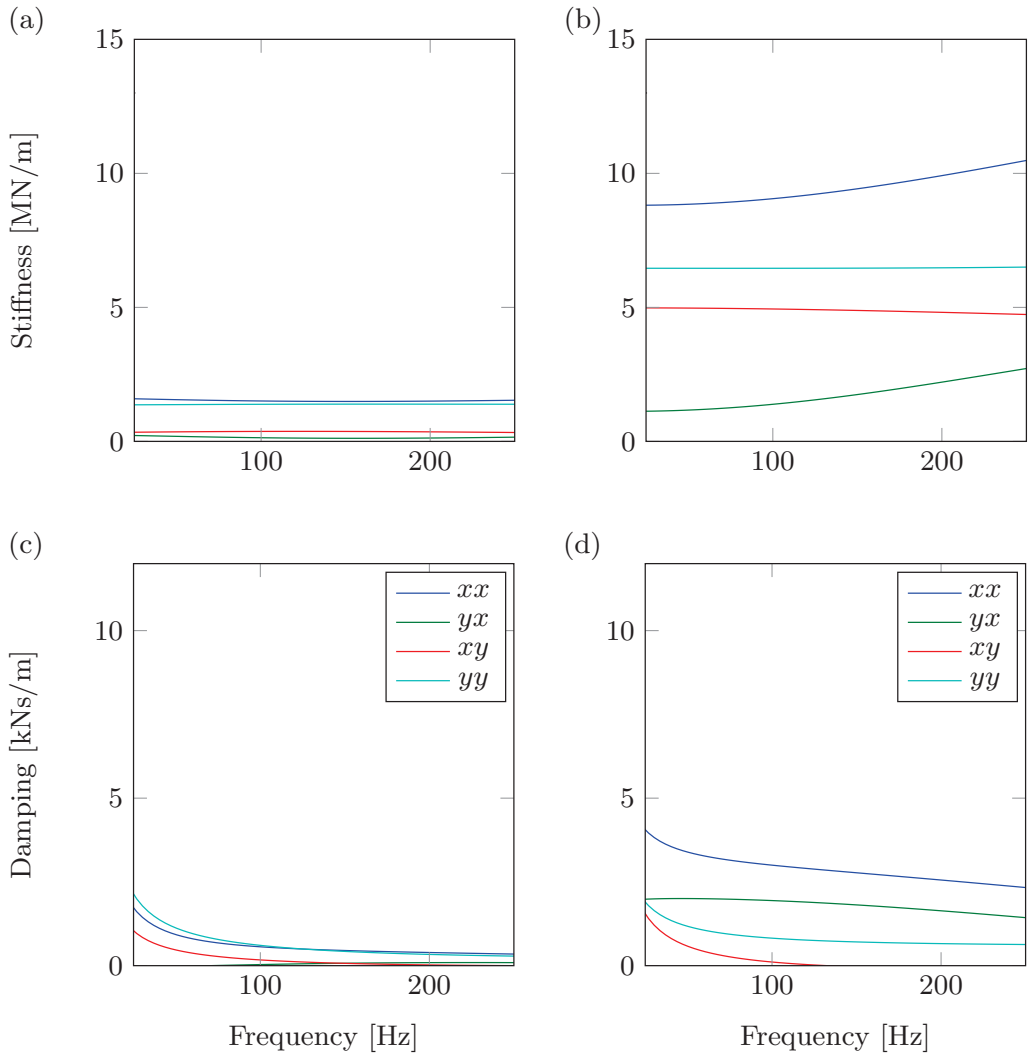

Figure 6.13: Theoretically predicted linear bearing coefficients versus excitation frequency ω_s at 20,000 RPM with a loss factor of $\eta = 0.25$: (a) Stiffness coefficients predicted by the SEFM. (b) Stiffness coefficients predicted by the CFSM. (c) Damping coefficients predicted by the SEFM. (d) Damping coefficients predicted by the CFSM.

equilibrium positions obtained with two methods is still seen. The stiffness and damping coefficients identified experimentally at 20,000 and 28,000 RPM are illustrated in Fig. 6.14. Comparing the bearing coefficients obtained theoretically and experimentally, it is clear that the SEFM yields poor agreement by significantly underestimating both stiffness and damping coefficients. In contrast, the results obtained by the CFSM generally indicates good agreement with the experimental results. Though, certain discrepancies related to the damping co-

Table 6.1: Predicted steady-state eccentricity ratios at 20,000 RPM using SEFM and CFSM respectively.

Method	ε_{x_0}	ε_{y_0}
SEFM	1.8511	0.2884
CFSM	1.0625	0.2480

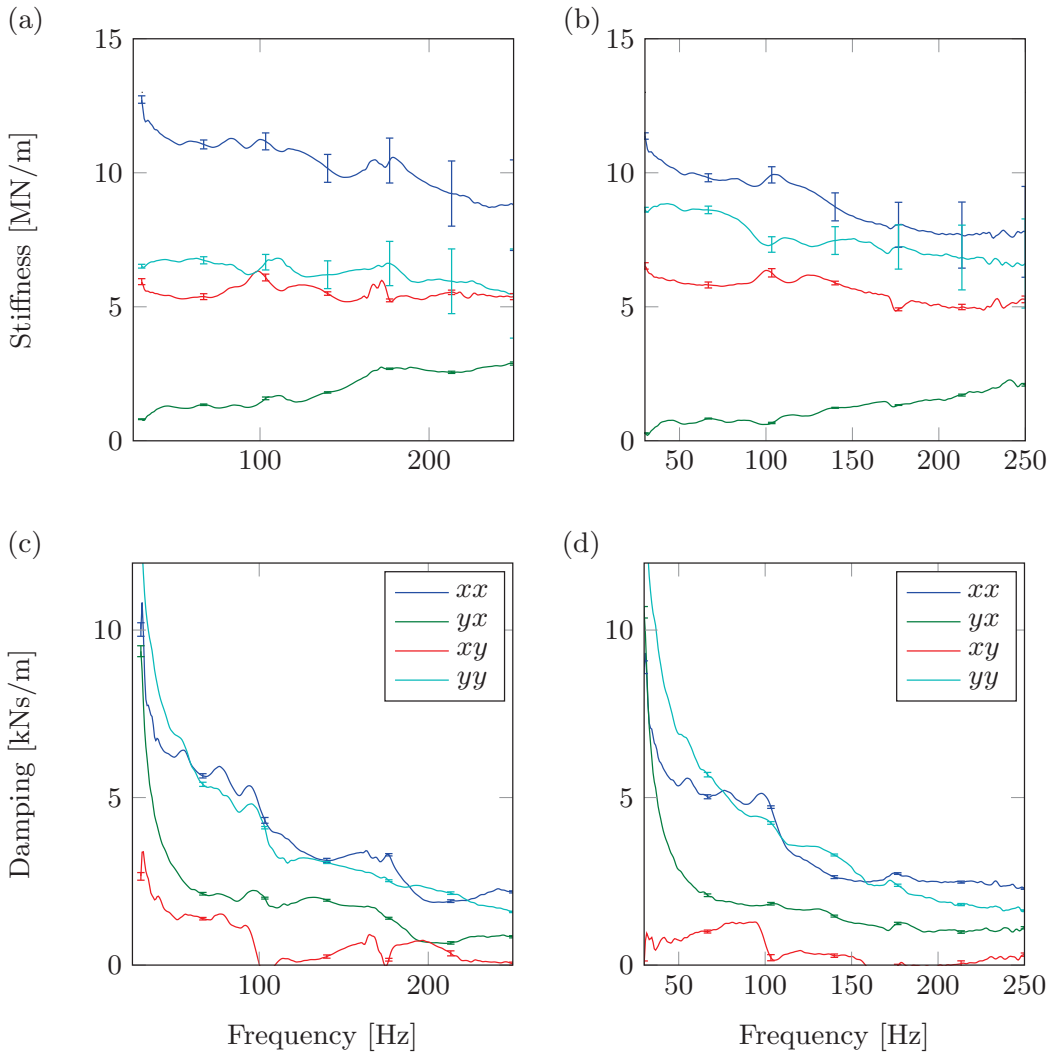

Figure 6.14: Experimentally obtained linear bearing coefficients versus excitation frequency ω_s: (a) Stiffness coefficients identified at 20,000 RPM. (b) Stiffness coefficients identified at 28,000 RPM. (c) Damping coefficients identified at 20,000 RPM. (d) Damping coefficients identified at 28,000 RPM.

efficients are observed. These discrepancies may be explained by the simplified equivalent loss factor. In the analysis, the loss factor is regarded constant for the entire foil structure, although, in reality, the loss factor will be dependent on preload and displacement amplitudes in the individual sliding points. As mentioned, results obtained at two different speeds are illustrated in Fig. 6.14. As seen, the speed dependency is very limited in this operating range. As mentioned in [P4], the experimental identification can only be performed in the sub-synchronous frequency range with the current test rig, which is the reason for the limited frequency range of the results.

6.2.1 Summary on perturbation analysis

The main findings from the theoretical and experimental results related to the perturbation analysis using the SEFM and the CFSM, presented in this chapter and in [P4], can be summarised by the following four points:

1) The discrepancies between the linear bearing coefficients predicted by the SEFM and CFSM are significant.

2) The SEFM leads to bearing coefficients an order of magnitude below the ones obtained experimentally and the CFSM predicts coefficients of the correct order of magnitude with minor discrepancies.

3) It is important to distinguish between the static and dynamic stiffness of the foil structure when solving the zero- and first-order equations respectively.

4) By determining the foil stiffness with the correct order of magnitude, the dynamic coefficients can be predicted with a reasonable accuracy.

6.3 Stability analysis and nonlinear unbalance response

As mentioned earlier, the rotor dynamical stability of rotors supported by AFBs are a major concern, and hence, the prediction of the stability at the design stage is of great importance. Here, the stability of the rotor-bearing test rig will be evaluated by means of a simple linear stability analysis. The analysis is based on the linearised bearing coefficients obtained by the CFSM method presented earlier. With the linear stability analysis, the local stability for the rotor operating

near its equilibrium position can be evaluated. The local stability is independent of external excitation like, for example rotor unbalance. The result of the linear stability analysis is compared to the result obtained experimentally and to the result of the nonlinear time domain solution. By simulating the rotor-bearing system using the nonlinear time domain method, the rotor response as well as the stability can be evaluated. The latter requires a simulation started from the rotor equilibrium position with no external dynamic excitation applied.

6.3.1 Linear stability analysis

A linear stability analysis based on the bearing coefficients predicted by the CFSM as illustrated in Fig. 6.13, Sec. 6.2, and the shaft model presented in Sec. 3.3 is performed in this subsection. By introducing the state vector as $\{z\} = \{\{q_{\mathrm{AB}}\}, \{\dot{q}_{\mathrm{AB}}\}\}^T$, the second-order system (3.47) can be rewritten into a first-order system of the form

$$\{\dot{z}\} = [A]\,\{z\} \tag{6.2}$$

where the state matrix is given as:

$$[A] = \begin{bmatrix} [0] & [I] \\ -[M]^{-1}[K] & -[M]^{-1}[D_s] \end{bmatrix} \tag{6.3}$$

and $[K(\omega, \omega_s)]$ and $[D_s] = -\omega\,[G] + [D(\omega, \omega_s)]$ are the speed and frequency dependent stiffness and damping matrices of the assembled rotor-bearing system. Then, by assuming a solution of the form $\{z\} = \{z_0\}e^{\lambda t}$ and substituting this into (6.2), the standard eigenvalue problem can be obtained, that is $[A]\,\{z\} = \lambda\{z\}$. Solving this eigenvalue problem yields eight complex eigenvalues that come in complex pairs. The linear stability analysis is basically an evaluation of these complex eigenvalues. If the real part of an eigenvalue is positive, it indicates that the associated eigenmode is unstable. Since $[A]$ is dependent on both shaft speed and perturbation frequency, ω and ω_s respectively, the eigenvalue problem can be solved in the range of interest, for example $\omega = [5; 27]$ kRPM and $\omega_s = [5; 450]$ Hz. A contour plot of the real part of the first eigenvalue is illustrated in Fig. 6.15. As seen from the plot, there is an area of which the real part of the first eigenvalue is positive. If the first eigenfrequency ω_1 (imaginary part) is plotted in the same diagram, the linear stability can be evaluated. That is at the point where ω_1 (green line) intersects the zero line and enters the area where the real part of λ_1 is positive, the mode will become unstable. In fact, a Hopf bifurcation [83] will occur due to changes in the dynamic system parameters, which effectively are the stiffness and damping coefficients of the bearings. According to the diagram, this is near 18 kRPM and the unstable

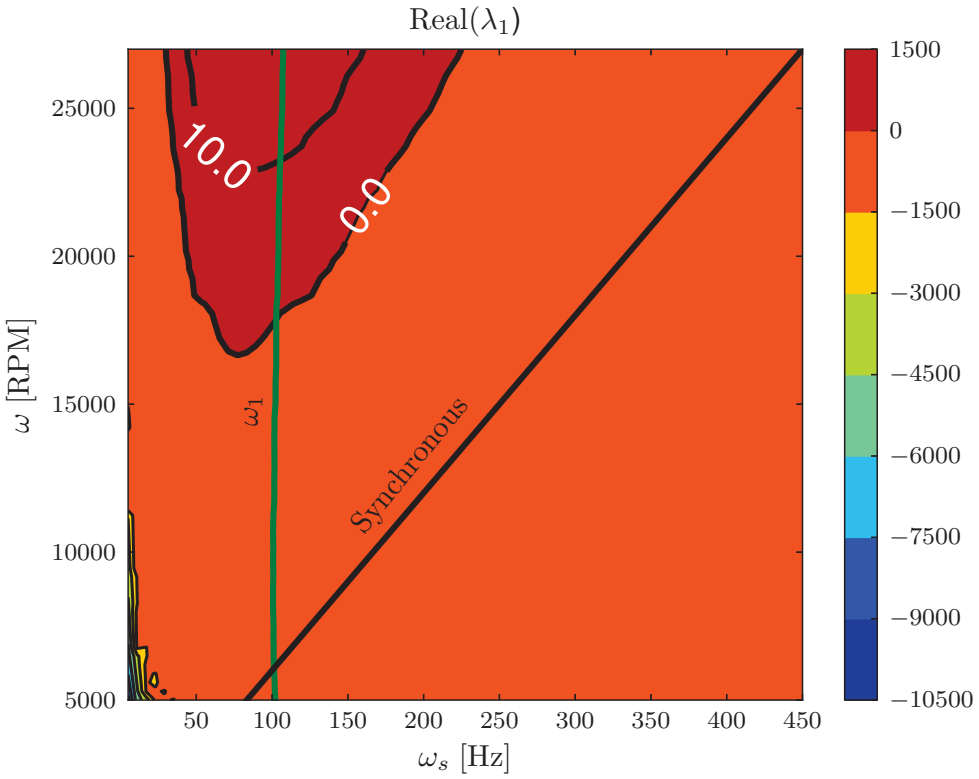

Figure 6.15: Stability diagram indicating the first eigenfrequency and the real part of the complex eigenvalue.

Table 6.2: Calculated eigenfrequencies of the rotor-bearing system at 20 kRPM.

No.	ω_1	ω_2	ω_3	ω_4
Frequency [Hz]	110	130	170	210

mode is then vibrating with a frequency of $\omega_1 \approx 100$ Hz. The vibration is self-excited with an increasing amplitude (according to linear theory). For the last three eigenmodes, a similar analysis indicated no instabilities. By evaluating the imaginary parts of the eigenvalues, the eigenfrequencies for a rotor speed of 20 kRPM are determined and listed in Tab. 6.2. These eigenfrequencies are in good agreement with previously reported values obtained experimentally [P4].

6.3.2 Nonlinear unbalance response

In this section, the nonlinear unbalance response of the test rig rotor is theoretically and experimentally investigated. The results obtained experimentally

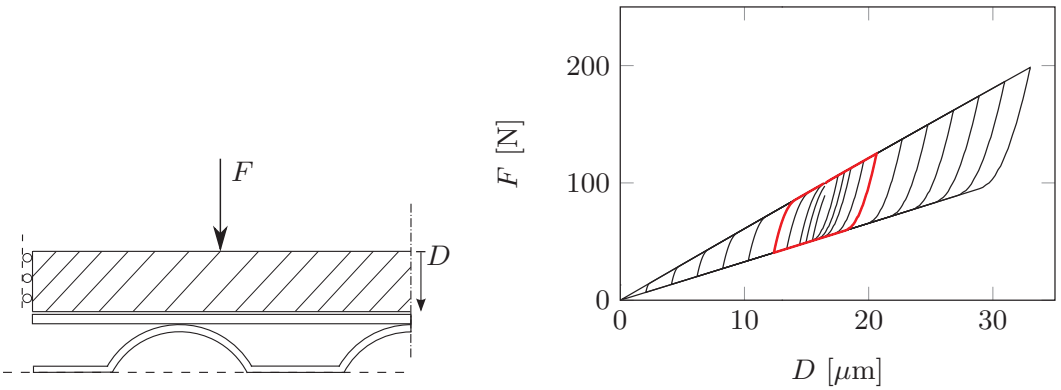

(a) Uncompressed bump foil section.

(b) Hysteresis curves of a bump foil strip consisting of four bumps.

Figure 6.16: Bump foil geometry and hysteresis loops obtained at varying deflection amplitudes.

are based on the test rig, which was previously presented in Sec. 5.2, and the theoretical results are based on the model presented in Sec. 4.3. All theoretical simulations are thus based on the geometry and dimensions from the test rig rotor as presented in Tabs. 5.4 and 5.5. Most of the results presented in this section, are included in the publications [P5] and [P6] of this thesis. However, [P5] and [P6] contain some additional results compared to this section, such as transient rotor drop simulations, nonlinear rotor orbits, etc.

Structural stiffness and energy dissipation

As mentioned, the SEFM is often implemented with the stiffness k estimated by the analytical expression derived by Walowit and Anno [84] and a loss factor $\eta = 0.25$ [30, 31, 40, 41] and [P1]. The detailed studies presented in Sec. 6.1 and [P2] have proven this analytically obtained stiffness to be significantly underestimated. In this perspective, both the stiffness and loss factor used for the time domain analysis are based on the the bump foil model described in Sec. 3.1. First, a set of closed hysteresis loops of a preloaded bump foil strip is simulated for compression cycles of different amplitudes as illustrated in Fig. 6.16. Next, the loss factor can be extracted from these loops using standard methods [37, 49] as:

$$\eta = \frac{\Delta E}{2\pi U} \tag{6.4}$$

where U is the peak potential energy and ΔE is the energy lost per cycle. The quantities U and ΔE are illustrated in Fig. 6.17a for a local hysteresis loop obtained for a preloaded foil strip consisting of four bumps. Finally, the stiffness k

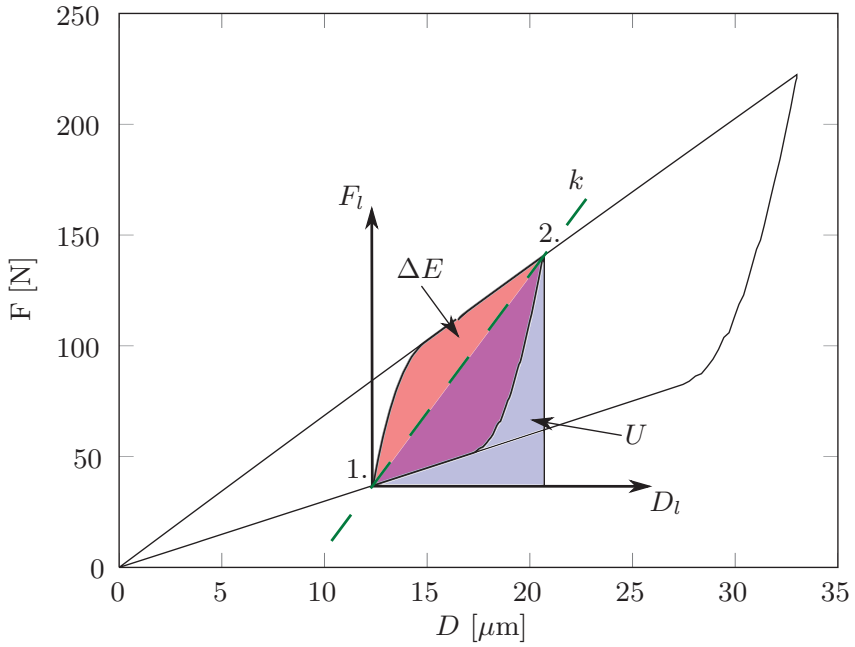

(a) Local hysteresis loop for a strip consisting of four preloaded bumps. The blue area equals the peak potential energy U and the red area the energy loss per load cycle ΔE. The slope of the dashed green line between points 1. and 2. corresponds to the stiffness k.

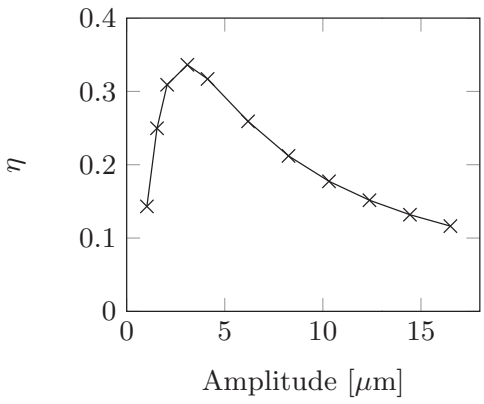

(b) Loss factor η at different deflection amplitudes.

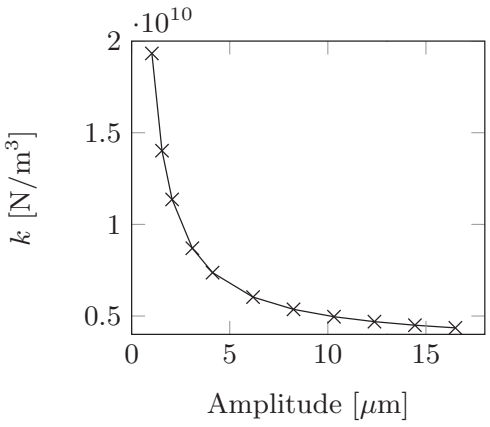

(c) Stiffness k at different deflection amplitudes.

Figure 6.17: (a) Local hysteresis curve for a preloaded bump foil composed of four bumps. (b) Stiffness obtained at varying deflection amplitudes. (c) Stiffness obtained at varying deflection amplitudes.

is defined as the slope of the dashed green line passing through points 1. and 2. Note that in this section the hysteresis loops are assumed to be frequency independent. Certain assumptions are required when reducing a complex nonlinear

structure, including friction, to two linear coefficients, k and η, by the described method above: 1) how many bumps should be included in the simulation and 2) which deflection amplitude should be employed. Here, the hysteresis loops are based on a strip of four bumps pinned in one end. This is a reasonable engineering assumption based on the shape of the film pressure profile forming a peak so that roughly 80% of the pad load is supported by these four bumps. Hence, the hysteresis loop simulation is based on the assumption that four bumps support a static load of approximately 80 N upon which a deflection oscillation is imposed. As illustrated in Fig. 6.16b, the deflection amplitude is varied between 1 and 17 μm. The parameters η and k, identified from the resulting hysteresis curves, are illustrated in Fig. 6.17b and 6.17c. Assuming the actual shaft vibration amplitudes in the range 2 to 6 μm, which are values commonly found during factory testing, and the foil deflections are half that, the stiffness and loss factor are estimated to be in the interval $k = [0.9; 2.5] \cdot 10^{10}$ N/m^3 and $\eta = [0.15; 0.3]$. If the rotor is initially assumed to run with small oscillations around a steady-state equilibrium, then the loss factor is in the low end of the interval $\eta = 0.15$ and the stiffness is in the high end $k = 2.5 \cdot 10^{10}$ N/m^3. In other words, in the vicinity of a growing vibration, the loss factor should be low but increasing with the amplitude of the vibration. As this is not possible because the loss factor is kept constant in the present analysis, it is chosen to be low $\eta = 0.15$. On the other hand, choosing the corresponding stiffness to be $k = 2.5 \cdot 10^{10}$ N/m^3 would result in an inaccurate prediction of the equilibrium position because the high stiffness reflects a stiffness for the preloaded foil, that is from its static equilibrium position. Basically, the dilemma is the same as discussed in Sec. 6.2 where a static and a dynamic stiffness, k_s and k_d respectively, were introduced in the perturbation analysis. Since the stiffness k is constant in the present analysis, a compromise must be made, and the stiffness is chosen to be in the low end of the range, that is $k = 0.9 \cdot 10^{10}$ N/m^3.

Nonlinear steady-state response

Using the stiffness and loss factor, as found above, with the nonlinear transient solution approach as described in Sec. 4.3, allows the simulation of the rotor-bearing system in the time domain. In [P5] and [P6], both transient as well as steady-state results are presented. Here, the focus is set on the steady-state rotor response to unbalance. In the following, the simulated results are compared to similar results obtained experimentally, in terms of waterfall plots obtained in the speed range of 5 to 27 kRPM. All waterfall plots are based on the vibration either simulated or measured in bearing A, vertical direction. The theoretical results are purely steady-state. For each spectrum in the waterfall, a simulation started from static steady-state conditions, with a duration of 1 s, is performed. Transient vibrations die out after approximately 0.2 s, which

consequently leaves 0.8 s blocks for the FFT, yielding a frequency resolution of 1.25 Hz. With regard to the experimental results, these are chosen to be the coast-down measurements obtained when switching of the drive motor at maximum speed. This is to eliminate the contamination of the measurements by force excitation and noise from the electrical drive (motor and VFD). Even though the coast-down time from 28 kRPM to 0 is measured to be approximately 140 s, which is a relatively long duration, it should be noted that the results are not completely steady-state, and hence divergence, from the purely steady-state response may be expected. When the rotor is balanced to the highest possible level, that is with the equipment available less than ISO G2.5, it is assumed that the unbalance in each bearing plane is approximately ± 2.5 g $\cdot$ mm. Waterfall plots for a rotor balanced to this level are illustrated in Fig. 6.18, theoretical as well as experimental. By comparing the waterfall plots, it is clear that the synchronous vibration amplitude for the theoretically obtained results are in an order of magnitude lower than the ones obtained experimentally. However, this can largely be attributed to the mechanical run-out on the bearing journals. The same run-out is most likely also the reason for the experimental results showing a clear 2 and 3 X component. The simulated results indicate two critical speeds at approximately 110 and 210 Hz respectively. However, the most important detail to note is that there is no sub-synchronous vibration components in either of the waterfalls, except for a very low amplitude component appearing at approximately 100 Hz. This is not the case at higher unbalance levels as illustrated in Fig. 6.19. Here, the unbalance is increased in bearing A to $u_{\mathrm{A}} \approx 40$ g $\cdot$ mm and it results in the birth of several sub-synchronous vibrations appearing and disappearing as the rotor speed changes. Ratios between the synchronous frequency and the fundamental frequencies of the sub-synchronous vibration may as illustrated be irrational resulting in quasi-periodic vibrations.

Comparing the theoretical and experimental results, Fig. 6.19a and Fig. 6.19b, the similarities are remarkable. In both figures, the sub-synchronous vibrations appear and disappear at nearly similar rotor speeds and their amplitudes are of the same order of magnitude. At the rotor speeds: 11.4, 13.2, 15, 18 and 25.2 kRPM, the spectra are marked with red for ease of comparison. Orbits obtained theoretically at these speeds are presented in [P6]. The appearance of a 2 and 3 X synchronous component in the experimentally obtained result may as mentioned previously be explained by the presence of run-out at the probe locations on the test rig rotor. Once again, it should be highlighted that even though the coast-down has a relatively long duration, there is a transient state of vibration in the experimentally obtained results.

By further investigating the waterfalls obtained theoretically in Figs. 6.18a and 6.19a, a low amplitude vibration component of approximately 100 Hz is identified for speeds above 22 kRPM.

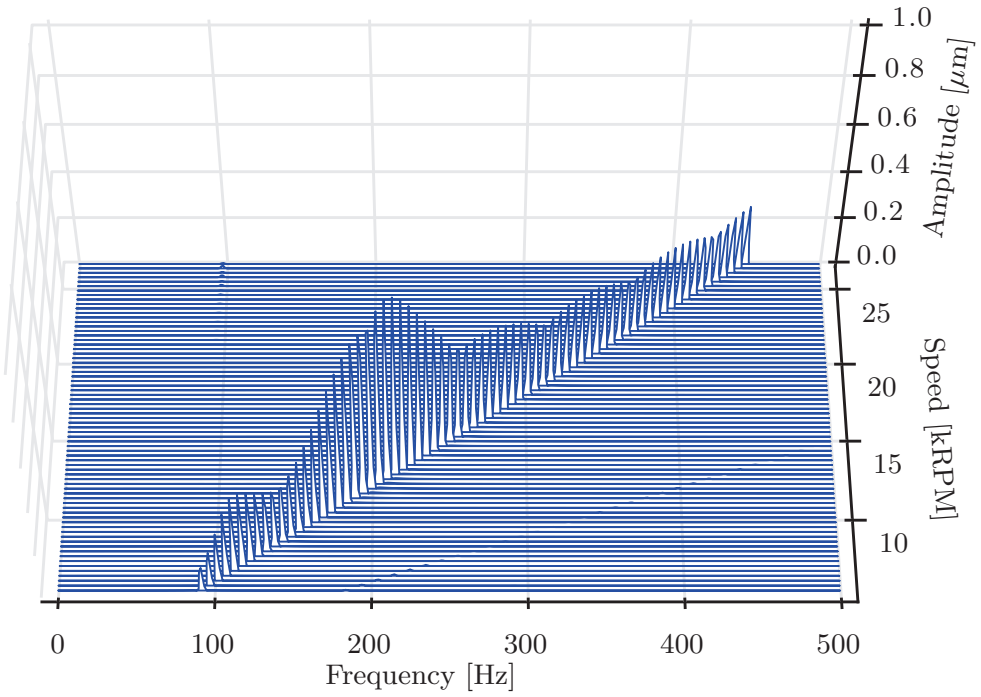

(a) Waterfall plot obtained theoretically for $u_A = 2.5\ \mathrm{g \cdot mm}$, $u_B = -2.5\ \mathrm{g \cdot mm}$.

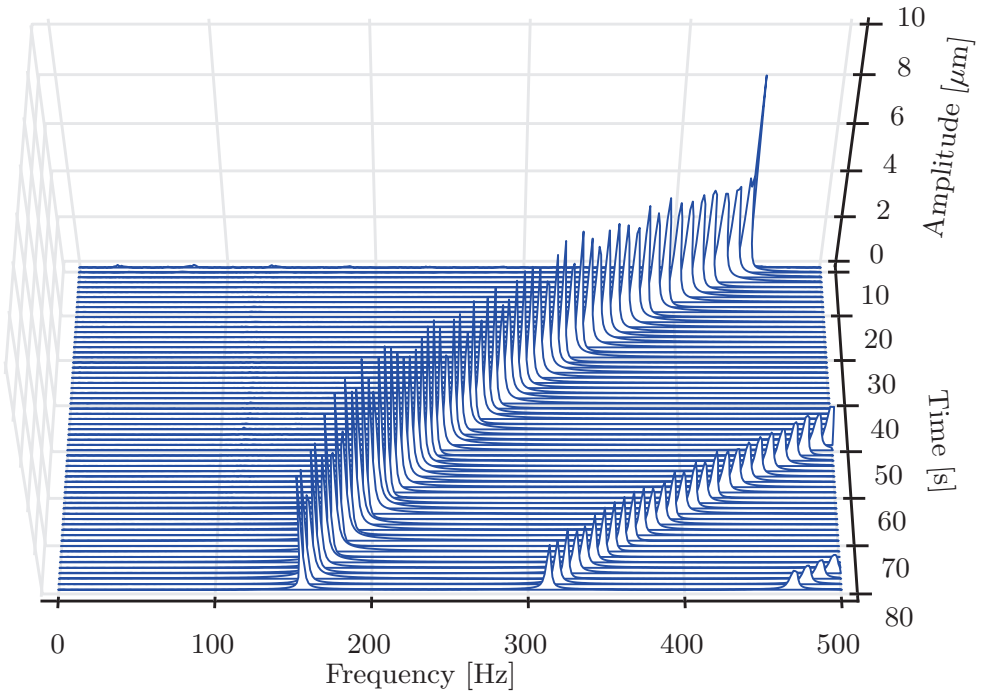

(b) Waterfall plot obtained experimentally for $u_A \approx \pm 2.5\ \mathrm{g \cdot mm}$, $u_B \approx \pm 2.5\ \mathrm{g \cdot mm}$.

Figure 6.18: Waterfall plots of the vibrations in bearing A, vertical direction. (a) Theoretical. (b) Experimental.

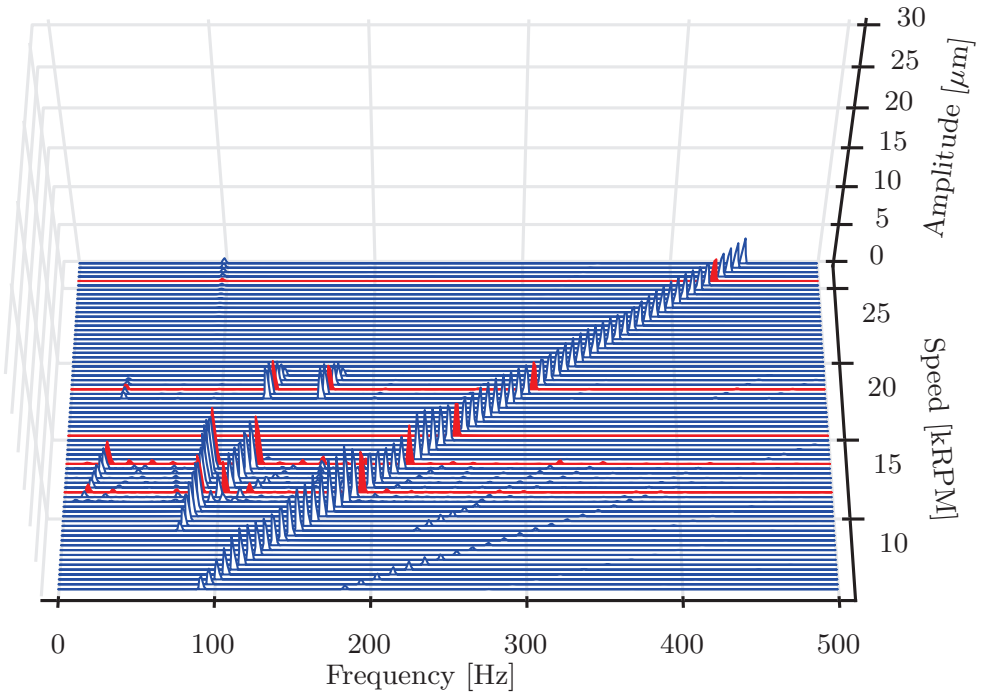

(a) Waterfall plot obtained theoretically for $u_A = 40$ g · mm, $u_B = -2.5$ g · mm.

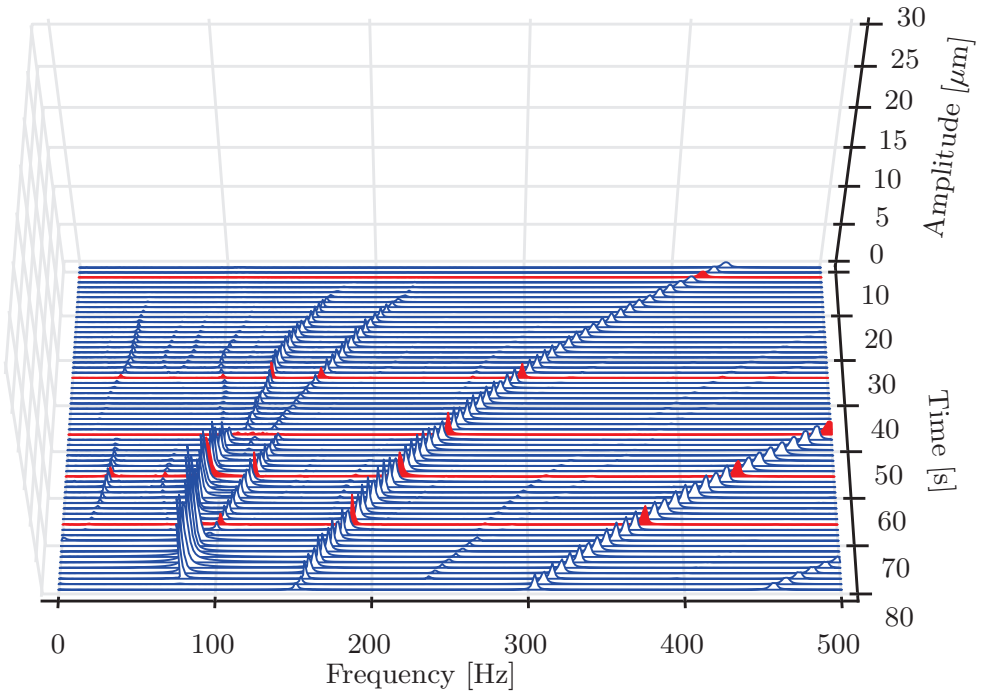

(b) Waterfall plot obtained experimentally for $u_A = 40$ g · mm, $u_B \approx \pm 2.5$ g · mm.

Figure 6.19: Waterfall plots of the vibrations in bearing A, vertical direction. (a) Theoretical. (b) Experimental.

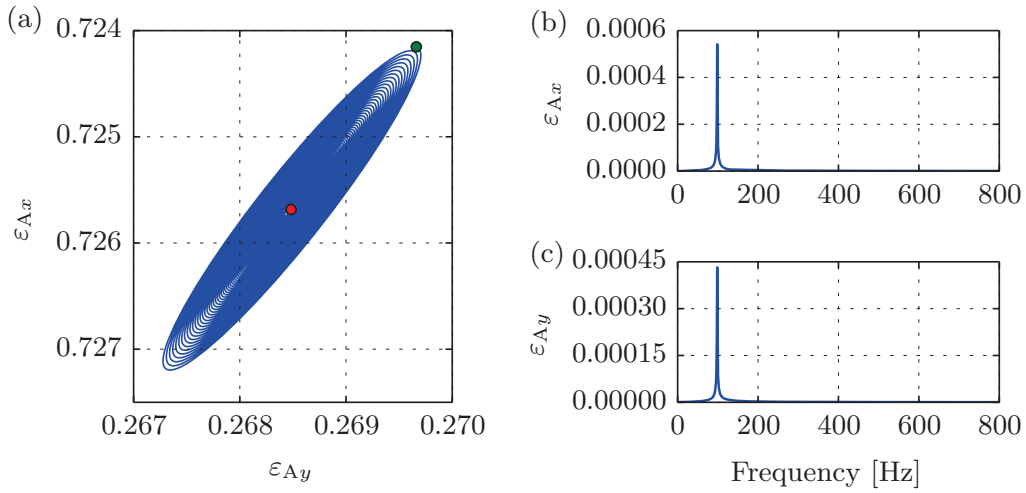

Figure 6.20: (a) Rotor orbit obtained at $\omega = 29,250$ RPM. The red dot indicates the starting point and the green dot is the end point. (b) FFT of the vibration in the x-direction. (c) FFT of the vibration in the y-direction.

This vibration may be related to the first mode, which was predicted unstable above 18 kRPM according to the linear theory. In order to evaluate the rotor dynamical stability by means of the nonlinear time domain method, the simulation needs to be performed from the equilibrium position without unbalance. Doing so for a variate of rotor speeds ω, while evaluating the rotor response at each speed, enables the identification of the threshold speed of instability as the speed where the vibration starts growing and becomes self-excited. As illustrated in Fig. 6.20a, this speed is found to be $\omega = 29,250$ RPM. From the FFT of this vibration, illustrated in Figs. 6.20a and 6.20b, its frequency is found to be 98.5 Hz which is most likely related to the first rotor mode. The resulting whirl frequency ratio becomes $\omega_s/\omega \approx 0.2$. At this point, it is clear that the threshold speed of instability predicted with the linear stability analysis ($\omega = 18$ kRPM) contradicts with both the experimentally obtained results and the instability predicted using the nonlinear time simulations. The rotor does not become unstable at 18 kRPM, in fact, the rotor proved to be stable within the entire operational speed range which is 15 to 30 kRPM. As a consequence, it is impossible with the current test rig to determine the actual threshold speed to instability to compare against the theoretical values. The poor agreement between the linear stability analysis and the experiments as well as the nonlinear time domain simulation may be explained by the linearised damping coefficients obtained theoretically which are slightly under-predicted. This is also seen when comparing to the linearised bearing coefficients obtained experimentally as illustrated in Figs. 6.13 and 6.14.

6.3.3 Summary of the stability analysis and nonlinear unbalance response

The result of the linear stability analysis is compared to nonlinear time domain simulations and experimental results. The linear stability analysis predicts that the first eigenmode becomes unstable above 18 kRPM. According to the nonlinear time domain analysis, the threshold speed of instability is found to be 29,250 RPM. It was not possible to experimentally detect any instability within the operating speed range of the test rig (15-30 kRPM). Based on this, the accuracy of the linear stability analysis is regarded as inadequate for predicting the rotor dynamical stability at the design stage.

The rotor response obtained experimentally, show that the lateral dynamics is strongly dependent on the rotor unbalance. At an unbalance level that might be expected in real life applications, several sub-synchronous vibrations appear and disappear dependent on the rotor speed. These sub-synchronous vibrations can be very harmful and cause the machine to fail. Similar rotor behaviour was found experimentally by San Andrés and Kim [75] and by Balducchi *et al.* [6]. Since these sub-synchronous vibrations are highly dependent on the rotor unbalance and completely disappear at low unbalance levels, they are not caused by the typical self-excited instability phenomenon related to large bearing cross-coupled stiffness compared to direct damping. It is rather caused by nonlinearities forced by the unbalance, for example a case of several subharmonic resonances [83]. In [75] a mathematical model based on the Duffing oscillator was proposed. A cubic bearing stiffness function based on dry measurements were used in this model. It was obtained from a bearing subjected to monotonically increasing loads when mounted on a non-rotating shaft. The mathematical model did predict subharmonic resonances at whirl speed ratios of 1/2 and 1/3, however, with significant discrepancies compared to the experiments. The same model was later used in [6] but with even larger discrepancies between theory and experiments. With the nonlinear time domain analysis presented here, these sub-synchronous vibrations can be predicted with a high degree of accuracy. Unfortunately, the nonlinear time domain analysis is dependent on the estimation of a foil stiffness and a loss factor, k and η respectively. The estimation of these two parameters are associated with some engineering assumptions and therefore uncertainties. The main findings of this chapter can be summarised as:

1) The linear stability analysis is insufficient for predicting the harmful sub-synchronous vibrations often experienced with rotors supported by AFBs.

2) The nonlinear time domain solution can predict the sub-synchronous vibrations with a good degree of accuracy.

3) The eigenfrequencies obtained theoretically using the mathematical rotor model and the linearised bearing coefficients obtained by the CFSM are in good agreement with experimentally obtained results [P4].

Chapter 7

Conclusions

Summary and discussion

The PhD work comprising this thesis was focused on experimental and theoretical investigations of a rigid rotor supported by AFBs. Numerical models were derived and two experimental test rigs were designed and built for the experimental investigations. The first test rig was designed for detailed investigations of the isolated bump foil behaviour and the second, which is a complete rotor-bearing system, was built to investigate the overall dynamics of a rigid rotor supported by AFBs. Detailed theoretical and experimental studies of the bump foil static behaviour showed that the existing and widely used analytical models, for example [84], significantly underestimates the foil stiffness. They define a linear stiffness that does not account for the stiffening effect of the friction force, which is assumed to only contribute to the loss factor. The studies indicated the need for distinguishing between a static and a dynamic stiffness, k_s and k_d respectively. The static stiffness can be obtained by applying a monotonically increasing load on the foils, whereas the dynamic stiffness can be obtained from a preloaded foil subjected to small oscillations and it is significantly higher than the static one. Two different foil specimens in terms of heat treatment were tested. One clearly indicated frequency dependent hysteresis curves in the initial tests reported in [P2]. However, in later tests, this frequency dependency could not be reproduced and it is assumed that the frequency dependency was

related to the heat treatment that left a black oxide layer on the specimens. The specimens without this black layer consistently showed low or insignificant frequency dependency.

An existing mathematical model commonly referred to as the SEFM was used to obtain the linearised bearing coefficients by following a perturbation method. These coefficients were compared to values obtained experimentally and revealed significant discrepancies. Similar results were obtained with a modified model (CFSM) incorporating a slightly more advanced foil model that took the findings from the detailed foil analysis into account, that is by distinguishing between the static and dynamic foil stiffness. These results showed relatively good agreement when compared to the values obtained experimentally, especially with regard to the stiffness coefficients. The damping coefficients were slightly under-predicted. The results of the CFSM indicate that linearised bearing coefficients can be theoretically obtained with a relatively simple mathematical model as long as the foil stiffness and loss factor are estimated with a sufficient accuracy. This is not the case when using common analytical models that neglect the stiffening effect of the friction force. They will often predict a foil stiffness in an order of magnitude lower than the actual stiffness, and hence, the predicted bearing coefficients are associated with large discrepancies. A parametric study regarding the bearing geometry highlighted the importance of modelling the AFB geometry with careful attention to the actual geometry details. It was shown how an inlet slope could significantly alter the calculated bearing coefficients.

Experiments performed with the rotor-bearing test rig revealed sub-synchronous vibrations for medium to high unbalance configurations. These sub-synchronous vibrations are common for rotors supported by AFBs and can ultimately cause failures. Therefore, the prediction of these sub-synchronous vibrations becomes very important. Linear analysis based on the mathematical model of the shaft coupled to the linear bearing coefficients could not predict these sub-synchronous vibrations. A nonlinear time domain simulation was performed for different rotor unbalance levels and compared to experimental results with good agreement. The speed at which the sub-synchronous vibrations appears could be predicted with this method, and to some extent also their amplitude. Again the relatively simple mathematical model, the SEFM, showed surprisingly good capabilities if the foil stiffness and loss factor were properly estimated. Regarding the stability of the rotor, both the linear stability analysis and nonlinear time-domain analysis was used to predict the threshold speed for instability. The accuracy of the linear stability analysis was found to be poor and the accuracy of the nonlinear time-domain analysis could not be tested as the rotor-bearing test rig was found to be stable in the entire operational speed range.

Future work

In the light of the findings gathered through this PhD work, it is clear that the future work should be focused on improving the theoretical time domain methods. This is mainly due to the fact that the greatest concern seen from a development engineer's point of view is the appearance of sub-synchronous vibrations that leads to bearing failures. Being able to predict these at a design stage is of highest interest and the time domain simulation presented in this work can do that. However, the uncertainties with regard to determining the stiffness and loss factor for the SEFM should be eliminated. It is the author's opinion that this should be done by carefully developing an equivalent mathematical model of the foils that accurately captures its mechanical behaviour but consists of a minimum of DOFs. Such a model should be able to predict the hysteresis loops with the same degree of accuracy as the complex computationally heavy model presented in this work. By keeping in mind that the foil stiffness and damping is linearised using the SEFM, the author is convinced that by coupling an accurate equivalent nonlinear foil model to the time domain techniques presented in this work, the mechanical behaviour of rotors supported by AFBs can be predicted with an extremely high degree of accuracy. Furthermore, the engineering assumptions that are related to uncertainties can be completely eliminated. For now, the method presented here is one small step in the right direction.

Appendix A

Derivation of rigid shaft model

In the following, a linearised mathematical model of a rigid spinning shaft with four degrees of freedom is derived. These four degrees of freedom are related to horizontal and vertical translatory motion in each shaft end, A and B, perpendicular to its centreline. The model takes into account the shaft mass, transverse mass moment of inertia and the gyroscopic moment.

Rigid shaft kinematics

The derivation of the model is based on Newtons second law, but first the shaft kinematics needs to be defined. A schematics of the shaft positioned with the centre of gravity CG in the origo of the inertial coordinate system/reference frame is illustrated in Fig. A.1. By applying two consecutive rotations of the inertial reference frame SI to first SM1 and second to SM2, as illustrated in Fig. A.2, the transformation matrices can be derived as:

$$[T_\Gamma] = \begin{bmatrix} \cos(\Gamma) & 0 & -\sin(\Gamma) \\ 0 & 1 & 0 \\ \sin(\Gamma) & 0 & \cos(\Gamma) \end{bmatrix}, \quad [T_\beta] = \begin{bmatrix} 1 & 0 & 0 \\ 0 & \cos(\beta) & \sin(\beta) \\ 0 & -\sin(\beta) & \cos(\beta) \end{bmatrix} \tag{A.1}$$

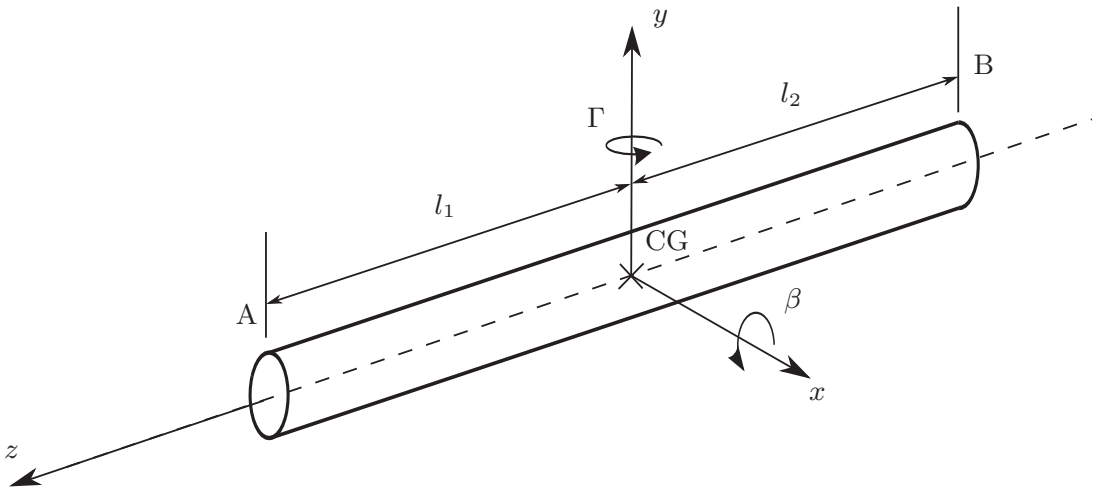

Figure A.1: Rigid undisplaced shaft with the mass centre of gravity CG in the inertial reference coordinate system.

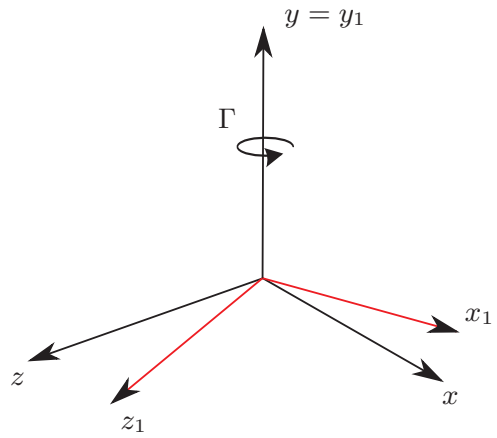

(a) Rotation one (SI to SM1) of the inertial reference frame SI around the y-axes.

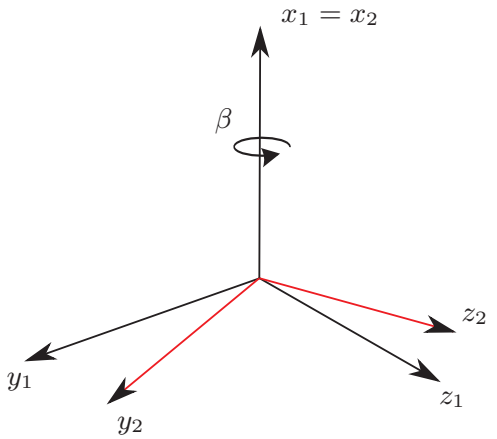

(b) Rotation two (SM1 to SM2) of moving frame SM1 around the x_1-axis.

Figure A.2: Two consecutive rotations of the inertial reference frame SI (x,y,z). a) Rotation around y-axis marked with red. b) Rotation around x_1-axis marked with red.

so that the following transformations hold:

$$\begin{aligned} \{S_{\mathrm{SM1}}\} &= [T_\Gamma]\,\{S_{\mathrm{SI}}\} \\ \{S_{\mathrm{SI}}\} &= [T_\Gamma]^T\,\{S_{\mathrm{SM1}}\} \\ \{S_{\mathrm{SM2}}\} &= [T_\beta]\,\{S_{\mathrm{SM1}}\} \\ \{S_{\mathrm{SM1}}\} &= [T_\beta]^T\,\{S_{\mathrm{SM2}}\}. \end{aligned} \tag{A.2}$$

From the consecutive rotations (A.2), we can establish the general rotation matrix between the inertial system SI and the moving reference frame SM2:

$$[T_{\beta\Gamma}] = [T_\beta]\,[T_\Gamma] = \begin{bmatrix} \cos(\Gamma) & 0 & -\sin(\Gamma) \\ \sin(\Gamma)\cos(\beta) & \cos(\beta) & \cos(\Gamma)\sin(\beta) \\ \sin(\Gamma)\cos(\beta) & -\sin(\beta) & \cos(\Gamma)\cos(\beta) \end{bmatrix}$$

$$[T_{\Gamma\beta}] = [T_\Gamma]^T\,[T_\beta]^T = \begin{bmatrix} \cos(\Gamma) & \sin(\Gamma)\sin(\beta) & \sin(\Gamma)\cos(\beta) \\ 0 & \cos(\beta) & -\sin(\beta) \\ -\sin(\Gamma) & \cos(\Gamma)\sin(\beta) & \cos(\Gamma)\cos(\beta) \end{bmatrix} \tag{A.3}$$

so that the following transformations hold:

$$\begin{aligned} \{S_{\mathrm{SM2}}\} &= [T_{\beta\Gamma}]\,\{S_{\mathrm{SI}}\} \\ \{S_{\mathrm{SI}}\} &= [T_{\Gamma\beta}]\,\{S_{\mathrm{SM2}}\}. \end{aligned} \tag{A.4}$$

At this point, we have the transformation matrices necessary to determine the force and position vectors to be used when setting up the dynamic system of equations. We start by defining the vectors of angular velocity. The vector of angular velocity around the y-axis is:

$$\{\dot\Gamma_{\mathrm{SI}}\} = \{0\ \dot\Gamma\ 0\}^T \tag{A.5}$$

and similarly around the x_1-axis:

$$\{\dot\beta_{\mathrm{SM1}}\} = \{\dot\beta\ 0\ 0\}^T \tag{A.6}$$

and the total angular velocity vector in SM2 can be written as:

$$\{\o_{\mathrm{SM2}}\} = [T_{\beta\Gamma}]\,\{\dot\Gamma_{\mathrm{SI}}\} + [T_\beta]\,\{\dot\beta_{\mathrm{SM1}}\} = \begin{Bmatrix} \dot\beta \\ \dot\Gamma\cos(\beta) \\ -\dot\Gamma\sin(\beta) \end{Bmatrix}. \tag{A.7}$$

The angular velocity around z_2, i.e. the spin velocity of the shaft, is defined as:

$$\{\omega_{\mathrm{SM2}}\} = \{0\ 0\ \omega\}^T \tag{A.8}$$

adding this to (A.7), the total angular velocity vector in SM2, now with 'spin' included, becomes

$$\{\tilde\omega_{\mathrm{SM2}}\} = \{\o_{\mathrm{SM2}}\} + \{\omega_{\mathrm{SM2}}\} = \begin{Bmatrix} \dot\beta \\ \dot\Gamma\cos(\beta) \\ \omega - \dot\Gamma\sin(\beta) \end{Bmatrix} \tag{A.9}$$

and its time-derivative

$$\frac{d}{dt}\left(\{\tilde\omega_{\mathrm{SM2}}\}\right) = \begin{Bmatrix} \ddot\beta \\ \ddot\Gamma\cos(\beta) - \dot\Gamma\dot\beta\sin(\beta) \\ \omega - \ddot\Gamma\sin(\beta) - \dot\Gamma\dot\beta\cos(\beta) \end{Bmatrix}. \tag{A.10}$$

The lateral acceleration of the shaft centre of gravity in the inertial frame SI is defined as:

$$\{\ddot{S}_{\mathrm{SI}}\} = \{\ddot{x}_{\mathrm{CG}}\ \ddot{y}_{\mathrm{CG}}\ \ddot{z}_{\mathrm{CG}}\}^T. \tag{A.11}$$

The inertia tensor for the shaft centre of gravity in the moving reference frame SM2 is defined as:

$$[I_{\mathrm{SM2}}] = \begin{bmatrix} I_{xx} & 0 & 0 \\ 0 & I_{yy} & 0 \\ 0 & 0 & I_{zz} \end{bmatrix}. \tag{A.12}$$

Reaction forces

The kinematics of the rigid shaft is now fully defined and the forces acting on it can now be evaluated. The force acting on the shaft due to gravity is

$$\{P_{\mathrm{SI}}\} = \begin{Bmatrix} 0 \\ -mg \\ 0 \end{Bmatrix} \tag{A.13}$$

and the reactions in the bearing positions A and B are

$$\{r_{\mathrm{A,SI}}\} = \begin{Bmatrix} r_{\mathrm{A}x} \\ r_{\mathrm{A}y} \\ r_{\mathrm{A}z} \end{Bmatrix}, \quad \{r_{\mathrm{B,SI}}\} = \begin{Bmatrix} r_{\mathrm{B}x} \\ r_{\mathrm{B}y} \\ r_{\mathrm{B}z} \end{Bmatrix}. \tag{A.14}$$

These bearing reactions can be expressed as the sum of deflection times stiffness and velocity times damping respectively. The reactions in bearings A and B can then be written as:

$$\{r_{\gamma,\mathrm{SI}}\} = \begin{Bmatrix} r_{\gamma x} \\ r_{\gamma y} \\ r_{\gamma z} \end{Bmatrix} = - \begin{bmatrix} k_{\gamma x} & 0 & 0 \\ 0 & k_{\gamma y} & 0 \\ 0 & 0 & k_{\gamma z} \end{bmatrix} \{\Delta S_{\gamma,\mathrm{SI}}\} - \begin{bmatrix} d_{\gamma x} & 0 & 0 \\ 0 & d_{\gamma y} & 0 \\ 0 & 0 & d_{\gamma z} \end{bmatrix} \{\Delta \dot{S}_{\gamma,\mathrm{SI}}\} \tag{A.15}$$

where $\gamma = \mathrm{A}, \mathrm{B}$. Referring the reaction vectors from the bearing positions, A and B, to the translation and rotation of the center of gravity CG, we get

$$\{r_{\mathrm{A,SI}}\} = \begin{Bmatrix} -k_{\mathrm{A}x}(x_{\mathrm{CG}} + l_1\Gamma) - d_{\mathrm{A}x}(\dot{x}_{\mathrm{CG}} + l_1\dot{\Gamma}) \\ -k_{\mathrm{A}y}(y_{\mathrm{CG}} - l_1\beta) - d_{\mathrm{A}y}(\dot{y}_{\mathrm{CG}} - l_1\dot{\beta}) \\ -k_{\mathrm{A}z}z_{\mathrm{CG}} - d_{\mathrm{A}z}\dot{z}_{\mathrm{CG}} \end{Bmatrix} \tag{A.16}$$

and

$$\{r_{\mathrm{B,SI}}\} = \begin{Bmatrix} -k_{\mathrm{B}x}(x_{\mathrm{CG}} - l_2\Gamma) - d_{\mathrm{B}x}(\dot{x}_{\mathrm{CG}} - l_2\dot{\Gamma}) \\ -k_{\mathrm{B}y}(y_{\mathrm{CG}} + l_2\beta) - d_{\mathrm{B}y}(\dot{y}_{\mathrm{CG}} + l_2\dot{\beta}) \\ -k_{\mathrm{B}z}z_{\mathrm{CG}} - d_{\mathrm{B}z}\dot{z}_{\mathrm{CG}} \end{Bmatrix}. \tag{A.17}$$

Note that (A.16) and (A.17) are the bearing reactions related to the inertial reference frame SI. Now that bearing reactions, mass and inertia matrices, position and velocity vectors are determined, we can apply Newton-Euler method to obtain the equations of motion for the rotor.

Newton-Euler equations of motion

We start by a summation of forces

$$\sum \{F_{\mathrm{SI}}\} = \begin{bmatrix} m & 0 & 0 \\ 0 & m & 0 \\ 0 & 0 & m \end{bmatrix} \{\ddot{S}_{\mathrm{CG,SI}}\} = \{P_{\mathrm{SI}}\} + \{r_{A,\mathrm{SI}}\} + \{r_{B,\mathrm{SI}}\} + \{f_{\mathrm{ext,SI}}\} \tag{A.18}$$

where $\{f_{\mathrm{ext,SI}}\}$ is the vector of external forces acting on the shaft. By neglecting the movements and forces acting in the z-direction and the static gravitational force and inserting (A.16) and (A.17) into (A.18), we get

$$\begin{bmatrix} m & 0 & 0 & 0 \\ 0 & m & 0 & 0 \end{bmatrix} \begin{Bmatrix} \ddot{x}_{\mathrm{CG}} \\ \ddot{y}_{\mathrm{CG}} \\ \ddot{\beta} \\ \ddot{\Gamma} \end{Bmatrix} + \begin{bmatrix} d_{\mathrm{A}x} + d_{\mathrm{B}x} & 0 & 0 & d_{\mathrm{A}x}l_1 - d_{\mathrm{B}x}l_2 \\ 0 & d_{\mathrm{A}y} + d_{\mathrm{B}y} & -d_{\mathrm{A}y}l_1 + d_{\mathrm{B}y}l_2 & 0 \end{bmatrix} \begin{Bmatrix} \dot{x}_{\mathrm{CG}} \\ \dot{y}_{\mathrm{CG}} \\ \dot{\beta} \\ \dot{\Gamma} \end{Bmatrix} + \begin{bmatrix} k_{\mathrm{A}x} + k_{\mathrm{B}x} & 0 & 0 & k_{\mathrm{A}x}l_1 - k_{\mathrm{B}x}l_2 \\ 0 & k_{\mathrm{A}y} + k_{\mathrm{B}y} & -k_{\mathrm{A}y}l_1 + k_{\mathrm{B}y}l_2 & 0 \end{bmatrix} \begin{Bmatrix} x_{\mathrm{CG}} \\ y_{\mathrm{CG}} \\ \beta \\ \Gamma \end{Bmatrix} = \begin{Bmatrix} f_x \\ f_y \end{Bmatrix}. \tag{A.19}$$

There are four degrees of freedom in the system (A.19) meaning that two additional equations are needed in order for it to be solved. We take the summation of moments around the shaft centre of gravity CG:

$$\sum \{M_{\mathrm{CG,SM2}}\} = \{I_{\mathrm{CG,SM2}}\} \frac{d}{dt} \left(\{\tilde{\omega}_{\mathrm{SM2}}\}\right) + \{\varnothing_{\mathrm{SM2}}\} \times \left(\{I_{\mathrm{CG,SM2}}\}\{\tilde{\omega}_{\mathrm{SM2}}\}\right) \tag{A.20}$$

which can be linearised (by assuming the angles β and Γ are small) to:

$$\sum \{M_{\mathrm{CG,SM2}}\} = \begin{Bmatrix} I_{xx}\ddot{\beta} \\ I_{yy}\ddot{\Gamma} \\ 0 \end{Bmatrix} - \omega \begin{Bmatrix} -I_{zz}\dot{\Gamma} \\ I_{zz}\dot{\beta} \\ 0 \end{Bmatrix}. \tag{A.21}$$

A summation of the moments around the shaft centre of gravity caused by the reaction forces in A and B can be written as:

$$\sum \{M_{\mathrm{CG,SM2}}\} = \{S_{\mathrm{A,SM2}}\} \times \{r_{\mathrm{A,SM2}}\} + \{S_{\mathrm{B,SM2}}\} \times \{r_{\mathrm{B,SM2}}\} + \{M_{\mathrm{ext}}\} \quad \text{(A.22)}$$

where $\{M_{\mathrm{ext}}\}$ is the external moments acting on the shaft. Recall that the reactions in SM2 can be found from $\{r_{\gamma,\mathrm{SM2}}\} = [T_{\beta\gamma}]\{r_{\gamma,\mathrm{SI}}\}$. Now, by combining (A.21) and (A.22) and rearranging, we get:

$$\begin{bmatrix} 0 & 0 & I_{xx} & 0 \\ 0 & 0 & 0 & I_{yy} \end{bmatrix} \begin{Bmatrix} \ddot{x}_{\mathrm{CG}} \\ \ddot{y}_{\mathrm{CG}} \\ \ddot{\beta} \\ \ddot{\Gamma} \end{Bmatrix} + \left(-\omega \begin{bmatrix} 0 & 0 & 0 & -I_{zz} \\ 0 & 0 & I_{zz} & 0 \end{bmatrix} + \right.$$

$$\left. \begin{bmatrix} 0 & -d_{\mathrm{A}y}l_1 + d_{\mathrm{B}y}l_2 & d_{\mathrm{A}y}l_1^2 + d_{\mathrm{B}y}l_2^2 & 0 \\ d_{\mathrm{A}x}l_1 - d_{\mathrm{B}x}l_2 & 0 & 0 & d_{\mathrm{A}x}l_1^2 + d_{\mathrm{B}x}l_2^2 \end{bmatrix} \right) \begin{Bmatrix} \dot{x}_{\mathrm{CG}} \\ \dot{y}_{\mathrm{CG}} \\ \dot{\beta} \\ \dot{\Gamma} \end{Bmatrix} +$$

$$\begin{bmatrix} 0 & -k_{\mathrm{A}y}l_1 + k_{\mathrm{B}y}l_2 & k_{\mathrm{A}y}l_1^2 + k_{\mathrm{B}y}l_2^2 & 0 \\ k_{\mathrm{A}x}l_1 - k_{\mathrm{B}x}l_2 & 0 & 0 & k_{\mathrm{A}x}l_1^2 + k_{\mathrm{B}x}l_2^2 \end{bmatrix} \begin{Bmatrix} x_{\mathrm{CG}} \\ y_{\mathrm{CG}} \\ \beta \\ \Gamma \end{Bmatrix} = \begin{Bmatrix} M_x \\ M_y \end{Bmatrix}. \quad \text{(A.23)}$$

Combining (A.19) and (A.23), the complete system of equations describing the motion of the rigid rotor can be written as:

$$[M_{\mathrm{CG}}]\{\ddot{q}_{\mathrm{CG}}\} + (-\omega[G_{\mathrm{CG}}] + [D_{\mathrm{CG}}])\{\dot{q}_{\mathrm{CG}}\} + [K_{\mathrm{CG}}]\{q_{\mathrm{CG}}\} = \{f_{\mathrm{CG}}\} \quad \text{(A.24)}$$

where the nodal deflection and force vectors are defined as:

$$\begin{aligned} \{q_{\mathrm{CG}}\} &= \{x_{\mathrm{CG}}\ y_{\mathrm{CG}}\ \beta\ \Gamma\}^T \\ \{f_{\mathrm{CG}}\} &= \{f_x\ f_y\ M_x\ M_y\}^T \end{aligned} \quad \text{(A.25)}$$

and the matrices are defined as:

$$[M_{\mathrm{CG}}] = \begin{bmatrix} m & 0 & 0 & 0 \\ 0 & m & 0 & 0 \\ 0 & 0 & I_{xx} & 0 \\ 0 & 0 & 0 & I_{yy} \end{bmatrix} \quad \text{(A.26)}$$

$$[G_{\mathrm{CG}}] = \begin{bmatrix} 0 & 0 & 0 & 0 \\ 0 & 0 & 0 & 0 \\ 0 & 0 & 0 & -I_{zz} \\ 0 & 0 & I_{zz} & 0 \end{bmatrix} \quad \text{(A.27)}$$

$$[D_{\mathrm{CG}}] = \begin{bmatrix} d_{\mathrm{A}x} + d_{\mathrm{B}x} & 0 & 0 & d_{\mathrm{A}x}l_1 - d_{\mathrm{B}x}l_2 \\ 0 & d_{\mathrm{A}y} + d_{\mathrm{B}y} & -d_{\mathrm{A}y}l_1 + d_{\mathrm{B}y}l_2 & 0 \\ 0 & -d_{\mathrm{A}y}l_1 + d_{\mathrm{B}y}l_2 & d_{\mathrm{A}y}l_1^2 + d_{\mathrm{B}y}l_2^2 & 0 \\ d_{\mathrm{A}x}l_1 - d_{\mathrm{B}x}l_2 & 0 & 0 & d_{\mathrm{A}x}l_1^2 + d_{\mathrm{B}x}l_2^2 \end{bmatrix} \tag{A.28}$$

$$[K_{\mathrm{CG}}] = \begin{bmatrix} k_{\mathrm{A}x} + k_{\mathrm{B}x} & 0 & 0 & k_{\mathrm{A}x}l_1 - k_{\mathrm{B}x}l_2 \\ 0 & k_{\mathrm{A}y} + k_{\mathrm{B}y} & -k_{\mathrm{A}y}l_1 + k_{\mathrm{B}y}l_2 & 0 \\ 0 & -k_{\mathrm{A}y}l_1 + k_{\mathrm{B}y}l_2 & k_{\mathrm{A}y}l_1^2 + k_{\mathrm{B}y}l_2^2 & 0 \\ k_{\mathrm{A}x}l_1 - k_{\mathrm{B}x}l_2 & 0 & 0 & k_{\mathrm{A}x}l_1^2 + k_{\mathrm{B}x}l_2^2 \end{bmatrix} \tag{A.29}$$

Equations of motion referred to A and B

In order to obtain a system of equations describing the movement of the rigid rotor in the bearing locations A and B, the following two linear transformation matrices are introduced:

$$[T_1] = \begin{bmatrix} 1 & 0 & 0 & l_1 \\ 0 & 1 & -l_1 & 0 \\ 1 & 0 & 0 & -l_2 \\ 0 & 1 & l_2 & 0 \end{bmatrix}, \quad [T_2] = \begin{bmatrix} 1 & 0 & 1 & 0 \\ 0 & 1 & 0 & 1 \\ 0 & -l_1 & 0 & l_2 \\ l_1 & 0 & -l_2 & 0 \end{bmatrix} \tag{A.30}$$

so that the following transformations hold:

$$\begin{aligned} \{q_{\mathrm{AB}}\} &= [T_1]\,\{q_{\mathrm{CG}}\} \\ \{f_{\mathrm{CG}}\} &= [T_2]\,\{f_{\mathrm{AB}}\}. \end{aligned} \tag{A.31}$$

The transformation matrices $[T_1]$ and $[T_2]$ can now be used to transform (A.29) into a system defined by the movements and forces in the bearing locations A and B instead of the centre of gravity. First, we substitute (A.31) into (A.29) to get:

$$\begin{aligned} &[M_{\mathrm{CG}}]\,[T_1]^{-1}\,\{\ddot{q}_{\mathrm{AB}}\} + (-\omega\,[G_{\mathrm{CG}}] + [D_{\mathrm{CG}}])\,[T_1]^{-1}\,\{\dot{q}_{\mathrm{AB}}\} + [K_{\mathrm{CG}}]\,[T_1]^{-1}\,\{q_{\mathrm{AB}}\} \\ &= [T_2]\,\{f_{\mathrm{AB}}\}. \end{aligned} \tag{A.32}$$

It can be shown that $[T_2]^{-1} = [T_1]^{-T}$. Multiplying (A.32) by $[T_1]^{-T}$ gives the system of equations referred to A and B as:

$$\begin{aligned} &[T_1]^{-T}\,[M_{\mathrm{CG}}]\,[T_1]^{-1}\,\{\ddot{q}_{\mathrm{AB}}\} + [T_1]^{-T}\,(-\omega\,[G_{\mathrm{CG}}] + [D_{\mathrm{CG}}])\,[T_1]^{-1}\,\{\dot{q}_{\mathrm{AB}}\} \\ &+ [T_1]^{-T}\,[K_{\mathrm{CG}}]\,[T_1]^{-1}\,\{q_{\mathrm{AB}}\} = \{f_{\mathrm{AB}}\}. \end{aligned} \tag{A.33}$$

And the system matrices can then be written as:

$$\begin{aligned}
[M_{\mathrm{AB}}] &= [T_1]^{-T}\,[M_{\mathrm{CG}}]\,[T_1]^{-1} \\
[G_{\mathrm{AB}}] &= [T_1]^{-T}\,[G_{\mathrm{CG}}]\,[T_1]^{-1} \\
[D_{\mathrm{AB}}] &= [T_1]^{-T}\,[D_{\mathrm{CG}}]\,[T_1]^{-1} \\
[K_{\mathrm{AB}}] &= [T_1]^{-T}\,[K_{\mathrm{CG}}]\,[T_1]^{-1}
\end{aligned} \tag{A.34}$$

where

$$[M_{\mathrm{AB}}] = \frac{1}{l^2}\begin{bmatrix} l_2^2 m + I_{yy} & 0 & l_1 l_2 m - I_{yy} & 0 \\ 0 & l_2^2 m + I_{xx} & 0 & l_1 l_2 m - I_{xx} \\ l_1 l_2 m - I_{yy} & 0 & l_1^2 m + I_{yy} & 0 \\ 0 & l_1 l_2 m - I_{xx} & 0 & l_1^2 m + I_{xx} \end{bmatrix}$$

$$[G_{\mathrm{AB}}] = \frac{1}{l^2}\begin{bmatrix} 0 & -I_{zz} & 0 & I_{zz} \\ I_{zz} & 0 & -I_{zz} & 0 \\ 0 & I_{zz} & 0 & -I_{zz} \\ -I_{zz} & 0 & I_{zz} & 0 \end{bmatrix}$$

$$[D_{\mathrm{AB}}] = \begin{bmatrix} d_{\mathrm{A}x} & 0 & 0 & 0 \\ 0 & d_{\mathrm{A}y} & 0 & 0 \\ 0 & 0 & d_{\mathrm{B}x} & 0 \\ 0 & 0 & 0 & d_{\mathrm{B}y} \end{bmatrix} \tag{A.35}$$

$$[K_{\mathrm{AB}}] = \begin{bmatrix} k_{\mathrm{A}x} & 0 & 0 & 0 \\ 0 & k_{\mathrm{A}y} & 0 & 0 \\ 0 & 0 & k_{\mathrm{B}x} & 0 \\ 0 & 0 & 0 & k_{\mathrm{B}y} \end{bmatrix}$$

$$\{q_{\mathrm{AB}}\} = \begin{Bmatrix} q_{\mathrm{Ax}} \\ q_{\mathrm{Ay}} \\ q_{\mathrm{Bx}} \\ q_{\mathrm{By}} \end{Bmatrix}, \quad \{f_{\mathrm{AB}}\} = \begin{Bmatrix} f_{\mathrm{Ax}} \\ f_{\mathrm{Ay}} \\ f_{\mathrm{Bx}} \\ f_{\mathrm{By}} \end{Bmatrix}$$

and $l = l_1 + l_2$. Note, that in the thesis, the AB-subscripts are dropped since the shaft forces and movements are always referred to the bearing locations.

Appendix B

Implicit incremental Newton-Raphson method

In the implicit incremental Newton-Raphson (NR) scheme, the load is applied in n increments, for each of which the displacement D^n is found iteratively by satisfying the nonlinear equilibrium condition that can be written in residual form as:

$$R(D^n) = R_{int}(D^n) - P^n. \tag{B.1}$$

If D_i^n is an approximate solution to the exact solution D^n, then a first-order Taylor expansion gives an equilibrium equation for the next NR-step as

$$R(D_{i+1}^n) \approx R(D_i^n) + \frac{dR(D_i^n)}{dD}\Delta D_i^n = 0. \tag{B.2}$$

If we now define the tangent as

$$K_t \equiv \frac{dR(D_i^n)}{dD}, \tag{B.3}$$

then the equilibrium equation (B.2) can be written as

$$K_t \Delta D_i^n = -R(D_i^n) \tag{B.4}$$

or inserting (B.1)

$$K_t \Delta D_i^n = -R_{int}(D_i^n) + P^n. \tag{B.5}$$

When the equilibrium equation (B.5) has been solved, the displacements are updated from

$$D_{i+1}^n = D_i^n + \Delta D_i^n. \tag{B.6}$$

The tangent is then updated with the new displacement $D_i^n = D_{i+1}^n$ and the procedure is repeated until the norm of the residual is sufficiently small. Here, the NR method was derived for a scalar problem, but it is directly applicable to vector problems.

References

[1] G. L. Agrawal. Foil air/gas bearing technology—an overview. *ASME paper*, (97-GT):347, 1997.

[2] E. Anderson, Z. Bai, C. Bischof, S. Blackford, J. Demmel, J. Dongarra, J. Du Croz, A. Greenbaum, S. Hammarling, A. McKenney, and D. Sorensen. *LAPACK Users' Guide*. Society for Industrial and Applied Mathematics, Philadelphia, PA, third edition, 1999.

[3] M. Arghir, S. Le Lez, and J. Frene. Finite-volume solution of the compressible reynolds equation: linear and non-linear analysis of gas bearings. *Proceedings of the Institution of Mechanical Engineers, Part J: Journal of Engineering Tribology*, 220(7):617–627, jan 2006.

[4] P. Arumugam, S. Swarnamani, and B. S. Prabhu. Experimental identification of linearized oil film coefficients of cylindrical and tilting pad bearings. *Journal of engineering for gas turbines and power*, 117(3):593–599, 1995.

[5] J. S. Ausman. An improved analytical solution for self-acting, gas-lubricated journal bearings of finite length. *Journal of Basic Engineering*, 83(2):188–192, 1961.

[6] F. Balducchi, M. Arghir, and S. Gaudillere. Experimental analysis of the unbalance response of rigid rotors supported on aerodynamic foil bearings. Düsseldorf, Germany, June 16 – 20 2014. GT2014-25552.

[7] F. Balducchi, M. Arghir, and R. Gauthier. Experimental analysis of the dynamic characteristics of a foil thrust bearing. In *ASME Turbo Expo 2014: Turbine Technical Conference and Exposition*, pages –07, 2014.

[8] IEC BIPM, ILAC IFCC, IUPAP IUPAC, and OIML ISO. Evaluation of measurement data—guide for the expression of uncertainty in measurement. jcgm 100: 2008, 2008.

[9] P. Bonello and H. M. Pham. The efficient computation of the nonlinear dynamic response of a foil–air bearing rotor system. *Journal of Sound and Vibration*, 333(15):3459–3478, 2014.

[10] P. Bonello and H. M. Pham. Nonlinear dynamic analysis of high speed oil-free turbomachinery with focus on stability and self-excited vibration. *Journal of Tribology*, 136(4):041705, June 16 – 20 2014. GT2014-25176.

[11] M. Carpino, L. A. Medvetz, and J.-P. Peng. Effects of membrane stresses in the prediction of foil bearing performance. *Tribology transactions*, 37(1):43–50, 1994.

[12] M. Carpino and G. Talmage. Prediction of rotor dynamic coefficients in gas lubricated foil journal bearings with corrugated sub-foils. *Tribology Transactions*, 49(3):400–409, 2006.

[13] H. M. Chen, R. Howarth, B. Geren, J. C. Theilacker, and W. M. Soyars. Application of foil bearings to helium turbocompressor. In *Proceedings of the 30th Turbomachinery Symposium*, pages 103–112, 2001.

[14] H. S. Cheng and C. H. T. Pan. Stability analysis of gas-lubricated, self-acting, plain, cylindrical, journal bearings of finite length, using galerkin's method. *Journal of Basic Engineering*, 87(1):185–192, 1965.

[15] N. T. Christensen. Experimental characterization of dynamic properties of corrugated structures. Master's thesis, Technical University of Denmark, August 2014.

[16] R. D. Cook, D. S. Malkus, M. E. Plesha, and J. W. Witt. *Concepts and applications of finite element analysis*. John Wiley, New York, 4 edition, 2002.

[17] C. Dellacorte, V. Lukaszewicz, M. J. Valco, K. C. Radil, and H. Heshmat. Performance and durability of high temperature foil air bearings for oil-free turbomachinery. *Tribology Transactions*, 43(4):774–780, 2000.

[18] C. DellaCorte, K. C. Radil, R. J. Bruckner, and S. A. Howard. Design, fabrication, and performance of open source generation i and ii compliant hydrodynamic gas foil bearings. *Tribology Transactions*, 51(3):254–264, 2008.

[19] C. DellaCorte and M. J. Valco. Load capacity estimation of foil air journal bearings for oil–free turbomachinery applications. *Tribology Transactions*, 43:795–801, 2000.

[20] B. Ertas, M. Drexel, J. Van Dam, and D. Hallman. A general purpose test facility for evaluating gas lubricated journal bearings. *Journal of Engineering for Gas Turbines and Power*, 131(2):022502, 2009.

[21] K. Feng and S. Kaneko. Analytical model of bump-type foil bearings using a link-spring structure and a finite-element shell model. *Journal of Tribology*, 132(2):021706, 2010.

[22] B. J. Hamrock. *Fundamentals of Fluid Film Lubrication*. McGRAW-HILL Series in Mechanical Engineering. McGRAW-HILL, Inc., New York, 1994.

[23] W. J. Harrison. The hydrodynamical theory of lubrication with special reference to air as a lubricant. *Transactions Cambridge Philosophical Society*, 22:34–54, 1913.

[24] M. A. Hassini and M. Arghir. A simplified nonlinear transient analysis method for gas bearings. *Journal of Tribology*, 134(1):011704, 2012.

[25] M. A. Hassini and M. Arghir. A new approach for the stability analysis of rotors supported by gas bearings. In *Proceedings of ASME Turbo Expo 2013*, pages 1–13, June 3-7 2013.

[26] M. A. Hassini and M. Arghir. A simplifie d and consistent nonlinear transient analysis method for gas bearing: Extension to flexible rotors. Düsseldorf, Germany, June 16 – 20 June 16 – 20, 2014. GT2014-25955.

[27] C. A. Heshmat, D. S. Xu, and H. Heshmat. Analysis of gas lubricated foil thrust bearings using coupled finite element and finite difference methods. *Journal of Tribology*, 122(1):199–204, 2000.

[28] H. Heshmat. Advancements in the performance of aerodynamic foil journal bearings: High speed and load capability. *Journal of Tribology*, 116(2):287–294, 1994.

[29] H. Heshmat and C. P. Ku. Structural damping of self-acting compliant foil journal bearings. *Journal of tribology*, 116(1):76–82, 1994.

[30] H. Heshmat, J. A. Walowit, and O. Pinkus. Analysis of gas lubricated compliant thrust bearings. *Journal of Lubrication Technology*, 105(4):638–646, 1983.

[31] H. Heshmat, J. A. Walowit, and O. Pinkus. Analysis of gas-lubricated foil journal bearings. *Journal of Lubrication Technology*, 105(4):647–655, 1983.

[32] A. C. Hindmarsh. Odepack, a systematized collection of ode solvers, steplеman rs, scientific computing, 55-64, 1983.

[33] R. Hoffmann, T. Pronobis, and R. Liebich. The impact of modified corrugated bump structures on the rotor dynamic performance of gas foil bearings. In *Proceedings of ASME Turbo Expo*, pages –07, 2014.

[34] S. Howard, C. Dellacorte, M. J. Valco, J. M. Prahl, and H. Heshmat. Dynamic stiffness and damping characteristics of a high-temperature air foil journal bearing. *Tribology transactions*, 44(4):657–663, 2001.

[35] S. A. Howard. Misalignment in gas foil journal bearings: An experimental study. *Journal of Engineering for Gas Turbines and Power*, 131(2):022501, 2009.

[36] S. A. Howard, C. Dellacorte, M. J. Valco, J. M. Prahl, and H. Heshmat. Steady-state stiffness of foil air journal bearings at elevated temperatures. *Tribology transactions*, 44(3):489–493, 2001.

[37] D. J. Inman. *Engineering vibration*. Prentice-Hall, Inc., New Jersey, 2000.

[38] I. Iordanoff. Analysis of an aerodynamic compliant foil thrust bearing: method for a rapid design. *Journal of tribology*, 121(4):816–822, 1999.

[39] I. Iordanoff, B. B. Said, A. Mezianne, and Y. Berthier. Effect of internal friction in the dynamic behavior of aerodynamic foil bearings. *Tribology International*, 41(5):387–395, 2008.

[40] D. Kim. Parametric studies on static and dynamic performance of air foil bearings with different top foil geometries and bump stiffness distributions. *Journal of Tribology*, 129(2):354–364, 2007.

[41] T. H. Kim and L. San Andrés. Heavily loaded gas foil bearings: A model anchored to test data. *ASME Conference Proceedings*, 2005(47276):763–771, 2005.

[42] Z. Kozanecki, J. Kicinski, and G. Zywica. Numerical model of the high speed rotors supported on variable geometry bearings. In *IUTAM Symposium on Emerging Trends in Rotor Dynamics*, pages 217–227, 2011.

[43] S. Krenk. *Non-linear modeling and analysis of solids and structures*. Cambridge University Press, 2009.

[44] C.-P. R. Ku and H. Heshmat. Compliant foil bearing structural stiffness analysis: Part i–-theoretical model including strip and variable bump foil geometry. *Journal of Tribology*, 114(2):394–400, 1992.

[45] C.-P. R. Ku and H. Heshmat. Compliant foil bearing structural stiffness analysis. ii: Experimental investigation. *Journal of tribology*, 115(3):364–369, 1993.

[46] C.-P. R. Ku and H. Heshmat. Effects of static load on dynamic structural properties in a flexible supported foil journal bearing. *ASME Transactions Journal of Vibration Acoustics*, 116:257–262, 1994.

[47] C.-P. R. Ku and H. Heshmat. Structural stiffness and coulomb damping in compliant foil journal bearings: parametric studies. *Tribology transactions*, 37(3):455–462, 1994.

[48] C.-P. R. Ku and H. Heshmat. Structural stiffness and coulomb damping in compliant foil journal bearings: theoretical considerations. *Tribology transactions*, 37(3):525–533, 1994.

[49] B. J. Lazan. Damping studies in materials science and materials engineering. *ASTM International*, 1965.

[50] S. Le Lez, M. Arghir, and J. Frene. A new bump-type foil bearing structure analytical model. *Journal of engineering for gas turbines and power*, 129(4):1047–1057, 2007.

[51] S. Le Lez, M. Arghir, and J. Frene. A dynamic model for dissipative structures used in bump-type foil bearings. *Tribology Transactions*, 52(1):36–46, 2008.

[52] S. Le Lez, M. Arghir, and J. Frêne. Nonlinear numerical prediction of gas foil bearing stability and unbalanced response. *Journal of Engineering for Gas Turbines and Power*, 131(1):012503, 2009.

[53] D. Lee, Y.-C. Kim, and K.-W. Kim. The dynamic performance analysis of foil journal bearings considering coulomb friction: Rotating unbalance response. *Tribology Transactions*, 52(2):146–156, 2009.

[54] D.-H. Lee, Y.-C. Kim, and K.-W. Kim. The static performance analysis of foil journal bearings considering three-dimensional shape of the foil structure. *Journal of Tribology*, 130(3):031102, 2008.

[55] J. W. Lund. Calculation of stiffness and damping properties of gas bearings. *Journal of Lubrication Technology*, pages 793–804, 1968.

[56] P. Matta, M. Arghir, and O. Bonneau. Experimental analysis of cylindrical air-bearing dynamic coefficients. *Tribology Transactions*, 53(3):329–339, 2010.

[57] R. J. Moffat. Describing the uncertainties in experimental results. *Experimental thermal and fluid science*, 1(1):3–17, 1988.

[58] S. Morosi and I. F. Santos. On the modelling of hybrid aerostatic-gas journal bearings. *Journal of Engineering Tribology*, 225:641–653, 2011.

[59] J. B. Olsen. Nonlinear dynamic behavior of rigid rotor foil bearing system. Master's thesis, Technical University of Denmark, 2014.

[60] B. T. Paulsen, S. Morosi, and I. F. Santos. Static, dynamic, and thermal properties of compressible fluid film journal bearings. *Tribology Transactions*, 54(2):282–299, 2011.

[61] J. P. Peng and M. Carpino. Calculation of stiffness and damping coefficients for elastically supported gas foil bearings. *Journal of Tribology*, 115(1):20–27, 1993.

[62] J. P. Peng and M. Carpino. Coulomb friction damping effects in elastically supported gas foil bearings. *Tribology transactions*, 37(1):91–98, 1994.

[63] J. P. Peng and M. Carpino. Finite element approach to the prediction of foil bearing rotor dynamic coefficients. *Journal of Tribology*, 119(1):85–90, 1997.

[64] Z. C. Peng and M. M. Khonsari. Hydrodynamic analysis of compliant foil bearings with compressible air flow. *Journal of Tribology*, 126(3):542–546, 2004.

[65] H. M. Pham and P. Bonello. Efficient techniques for the computation of the nonlinear dynamics of a foil-air bearing rotor system. In *ASME Turbo Expo 2013: Turbine Technical Conference and Exposition*, pages –07, 2013.

[66] J. W. Powell. A review of progress in gas lubrication. *Review of Physics and Technology*, 1(2):96, 1970.

[67] K. Radil, S. Howard, and B. Dykas. The role of radial clearance on the performance of foil air bearings. Technical report, 2002.

[68] K. C. Radil and C. Dellacorte. The effect of journal roughness and foil coatings on the performance of heavily loaded foil air bearings. *Tribology Transactions*, 45(2):199–204, 2002.

[69] D. Rubio and L. San Andrés. Bump-type foil bearing structural stiffness: experiments and predictions. *Journal of engineering for gas turbines and power*, 128(3):653–660, 2006.

[70] D. Rubio and L. San Andrés. Structural stiffness, dry friction coefficient, and equivalent viscous damping in a bump-type foil gas bearing. *Journal of engineering for gas turbines and power*, 129(2):494–502, 2007.

[71] D. Ruscitto, J. McCormick, and S. Gray. Hydrodynamic air lubricated compliant surface bearing for an automotive gas turbine engine. i. journal bearing performance. Technical Report NASA CR-135368, NASA, 1978.

[72] M. Salehi, H. Heshmat, and J. F. Walton. On the frictional damping characterization of compliant bump foils. *Journal of tribology*, 125(4):804–813, 2003.

[73] L. San Andrés. Hybrid flexure pivot-tilting pad gas bearings: analysis and experimental validation. *Journal of tribology*, 128(3):551–558, 2006.

[74] L. San Andrés and T. H. Kim. Improvements to the analysis of gas foil bearings: integration of top foil 1d and 2d structural models. 2007.

[75] L. San Andrés and T. H. Kim. Forced nonlinear response of gas foil bearing supported rotors. *Tribology International*, 41(8):704–715, 2008.

[76] L. San Andrés and T. H. Kim. Analysis of gas foil bearings integrating fe top foil models. *Tribology International*, 42(1):111–120, 2009.

[77] L. San Andrés and T. H. Kim. Thermohydrodynamic analysis of bump type gas foil bearings: A model anchored to test data. *Journal of Engineering for Gas Turbines and Power*, 132(4):042504, 2010.

[78] L. San Andrés, D. Rubio, and T. H. Kim. Rotordynamic performance of a rotor supported on bump type foil gas bearings: experiments and predictions. *Journal of engineering for gas turbines and power*, 129(3):850–857, 2007.

[79] J.-H. Song and D. Kim. Foil gas bearing with compression springs: Analyses and experiments. *ASME Journal of Tribology*, 129(3):628–639, 2007.

[80] B. Sternlicht. Gas-lubricated cylindrical journal bearings of the finite length: Static loading. *Journal of Applied Mechanics*, 28(4):535–543, 1961.

[81] B. Sternlicht and R. C. Elwell. Theoretical and experimental analysis of hydrodynamic gas-lubricated journal bearings. *American Society of Mechanical Engineers – Papers*, (57), 1957.

[82] V. Stingelin. *Theoretische und experimentelle Untersuchungen an Gaslagern*. PhD thesis, Eidgenössischen Technischen Hochschule in Zürich, 1963.

[83] J. J. Thomsen. *Vibrations and stability: advanced theory, analysis, and tools*. Springer, 2003.

[84] J. A. Walowit and J. N. Anno. *Modern developments in lubrication mechanics*. Applied Science Publishers London, 1975.

[85] J. F. Walton, H. Heshmat, and M. J. Tomaszewski. Design and test program in the developmen of a 100 hp oil-free high-speed blower. In *Proceedings of ASME Turbo Expo*, 2007.

[86] C.-C. Wang and C.-K. Chen. Bifurcation analysis of self-acting gas journal bearings. *Journal of Tribology*, 123(4):755, 2001.

[87] J. X. Yuan and X. M. Wu. Identification of the joint structural parameters of machine tool by dds and fem. *Journal of engineering for industry*, 107(1):64–69, 1985.

[88] J. Zhang, W. Kang, and Y. Liu. Numerical method and bifurcation analysis of jeffcott rotor system supported in gas journal bearings. *Journal of Computational and Nonlinear Dynamics*, 4(1):011007, 2009.

[89] G. Zywica. The static performace analysis of the foil bearing structure. *acta mechanica et automatica*, 5(4), 2011.

[90] G. Zywica. The dynamic performance analysis of the foil bearing structure. *Acta mechanica et automatica*, 7(1), 2013.

[P1] Compliant Foil Journal Bearings - Investigation of Dynamic Properties

---

This paper was submitted to and presented at the *10th International Conference on Schwingungen in Rotierenden Maschinen* (SIRM2013), Berlin, Germany, 25-27 February, 2013.

SIRM 2013 – 10th International Conference on Vibrations in Rotating Machines,
Berlin, Deutschland, 25. – 27. February 2013

Compliant Foil Journal Bearings - Investigation of Dynamic Properties

Jon Steffen Larsen [1,2], **Ilmar F. Santos** [1]

[1] Department of Mechanical Engineering, DTU - Technical University of Denmark, 2800 Kgs. Lyngby, Denmark
[2] Siemens A/S - Turbomachinery Solutions, 3000 Helsingør, Denmark

Abstract

Through the past three decades gas bearings have found way into an increasing number of industrial applications within high speed rotating machinery. Especially the compliant foil type of bearings has gained large popularity. Much theoretical and experimental work has been conducted on the compliant foil bearings, and the understanding of their dynamic behaviour is growing. However, practical design involving these bearings are still associated with a large degree of trial and error. This study aims at establishing an accurate mathematical model, to calculate the pressure, film height and dynamic coefficients, of the compliant foil bearing together with an efficient solution method, which can be easily adopted and implemented by mechanical engineers. A theoretical model of a radial compliant foil bearing that incorporates compressibility of the lubricating gas and flexibility/compliance of the foil structure is presented. The compliance of the foil structure is incorporated implicitly in the Reynolds equation which is accomplished through a modification of the film gap function [8]. The resulting non-linear equation is perturbed and solved by use of the finite element method following a Bubnow-Galerkin approach. This constitutes the main original contribution of this work, considering the fact that the finite difference method is commonly used and thouroughly investigated in the literature. The finite element method leads to a set of non-linear equations for the static fluid film pressure (zeroth order) which can be solved by an iterative approach, where the pressure field is the converging parameter. The equations for the dynamic pressures (first order) becomes linear and can be solved directly to obtain the linearised stiffness and damping coefficients of the bearing. The influence of explicit and implicit boundary conditions are also investigated. Theoretical results for pressures, shaft equilibrium positions and film thickness are presented and compared to experimental results [18, 20]. A good agreement between experimental and theoretical results are found for large loads. For lower loads, some discrepancies are observed and discussed in details. The dynamic stiffness and damping coefficients are calculated and compared to theoretical results reported in [10]. A good agreement are observed for both stiffness and damping coefficients.

Nomenclature

$B_{\alpha\beta}$	damping coefficients, $\alpha\beta = x, y$	l_0	bump half length
C	radial clearance	p	pressure
D	bearing diameter	p_0	static pressure
E	modulus of elasticity of foil	p_a	ambient pressure
K	foil flexibility	p_x, p_y	perturbed pressures
K_c	foil mobility	t	time
$K_{\alpha\beta}$	stiffness coefficients, $\alpha\beta = x, y$	t_b	thickness of bump foil
L	bearing length	x, y, z	Cartesian coordinates
R	journal radius	$\Delta e_{x,y}$	perturbation of journal equilibrium position
S	bump foil pitch	η	structural loss factor of foils
$W_{x,y}$	static load components	μ	absolute viscosity
b_{foil}	equivalent viscous damping of foil	ν	Poisson's ratio of foil
$e_{x,y}$	journal eccentricity components	ω	angular speed of journal
e_{x_0,y_0}	journal equilibrium position	ω_s	excitation frequency of journal
h	film height	ϕ	attitude angle
h_c	film height correction	θ	circumferential coordinate
h_r	film height (rigid)	$\{U\}$	film speed, $\{U\} = \{\omega R/2,\ 0\}^T$

1 Introduction

Gas bearings has been the subject for research within mechanical engineering for five decades [14]. Through the past three decades, compliant foil bearings have found way into an increasing number of industrial applications within high speed rotating machinery. The current tendency is, that the technology is progressing from small high speed rotating machinery, like dental drills and micro turbines and specialized equipment related to the aeronautical industries, toward larger mass-produced industrial compressors and turbines [6, 9]. In such industrial compressors, widely available today, the assembled rotor weight is often above 50 kg and the rated power over 200 kW. The advantages compared to conventional oil lubricated bearings are many, for instance low mechanical power loss and completely clean and non oil contaminating operation. The disadvantages over oil lubricated bearings are lower load carrying capacity, though greatly improved within the recent decade [4], and wear during starts and stops due to breakdown of the air lubrication film at low journal speeds. Solid lubricants are used to increase the start-stop capacity. PTFE coatings are commonly utilized for this purpose but other types of coatings for instance PS304 has been investigated, in particular for higher temperature applications [3, 19]. Though compliant foil bearings offer significantly better stability characteristics compared to rigid gas bearings, the stability of the rotor bearing system is still a major concern, seen from an engineering perspective. As a result, much experimental and theoretical work has been conducted to achieve accurate mathematical models of the compliant foil bearing dynamics. Heshmat [7, 8] originally included the flexibility of the compliant foil implicitly in the Reynold's equation by introducing a linear elastic displacement as function of the fluid film pressure, $h_c = K(p - p_a)$. This *simple elastic foundation model* was extended by several authors [10, 11, 15] to include a structural loss factor for the compliant foil and a perturbation method to obtain equations for the linearised stiffness and damping coefficients, which where solved by a finite difference scheme. San Andrés and Kim [21] later extended the model to include thermohydrodynamic effects (THD). Besides the theoretical work related to the *simple elastic foundation model*, there has been many other significant contributions dealing with the complex behaviour of the compliant bump-foil structures interacting with the housing surface [13]. Highly worth mentioning is the work of Peng and Carpino [16, 1], in which, detailed FE models of the compliant foil structure including equivalent frictional damping is coupled to the FE model of the lubrication film.

In this paper, the *simple elastic foundation model* is also used as described in [8]. The model is perturbed using complex mathematical notation enabling the introduction of a complex frequency dependant flexibility for the compliant foil structure. This complex frequency dependant flexibility, or mobility, allows for the introduction of an equivalent structural damping or a loss factor. The perturbed equations, for the static and dynamic pressures, are solved by following a Bubnov-Galerkin Finite Element approach, which is the main original contribution of this work. It is shown, that the FE analysis is not only dependant on the explicit boundary conditions but also on an implicit boundary condition. Two different implicit boundary conditions are introduced and compared.

2 Theoretical Model

For a journal bearing with the nomenclature as given in Figure 1a, the compressible Reynolds equation can be written in vector form [5] as

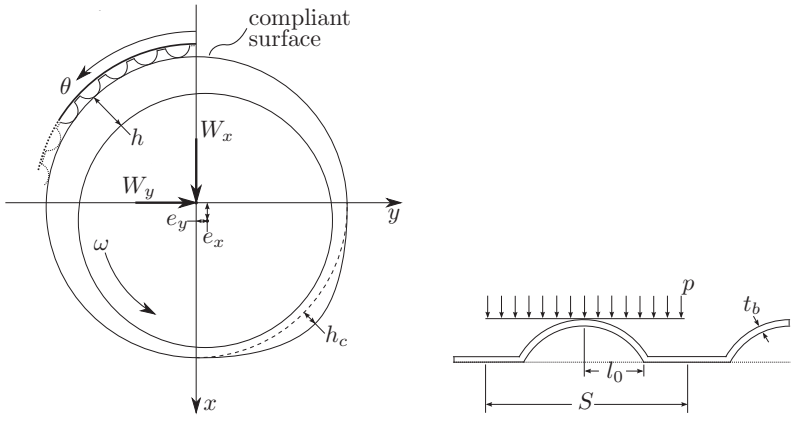

(a) Shaft and bearing (b) Detailed view of bump and top foil

Figure 1: Schematics and nomenclature of a foil journal bearing with compliant outer surface

$$\nabla \cdot \left(\frac{ph^3}{12\mu} \nabla p \right) = \nabla \cdot (ph)\{U\} + \frac{\partial}{\partial t}(ph) \tag{1}$$

where the film height $h(\theta, z, p)$ is defined as the film height of a rigid journal bearing $h_r(\theta)$, with the addition of a compliance, or deflection term $h_c(p) = K(p - p_a)$, which is dependant on the hydrodynamic pressure field and was first suggested by Heshmat [8]. The film height becomes

$$h = h_r + h_c = C + e_x \cos(\theta) + e_y \sin(\theta) + K(p - p_a) \tag{2}$$

where K is the structural flexibility related to the area of the compliant foil layers. With the notation defined in Figure 1b, K was given by Heshmat [8] as

$$K = \frac{2S}{E} \left(\frac{l_0}{t_b} \right)^3 (1 - \nu^2) \tag{3}$$

Expanding Reynolds equation (1) by inserting (2) leads to a modified Reynold equation with the structural foil flexibility included implicitly

$$\begin{aligned} &\nabla \cdot \left(\frac{ph_r^3}{12\mu} \nabla p \right) + \nabla \cdot \left(\frac{p(p - p_a)^3 K^3}{12\mu} \nabla p \right) + \nabla \cdot \left(\frac{ph_r(p - p_a)^2 K^2}{4\mu} \nabla p \right) + \nabla \cdot \left(\frac{ph_r^2(p - p_a)K}{4\mu} \nabla p \right) \\ &= \nabla \cdot (ph_r)\{U\} + \nabla \cdot (p(p - p_a)K)\{U\} + \frac{\partial}{\partial t}(ph) + \frac{\partial}{\partial t}(p(p - p_a)K) \end{aligned} \tag{4}$$

2.1 Assumptions and Limitations

Solving this equation, for a given set of eccentricities (e_x, e_y) and speed $\{U\}$, yields the hydrodynamic pressure p, in the fluid film, by implicitly taking into account the deformations in the compliant foil layers. In addition to the assumptions of laminar, Newtonian, thin film flows, which together with the Navier-Stokes and the continuity equation leads to the Reynold equation, the viscosity is assumed constant i.e. isothermal condition. Furthermore, by including the foil flexibility in the radial direction as in (4), it is assumed that the foil radial stiffness is linear and that the radial deformation in any foil position (θ, z) is completely independent of the radial deformation in any neighbouring positions. Dependent on the particular foil configuration (bump geometry and top foil thickness) this will limit the validity of (4). Finally, the flexibility (3) does not take into account the possible top foil "sag" between bumps. To include this "sagging" effect, the flexibility K could be chosen as a vector field, with unequal flexibility components, rather than a scalar. The mentioned limitations related to the flexible foils are a consequence of introducing the *simple elastic foundation model*. Several authors [1, 12, 13, 16] contributed with more complex methods of including the flexible foil structure, in the mathematical model, in order to address these limitations.

2.2 Perturbed Equations

To investigate the dynamic performance of the bearing, a harmonic perturbation method is employed. The method, which was first introduced by Lund [14], is a commonly used and widely accepted method. Assuming that the rotor exhibits small harmonic oscillations around its equilibrium position in the bearing (e_{x_0}, e_{y_0}), the shaft motion is given by

$$e_x = e_{x_0} + \Delta e_x e^{i\omega_s t} \text{ and } e_y = e_{y_0} + \Delta e_y e^{i\omega_s t} \tag{5}$$

Assuming the amplitudes to be small $\Delta e_x \ll C$ and $\Delta e_y \ll C$, a first order Taylor expansion of the pressure can be written as

$$p = p_0 + (\Delta e_x p_x + \Delta e_y p_y) e^{i\omega_s t} \tag{6}$$

In (6), the pressure p is a harmonic oscillating field which enables the introduction of a frequency dependant mobility in the deflection term h_c of the film height, rather than a regular flexibility K. The mobility can written as

$$K_c = K + i\eta K \tag{7}$$

where $\eta = (\omega_s b_{foil})/K$ is the mechanical energy loss factor related to the foils. Substituting (5), (6), (7) into (2) and (4), discarding second and higher order terms yields, upon separation of variables, the zeroth and first order equations:

- Zeroth order

$$\begin{aligned}&\nabla \cdot \left(\frac{p_0 h_r^3}{12\mu} \nabla p_0 \right) + \nabla \cdot \left(\frac{p_0 (p_0 - p_a)^3 K_c^3}{12\mu} \nabla p_0 \right) + \nabla \cdot \left(\frac{p_0 h_r (p_0 - p_a)^2 K_c^2}{4\mu} \nabla p_0 \right) \\ &+ \nabla \cdot \left(\frac{p_0 h_r^2 (p_0 - p_a) K_c}{4\mu} \nabla p_0 \right) = \nabla \cdot (p_0 h_r)\{U\} + \nabla \cdot (p_0 (p_0 - p_a) K_c)\{U\}\end{aligned} \tag{8}$$

- First order

$$\begin{aligned}&\nabla \cdot \left(\frac{p_0 h_r^3}{12\mu} \nabla p_\gamma \right) + \nabla \cdot \left(\frac{p_0 (p_0 - p_a)^3 K_c^3}{12\mu} \nabla p_\gamma \right) + \nabla \cdot \left(\frac{p_0 h_r (p_0 - p_a)^2 K_c^2}{4\mu} \nabla p_\gamma \right) \\ &+ \nabla \cdot \left(\frac{p_0 h_r^2 (p_0 - p_a) K_c}{4\mu} \nabla p_\gamma \right) + \nabla \cdot \left(\frac{(4p_0^3 - 9p_0^2 p_a + 6p_0 p_a^2 - p_a^3) K_c^3}{12\mu} \nabla p_0 p_\gamma \right) \\ &+ \nabla \cdot \left(\frac{h_0 (3p_0^2 - 4p_0 p_a + p_a^2) K_c^2}{4\mu} \nabla p_0 p_\gamma \right) + \nabla \cdot \left(\frac{h_0^2 (2p_0 - p_a) K_c}{4\mu} \nabla p_0 p_\gamma \right) + \nabla \cdot \left(\frac{h_0^3}{12\mu} \nabla p_0 p_\gamma \right) \\ &- \nabla \cdot \left((2p_0 - p_a) K_c p_\gamma \right) \{U\} - \nabla \cdot (h_0 p_\gamma) \{U\} - 2i\omega_s (p_0 K_c p_\gamma) - i\omega_s (h_0 p_\gamma) + i\omega_s (p_a K_c p_\gamma) = \\ &- \nabla \cdot \left(\frac{p_0 (p_0^2 - 2p_0 p_a + p_a^2) K_c^2 \mathrm{f}_\gamma}{4\mu} \nabla p_0 \right) - \nabla \cdot \left(\frac{p_0 h_0 (p_0 - p_a) K_c \mathrm{f}_\gamma}{2\mu} \nabla p_0 \right) \\ &- \nabla \cdot \left(\frac{3p_0 h_0^2 \mathrm{f}_\gamma}{12\mu} \nabla p_0 \right) + \nabla \cdot (p_0 \mathrm{f}_\gamma)\{U\} + i\omega_s (p_0 \mathrm{f}_\gamma)\end{aligned} \tag{9}$$

where $\gamma = x, y$ and $\mathrm{f_x} = \cos(\theta)$ and $\mathrm{f_y} = \sin(\theta)$. Solving the zeroth order equation (8) for a static eccentricity (e_{x_0}, e_{y_0}) and speed $\{U\}$ yields the static film pressure p_0. This pressure is then used when solving the first order equation (9) to obtain the dynamic pressures p_x and p_y. The bearing reaction forces are found by integration of the static pressure p_0 over the bearing surface

$$\begin{Bmatrix} W_x \\ W_y \end{Bmatrix} = -\int_0^L \int_0^{2\pi} (p_0 - p_a) \begin{Bmatrix} \cos(\theta) \\ \sin(\theta) \end{Bmatrix} R d\theta dz \tag{10}$$

and similar integration of the dynamic pressures (p_x, p_y) determines the dynamic stiffness and damping coefficients

$$\begin{bmatrix} K_{xx} & K_{yx} \\ K_{xy} & K_{yy} \end{bmatrix} + i\omega_s \begin{bmatrix} B_{xx} & B_{yx} \\ B_{xy} & B_{yy} \end{bmatrix} = \int_0^L \int_0^{2\pi} \begin{bmatrix} p_x \cos(\theta) & p_x \sin(\theta) \\ p_y \cos(\theta) & p_y \sin(\theta) \end{bmatrix} R d\theta dz \tag{11}$$

3 Finite Element Formulation and Solution

A linear four node quadrilateral element is used in the finite element formulation, which follows a Bubnov-Galerkin scheme [2]. The zeroth order perturbation equation for the static pressure (8) is a non-linear PDE. Upon the application of the finite element scheme, a set of algebraic equations appears

$$[Kp(p_0, e_x, e_y)]\{p_0\} + [Ku(p_0, e_x, e_y)]\{u\} = 0 \tag{12}$$

These are non-linear in the sense that the system matrices $[Kp(p_0, e_x, e_y)]$ and $[Ku(p_0, e_x, e_y)]$ are dependant on the pressure p_0, in addition to the shaft eccentricities e_x and e_y. In order to solve (12) for a given set of eccentricities, an iterative approach must be implied. This is accomplished by guessing an initial pressure field $\{p_{0_n}\}$, to be used in forming the system matrices for the first iteration. Solving the system yields a new pressure field $\{p_{0_{n+1}}\}$, which is then used in the next iteration i.e. $\{p_{0_n}\} = \{p_{0_{n+1}}\}$. The procedure is repeated until convergence is achieved. A simple under relaxation procedure $p_{0_{n+1}} = \beta p_{0_n} + (1-\beta)p_{0_{n-1}}$ where $\beta = [0:1]$ has been successfully applied to improve the convergence of the solution.

In order to find the bearing equilibrium position (e_{x0}, e_{y0}) for a given set of loads (W_x, W_y), the above iterative procedure is used within a Newton-Raphson scheme with the eccentricities as variables.

The first order perturbation equation (9) for the dynamic pressures is linear. Implying a Bubnov-Galerkin finite element approach, leads to a set of linear algebraic equations

$$[Kp(p_0, e_{x0}, e_{y0})]\{p_\gamma\} + [Ku(p_0, e_{x0}, e_{y0})]\{u\} = 0 \tag{13}$$

where $\gamma = x, y$. When the bearing equilibrium position (e_{x0}, e_{y0}) and the static pressure p_0 is found by solving (12), this set of linear equations (13) can be solved directly yielding the dynamic pressures p_x and p_y.

3.1 Boundary Conditions

A general advantage of the finite element method, is the allowances of explicit application of boundary conditions. Explicit in the sense that all coefficients of the system of equations, $[K_p]$ and $[K_u]$, are computed one after another and then the boundary conditions are applied. For a compliant foil bearing as depicted in Figure 1a, the boundary conditions for the perturbed equations (8) and (9) would be

$$p_0 : \begin{cases} p_0(0,z) = p_0(2\pi,z) \\ p_0(\theta, L/2) = p_0(\theta, -L/2) = p_a \end{cases} \quad p_\gamma : \begin{cases} p_\gamma(0,z) = p_\gamma(2\pi,z) \\ p_\gamma(\theta, L/2) = p_\gamma(\theta, -L/2) = 0 \end{cases} \tag{14}$$

Applying these boundary conditions will pose a problem when bearing eccentricities are high as the foil deflection $h_c(p) = K(p - p_a)$ becomes zero where $p = p_a$. This is the case on the edge of the axial ends of the bearing. As shall be seen later, the eccentricity ratio $\epsilon = e/C$, for a compliant foil bearing, can easily take on values of 1 or higher. In such cases, the film height (2) becomes zero or even negative on the sides where ambient pressure has been prescribed. This obviously introduces an error in the solution. To overcome this problem, one has to assure that the foil deflections on the bearing sides are inside of a realistic range of values. This can be achieved by meshing with a narrow band of elements, having the width of $L/100$ or less, along the bearing edges subjected to ambient pressure. Following by letting the foil deflection $h_c(p)$ in the outermost nodes of these elements (on the bearing edge), adopt the deflection values of the innermost nodes (away from the bearing edge) on that element. This implicit boundary condition is referred to as b.c.1 and it allows for a curved foil surface deflection along the axial direction of the bearing.

An alternative approach is to use the arithmetic mean pressure over the axial direction, of the bearing, when calculating the foil deflection $h_c(p)$ [17]. This implicit boundary condition is referred to as b.c.2. One obvious consequence of applying b.c.2 is, that the bearing surface will be restricted to deflect evenly, without curvature, along the axial direction of the bearing.

4 Results

The results of a computer code, based on the theory of section 3, is compared to existing experimental data [18, 20]. The simulations are based on the implicit boundary conditions b.c.1 and b.c.2, introduced in Section 3.

4.1 Theoretical and Experimental Comparison For Rigid Surface

For an initial validation of the theory and complementary computer program, the theoretical pressure distributions around the centre of a rigid bearing has been compared to experimental results, as reported by Powell [18]. The results are shown in Figure 2 and good theoretical and experimental agreements are achieved. Small deviations are detected around the maximum pressure. The theoretical model is though more conservative and predicts maximum pressure slightly higher than measured by Powell [18].

4.2 Theoretical and Experimental Comparison With Compliant Surface

In order to validate the theoretical model taking into account the compliance of the bearing surface, the theoretical results are compared to the experimental results reported by Ruscitto at NASA in 1978 [20]. A subset of the experimental test cases are simulated. The simulations are based on the bearing properties and test conditions listed in Table 1.

The main objective of the experimental work performed by Ruscitto [20] was to determine the fluid film height h of a compliant foil bearing operating at a variety of loads, clearances and speeds and to determine the load carrying capacity which relates to the minimum fluid film height h_{min}. The film height was measured directly using a proximity sensor mounted inside the rotating shaft. In this way, the film height was measured around the bearing centre at $z = 0$.

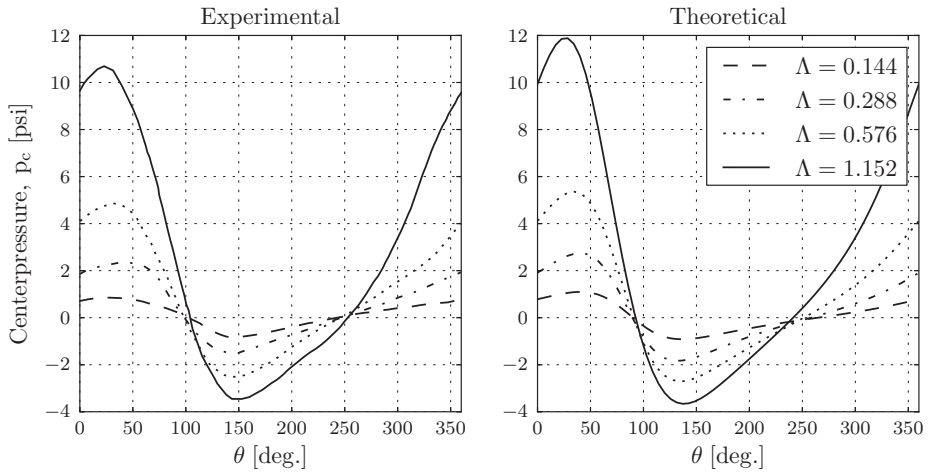

Figure 2: Experimental [18] and theoretical pressure distributions around the centre of a rigid journal bearing with dimensions, $L = 101.6$ mm, $D = 50.8$ mm, $C = 26.54$ μm for bearing numbers $\Lambda = [0.144, 0.288, 0.576, 1.152]$ and associated bearing loads $-W = [7.4, 16.4, 30.4, 61.4]$ (lbf) respectively

Table 1: Geometry, material properties and operating conditions of the NASA test bearing

(a) Bearing properties

Parameters	Values
Bearing radius, R	19.05 mm
Bearing length, L	38.1 mm
Bump foil thickness, t	0.1016 mm
Bump foil pitch, S	4.572 mm
Bump half length, l_0	1.778 mm
Young's modulus of bump foil, E	2.07×10^{11} Pa
Poisson's ratio of bump foil, ν	0.3
Ambient pressure, P_a	1×10^5 Pa
Air viscosity, μ	1.836×10^{-5} Pa·s
Air density, ρ	$1.1614\ \mathrm{kg/m^3}$

(b) Test cases

Case	Clearance, C	Journal Speed, Ω
#101	57 μm	30,000 RPM
#102	57 μm	45,000 RPM
#103	57 μm	60,000 RPM
#108	31.8 μm	55,500 RPM

Comparing the minimum film height h_{min} found experimentally, for the test cases listed in Table 1, to theoretical results, as shown in Figure 3, indicates good correlation for test runs #102, #103, #108 for loads above 0.3. However, for test run #101 the correlation is poor. The dimensionless minimum film height h_{min}/C should originate at close to 1 for zero loading. However, this condition can only occur if the smooth top foil and the rotating shaft is completely circular and conform and the supporting stiffness provided by the bump foil is evenly distributed on the entire bearing surface and in the absences of frictional hysteresis. In reality, these conditions can only be meet to a certain degree which is reflected by the experimental results. Based on this knowledge, the validity of the individual experimental results can be evaluated. In that sense, the validity of experiment #102, #103, #108 is regarded as higher than #101 in which h_{min}/C converge to 0.2 The reason for h_{min}/C converging towards 0.2, in test #101, is unknown. One probable reason for such discrepancies could be related to the clearance adjustment and manufacturing tolerances. Bearing manufacturing technology and tolerances plays a significant role in terms of achieving the afore mentioned conditions and being able to produce consistent experimental results. The technology has been improved since the experiments were performed at NASA in 1978 [20] and the ability to achieve consistent performance characteristics of each individual bearing has increased since then. As an example, it has been observed during industry testing, that the clearance C of certain bearings increases significantly (sometimes doubles) after the first few runs which means that they have to be readjusted. For bearings manufactured at a higher degree of precision this phenomenon is less prevailed. Whether this has been an issue during the testing

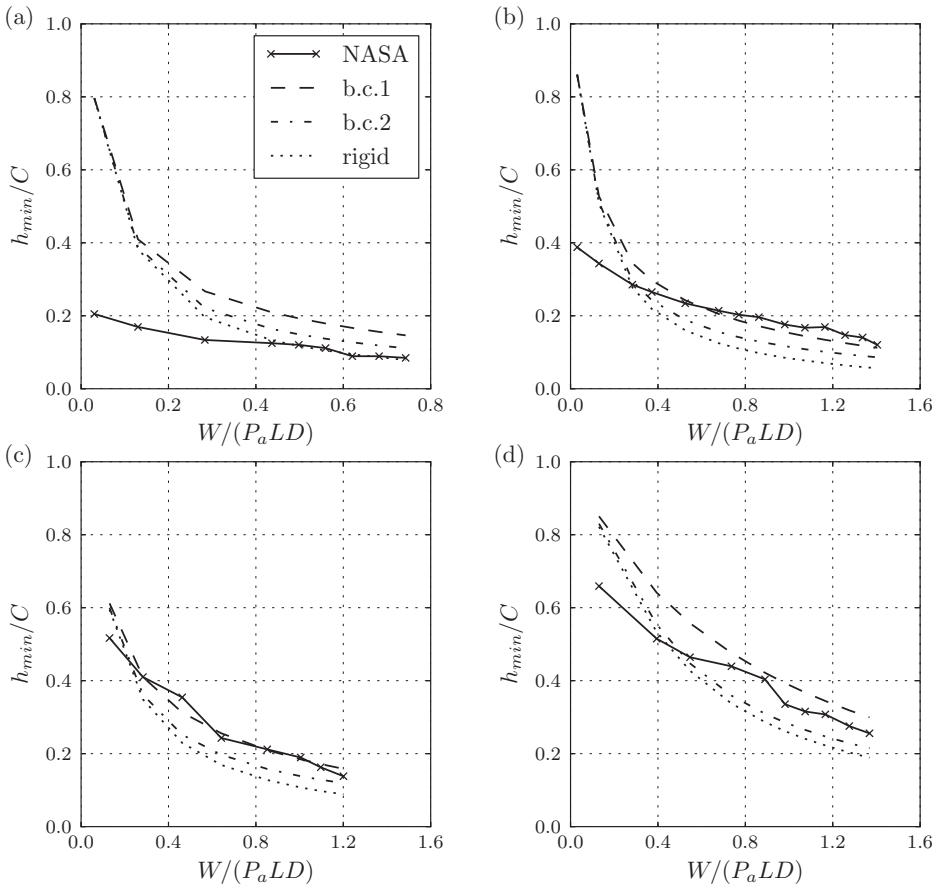

Figure 3: Dimensionless minimum film height h_{min} for; (a) test run #101, (b) test run #102, (c) test run #103, (d) test run #108

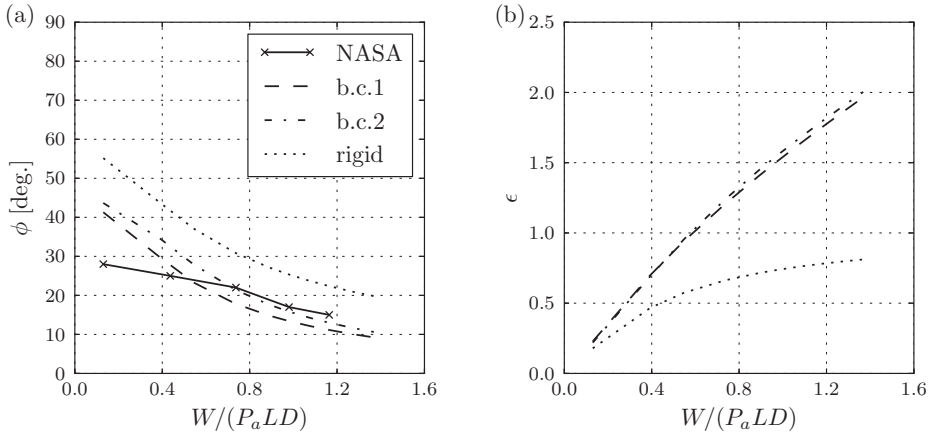

Figure 4: (a) attitude angles from test case #108, (b) calculated eccentricities

at NASA is unknown but it is likely. The theoretical results, shown in Figure 3, indicate that the minimum film height in the centre of the bearing is generally lower and slightly underestimated when using b.c.2 and in some cases approaching the results of an equivalent rigid bearing.

Since the fluid film height was measured continuously around the circumference of the bearing, the attitude angle ϕ could be determined (as the angle at which the minimum film height occurred). In Figure 4, the attitude angle found experimentally is compared to simulated values, using b.c.1 and b.c.2 and the rigid case. The correlation is good at dimensionless loads above 0.3. A reduced attitude angle is detected for the flexible bearing. For oil lubricated bearings, a lower attitude angle generally leads to better stability characteristics. However, for gas bearings, the cross-coupling stiffness coefficients are small, and the stability is strongly affected by the cross-coupling damping coefficients instead. Therefore, it is hard to conclude whether the reduced attitude angle is leading to increased stability characteristics or not.

No experimental data is available for the eccentricity ϵ. However, the theoretical results shows that the eccentricity using b.c.1 and b.c.2 yields almost similar results and that it can take on values higher than 1 which clearly distinguish these cases from the rigid case. The theoretical and experimental [18] pressure curves for a rigid gas bearing was presented in Figure 2. Similar pressure curves are calculated for the compliant foil bearing, case #102 at maximum loading ($W = 203.8$ N), and compared to the results of an equivalent rigid bearing in

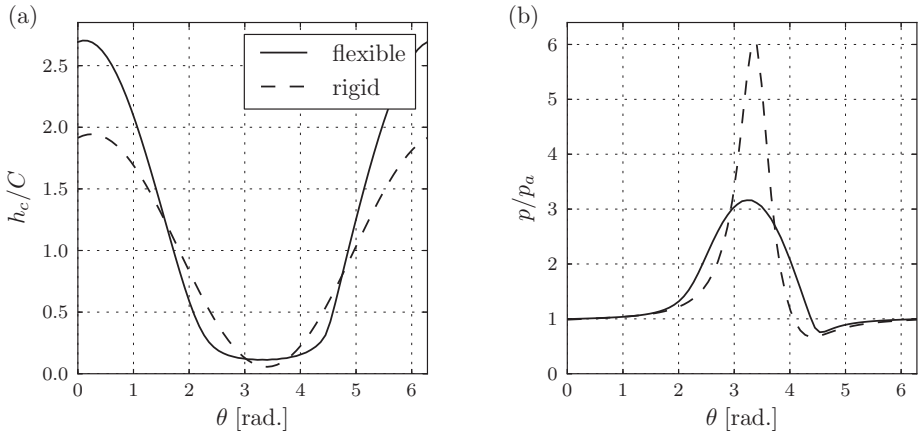

Figure 5: Theoretical results of case #102 calculated for a bearing clearance and load of $C = 57$ μm and $W = 203.8$ N respectively; (a) height profile at the bearing centre, (b) pressure profile at the bearing centre

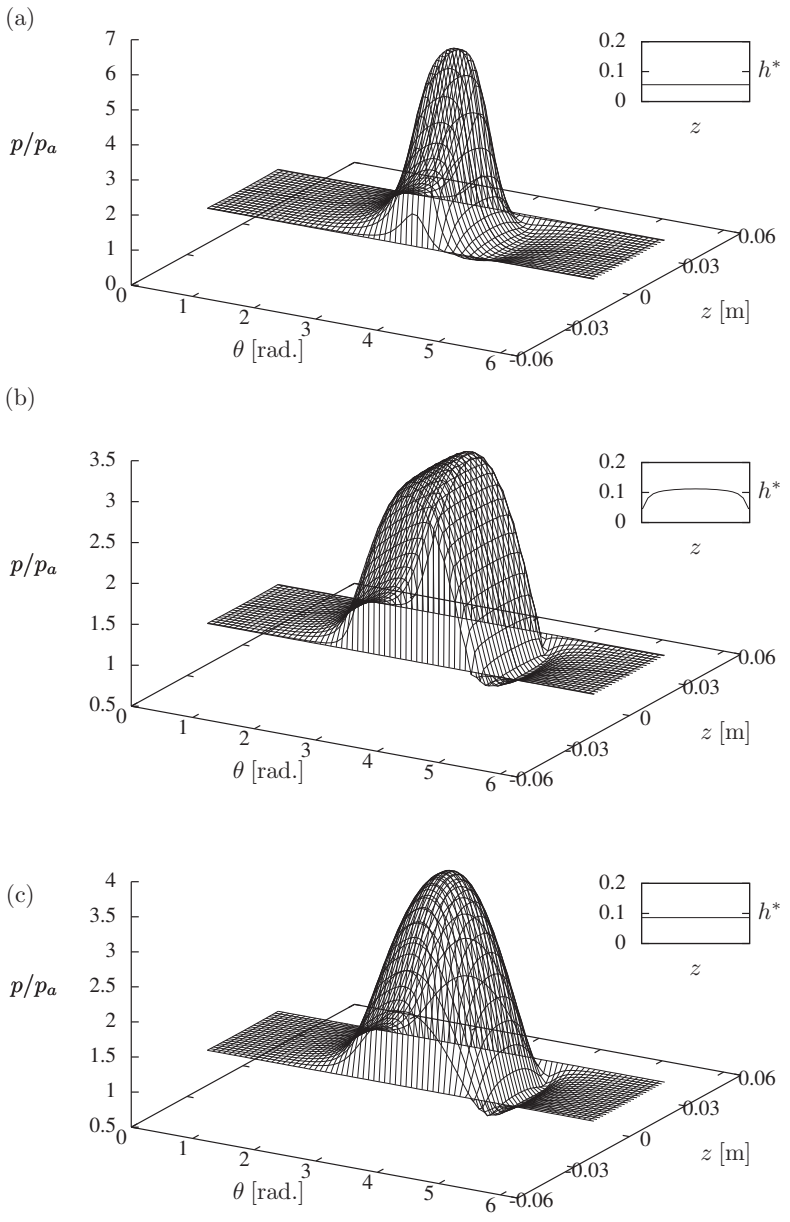

Figure 6: Pressure fields and non-dimensional height profiles for NASA test bearing calculated for a bearing clearance and load of $C = 57$ μm and $W = 203.8$ N respectively (case #102); (a) rigid bearing, (b) flexible bearing based on b.c.1, (c) flexible bearing based on b.c.2

Figure 5. The maximum pressure for the compliant foil bearing is significantly lower than for the equivalent rigid bearing. Instead the pressure is distributed wider and more evenly over the circumference. Similarly, the film height profile around the centre of the flexible bearing shows larger minimum film height, indicating higher load carrying capacity, than for the rigid bearing. The height profile clearly indicates a deformation of the foils as it is no longer pure sinusoidal. In fact the deformation of the top foil is providing a wider convergent region for film pressure generation which in turn results in higher load carrying capacity. The eccentricity ratios for the rigid and compliant case were calculated to $\epsilon_r = 0.944$ and $\epsilon_f = 1.705$ respectively.

As discussed, the centre pressure of a compliant foil bearing is distributed over a wider portion of the circumference compared to a rigid bearing, Figure 5. Depending on the boundary condition used, the theoretical pressure becomes more uniformly distributed over the length L too. This is seen in Figure 6. Here the pressure distributions calculated for both boundary conditions and the equivalent rigid case are compared. Clearly, the pressure field is different between the compliant and rigid cases, but even the two sets of boundary conditions changes the pressure field significantly. This is a consequence of the uniform foil deflection over L i.e. in the z-direction that is implied by b.c.2. The foil deflection curves in the axial direction of the bearing are also shown in Figure 6. Allowing the foils to deflect non-uniformly over the length L, i.e. by implying b.c.1, will prevent the pressure field to peak in the centre-line of the bearing, since the foils will deflect in a curved shape causing the diffusion towards the edges to be limited, as a result of the converging film height h in the axial direction. The maximum film pressure calculated when using b.c.1 is thus slightly lower than when using b.c.2

4.3 Theoretical Stiffness and Damping Coefficients

A comparison between dynamic coefficients calculated from the computer code and similar results obtained by Kim 2007 [10] is made in Figure 7. The comparison is made for a bearing with the geometry given in Table 1a and with a clearance of $C = 32\mu\text{m}$ and a static load $W_x = 30$ N and a journal speed of $\omega = 40,000$ RPM. Fur-

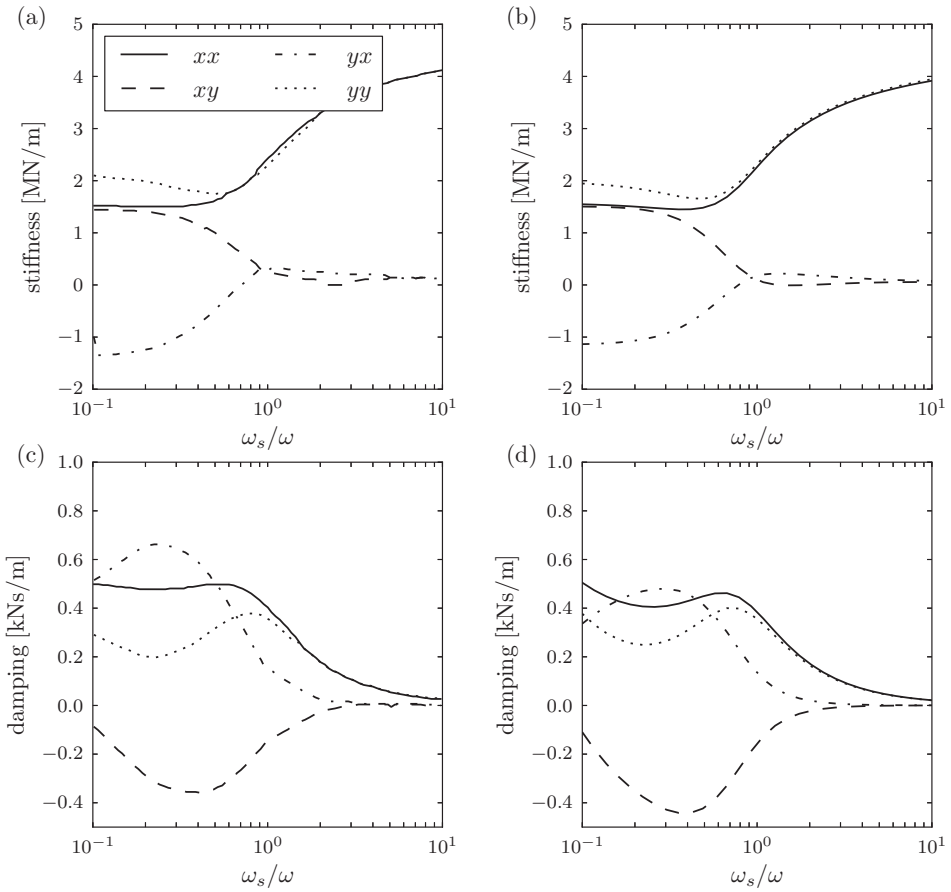

Figure 7: Stiffness and Damping coefficients $K_{\alpha\beta}$ and $B_{\alpha\beta}$, $\alpha\beta = x, y$; (a) stiffness coefficients obtained by Kim 2007 [10], (b) stiffness coefficients from current study, (c) damping coefficients obtained by Kim 2007 [10], (d) damping coefficients from current study

thermore, the boundary conditions (14) are applied together with b.c.1 and the stiffness and damping coefficients $K_{\alpha\beta}$, $B_{\alpha\beta}$ are calculated for a range of excitation frequencies $\omega_s/\omega = [0.1 : 10]$. A good agreement is observed between the results of the current study and the results obtained by Kim [10]

5 Conclusions and Future Aspects

This paper presents a theoretical model to predict the dynamics of a compliant foil bearing in terms of pressure profiles, film height, eccentricity and stiffness and damping coefficients. The results of the theoretical model, except the calculated stiffness and damping coefficients, are compared to experimental results available from the literature and a good agreement is generally observed. The stiffness and damping coefficients are compared to similar theoretical results and a good agreement is observed. Two boundary conditions, b.c.1 and b.c.2, are compared. Whether b.c.1 or b.c.2 is the more appropriate boundary condition is ambiguous. It depends on the compliant foil configuration, in the sense that if the top foil is thick and rigid, the b.c.2 will most likely lead to the most accurate results, but if the top foil is thin and flexible, as is the case for the bearing treated in this study, it will be b.c.1 which will be the most appropriate choice. To eliminate the need for the implicit boundary conditions, b.c.1 and b.c.2, a detailed mathematical model of the foil structure should be established and coupled with the solution of the Reynold's equation. In this way, the foil radial flexibility and its radial deformation at any foil position (θ, z) should be dependent on the radial deformation in neighbouring positions. Such a modelling improvement will be theoretically investigated in the near future.

The implementation of the mathematical model presented in this paper is straight forward and the convergence is generally good. For large eccentricities though, a modified Newton-Raphson scheme can be applied with success.

Acknowledgment

This study is a part of the industrial Ph.d. program. The author acknowledge the support from Siemens A/S - Turbomachinery Solutions and the Danish government '*Styrelsen for Forskning og Inovation*'.

REFERENCES

[1] M. Carpino and G. Talmage. Prediction of rotor dynamic coefficients in gas lubricated foil journal bearings with corrugated sub-foils. *Tribology Transactions*, 49(3):400–409, 2006.

[2] R. D. Cook. *Concepts and applications of finite element analysis*. John Wiley, New York, 2007.

[3] C. Dellacorte, V. Lukaszewicz, M. J. Valco, K. C. Radil, and H. Heshmat. Performance and durability of high temperature foil air bearings for oil-free turbomachinery. *Tribology Transactions*, 43(4):774–780, 2000.

[4] C. DellaCorte and M. J. Valco. Load capacity estimation of foil air journal bearings for oil–free turbomachinery applications. *Tribology Transactions*, 43:795–801, 2000.

[5] B. J. Hamrock. *Fundamentals of Fluid Film Lubrication*. McGRAW-HILL Series in Mechanical Engineering. McGRAW-HILL, Inc., New York, 1994.

[6] H. Heshmat. Advancements in the performance of aerodynamic foil journal bearings: High speed and load capability. *Journal of Tribology*, 116(2):287–294, 1994.

[7] H. Heshmat, J. A. Walowit, and O. Pinkus. Analysis of gas lubricated compliant thrust bearings. *Journal of Lubrication Technology*, 105(4):638–646, 1983.

[8] H. Heshmat, J. A. Walowit, and O. Pinkus. Analysis of gas-lubricated foil journal bearings. *Journal of Lubrication Technology*, 105(4):647–655, 1983.

[9] J. F. Walton II, H. Heshmat, and M. J. Tomaszewski. Design and test program in the development of a 100 hp oil-free, high-speed blower. In *Proceedings of ASME Turbo Expo*, 2007.

[10] D. Kim. Parametric studies on static and dynamic performance of air foil bearings with different top foil geometries and bump stiffness distributions. *Journal of Tribology*, 129(2):354–364, 2007.

[11] T. H. Kim and L. San Andrés. Heavily loaded gas foil bearings: A model anchored to test data. *ASME Conference Proceedings*, 2005(47276):763–771, 2005.

[12] C. P. Roger Ku and H. Heshmat. Compliant foil bearing structural stiffness analysis: Part i–-theoretical model including strip and variable bump foil geometry. *Journal of Tribology*, 114(2):394–400, 1992.

[13] S. Le Lez, M. Arghir, and J. Frene. A dynamic model for dissipative structures used in bump-type foil bearings. *Tribology Transactions*, 52(1):36–46, 2008.

[14] J. W. Lund. Calculation of stiffness and damping properties of gas bearings. *Journal of Lubrication Technology*, pages 793–804, 1968.

[15] J.-P. Peng and M. Carpino. Calculation of stiffness and damping coefficients for elastically supported gas foil bearings. *Journal of Tribology*, 115(1):20–27, 1993.

[16] J.-P. Peng and M. Carpino. Finite element approach to the prediction of foil bearing rotor dynamic coefficients. *Journal of Tribology*, 119(1):85–90, 1997.

[17] Z.-C. Peng and M. M. Khonsari. Hydrodynamic analysis of compliant foil bearings with compressible air flow. *Journal of Tribology*, 126(3):542–546, 2004.

[18] J. W. Powell. A review of progress in gas lubrication. *Review of Physics and Technology*, 1(2):96, 1970.

[19] K. C. Radil and C. Dellacorte. The effect of journal roughness and foil coatings on the performance of heavily loaded foil air bearings. *Tribology Transactions*, 45(2):199–204, 2002.

[20] D. Ruscitto, J. Mc Cormick, and S. Gray. Hydrodynamic air lubricated compliant surface bearing for an automotive gas turbine engine i - journal bearing performance. Technical Report NASA CR-135368, 1978.

[21] L. San Andrés and T. H. Kim. Thermohydrodynamic analysis of bump type gas foil bearings: A model anchored to test data. *Journal of Engineering for Gas Turbines and Power*, 132(4):042504, 2010.

[P2] Numerical and experimental investigation of bump foil mechanical behaviour

This paper was submitted to the journal *Tribology International* in November 2013 and published online 18 February, 2014.

Tribology International 74 (2014) 46–56

Contents lists available at ScienceDirect

Tribology International

journal homepage: www.elsevier.com/locate/triboint

Numerical and experimental investigation of bump foil mechanical behaviour

Jon S. Larsen [a,b], Alejandro C. Varela [a], Ilmar F. Santos [a,*]

[a] Department of Mechanical Engineering, Technical University of Denmark, 2800 Kgs. Lyngby, Denmark
[b] Siemens A/S - Aeration Competence Centre, 3000 Helsingør, Denmark

ARTICLE INFO

Article history:
Received 26 November 2013
Received in revised form
4 February 2014
Accepted 10 February 2014
Available online 18 February 2014

Keywords:
Gas foil bearing
Foil structure
Finite element method
Hysteresis

ABSTRACT

Corrugated foils are utilised in air foil bearings to introduce compliance and damping thus accurate mathematical predictions are important. A corrugated foil behaviour is investigated experimentally as well as theoretically. The experimental investigation is performed by compressing the foil, between two parallel surfaces, both statically and dynamically to obtain hysteresis curves. The theoretical analysis is based on a two dimensional quasi static FE model, including geometrical non-linearities and Coulomb friction in the contact points and neglects the foil mass. A method for implementing the friction is suggested. Hysteresis curves obtained via the FE model are compared to the experimental results obtained. Good agreement is observed in the low frequency range and discrepancies for higher frequencies are thoroughly discussed.

1. Introduction

The static and dynamic characteristics of compliant foil bearings are determined by the behaviour of the fluid film and a flexible element underneath the bearing surface altering its compliance. Several configurations are possible to obtain compliance, being the usage of corrugated bump foils one of the most widely used. The addition of these compliant elements into the design enables to introduce additional damping to the one generated in the fluid film. The increase of the energy dissipation is obtained due to the sliding friction forces, generated as the bearing surface deforms and induces displacements in the foil layers. However, the mechanism for obtaining the additional damping characteristics exhibits highly non-linear behaviour, which introduces significant complexities considering the obtention of an acceptable level of predictability for this bearing design.

The challenges related to the technology have generated a significant number of publications, dealing with the theoretical modelling and experimental testing of bump foil bearings. The presentation given here tries to follow a chronological progression, and focusses on the ones that have influenced the development of the work presented in this paper. Namely, the isolated static and dynamic characterisation of the corrugated foil structure by neglecting the fluid film effects.

Ku and Heshmat [1–3] presented an analytical mathematical bump foil model based on the work of Walowit and Anno [4]. The model considered a circular bearing and took into account the effect of the pad location. The model provided predictions for stiffness, hysteresis and equivalent viscous damping. Non-linear stiffness behaviour was attributed to the geometrical effects of having a circular journal loading the foils. They predicted that the dynamic coefficients were anisotropic and highly non-linear and that the stiffness and damping were dependant on the pad angle. Bump stiffness under different load distributions along the bump strip was also investigated [1] and the theoretical prediction followed the trend of earlier experimental data, regarding the higher stiffness of the bumps located at the fixed end compared to those closer to the free end. Lower friction coefficients were found to make bumps softer, whereas an increment in friction increased the stiffness and could result in pinned bump ends for the bumps close to the fixed end.

Experimental results of hysteresis curves for bump strips deformed between two straight surfaces were presented in [5]. One of the surfaces featured a pivot to enable tilting motion, in order to obtain different load distributions over the foils. The effect of pivot location and different surface coatings was investigated and the bump deflections were recorded using an optical tracking system. 'Local' stiffness and damping were identified and found to be dependant on amplitude and load.

Peng and Carpino [6] were among the first ones to couple the bump structure with the fluid film in a mathematical model. Coulomb friction forces and bump flexibility were included by means of an equivalent continuous friction force and a spring

* Corresponding author.
E-mail addresses: josla@mek.dtu.dk (J.S. Larsen), acer@mek.dtu.dk (A.C. Varela), ifs@mek.dtu.dk (I.F. Santos).

http://dx.doi.org/10.1016/j.triboint.2014.02.004
0301-679X

Nomenclature

A	area
E	modulus of elasticity of foil
F_n	normal force in contact point
F_μ	friction force in contact point
K	foil stiffness
L_0	initial length
L_1	current length
N^e	element force
Q	foil flexibility
S	bump foil pitch
V	volume
W	vertical load on foil strip
$\tilde{w_0}$	dimensionless foil deflection
e	element
h_0	bump foil height
k	spring stiffness
l_0	bump half length
t_b	thickness of bump foil
u, v	nodal deformations
w_b	width of bump foil
x, y	Cartesian coordinates
x_r	relative deflection
ΔL	$L_1 - L_0$
Δu	$u_j - u_i$
Δu_s	shift
Δx	$x_j - x_i$
δ	variation
μ	coefficient of friction
ν	Poisson's ratio of foil
σ	stress
θ_0	bump angular extend
ε	strain
ε_s	smoothing factor
$\{B_0\}$	independent strain displacement vector
$\{D\}$	global displacement vector
$\{F\}$	surface traction vector
$\{P\}$	global load vector
$\{R_{ext}\}$	external residual vector
$\{R_{int}\}$	internal residual vector
$\{R\}$	residual vector
$\{\Phi\}$	body force vector
$\{\bar{B}\}$	strain displacement vector
$\{\sigma\}$	stress vector
$\{\mathbf{u}\}$	nodal displacements
$\{\varepsilon\}$	strain vector
$\{d\}$	local displacement vector
$\{p\}$	nodal load vector
$[K_t]$	tangential matrix

constant. Stiffness and damping coefficients were calculated using the coupled model. No isolated validation of the foil structural model was included in this work.

Ku and Heshmat [7,8] performed an experimental investigation of the dynamic behaviour of a compliant foil bearing and compared the results to the mathematical model presented in [1–3]. Agreement between the theoretical and experimental results was reasonably good. The results showed that the cross coupling stiffness and damping are negligible and that the direct terms decrease with increasing dynamic amplitude. An increase of the excitation frequency was found to decrease the equivalent viscous damping and to increase the stiffness.

Similar experiments were performed by Rubio and San Andres [9,10]. These authors compared the experimental results to the ones obtained using a simplified mathematical model, in which the bump foil contribution was represented by simple elastic springs. The stiffness of these springs was calculated by the analytical expression of Iordanoff [11]. Furthermore, the equivalent damping was determined experimentally, for a given bump geometry, by assuming a one DOF system to which the experimental data was fitted [12,13]. This method is based on the assumption of harmonic oscillations which can be hard to obtain in an experimental set-up. Temperature effects were also investigated [12] and found to be negligible. The dry friction coefficient was found to be nearly constant with the excitation frequency but dependent on the load amplitudes. The obtained friction coefficient values varied between 0.05 and 0.2.

An NDOF discrete bump formulation model including the effect of Coulomb friction was presented by Le Lez et al. [14,15]. The foil structural model was composed of simple spring elements with elementary stiffness given by analytical expressions. The results were compared to a detailed finite element (FE) model based on a commercial software as well as experimental data [14] with good agreement. Furthermore, the calculated stiffness was compared to the simple foil flexibility given by Walowit and Anno [4] and implemented in the simple elastic foundation model by Heshmat et al. [16,17]. The updated results were found to be significantly stiffer than the reference ones, due to the inclusion of the dry friction effect.

Lee et al. [18] presented a mathematical model incorporating both the fluid film pressure field described by the Reynolds equation and the structural dynamics of the foil structure. The solution was based on FEM analysis, and it was performed using a time domain integration routine. An algorithm to deal with the stick slip phenomenon related to friction forces was incorporated as well. A parametric study was performed and hysteresis loops were presented for the bearings running under steady state conditions. The dissipated energy for the individual bumps was calculated at a given unbalance. The study indicated that optimum values of bump stiffness and friction coefficients exist with regard to minimising the resonance vibration response of a rotor mounted on foil bearings.

Zywica [19,20] simulated the top foil structure using commercial FE programs and compared to results previously published in [10]. This structural model was applied in a complex model [21] taking into account the fluid film pressure by solving the Reynolds equation. The study was of purely theoretical nature.

Considering the literature background given here, this paper is focussed on the global, quasi-static and dynamic behaviour of a bump foil strip and the local behaviour in its individual sliding contact points. This is achieved through mathematical modelling and experimental observations. The study focusses on a bump foil strip, pressed between two parallel surfaces. This original approach enables a direct comparison between experimental and theoretical results. The structural mathematical model is based on the finite element method (FEM) and the virtual work principle, applied to the studied foil geometry. Hence, the entire bump foil strip is modelled explicitly, using non-linear large deformation theory. The Coulomb friction forces are modelled using an original approach, based on equivalent non-linear springs located in the contact points between the bump foils and the mating surfaces, acting in the direction of the bump longitudinal displacement. The model is set up so that the correct direction of the friction force at each contact point is directly obtained, eliminating the need for updating the forcing term. It was implemented in a dedicated computer program and the theoretical

results, concerning the quasi-static behaviour of the bump foils, are compared against results both from the literature, but mainly against the experimental data obtained in a test rig designed and built for this purpose.

2. Theoretical model

A theoretical model of the foil structure has been developed and implemented. It takes into account large bump foil deflections and Coulomb sliding friction. The model is based on a non-linear FE procedure following the iterative Newton–Raphson (NR) approach derived in Appendix A. The foil structure is discretised following the virtual work principle (VWP) and a bilinear quadrilateral (Q4) iso-parametric plain strain element and the Green–Lagrange strain measure for large displacements are implemented.

The mathematical model is quantified in terms of the residual vector $\{R\}$ and the tangent matrix $[K_t]$ which, combined with the NR approach, solves for the displacement vector $\{D\}$. With the exception of the friction elements, the derivation of these quantities is thoroughly described in the literature [22,23] and for the sake of briefness omitted here.

2.1. Modelling friction

The reaction force between two contacting bodies can be decomposed in two forces; the normal force F_n and the friction force F_μ. If Coulomb friction law is assumed and the static and dynamic friction coefficients are equal, the friction force F_μ can be written as

$$F_\mu = \begin{cases} F_n\mu & \text{if } \dot{x}_r < 0 \\ -F_n\mu & \text{if } \dot{x}_r > 0 \end{cases} \tag{1}$$

and

$$-F_n\mu \le F_\mu \le F_n\mu \quad \text{if } \dot{x}_r = 0 \tag{2}$$

where $\dot{x}_r$ is the relative sliding velocity in the contact point and μ is the coefficient of friction. Consequently, the friction force F_μ is a function of the sliding velocity $\dot{x}$ and is continuous but non-linear. It could be included in the FE model as a nodal load, illustrated in Fig. 1a, in which case, the magnitude and sign of the force would be unknown unless an iterative procedure with checks for sliding direction i.e. sign of $\dot{x}_r$ and updates of the nodal reaction force F_n were introduced.

An alternative method is to add a spring in the point of contact as illustrated in Fig. 1b. The first thing to note when considering this method is, that the problem of determining the sign of the force F_μ is eliminated since the reaction force of the spring k will automatically be in the opposite direction of the motion $\dot{x}_r$. The magnitude of the reaction force would not be constant if the spring k is linear though. Then it would increase linearly with the movement of the contact point, which is obviously wrong. However, by choosing the stiffness k to be non-linear and softening, the reaction force versus deflection can be made constant and fulfilling (1). Choosing a proper stiffness function for k, can even eliminate the problem of determining the magnitude of the friction force F_μ when there is no motion $\dot{x}_r = 0$. This corresponds to (2).

2.1.1. Non-linear spring element

The objective is to derive a non-linear spring element to be used in the implicit incremental NR scheme, which will mimic the behaviour of a friction force. The schematics and nomenclature of the spring are illustrated in Fig. 2.

The VWP for a general elastic body may be stated as [23,22]:

$$\int_V \{\delta\varepsilon\}^T\{\sigma\}\,dV = \int_A \{\delta\mathbf{u}\}^T\{F\}\,dA + \int_V \{\delta\mathbf{u}\}^T\{\Phi\}\,dV + \sum_i \{\delta\mathbf{u}\}_i^T\{p\}_i. \tag{3}$$

Assuming body forces negligible and writing the internal work as a summation over the elements and assuming the external forces are only applied in nodes (i.e. $\{\Phi\} = \{0\}$ and $\{F\} = \{0\}$) and given by the global force vector $\{P\}$, the VWP can be reduced to

$$\sum_e \int_{V_e} \delta\varepsilon\sigma\,dV = \{\delta D\}^T\{P\} \tag{4}$$

where displacements are described by the element nodal displacement vector $\{d\}$ or the global displacement vector $\{D\}$. Assuming the stress and strains are constant in each spring element, the integral on the left hand side of (4) can be evaluated as

$$\sum_e \delta\varepsilon N^e L_0^e = \{\delta D\}^T\{P\} \tag{5}$$

where the element forces are defined as $N^e = \varepsilon L_0^e k^e$ in which $k^e(\varepsilon)$ is a general non-linear stiffness dependent on the strain and L_0^e is the initial length of the element e. The strain variations for each

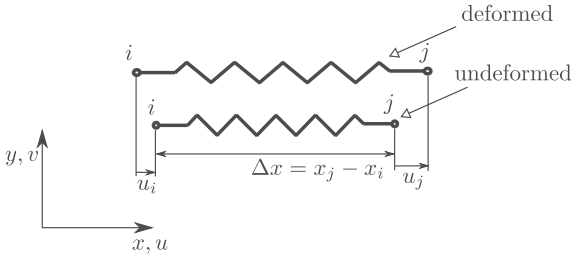

Fig. 2. Deformed and undeformed one dimensional spring.

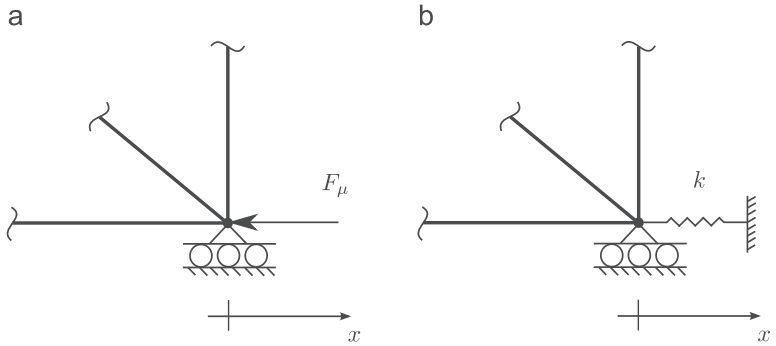

Fig. 1. (a) Modelling friction with a nodal load F_μ. (b) Modelling friction by use of a non-linear spring $k(\varepsilon)$.

element are related to the displacement variations by

$$\delta\varepsilon = \{\overline{B}\}^T\{\delta d\} \tag{6}$$

where $\{\overline{B}\}$ is the strain–displacement vector. The strain–displacement vector can now be found by use of the Cauchy strain assumption $\varepsilon = \Delta L/L_0$. If the vertical and horizontal displacements of the two nodes, i and j (Fig. 2), are described by the vector

$$\{d\} = \{u_i \;\; v_i \;\; u_j \;\; v_j\}^T \tag{7}$$

then the strain in the spring element can be written as

$$\varepsilon = \frac{L_1 - L_0}{L_0} = \frac{(x_j - u_j) - (x_i - u_i) - (x_j - x_i)}{(x_j - x_i)} = \frac{\Delta u}{\Delta x} \tag{8}$$

where $\Delta u = u_j - u_i$. By use of (7) and (8), the strain can now be written as

$$\varepsilon = \{d\}^T \frac{1}{L_0}\{-1 \;\; 0 \;\; 1 \;\; 0\}^T = \{d\}^T\{B_0\} \tag{9}$$

where the strain displacement vector $\{B_0\}$ is independent of the displacements and hence it is given the zero subscript. The variation in strain (6) then becomes $\delta\varepsilon = \{\delta d\}^T\{B_0\}$, which inserted into (5) gives

$$\sum_e \{\delta d\}^T\{B_0\}N^e L_0^e = \{\delta D\}^T\{P\}. \tag{10}$$

The VWP should hold for any virtual displacements which means that (10) reduces to

$$\sum_e \{B_0\}N^e L_0^e = \{P\} \tag{11}$$

which can be put on residual form as

$$\{R\} = \{R_{int}\} - \{R_{ext}\} = \sum_e \{B_0\}N^e L_0^e - \{P\} = \{0\} \tag{12}$$

and from the definition of the tangent stiffness matrix we have

$$[K_t] = \frac{\partial\{R\}}{\partial\{D\}} = \sum_e \{B_0\}\frac{\partial N^e}{\partial\varepsilon}\frac{d\varepsilon}{\partial\{D\}}L_0^e = \sum_e \{B_0\}\{B_0\}^T L_0^e \frac{\partial N^e}{\partial\varepsilon} \tag{13}$$

where $\partial N^e/\partial\varepsilon = L_0^e k^e(\varepsilon)$. Finally, the tangent stiffness matrix becomes

$$[K_t] = \sum_e \{B_0\}\{B_0\}^T L_0^e 2k^e(\varepsilon). \tag{14}$$

2.1.2. Choosing a spring stiffness function

From the definition of the strain–displacement vector (9), it is seen that the length of the spring L_0^e cancels out from the tangent matrix (14). Therefore, it is convenient to redefine the non-linear element stiffness k^e to be dependent on the displacement rather than the strain such that the length L_0^e is eliminated in the element definition. A suitable element stiffness function is

$$k^e(\Delta u) = \frac{F_n\mu}{|\Delta u| + \varepsilon_s} \tag{15}$$

where ε_s is introduced to avoid zero division and to obtain a smoothing element force curve. The element stiffness and force curves are illustrated in Fig. 3.

Examining the element force curve $N^e(\Delta u)$ in Fig. 3, it is clear that the stiffness function (15) is a good choice as it produces a force curve very similar to that of a friction force. The optimal value of ε_s depends on the amount of movement in the sliding contact. For small movements ε_s should be chosen small. Choosing too small values, the convergence of the incremental solver will be affected negatively and choosing too large values will affect the accuracy of the solution. A good choice (according to Fig. 3) is $\varepsilon_s \approx \Delta u_{max}/100$.

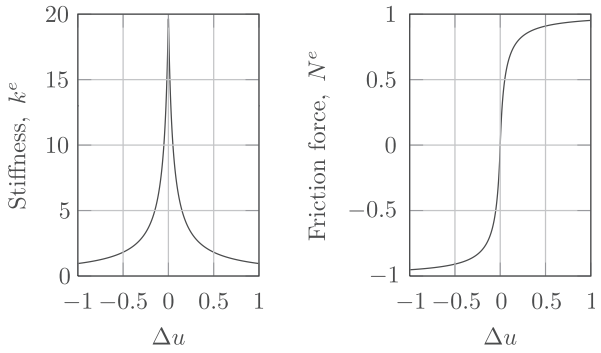

Fig. 3. Element stiffness and force curves for $F_n\mu = 1$ and $\varepsilon_s = 0.05$.

The theory presented will enable the modelling of sliding friction for several contact points in an FE model. Independent of the sliding direction in each point, the resulting friction force will have the correct sign. However, this is under the assumption that the sliding does not change direction for $\Delta u \neq 0$. To assure the correct sign of the friction force a 'shift' is introduced such that

$$k^e(\Delta u - \Delta u_s) = \frac{F_n\mu}{|\Delta u - \Delta u_s| + \varepsilon_s} \tag{16}$$

where Δu_s is set to Δu in the event of changing sliding direction.

2.1.3. Assumptions and limitations

The solution is quasi-static meaning that all frequency dependencies are discarded. The friction model is a Coulomb model and coefficients of friction are assumed constant and static and dynamic friction is equal.

3. Theoretical results – validation

In the following, bump foil strips with varying number of bumps are analysed using the numerical method, outlined in the previous section, and compared to analytical results. The geometry and nomenclature of the bump foils are illustrated in Fig. 4 and Table 1. For foil strips consisting of more than one bump, all bumps are given the same deflections.

Walowit and Anno [4] gave an analytical expression for the dimensionless deflection $\tilde{w}_0$, of the centre position of a single bump, when subjected to a vertical load W. They assumed the bump ends free to rotate and move horizontally but restrained in the vertical direction. This analytical expression is compared to results obtained from an equivalent FE model as illustrated in Fig. 5.

A mesh convergence study of the model showed, that sufficient accuracy may be obtained by having 8 layers of elements over the thickness and approximately 400 elements over the longitudinal direction.

The dimensionless deflection $\tilde{w}_0$, calculated analytically and numerically, is illustrated in Fig. 6 for different angular extends θ_0 of the bump and for varying coefficients of friction μ. Good agreement between the analytical and numerical results is observed for friction coefficients up to $\mu \approx 0.5$. Discrepancies begin to occur at $\mu > 0.5$. However, the numerical analysis is not subjected to the same limiting assumptions as the analytical like e.g. longitudinal deflection correction [4].

Walowit and Anno [4] also derived an analytical expression for the foil flexibility which is commonly used together with 'the

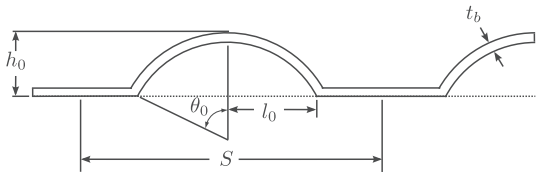

Fig. 4. Bump foil geometry and nomenclature.

Table 1
Geometry and material properties of the bump foil.

Parameters	Values
Bump foil thickness, t_b	0.127 mm
Bump foil height, h_0	0.9 mm
Bump foil pitch, S	7.00 mm
Bump half length, l_0	3.30 mm
Bump foil width, w_b	18 mm
Young's modulus of bump foil, E	2.07×10^{11} Pa
Poisson's ratio of bump foil, ν	0.3
Coefficient of friction, μ	0.20

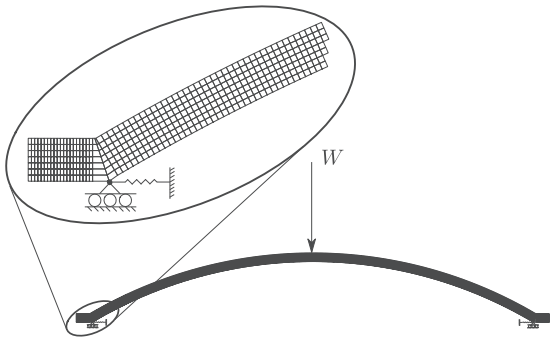

Fig. 5. Finite element model and applied boundary conditions for numerical comparison to analytical results from Walowit and Anno [4].

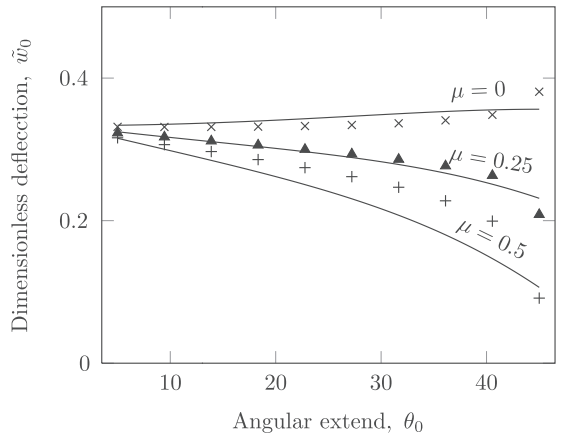

Fig. 6. Single bump dimensionless deflection; analytical results (full lines) [4], numerical results (markers).

simple elastic foundation model' [16,17]. It is given as

$$Q \approx \frac{2S}{E}\left(\frac{l_0}{t_b}\right)^3 (1-\nu^2) \tag{17}$$

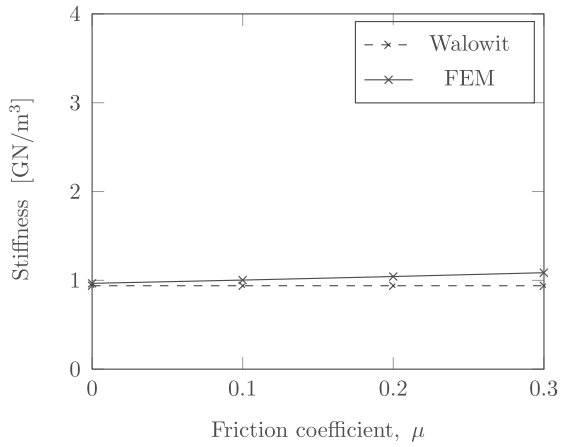

Fig. 7. Stiffness of a single bump numerically calculated as a function of varying coefficients of friction – comparison to analytical results of Walowit and Anno [4].

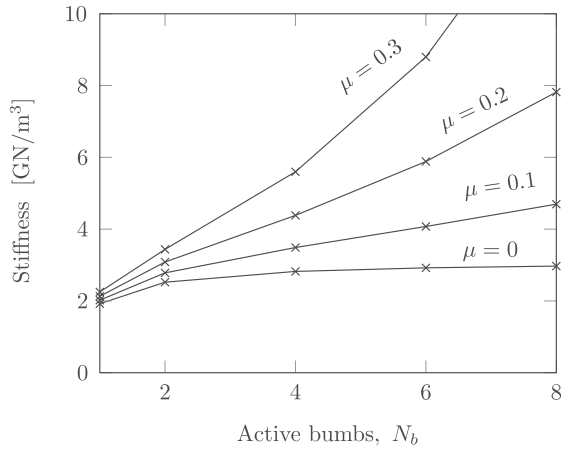

Fig. 8. Stiffness calculated numerically – varying coefficients of friction and number of bumps in the foil strip.

and consequently, the stiffness per area is $K = 1/Q$. Comparing this stiffness to the results of the numerical model of a single bump, as illustrated in Fig. 7, yields good agreement for varying coefficient of friction.

For the case of more than one bump and with the bump strip fixed in one end, the stiffness calculated numerically is diverging significantly from the analytical result [4]. This is illustrated in Fig. 8 and in accordance with e.g. [1,5,15–18]. The stiffness, predicted by the numerical procedure, is unequal during loading and unloading for $\mu \neq 0$. Fig. 8 is based on the loading process and the difference between loading and unloading is clearly illustrated in Fig. 9, which displays a load displacement diagram for $\mu = 0.1$ and $\mu = 0.2$. Here, a strip with four bumps is simulated by giving all bumps a gradual compression to approximately 25 μm with small oscillations of 1.5 μm amplitude occurring at approximately 5, 10, 15, 20 μm during the loading process. The particular bump foil geometry was designed for a journal bearing having a clearance of 50 μm, meaning that a compression of 25 μm would result in a bearing eccentricity ratio of approximately 1.5, which is a common value. The stiffness, related to the small 'local' hysteresis loops contained in the large 'global' hysteresis loop, is referred to as the local stiffness. It is found to be non-linear and significantly higher than the global. This is in good agreement with previous experimental studies performed by Ku and Heshmat [5].

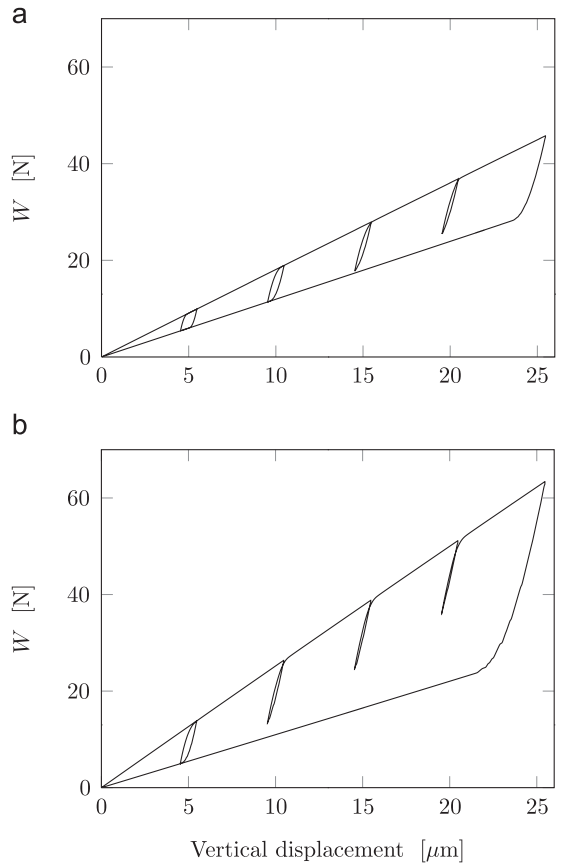

Fig. 9. Theoretical results of a bump strip, given a global compression of approximately 25 μm with local oscillations of 1.5 μm amplitude occurring at approximately 5, 10, 15, and 20 μm during the loading process. (a) Using a coefficient of friction $\mu = 0.1$. (b) Using a coefficient of friction $\mu = 0.2$.

The hysteresis loops cause the bump foil strip to provide Coulomb damping proportional to its confined area. The size of the confined area is dependent on where at the global hysteresis curve the deflection oscillation is taking place (5, 10, 15 or 20 μm). If the deflection is sufficiently large, the load versus displacement will track the global hysteresis curve during the unloading process. This situation is seen in Fig. 9a, for the oscillation around 5 μm. In this case, the confined area grows significantly leading to more Coulomb damping, and the stiffness becomes highly non-linear, as it changes significantly at the points where the local load–displacement coincide with the global hysteresis loop. Tracking the global hysteresis curve corresponds to the situation where all contact points are sliding.

This can be seen in Fig. 10. Here a strip of four bumps, as illustrated in Fig. 10a, is subjected to displacement oscillations upon given a compression of 20 μm. The displacement oscillations are of amplitudes 1, 3, and 5 μm and the corresponding hysteresis curve is seen in Fig. 10b. In Fig. 10c, the friction forces versus the horizontal displacement for five selected contact points are illustrated. These hysteresis loops visually illustrate the amount of energy dissipation taking place in each of the selected contact points. For the low amplitude of 1 μm (green line), it is clear that the movement in sliding points #1 through #5 is zero, meaning that energy is only dissipated in the contact points #6, #7, and #8. For the higher amplitudes of 3 μm and 5 μm (red and blue lines

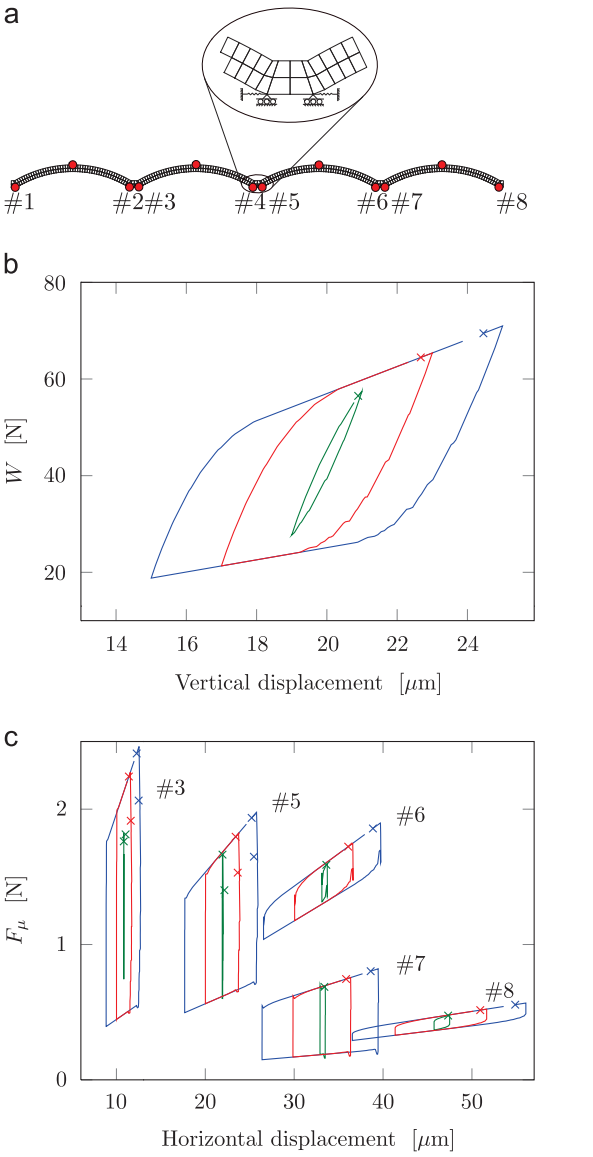

Fig. 10. (a) Bump foil strip. Contact points including friction marked with a red dot. The foil thickness is magnified for illustration purpose. (b) Local hysteresis curves for different load amplitudes. (c) Friction force versus horizontal deflection in selected contact points. (For interpretation of the references to colour in this figure caption, the reader is referred to the web version of this paper.)

respectively) all the points are sliding when the local load–displacement curves (Fig. 10b) track the global curve.

It is important to highlight how a relatively small increase in the load amplitude, from 15 N to 20 N, will increase the energy dissipation by approximately 10 times and at the same time, the energy dissipation only doubles for an amplitude increase from 20 N to 25 N. This is a consequence of the left most bumps being pinned for the lowest load amplitudes, and it illustrates the importance of the bump geometry and friction properties in terms of maximising the energy dissipation. For instance, the dissipated energy would have been much higher, for an amplitude of 15 N, if the coefficient of friction had been lower, since this would have prevented bumps from being pinned.

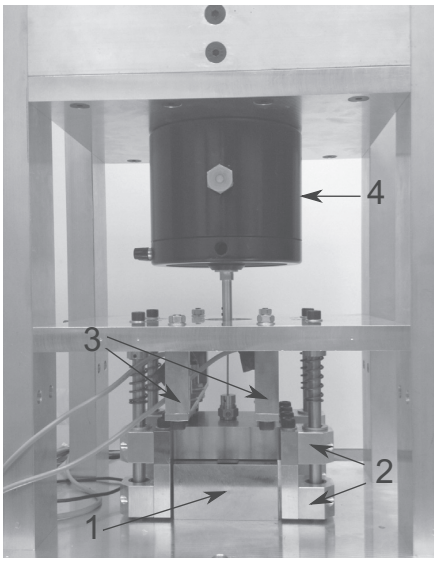

Fig. 11. Test setup for characterising the static and dynamic properties of the bump foil.

4. Experimental results

In order to validate the implemented numerical model of the bump foil, its results are compared to experimental results. In this section, the focus is set on the static as well as the dynamic behaviour of the bump foil. The data is obtained using an experimental test rig at the Technical University of Denmark (DTU), designed and constructed specifically for this purpose.

4.1. Experimental setup at DTU

The test rig used for characterising the bump foil behaviour can be seen in Fig. 11. This test rig enables us to study the static and dynamic characteristics of the bump foils.

The core of the setup is composed by two steel blocks (FE 510 D, ISO 630), labelled number 1 in Fig. 11. The upper block features linear ball bearings that follow four vertical guiding rods, see number 2 in Fig. 11. Two bearings are mating with each guiding rod. This arrangement enables the upper block to move vertically minimising tilting motion, while the lower block is fixed to the base. The tested foil strip is placed in between the parallel mating surfaces of these blocks. One of the foil strip ends is clamped and the other one is free.

The arrangement enables us to relate directly the vertical displacement of the upper block with the deflections of the bumps of the foil strip tested. The displacements are measured using three displacement probes looking at the upper surface of the moving block, see number 3 in Fig. 11. The sensors are located in a 'triangle' arrangement, to detect if any undesired tilting motion is taking place during the experimental tests. The upper block can be loaded statically or dynamically, in order to induce deflections of the foil strip placed underneath. Static load is applied by means of calibrated weights, whereas dynamic load is obtained by using an electromagnetic shaker, a steel stinger with a diameter of 2 mm and a piezoelectric load cell, see number 4 in Fig. 11.

4.2. Static results

The test rig was used to obtain experimental results regarding the relationship between applied static load and resulting deflection of the bump foil. The geometry and material properties of the tested foil are listed in Table 1 and the foil material is Inconel X750 hardened for maximum yield stress. A foil specimen originally consisting of 10 bumps was progressively shortened down to 8, 6, 4 and 2 bumps. For each configuration, five full load cycles (loading and unloading) were performed. The standard deviation of the measured deflections was calculated, in order to check the influence of random errors over the results. The largest uncertainty interval obtained is 8 μm and the lowest one is 2 μm. The uncertainty intervals are not included in the figures to avoid overcrowding.

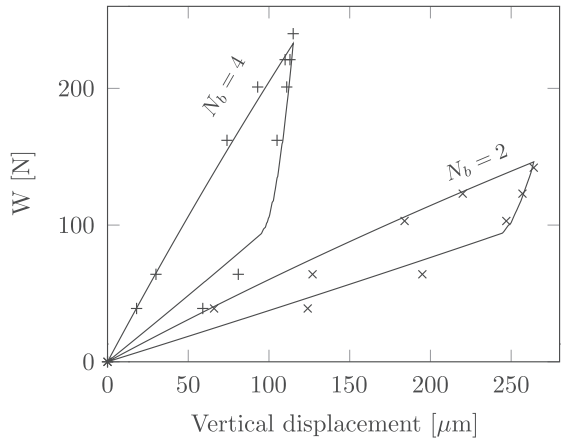

Fig. 12. Hysteresis loops for two and four bump strips; numerical results using $\mu = 0.2$ (full lines), experimental results (markers).

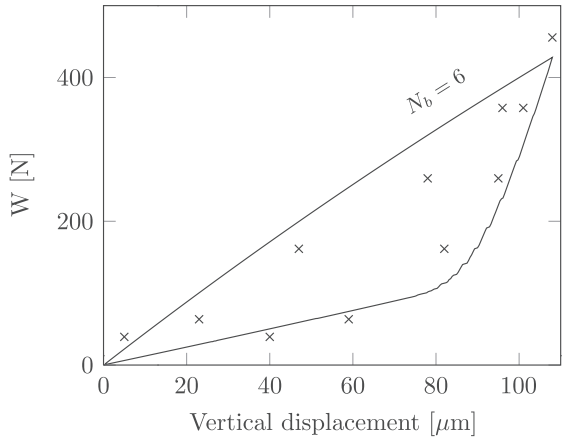

Fig. 13. Hysteresis loops for a six bump strip; numerical results using $\mu = 0.2$ (full lines), experimental results (markers).

The results obtained with strips of two and four bumps are compared to theoretical results and illustrated in Fig. 12 and the results of a strip with six bumps are illustrated in Fig. 13.

Good agreement between the experimental and theoretical results is found when using a coefficient of friction $\mu = 0.2$ for the simulations. This value corresponds well with common values which is typical in the range $0.1 < \mu < 0.5$ for steel against steel (0.5 in vacuum) and also with the results obtained by e.g [5,12]. For strips with higher number of bumps, higher global stiffness and larger discrepancies with theoretical results are observed. The results obtained for a strip with 6 bumps, see Fig. 13, portray these trends. The discrepancies can be attributed to geometrical imperfections of the foils, specifically different bump heights, that entail that not all

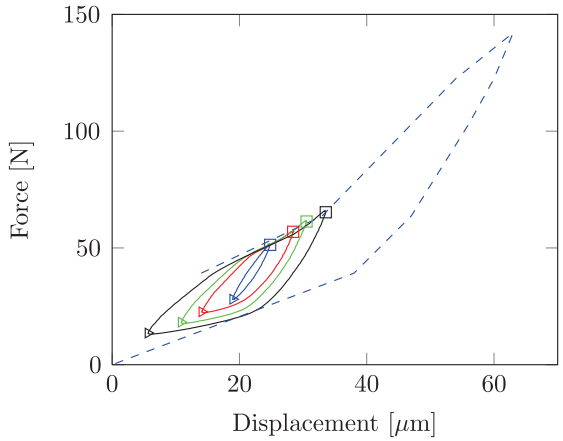

Fig. 14. Comparison of the static (dashed blue line) and dynamic testing results, for different displacement amplitudes (2 (blue), 4 (red), 8 (green), 12 (black) microns). The applied load frequency is 1 Hz. The preload is 40 N, and the foil strip contains 4 bumps. (For interpretation of the references to colour in this figure caption, the reader is referred to the web version of this paper.)

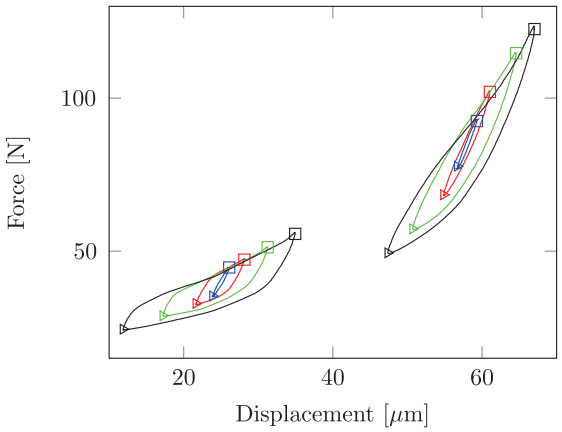

Fig. 15. Results of the dynamic testing, for different displacement amplitudes (2 (blue), 4 (red), 8 (green), 12 (black) microns). The applied load frequency is 1 Hz. The preloads are 40 N and 90 N. The foil strip contains 3 bumps. (For interpretation of the references to colour in this figure caption, the reader is referred to the web version of this paper.)

bumps are in contact with the mating surface from the beginning of the loading cycle. This effect becomes more relevant for higher number of bumps. Similar trends are observed when testing strips of 8 and 10 bumps.

4.3. Dynamic results

The next set of experimental results deals with the effect of applied load frequency over the hysteresis curves. A static preload and a dynamic load are simultaneously applied on the foil strip. The preload was adjusted to 40 N and 90 N, in order to study the effect of this parameter over the obtained results. Regarding the dynamic load, a sine wave of fixed amplitude and frequency was fed into the electromagnetic shaker in order to induce the foil deflections. The amplitude of the dynamic load was tuned to obtain different displacement amplitudes for the hysteresis cycles. Hence, results for 2 (blue), 4 (red), 8 (green), 12 (black) microns of displacement amplitude are obtained.

The reported applied force over the foil specimen is determined as the summation of the preload, the value measured by the piezoelectric load cell associated with the shaker stinger, plus the inertia force coming from the upper steel block, quantified using a piezoelectric accelerometer. The deflections are measured using the displacement probes. The reported hysteresis curves are obtained by averaging the loading cycles obtained over a 1 min long test. Repeatability was checked by repeating the test five times, with different foil specimens, obtaining similar results. Variability of the results was on the same order of magnitude as the one registered for the static testing.

In order to check for the influence of the test rig arrangement on the measured hysteresis curves, the foil specimen was replaced with a coil spring. Assuming that the damping contribution from this element is negligible, the setup enabled to determine the baseline damping coming from the test rig. Up to 60 Hz of excitation frequency, such effect was found to be negligible, compared with the energy dissipation observed when the foil specimen was tested.

The first set of results compares the static and dynamic testing results obtained for a four bump foil strip, see Fig. 14. The static results are obtained by loading the foil using calibrated weights, whereas the dynamic ones correspond to a preload of 40 N and a dynamic loading frequency of 1 Hz. The amplitude of the dynamic loading is tuned to obtain four different displacement amplitudes. Although the results obtained with a loading frequency of 1 Hz do not have relevance from the practical point of view, they do enable to establish a direct link between the static results shown in the previous section and the dynamic ones presented here.

In Fig. 14, the local hysteresis curves follow an almost purely harmonic motion for small displacement amplitude, and they are placed inside the global loop. However, when the displacement amplitude surpasses a threshold value, they start to track the global hysteresis curve. For that condition, two stages can be easily recognised in both the loading and unloading path of the cycle, characterised by two different slopes for the curve. These results are qualitatively coincident with the results from the quasistatic theoretical model shown before in Fig. 10b, regarding the dependence of the hysteresis loop shape on the motion amplitude. According to the theoretical model, the 'high slope' behaviour can be explained by the fact that some bumps of the strip are sticking, hence the stiffness is dominated by elastic deformation of the bumps. When they start to slide, the hysteresis path switches to a 'low slope' behaviour, where the stiffness is dominated by the friction forces.

Since the local hysteresis curves are amplitude dependant, both the stiffness and damping properties are strongly influenced by it. Even though for small motion amplitude it could be possible to assume that the resulting foil displacement is harmonic, once the local curve hits the global one a highly non-linear motion is achieved. This behaviour could have significant effects when calculating an equivalent linearised damping coefficient based on the energy dissipated during one local hysteresis cycle, since such analysis is based on assuming pure harmonic motion for the load displacement curve.

In order to check for loading frequency dependency of the observed local hysteresis curves, the results for a strip containing 3 bumps were obtained. Two different preloads are applied, and the loading frequency is set to 1 Hz, 10 Hz, 20 Hz, 40 Hz. The loading frequencies tested here are well below the first resonant frequency of the setup, which is around 100 Hz. Although the studied frequency range might seem quite limited when compared to the broad frequency range in which an industrial bump foil bearing operates, a distinctive modification in the overall behaviour of the hysteresis loops is already observed within the studied range. Furthermore, the maximum frequency for performing the dynamic testing is limited by the natural frequency of the setup

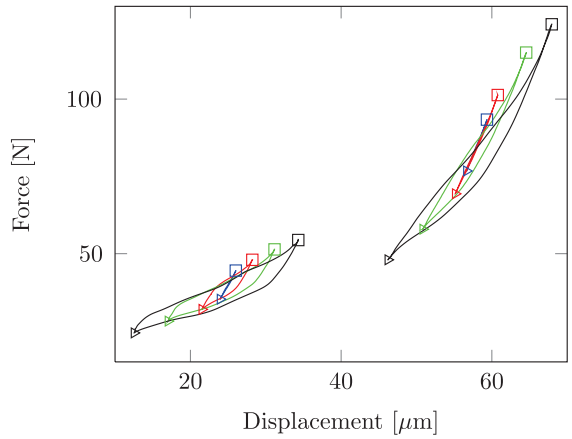

Fig. 16. Results of the dynamic testing, for different displacement amplitudes (2 (blue), 4 (red), 8 (green), 12 (black) microns). The applied load frequency is 10 Hz. The preloads are 40 N and 90 N. The foil strip contains 3 bumps. (For interpretation of the references to colour in this figure caption, the reader is referred to the web version of this paper.)

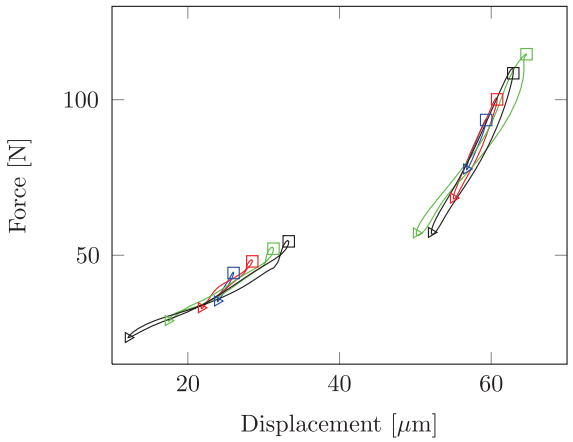

Fig. 18. Results of the dynamic testing, for different displacement amplitudes (2 (blue), 4 (red), 8 (green), 12 (black) microns). The applied load frequency is 40 Hz. The preloads are 40 N and 90 N. The foil strip contains 3 bumps. (For interpretation of the references to colour in this figure caption, the reader is referred to the web version of this paper.)

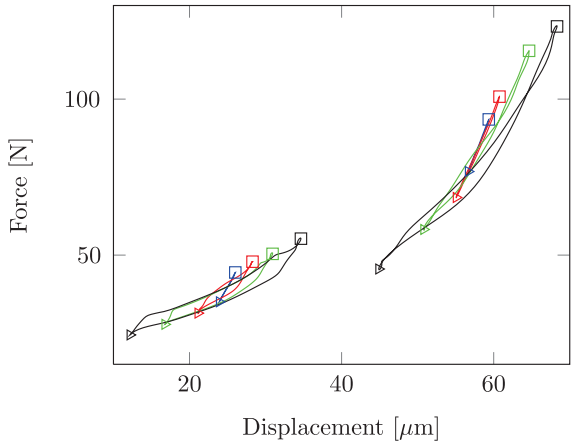

Fig. 17. Results of the dynamic testing, for different displacement amplitudes (2 (blue), 4 (red), 8 (green), 12 (black) microns). The applied load frequency is 20 Hz. The preloads are 40 N and 90 N. The foil strip contains 3 bumps. (For interpretation of the references to colour in this figure caption, the reader is referred to the web version of this paper.)

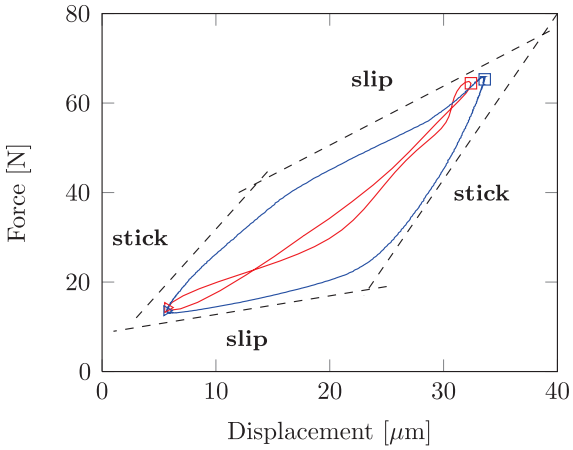

Fig. 19. Comparison of results for the dynamic testing: local hysteresis loop measured for loading frequency 1 Hz (blue) and 40 Hz (red). The foil strip contains 3 bumps and the preload is 40 N. (For interpretation of the references to colour in this figure caption, the reader is referred to the web version of this paper.)

and by the influence of the baseline damping generated by the test rig itself, as discussed previously.

The results obtained for a loading frequency of 1 Hz, see Fig. 15, are coincident with the ones reported before for the 4 bumps strip, see Fig. 14. By increasing the loading frequency, significant changes in the hysteresis behaviour are observed. This is especially true at the larger displacement amplitudes, as it can be seen in Figs. 16–18. A direct comparison between the results for 1 Hz and 40 Hz can be seen in Fig. 19. For higher loading frequency, the area enclosed by the local hysteresis curves tends to become smaller, and it seems that they are not tracing the global static one any more. Closer inspection reveals that the 'high slope' behaviour observed for the low frequency results tends to diminish or disappear for excitations with a higher frequency. Following the reasoning established before, this could be attributed to the fact that all the bumps exhibit sliding motion, without switching to a sticking phase when the direction of the displacement is inverted. The comparison depicted in Fig. 19 shows clearly this trend.

It can be observed that the end points for the load–displacement curves for the low and high frequency test are the same. The mathematical model showed that this would not be the case if the friction coefficient was reduced as can be seen in Fig. 9a and b. This indicates, that a reduction of the constant coefficient of friction alone, cannot explain the 'flattening' of the hysteresis curves.

One could argue that the bumps inertia forces could play a role in the observed behaviour, however the maximum acceleration measured in the vertical direction is around 1.5–2.0 m/s^2. Assuming the entire mass of the foil specimen, which is 0.45 g, to be concentrated in one sliding point and multiplying it with the horizontal acceleration of this point would yield a very small force. In fact a force with an order $F_\mu/1000$, if comparing to the numerical results illustrated in Fig. 10.

The apparent reduction of the bump sticking phase for higher excitation frequencies could be attributed to a momentary modification of the friction coefficient in or around the transition

between sliding and sticking. An acceleration $\ddot{x}_r$ dependant friction coefficient was described as early as 1943 by Sampson et al. [24]. They showed that the dry friction coefficient would decrease in the acceleration stage of the slip and remain low during the deceleration. Later investigations by Sakamoto [25] confirmed this phenomenon. The friction coefficient was obtained experimentally to $\mu \approx 0.4$ in the beginning of the slip and dropped significantly to $\mu \approx 0.1$ over the acceleration stage where after it remained constant. Their experiments did not deal with the transition between the stick and slip phase. However, the results may still serve to explain why the global hysteresis curve becomes narrower at increasing frequency i.e. higher accelerations close to the transition between stick and slip.

Other literature in the field of tribology addresses the effect of vibration in the normal direction of two mating surfaces over the friction coefficient. Chowdhury and Helali [26] performed an experiment regarding this issue. A clear trend is observed, regarding the reduction of the friction coefficient with both the amplitude and the frequency of the normal vibration, for different tested materials. These authors relate the observed trend to an eventual reduction of the effective contact area between the mating surfaces when vibrations are taking place. This effect may also be relevant for the bump foil strip, as the normal loads in the contact points are oscillating.

5. Conclusion and future aspects

In this paper, a theoretical and experimental study has been carried out, aimed at investigating the behaviour of bump foils used in compliant gas bearings. The investigation has focussed on the static and dynamic behaviour of a bump foil pressed between two rigid parallel surfaces. A quasi-static non-linear finite element model of the complete foil geometry has been developed, including the effects of the foil flexibility and the friction forces in the contact points. An original approach for modelling the friction forces was implemented, based on the usage of non-linear spring elements. The results from the numerical model regarding load–displacement behaviour have been compared with theoretical and experimental results coming from the literature, as well as experimental data obtained from a dedicated test rig.

The numerical model was compared to previously published analytical results [4]. For the stiffness of a single bump (free–free) good agreement between analytical and numerical results was observed at different coefficients of friction. The analytically calculated stiffness is commonly used in combination with the 'simple elastic foundation model'. However, for a strip consisting of several bumps (fixed-free), the numerical model indicated that the analytical method significantly underestimates the stiffness, hence the 'simple elastic foundation model' is generally underestimating the contribution of the structural stiffness.

The hysteresis loops obtained numerically, corresponded well with the experimentally obtained hysteresis loops for low load frequencies < 5 Hz and both stiffness and damping were found to be highly non-linear. The numerical model was able to reproduce both the global load–displacement curves and the local ones, considering smaller vertical displacements around an equilibrium position. Two distinctive patterns of motion were observed for the local hysteresis loop based on the theoretical and experimental results. If the vertical displacement perturbations are small enough, then the hysteresis loop tends to follow a sinusoidal motion, where the dominant effect corresponds to the bumps flexibility since most of the bumps are pinned due to friction forces. If the displacement surpasses a threshold value, then the local hysteresis loop tracks the global one, exhibiting two distinctive slopes associated with the dominance of the bumps elastic forces or the sliding friction forces respectively. In this condition, the transition towards sliding friction behaviour greatly enhances the energy dissipation properties of the foil, and the resulting vertical displacements deviate significantly from the purely harmonic motion.

The experimental determination of the local hysteresis curves for higher loading frequencies revealed that both the stiffness and equivalent damping properties of the bump are strongly load frequency dependant. At higher frequencies, the experimental results deviate significantly from the theoretical as the hysteresis loops tend to 'flatten' and the energy dissipated per load cycle reduces significantly. This phenomenon tends to alter the stiffness such that it becomes less non-linear but still of the same approximate magnitude. For small load amplitudes and high frequency, the motion of the bump deflection is nearly harmonic, but for larger load amplitudes the motion is still non-harmonic, even though less distorted compared to the low frequency case.

The 'flattening' of the hysteresis loops at high frequency seems to be caused by the absence of the stick phase i.e. the foil contacts are operating constantly in the slip phase. The authors are under the impression, that inertia effects will be small and that the phenomenon may as well be related to instantaneous variations in the coefficient of friction or other local contact phenomena.

In order to improve the numerical model to a state of accuracy desired in the design of foil bearings, the effect of the load frequency needs to be taken into account. In that regard, more research needs to be conducted to properly understand the 'flattening' phenomenon of the hysteresis curves experimentally obtained and documented in this work. This future work can be divided in the following steps:

- The effect of inertia forces needs to be investigated by including mass in the numerical model and perform a time integration analysis.
- Previous published results [24–26] have proven significant friction variations due to vibrations in the normal and perpendicular direction of the contact points as well a significant dependency of sliding acceleration. These and related effects need to be studied in more detail.

Appendix A. Iterative solution based on the Newton–Raphson method

In the implicit incremental Newton–Raphson (NR) scheme, the load is applied in n increments, for each of which the displacement D^n is found iteratively by satisfying the non-linear equilibrium condition which can be written in residual form as

$$R(D^n) = R_{int}(D^n) - P^n. \tag{A.1}$$

If D_i^n is an approximate solution to the exact solution D^n, then a first order Taylor expansion gives an equilibrium equation for the next NR-step as

$$R(D_{i+1}^n) \approx R(D_i^n) + \frac{dR(D_i^n)}{dD}\Delta D_i^n = 0. \tag{A.2}$$

If we now define the tangent as

$$K_t \equiv \frac{dR(D_i^n)}{dD} \tag{A.3}$$

then the equilibrium equation (A.2) can be written as

$$K_t \Delta D_i^n = -R(D_i^n) \tag{A.4}$$

or inserting (A.1)

$$K_t \Delta D_i^n = -R_{int}(D_i^n) + P^n. \tag{A.5}$$

When the equilibrium equation (A.5) has been solved the displacements are updated from

$$D_{i+1}^n = D_i^n + \Delta D_i^n. \tag{A.6}$$

The tangent is then updated with the new displacement $D_i^n = D_{i+1}^n$ and the procedure is repeated until the norm of the residual is sufficiently small. Here, the NR method was derived for a scalar problem, but it is directly applicable to vector problems.

References

[1] Ku C-PR, Heshmat H. Compliant foil bearing structural stiffness analysis. Part I: theoretical model including strip and variable bump foil geometry. J Tribol 1992;114:394–400.

[2] Ku C-PR, Heshmat H. Structural stiffness and coulomb damping in compliant foil journal bearings: theoretical considerations. Tribol Trans 1994;37:525–33.

[3] Ku C-PR, Heshmat H. Structural stiffness and coulomb damping in compliant foil journal bearings: parametric studies. Tribol Trans 1994;37:455–62.

[4] Walowit JA, Anno JN. Modern developments in lubrication mechanics. London: Applied Science Publishers; 1975.

[5] Ku C-PR, Heshmat H. Compliant foil bearing structural stiffness analysis. II: experimental investigation. J Tribol 1993;115:364–9.

[6] Peng JP, Carpino M. Coulomb friction damping effects in elastically supported gas foil bearings. Tribol Trans 1994;37:91–8.

[7] Heshmat H, Ku CP. Structural damping of self-acting compliant foil journal bearings. J Tribol 1994;116:76–82.

[8] Ku C-PR, Heshmat H. Effects of static load on dynamic structural properties in a flexible supported foil journal bearing. ASME Trans J Vib Acoust 1994;116:257–62.

[9] Rubio D, San Andrés L. Bump-type foil bearing structural stiffness: experiments and predictions. In: ASME conference proceedings 2004; 2004. p. 671–9.

[10] Rubio D, San Andrés L. Bump-type foil bearing structural stiffness: experiments and predictions. J Eng Gas Turbines Power (Trans ASME) 2006;128:653–60.

[11] Iordanoff I. Analysis of an aerodynamic compliant foil thrust bearing: method for a rapid design. J Tribol 1999;121:816–22.

[12] Rubio L, San Andrés D. Structural stiffness, dry friction coefficient, and equivalent viscous damping in a bump-type foil gas bearing. J Eng Gas Turbines Power 2007;129:494–502.

[13] Salehi M, Heshmat H, Walton JF. On the frictional damping characterization of compliant bump foils. J Tribol 2003;125:804–13.

[14] Le Lez S, Arghir M, Frene J. A new bump-type foil bearing structure analytical model. J Eng Gas Turbines Power 2007;129:1047–57.

[15] Le Lez S, Arghir M, Frene J. A dynamic model for dissipative structures used in bump-type foil bearings. Tribol Trans 2008;52:36–46.

[16] Heshmat H, Walowit JA, Pinkus O. Analysis of gas lubricated compliant thrust bearings. J Lubr Technol 1983;105:638–46.

[17] Heshmat H, Walowit JA, Pinkus O. Analysis of gas-lubricated foil journal bearings. J Lubr Technol 1983;105:647–55.

[18] Lee D, Kim Y-C, Kim K-W. The dynamic performance analysis of foil journal bearings considering coulomb friction: rotating unbalance response. Tribol Trans 2009;52:146–56.

[19] Zywica G. The static performance analysis of the foil bearing structure. Acta Mech Autom 2011;5.

[20] Zywica G. The dynamic performance analysis of the foil bearing structure. Acta Mech Autom 2013;7.

[21] Kozanecki Z, Kicinski J, Zywica G. Numerical model of the high speed rotors supported on variable geometry bearings. In: IUTAM symposium on emerging trends in rotor dynamics; 2011. p. 217–27.

[22] Krenk S. Non-linear modeling and analysis of solids and structures. Cambridge, England: Cambridge University Press; 2009.

[23] Cook RD, Malkus DS, Plesha ME, Witt JW. Concepts and applications of finite element analysis. 4th ed. New York: John Wiley; 2002.

[24] Sampson JB, Morgan F, Reed DW, Muskat M. Studies in lubrication. XII: friction behavior during the slip portion of the stick–slip process. J Appl Phys 1943;14:689–700.

[25] Sakamoto T. Normal displacement and dynamic friction characteristics in a stick–slip process. Tribol Int 1987;20:25–31.

[26] Chowdhury MA, Helali MM. The effect of frequency of vibration and humidity on the coefficient of friction. Tribol Int 2006;39:958–62.

[P3] Efficient solution of the non-linear Reynolds equation for compressible fluid using the finite element method

---

This paper was submitted to the *Journal of the Brazilian Society of Mechanical Sciences and Engineering* in January 2014 and published online 27 July, 2014.

Efficient solution of the non-linear Reynolds equation for compressible fluid using the finite element method

Jon S. Larsen & Ilmar F. Santos

Journal of the Brazilian Society of Mechanical Sciences and Engineering

ISSN 1678-5878

J Braz. Soc. Mech. Sci. Eng.
DOI 10.1007/s40430-014-0220-5

Springer

J Braz. Soc. Mech. Sci. Eng.
DOI 10.1007/s40430-014-0220-5

TECHNICAL PAPER

Efficient solution of the non-linear Reynolds equation for compressible fluid using the finite element method

Jon S. Larsen · Ilmar F. Santos

Received: 6 January 2014 / Accepted: 6 July 2014

Abstract An efficient finite element scheme for solving the non-linear Reynolds equation for compressible fluid coupled to compliant structures is presented. The method is general and fast and can be used in the analysis of airfoil bearings with simplified or complex foil structure models. To illustrate the computational performance, it is applied to the analysis of a compliant foil bearing modelled using the simple elastic foundation model. The model is derived and perturbed using complex notation. Top foil sagging effect is added to the bump foil compliance in terms of a close-form periodic function. For a foil bearing utilized in an industrial turbo compressor, the influence of boundary conditions and sagging on the pressure profile, shaft equilibrium position and dynamic coefficients is numerically simulated. The proposed scheme is faster, leading to the conclusion that it is suitable, not only for steady-state analysis, but also for non-linear time domain analysis of rotors supported by airfoil bearings.

Keywords Reynolds equation · Compressible fluid · Finite element method

List of Symbols

$B_{\alpha\beta}$	Damping coefficients, $\alpha\beta = x, y$
C	Radial clearance
D	Bearing diameter
D	Diffusion
E	Modulus of elasticity of foil
K	Foil flexibility
K_c	Foil mobility
$K_{\alpha\beta}$	Stiffness coefficients, $\alpha\beta = x, y$
L	Bearing length
N	Shape function
N_p	Number of pads
R	Journal radius
S	Bump foil pitch
S	Surface
V	Volume
$W_{x,y}$	Static load components
f_γ	Trigonometric functions
$\tilde{p}_0$	Approximating pressure
b_{foil}	Equivalent viscous damping of foil
$e_{x,y}$	Journal eccentricity components
e_{x_0,y_0}	Journal equilibrium position
h	Film height
h_0	Steady-state film height
h_c	Film height correction
h_r	Film height (rigid)
l_0	Bump half length
p	Pressure
p_0	Static pressure
p_a	Ambient pressure
p_x, p_y	Perturbed pressures
p_γ	Dynamic pressure
t	Time
t_b	Thickness of bump foil
t_t	Thickness of top foil
x, y, z	Cartesian coordinates

Technical Editor: Fernando Alves Rochinha.

J. S. Larsen (✉) · I. F. Santos
Department of Mechanical Engineering, Technical University of Denmark, DTU, Kongens Lyngby 2800, Denmark
e-mail: josla@mek.dtu.dk

I. F. Santos
e-mail: ifs@mek.dtu.dk

J. S. Larsen
Siemens A/S - Aeration Competence Center, Helsingør 3000, Denmark

Published online: 27 July 2014

$\Delta e_{x,y}$	Perturbation of journal equilibrium position
α	Convergence rate
β	Relaxation factor for SUR
ϵ	Error
η	Structural loss factor of foils
λ	Convergence factor
μ	Dynamic viscosity
$\nabla\cdot$	Divergence
∇	Gradient, $\nabla = \left\{\frac{\partial}{\partial\theta}, \frac{\partial}{\partial z}\right\}$
ν	Poisson's ratio of foil
ω	Angular speed of journal
ω_{s}	Excitation frequency of journal
ϕ	Attitude angle
ρ	Density
θ	Circumferential angle
θ_l	First pad leading edge angle
θ_{t}	First pad trailing edge angle
$\tilde{\theta}$	Circumferential coordinate, $\tilde{\theta} = \theta R$
ε	Eccentricity ratio, $\varepsilon = \sqrt{e_x^2 + e_y^2}/C$
$\varepsilon_x, \varepsilon_y$	Eccentricity ratio
ξ, η	Gauss points
$[B]$	Shape function derivatives matrix
$[K_t]$	Tangential matrix
$[K]$	Stiffness matrix
$[N]$	Shape function matrix
$\{P_0\}$	Static nodal pressure
$\{P_\gamma\}$	Dynamic nodal pressure
$\{R\}$	Residual vector
$\{U\}$	Speed, $\{U\} = \{\omega R/2,\, 0\}^T$
$\{\mathbf{n}\}$	Unit normal vector
$\{q\}$	Right-hand side vector

1 Introduction

Gas bearings have been the subject for research within mechanical engineering for five decades [23]. Through the past three decades, compliant foil bearings (CFB) have found way into an increasing number of industrial applications within high-speed rotating machinery. The current tendency is, that the technology is progressing from small, high-speed rotating machinery, like dental drills and microturbines and specialized equipment related to the aeronautical industries, toward larger, mass-produced industrial compressors and turbines [8, 32]. In today's industrial compressors supported by CFB's, the assembled rotor weight is often above 50 kg and the rated power over 200 kW. The advantages of these compressors compared to conventional oil-lubricated compressors are many, for instance low mechanical power loss, clean non-contaminating operation and the fundamental simplicity of the mechanical design. The main disadvantage of CFB's is related to their limited mechanical damping. Consequently, rotordynamic stability of CFB-supported compressors becomes a fundamental design issue. Though CFB's generally offer significantly better stability characteristics compared to rigid gas bearings, the stability of the rotor bearing system is still a major concern seen from an engineering perspective. As a result, much experimental and theoretical work has been conducted to achieve accurate mathematical models of the CFB dynamics.

Heshmat [9, 10] originally included the flexibility of the compliant foil implicitly in the Reynolds equation by introducing a linear elastic displacement as function of the fluid film pressure, $h_{\mathrm{c}} = K(p - p_{\mathrm{a}})$. This simple elastic foundation model (SEFM) was extended by several authors [12, 15, 24, 25] to include a structural loss factor for the compliant foil and a perturbation method to obtain equations for the linearised stiffness and damping coefficients, which were solved by a finite difference scheme. San Andrés and Kim [30] later extended the model to include thermohydrodynamic effects (THD). Besides the theoretical work related to the SEFM, there has been many other significant contributions dealing with the complex behaviour of the compliant bump foil structures interacting with the housing surface [19, 20]. Highly worth mentioning is the work of Peng and Carpino [4], in which, detailed FE models of the compliant foil structure including equivalent frictional damping are coupled to the FE model of the lubrication film. In the attempt to couple complex structural FE models directly to the fluid film FE model, it is the authors' experience that there is a need for a fast converging and robust solution scheme.

In this paper, an efficient FE solution scheme based on the Newton-like (Nl) method [5] is introduced. Newton-like in the sense that it does not implement the true Jacobian. The solution scheme is applied to the SEFM but it is not limited to this model alone. It is suited for models including more detailed foil structure formulations as well. The method is compared to a standard iterative procedure, based on successive under relaxation (SUR). In this comparison, the SEFM is extended to include the effect of top foil sagging. Sagging occurs when the hydrodynamic film pressure causes a top foil deflection between bumps. The phenomenon was thoroughly investigated using both beam theory considerations [14] as well as analytical 2D plate theory [3, 21] and FE-based models [22, 28, 29, 34, 36]. Here, a periodic expression, based on simple beam theory, approximates the sagging effect analytically and is added to the foil flexibility originally given by Wallowit and Anno [31]. It is a close-form expression and allows for an arbitrary nodal discretization and makes numerical implementation straightforward compared to [14]. However, this expression is only valid for periodic bump foil distributions.

The SEFM is perturbed using complex mathematical notation, enabling the introduction of a complex frequency-dependant flexibility for the compliant foil structure, and FE formulations for the perturbed equations are derived. The zeroth-order FE equation is non-linear, and is solved using both SUR and the proposed Nl-based schemes. The two solution schemes are compared and the Nl-based scheme is found faster. The effective FE solution scheme constitutes the main original contribution of this work.

A Siemens foil bearing from an industrial compressor is analysed theoretically and the effect of the top foil sagging is investigated. Static and dynamic results from the analysis are presented for different sets of boundary conditions. While the actual time savings for the analysis presented are limited, the fast solution is still important in the case of a non-linear rotor simulation in time, where bearing forces need to be calculated between each time step. The method described in this paper was derived to be used for non-linear analysis as well as to be extended by incorporating more complex foil structure models based on FEM [18]. Non-linear dynamic simulation tools applied to complex industrial rotors supported by CFB is still demanding faster numerical methods [2, 7, 13, 33, 35].

2 Theoretical model

For a journal bearing with the nomenclature as given in Fig. 1a, the compressible Reynolds equation can be written in vector form [6] as

$$\nabla \cdot \left(\frac{ph^3}{12\mu} \nabla p \right) = \nabla \cdot (ph)\{U\} + \frac{\partial}{\partial t}(ph) \tag{1}$$

where the film height $h(\theta, z, p)$ is defined as the film height of a rigid journal bearing $h_r(\theta)$, with the addition of a compliance, or deflection term $h_c(p) = K(p - p_a)$, which is dependant on the hydrodynamic pressure field and was first suggested by Heshmat [9]. The film height becomes

$$h = h_r + h_c = C + e_x \cos(\theta) + e_y \sin(\theta) + K(p - p_a) \tag{2}$$

where K is the structural flexibility related to the area of the compliant foil layers. With the notation defined in Fig. 1b, K can be approximated as

$$K(\tilde{\theta}) \approx \frac{S^4(1-\nu^2)}{Et_t^3} \left(\frac{1}{60} - \frac{3}{2\pi^4} \cos\left(\frac{2\pi\tilde{\theta}}{S} \right) \right) + \frac{2S}{E} \left(\frac{l_0}{t_b} \right)^3 (1-\nu^2) \tag{3}$$

which is a superposition of the bump foil deflection given by Heshmat [9] and the top foil deflection given in Appendix 1. Expanding Reynolds Eq. (1) by inserting the film height (2) leads to a modified Reynolds equation with the structural foil flexibility included implicitly

$$\begin{aligned} &\nabla \cdot \left(\frac{ph_r^3}{12\mu} \nabla p \right) + \nabla \cdot \left(\frac{p(p-p_a)^3 K^3}{12\mu} \nabla p \right) \\ &\quad + \nabla \cdot \left(\frac{ph_r(p-p_a)^2 K^2}{4\mu} \nabla p \right) \\ &\quad + \nabla \cdot \left(\frac{ph_r^2(p-p_a)K}{4\mu} \nabla p \right) = \nabla \cdot (ph_r)\{U\} \\ &\quad + \nabla \cdot (p(p-p_a)K)\{U\} \\ &\quad + \frac{\partial}{\partial t}(ph_r) + \frac{\partial}{\partial t}(p(p-p_a)K). \end{aligned} \tag{4}$$

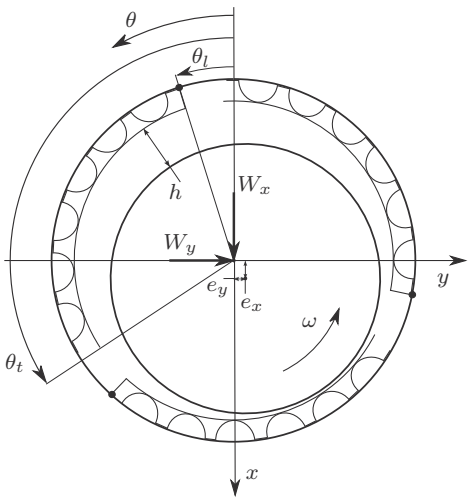

(a) Shaft and bearing.

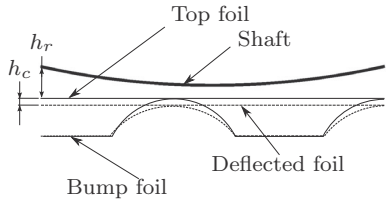

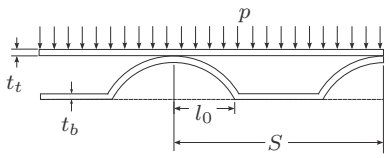

(b) Detailed view of bump and top foil.

Fig. 1 Schematics and nomenclature of a foil journal bearing with compliant outer surface

2.1 Assumptions and limitations

Solving this equation, for a given set of eccentricities (e_x, e_y) and speed $\{U\}$, yields the hydrodynamic pressure p, in the fluid film, by implicitly taking into account the deformations in the compliant foil layers. In addition to the assumptions of laminar, Newtonian, thin-film flows, which together with the Navier–Stokes and the continuity equation leads to the Reynolds equation, the viscosity is assumed constant, i.e. isothermal condition. Furthermore, by including the foil flexibility in the radial direction as in (4), it is assumed that the foil radial stiffness is linear and that the radial deformation in any foil position (θ, z) is completely independent of the radial deformation in any neighbouring positions. Dependent on the particular foil configuration, bump geometry and top foil thickness, this may limit the validity of (4) and is discussed further in Sect. 3.3.

2.2 Perturbed equations

To investigate the dynamic performance of the bearing, a harmonic perturbation method is employed. The method, which was first introduced by Lund [23], is a commonly used and widely accepted method. Assuming that the shaft exhibits small harmonic oscillations around its equilibrium position in the bearing (e_{x_0}, e_{y_0}), the shaft motion is given by

$$e_x = e_{x_0} + \Delta e_x \mathrm{e}^{i\omega_s t} \text{ and } e_y = e_{y_0} + \Delta e_y \mathrm{e}^{i\omega_s t}. \tag{5}$$

Assuming the amplitudes to be small $\Delta e_x \ll C$ and $\Delta e_y \ll C$, a first-order Taylor expansion of the pressure can be written as

$$p = p_0 + (\Delta e_x p_x + \Delta e_y p_y)\mathrm{e}^{i\omega_s t}. \tag{6}$$

According to (6), the pressure p is a harmonic oscillating field. This enables the introduction of a frequency-dependant mobility, in the film height function, rather than a static flexibility K. The mobility can be written as

$$K_\mathrm{c} = K\frac{1 - i\eta}{1 + \eta^2} \tag{7}$$

where $\eta = \omega_s b_\mathrm{foil} K$ is the mechanical energy loss factor related to the foils [11]. Implementing the mobility K_c, the film height becomes

$$h = h_\mathrm{r} + h_\mathrm{c} = C + e_x\cos(\theta) + e_y\sin(\theta) + K_\mathrm{c}(p - p_\mathrm{a}). \tag{8}$$

Substituting (5), (6), (7) into (4) and (8), discarding second- and higher-order terms yields, upon separation of variables, the zeroth- and first-order equations:

Zeroth order

$$\nabla\cdot\left(\frac{p_0 h_0^3}{12\mu}\nabla p_0\right) - \nabla\cdot(p_0 h_0)\{U\} = \{0\} \tag{9}$$

First order

$$\begin{aligned}&\nabla\cdot\left(\frac{p_0 h_0^3}{12\mu}\nabla p_\gamma\right) + \nabla\cdot\left(\frac{h_0^3 + 3h_0^2 p_0 K_\mathrm{c}}{12\mu}\nabla p_0 p_\gamma\right)\\ &\quad - \nabla\cdot\big((h_0 + p_0 K_\mathrm{c})p_\gamma\big)\{U\}\\ &\quad - i\omega_\mathrm{s}(h_0 + p_0 K_\mathrm{c})p_\gamma = -\nabla\cdot\left(\frac{p_0 h_0^2 f_\gamma}{4\mu}\nabla p_0\right)\\ &\quad + \nabla\cdot(p_0 f_\gamma)\{U\} + i\omega_\mathrm{s}(p_0 f_\gamma)\end{aligned} \tag{10}$$

where

$$h_0 = h_{r_0} + h_{c_0} = C + e_{x_0}\cos(\theta) + e_{y_0}\sin(\theta) + K_c(p_0 - p_\mathrm{a}) \tag{11}$$

and $\gamma = x, y$ and $f_x = \cos(\theta)$ and $f_y = \sin(\theta)$. Solving the zeroth-order Eq. (9) for an eccentricity (e_{x_0}, e_{y_0}) and $\eta = 0$ yields the static film pressure p_0. This pressure is then used when solving the first-order Eq. (10) to obtain the dynamic pressures p_x and p_y. The bearing reaction forces are found by integration of the static pressure p_0 over the bearing surface

$$\begin{Bmatrix} W_x \\ W_y \end{Bmatrix} = -\int_0^L\int_0^{2\pi}(p_0 - p_\mathrm{a})\begin{Bmatrix}\cos(\theta)\\ \sin(\theta)\end{Bmatrix} R\mathrm{d}\theta\mathrm{d}z \tag{12}$$

and a similar integration of the dynamic pressures (p_x, p_y) determines the dynamic stiffness and damping coefficients as

$$\begin{aligned}&\begin{bmatrix}K_{xx} & K_{xy}\\ K_{yx} & K_{yy}\end{bmatrix} + i\omega_\mathrm{s}\begin{bmatrix}B_{xx} & B_{xy}\\ B_{yx} & B_{yy}\end{bmatrix}\\ &\quad = \int_0^L\int_0^{2\pi}\begin{bmatrix}p_x\cos(\theta) & p_y\cos(\theta)\\ p_x\sin(\theta) & p_y\sin(\theta)\end{bmatrix} R\mathrm{d}\theta\mathrm{d}z.\end{aligned} \tag{13}$$

3 Finite element formulation and solution

The FE formulation is divided into two parts. The first part is dealing with the zeroth-order non-linear parabolic partial differential Eq. (9), for the static pressure p_0, which needs to be solved iteratively. The second part deals with the first-order linear complex differential Eq. (10), for the dynamic pressures p_γ, which can be solved directly.

While the first-order equation is easily solved, the solution of the zeroth-order equation is more complicated. Standard FE methods, like, e.g. the Bubnov–Galerkin method [5] could be employed to derive a system of equations of the form $[K(p_0)]\{p_0\} = \{q(p_0)\}$. The challenge in solving such a system for the pressure $\{p_0\}$ lies in the pressure dependency of the coefficient matrix $[K(p_0)]$ and the right-hand side $\{q(p_0)\}$. A straightforward method of overcoming this is to rewrite the system to an iterative form:

$$[K(p_{0_i})]\{p_{0_{i+1}}\} = \{q(p_{0_i})\} \text{ for } i = 1, 2, \ldots \tag{14}$$

which can be solved by consecutive updates of the pressure $\{p_{0_i}\} = \{p_{0_{i+1}}\}$ after each solution iteration i. However, this method will only converge for an extremely good starting guess of the initial pressure $\{p_{0_1}\}$. To improve the convergence, an SUR method of the form $p_{0_{i+1}} = \beta p_{0_i} + (1-\beta)p_{0_{i-1}}$ where $\beta \in [0, 1]$ can be applied. However, the relaxation factor β needs to be very small to achieve convergence, meaning that the solution becomes slow, and often convergence is hardly achieved. To overcome this problem, an FE formulation which can be combined with the iterative Newton–Raphson solution scheme, as outlined in Appendix 2, is sought. The solution derived here, can be seen as the equivalent to solving structural problems including material non-linearities [5, 16]. The procedure can be used on not only the SEFM, but also in combination with more complex mathematical models including detailed foil structure formulations.

3.1 Zeroth-order equation

A Bubnov–Galerkin FE procedure with implementation of an isoparametric element formulation is followed [5]. First (9) is rewritten into the compact form as

$$\nabla \cdot (D\nabla p_0) = \nabla \cdot (p_0 h)\{U\} \tag{15}$$

where the diffusion coefficient $D(p_0) = \frac{p_0 h^3}{12\mu}$ is a scalar and real field (only the real part of the foil mobility is used in the zeroth-order equation). Second, an approximating pressure field $\tilde{p}_0 = [N]\{p_0^e\}$ over an element is introduced, where $\{p_0^e\}$ is the nodal pressure and $[N]$ is the shape function matrix. Thus the Galerkin residual equation for (15), on the element level, is

$$\int_{V^e} [N]^T \nabla \cdot (D\nabla \tilde{p}_0)\,\mathrm{d}V - \int_{V^e} [N]^T \nabla \cdot (\tilde{p}_0 h)\{U\}\,\mathrm{d}V = \{0\} \tag{16}$$

where V^e is the element volume. Applying Green's theorem on (16) yields

$$\begin{aligned} &- \int_{V^e} [B]^T (D\nabla \tilde{p}_0)\,\mathrm{d}V + \int_{S^e} [N]^T (D\nabla \tilde{p}_0)\{\mathbf{n}\}\,\mathrm{d}S \\ &+ \int_{V^e} [B]^T (\tilde{p}_0 h)\{U\}\,\mathrm{d}V - \int_{S^e} [N]^T (\tilde{p}_0 h)\{U\}\{\mathbf{n}\}\,\mathrm{d}S = \{0\} \end{aligned} \tag{17}$$

where matrix $[B]^T = \left[\left[N_{,\tilde{\theta}}\right]^T \left[N_{,z}\right]^T\right]$ contains the spatial derivatives of the shape functions and $\{\mathbf{n}\}$ is the outward pointing unit normal vector of surface element dS. Due to continuity conditions, the boundary integrals vanishes and (17) reduces to

$$\int_{V^e} [B]^T D\nabla \tilde{p}_0\,\mathrm{d}V - \int_{V^e} [B]^T \tilde{p}_0 h\{U\}\,\mathrm{d}V = \{0\}. \tag{18}$$

The spatial derivatives of the approximating pressure field are $\tilde{p}_{0,i} = [N_{,i}]\{p_0^e\}$ with $i = \tilde{\theta}, z$ or in vector form, $\nabla \tilde{p}_0 = [B]\{p_0^e\}$. Inserting this into (18) gives

$$\begin{aligned} \{R^e\} = \{R^e_{\text{ext}}\} - \{R^e_{\text{int}}\} = \{0\} &- \int_{V^e} [B]^T D[B]\{p_0^e\}\,\mathrm{d}V \\ &+ \int_{V^e} [B]^T \{U\} h[N]\{p_0^e\}\,\mathrm{d}V \end{aligned} \tag{19}$$

where $\{R^e_{\text{int}}\}$ and $\{R^e_{\text{ext}}\}$ are the internal and external residuals. The tangent matrix on element level [16] is then:

$$\left[K_{\text{t}}^e\right] = \frac{\partial\{R^e_{\text{int}}\}}{\partial\{p_0^e\}} = \int_{V^e} [B]^T D[B]\,\mathrm{d}V - \int_{V^e} [N]^T \{U\}^T h[B]\,\mathrm{d}V. \tag{20}$$

It is important to highlight that Newton's method, or the frequently called Newton–Raphson method in the engineering is second-order accurate when: (a) the true Jacobian is used, for example, obtained explicitly from the set of non-linear equations and (b) the solution of the linearised systems of equations is obtained to machine precision. In this framework, the procedure presented here only satisfies (b) since D was kept constant when taking the derivative $\partial\{R^e_{\text{int}}\}/\partial\{p_0^e\}$. Being strictly rigorous, hereby (15) is solved using a 'Newton-like' procedure, since the true Jacobian is not used.

The element vectors and matrices are expanded to structure size by the usual element summation:

$$[K_{\text{t}}] = \sum_e \left[K_t^e\right]; \quad \{R\} = \sum_e \{R^e\}; \quad \{p\} = \sum_e \{p^e\} \tag{21}$$

where the volume integrals are numerically integrated using a quadrature rule [5]. The scalar field quantities p_0, h, K_{c} in D are calculated in the respective Gauss points (ξ_i, η_j) using the interpolation functions as:

$$q(\xi_i, \eta_j) = \left[N(\xi_i, \eta_j)\right]\{q^e\} \tag{22}$$

where q and $\{q^e\}$ are the scalar field quantities and nodal vectors, respectively. Full integration must be employed, which in case of linear four-node quadrilateral elements (Q4) means that 2 by 2 Gauss points are used. An algorithm for implementing the Nl scheme (as outlined in Appendix 2) is given as a pseudocode in Appendix 3. The Nl scheme provides the solution p_0 for a given set of eccentricities (e_{x_0}, e_{y_0}). Upon integration of p_0, using (12), a set of reaction forces (W_x, W_y) is obtained which needs to be balanced with the prescribed bearing loads. This force/reaction balance is established iteratively using common root finding

algorithms, e.g. the Newton–Raphson method for systems of equations. During this step, the film height h is updated in $[K_t]$ and $\{R\}$ based on (8). In contrary to the SEFM, h might also be updated by means of a more complex formulation of the foil structure, e.g. a non-linear FE model.

3.2 First-order equation

The first-order Eq. (10) is a linear complex differential equation. Following the same Bubnov–Galerkin FE procedure as for the zeroth-order equation leads to a linear set of complex algebraic equations

$$\left[K_\gamma\right]\{p_\gamma\} = \{q_\gamma\} \tag{23}$$

which can be solved by factorization for the dynamic pressures. The coefficient matrix $\left[K_\gamma\right]$ and right-hand side $\{q_\gamma\}$ on the element level are given by

$$\begin{aligned}\left[K_\gamma^e\right] &= \int_{V^e} \left([B]^T C_1 [B] + [B]^T C_2 [B]\{p_0\}[N] + [B]^T C_4 \{U\}[N] \right. \\ &\quad \left. - [N]^T i\omega_s C_4 [N]\right) \mathrm{d}V \\ \{q_\gamma^e\} &= \int_{V^e} \left([B]^T C_3 f_\gamma [B]\{p_0\} + [B]^T p_0 f_\gamma \{U\} - i\omega_s p_0 f_\gamma [N]^T\right) \mathrm{d}V\end{aligned} \tag{24}$$

where the coefficients are

$$\begin{aligned} C_1 &= \frac{p_0 h_0^3}{12\mu} \\ C_2 &= \frac{h_0^3 + 3h_0^2 p_0 K_c}{12\mu} \\ C_3 &= -\frac{p_0 h_0^2}{4\mu} \\ C_4 &= -(h_0 + p_0 K_c). \end{aligned} \tag{25}$$

During the numerical integration procedure of the coefficient matrix and right-hand side vector (24), all field quantities are calculated in the Gauss points using the shape functions.

3.3 Mesh and boundary conditions

The boundary conditions for the zeroth- and first-order systems (19), (20), (23), are applied following the common methods. For a compliant foil bearing as depicted in Fig. 1a, the boundary conditions are

$$\begin{aligned} p_0 &: \begin{cases} p_0(\theta_l, z) = p_0(\theta_t, z) = p_a \\ p_0(\theta, L/2) = p_0(\theta, -L/2) = p_a \end{cases} \\ p_\gamma &: \begin{cases} p_\gamma(\theta_l, z) = p_\gamma(\theta_t, z) = 0 \\ p_\gamma(\theta, L/2) = p_\gamma(\theta, -L/2) = 0. \end{cases} \end{aligned} \tag{26}$$

The boundary condition for the zeroth-order equation of p_0 is implemented in the solution algorithm, as outlined in Appendix 3. In short, it should only be applied for the first iteration of the solution. The boundary condition for the first-order equation of p_γ is prescribed by standard FE techniques.

As illustrated in Fig. 2, the prescribed boundary conditions (26) will pose a problem for large journal eccentricities. The foil deflection $h_c(p_0) = K_c(p_0 - p_a)$ becomes zero in the nodes where $p_0 = p_a$. This is the case on the pad edges. If the bearing pad mesh in Fig. 2a is subjected to ambient pressure p_a on its left edge and the bearing eccentricity ratio is approaching 1, the resulting film height h and the deflected pad profile will take a form as illustrated in Fig. 2b (Standard BC). This is obviously incorrect, since the radial deflection of the top foil along the axial direction z should be smooth. In the situation illustrated, with zero film height h on the edge, the air leakage will become zero with an elevated pressure along the edge as a consequence. This is a problem specifically related to the SEFM. To correct it, one has to assure that the foils take on realistic deflections on the pad edges. This can be achieved by meshing with a narrow band of elements, having the width of $L/50$ or less, along the bearing edges subjected to ambient pressure and letting the foil deflection $h_c(p)$ in the outermost nodes of these elements (on the bearing edge), adopt the deflection values of the innermost nodes (away from the bearing edge) on that element. This situation is shown in Fig. 2b (BC1).

For foil configurations where the top foil is stiffer than the bump foil, the top foil deflection can be regarded as constant along the axial direction of the bearing [26]. In these cases, the deflection $h_c(p_m)$ can be used where the pressure p_m is taken as the arithmetic mean pressure along the axial direction for a given angle θ. This situation is illustrated in Fig. 2b (BC2).

In gas bearings, where the fluid is compressible, significant sub-ambient pressures may arise. These sub-ambient pressures will cause the top foil to separate from the bumps into a position in which the pressure on both sides of the pad is equalized. Heshmat [10] introduced a set of boundary conditions accounting for this separation effect. However, in this work, a simple Gümbel [6] boundary condition is imposed, which means that sub-ambient pressures are discarded when integrating the pressure to obtain the bearing force components (W_x, W_y). This means that the parts of the bearing having sub-ambient pressures are inactivated and hence these areas need prescribed boundary conditions, $p_\gamma = 0$ where $p_0 < p_a$, when solving the first-order equation.

3.4 Numerical implementation

The foil flexibility $K(\theta)$ is a periodic expression (3) in the circumferential direction, it is therefore important to define

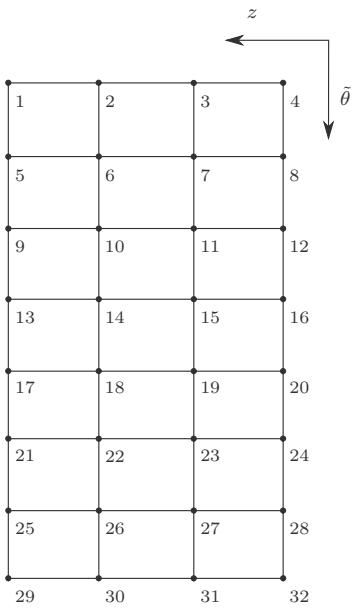

(a) FE mesh of a single pad.

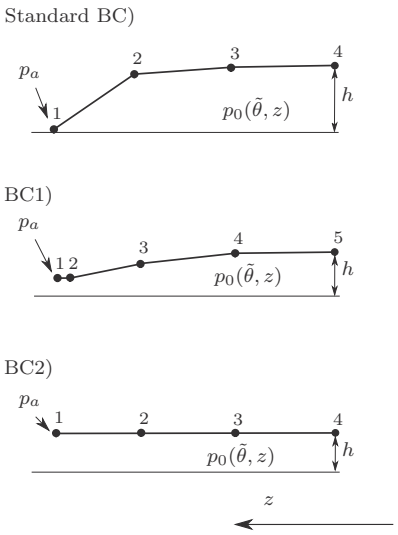

(b) Film height and pad deflection along axial direction.

Fig. 2 Schematics of FE mesh for a single pad and the effect of boundary conditions on its edges

an FE mesh having a sufficient number of element divisions in θ, to avoid aliasing which may lead to significant errors in the pressure solution. This means a minimum of two element divisions per bump is required. In practice, a larger number may be desirable to obtain an accurate solution of the pressure field $p_0(\theta, z)$. The adequate number of element divisions should be determined from case to case by a mesh convergence study. Dependent on the amount of top foil sagging a smaller or larger amount of element divisions may be necessary.

To improve convergence of the outer Newton–Raphson scheme, which balances the bearing loads (W_x, W_y) with the pressure $p_0(e_x, e_y)$, the integration of the pressure (12) should preferably be carried out by an accurate integration algorithm. Good results are obtained using a modified Simpson algorithm, modified to cope with uneven nodal spacing and both equal and odd number of element divisions. An accurate integration of the dynamic pressure p_γ will improve the accuracy of the calculated bearing coefficients (13) as well.

The coefficient matrices of both the zeroth- and first-order systems, $[K_t]$ and $[K_\gamma]$, are banded. This feature should be exploited by utilizing a sparse matrix storage format and a sparse solver. In the current implementation, the LAPACK dgbsv solver is used [1].

3.5 Performance

The performance of the Nl solution scheme, for solving the zeroth-order equation, outlined in Sect. 3.1 and Appendix 2, is compared to the SUR scheme. For this comparison, a single pad bearing often referred to in the literature [27], is analysed and the static shaft equilibrium position and film pressure profile is calculated. To investigate how the foil flexibility $h_c = K(p_0 - p_a)$ affects the convergence of the two methods, both a rigid ($h_c = 0$) version and a flexible ($h_c \neq 0$) version of the bearing are analysed. The geometry of the bearing is outlined in Table 1.

A relaxation factor of $\beta = 0.1$ is used with the SUR solution. This value is found to be near optimal for the given bearing and operating conditions. Using a starting guess for the eccentricity $(\varepsilon_x, \varepsilon_y) = (0.3, 0.3)$, the BC1 and no Gumbel boundary condition, the solution converges to the equilibrium positions $(\varepsilon_{x_0}, \varepsilon_{y_0}) = (0.62, 0.42)$ with foil flexibility included and $(\varepsilon_{x_0}, \varepsilon_{y_0}) = (0.36, 0.39)$ when foil flexibility is neglected ($h_c \neq 0$). The convergence, in terms of the Euclidean norm of the pressure difference between consecutive iterations, is illustrated in Fig. 3 for each of the four cases.

For all cases, a mesh consisting of 594 elements and 670 nodes is used. Refining the mesh is not found to change pressure convergence. It is clear from Fig. 3, that the Nl solutions converge faster than the SUR solutions. In this example, the iterations are stopped when $\|\{p_{i+1}\} - \{p_i\}\| < 1$. However, the convergence criteria of the Nl method is normally based on the residual (19), such that convergence is obtained when $\|\{R\}\| < 10^{-6}$.

To evaluate the convergence, the error ϵ between two consecutive iterations is assumed to follow the relation [5]

Table 1 Geometry, material properties and operating conditions of a single pad foil bearing

Parameters	Values
Bearing radius (R)	19.05 mm
Bearing length (L)	38.10 mm
Bearing clearance (C)	32 μm
Bump foil thickness (t_b)	0.1016 mm
Top foil thickness (t_t)	0.2032 mm
Bump foil pitch (S)	4.572 mm
Bump half length (l_0)	1.778 mm
Young's modulus of bump foil (E)	2.07×10^{-11} Pa
Poisson's ratio of bump foil (v)	0.3
Loss factor (η)	0.25
Ambient pressure (P_a)	1×10^{-5} Pa
Air viscosity (μ)	95×10^{-5} Pa·s
Air density (ρ)	1.06 kg m^{-3}
Load $[(W_x, W_y)]$	(50, 0) N
Speed (ω)	40,000 RPM

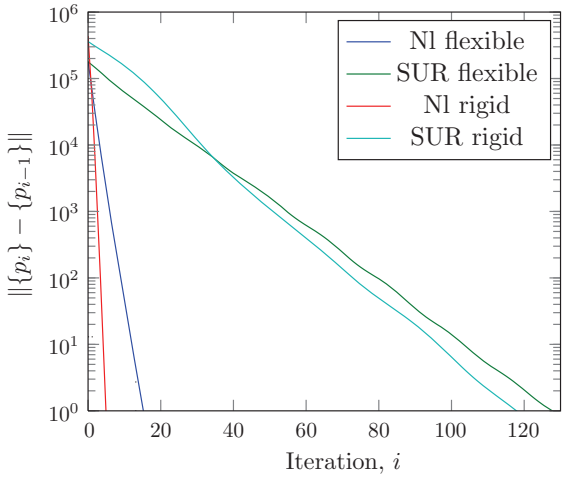

Fig. 3 Pressure convergence for the first eccentricity step. Successive under relaxation with a factor $\beta = 0.1$ compared to the Newton-like method for flexible and rigid bearings

$$\epsilon_{i+1} = \lambda \epsilon_i^{\alpha} \tag{27}$$

where α is the rate of convergence and λ is the convergence factor. If the ratio of consecutive errors is approximated by the ratio of consecutive differences as

$$\frac{\epsilon_{i+1}}{\epsilon_i} \approx \frac{\|\{p_{i+1}\} - \{p_i\}\|}{\|\{p_i\} - \{p_{i-1}\}\|} \tag{28}$$

then the convergence rate α can be estimated as

$$\alpha \approx \frac{\log(\|\{p_{i+1}\} - \{p_i\}\| / \|\{p_i\} - \{p_{i-1}\}\|)}{\log(\|\{p_i\} - \{p_{i-1}\}\| / \|\{p_{i-1}\} - \{p_{i-2}\}\|)} \tag{29}$$

Table 2 Estimated convergence rate and factor for each calculation case

Case	α	λ
Nl flexible	1.0	0.52
SUR flexible	1.0	0.94
Nl rigid	1.1	0.04
SUR rigid	1.0	0.90

The values are averaged over all iterations

and the convergence factor λ can be estimated by:

$$\lambda \approx \frac{\|\{p_{i+1}\} - \{p_i\}\|}{\|\{p_i\} - \{p_{i-1}\}\|^{\alpha}}. \tag{30}$$

In Table 2 the convergence rates and factors for the four cases, estimated by (29) and (30), are listed.

The convergence rate is found to be $\alpha = 1.1$ for the Nl solution of the rigid bearing and $\alpha = 1$ for all other cases. This is far from second-order convergence ($\alpha = 2$) which is theoretically obtainable with the Newton–Raphson method. When taking the derivative of the residual $\{R_i\}$ to obtain the tangential matrix $[K_t]$ in (20), the diffusion coefficient D is kept constant. In fact it is not constant but updated between each iteration, hence the full Jacobian is not obtained. However, the Nl solutions are found to have lower convergence factors λ than the SUR solutions which explains the faster convergence. For both schemes, a pressure equilibrium iteration is equivalent to inverting the coefficient matrix $[K]$ or $[K_t]$ which in this example corresponds to solving a system of 670 linear equations per pressure iteration i.

4 Analysis of industrial foil bearing

The static results of the SEFM, i.e. pressure profile, film height, eccentricity ratio have been compared and validated to experimental results in [17]. Here, the pressure profiles, equilibrium position and the stiffness and damping coefficients are calculated theoretically.

The investigated bearing is that of a Siemens direct-driven compressor with the geometry and material properties as outlined in Table 3. The real bearing has a top foil thickness t_t of twice the value given in the table, but to exaggerate the sagging effect, only half the real thickness is used in the calculation. The bearing is subjected to loads $W_x = 115\,\text{N}$, $W_y = 0$ and the shaft is rotated at $\omega = 15.000\,\text{RPM}$. A total of four different cases has been investigated. Each of these cases involves a different set of boundary conditions outlined in Table 4 together with the calculated eccentricity ratio ε. Based on a mesh convergence analysis, as illustrated in Fig. 4, a grid of 9 elements over the length and 88 elements in circumferential

Table 3 Geometry, material properties and operating conditions of the Siemens airfoil bearing

Parameters	Values
Bearing radius (R)	50.00 mm
Bearing length (L)	78.00 mm
Bearing clearance (C)	70 μm
Number of pads (N_p)	3
First pad leading edge (θ_l)	30°
First pad trailing edge (θ_t)	145°
Bump foil thickness (t_b)	0.127 mm
Top foil thickness (t_t)	0.127 mm
Bump foil pitch (S)	7.00 mm
Bump half length (l_0)	3.30 mm
Young's modulus of bump foil (E)	2.07×10^{11} Pa
Poisson's ratio of bump foil (ν)	0.3
Loss factor (η)	0.25
Ambient pressure (P_a)	1×10^5 Pa
Air viscosity (μ)	1.95×10^{-5} Pa·s
Air density (ρ)	1.06 kg m^{-3}

direction per pad amounting to 2,670 nodes are used for all cases. The low number of elements over the length of the bearing is achieved by exploiting the symmetry around $z = L/2$.The eccentricity ratio is found to be nearly constant for the four different cases. The tendency is that the eccentricity ratio increases slightly by including the sagging effect. Similarly, the eccentricity ratio is slightly higher when using BC1 compared to BC2. This makes sense since BC1 allows for an uneven foil deflection along the length of the bearing. Overall, the effect of the boundary conditions on the eccentricity ratio is regarded as negligible for this medium loaded bearing. Previous results [17] showed that the two boundary conditions have a significant effect on the shape of the film pressure profiles. It was found that the BC1 resulted in an almost flat pressure distribution along the length of the bearing and BC2 gave a more pointed pressure with a slightly higher maximum. In Figs. 5 and 6, the pressure profiles for case 1 and 2 using the BC2 are illustrated. Comparing these, it is clear that the maximum pressure $p/p_a = 1.35$ is the same for both cases but the shape of the pressure profile is altered for the second case, where the sagging effect is included. The sagging clearly alters the pressure profile, especially on the second pad where the pressures are highest.

The stiffness and damping coefficients of the bearing are calculated for all four cases in a range of excitation frequencies $\omega_s/\omega = [0.1; 100]$. The results are illustrated in Fig. 7. Due to the compressibility of the lubricant, both the stiffness and damping are highly frequency dependant. It is observed that the direct stiffness K_{xx} in the load direction is slightly dependant on the boundary conditions imposed on the pad edges (BC1 vs. BC2). However, the effect of including the sagging effect is regarded as being insignificant.

Table 4 Boundary conditions and calculated eccentricities for the four cases under investigation

Case	B.C. on edges	Foil separation	Foil sagging	Eccentricity ratio, ε
1	BC2	Gumbel b.c.	Excluded	1.218
2	BC2	Gumbel b.c.	Included	1.264
3	BC1	Gumbel b.c.	Excluded	1.224
4	BC1	Gumbel b.c.	Included	1.262

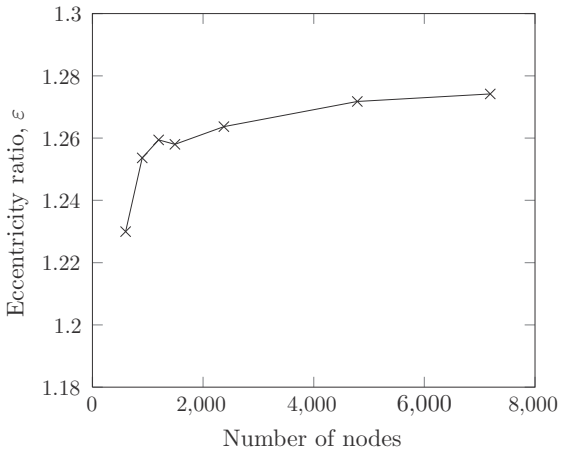

Fig. 4 Mesh convergence curve—calculated eccentricity ratio at different mesh sizes for Case 2

For the above analysis, the zeroth-order non-linear equation was solved using both the SUR method and the proposed Nl solution scheme. Again, a speed up of approximately a factor 10 was seen for the Nl solution scheme.

5 Conclusions and future aspects

Two solutions of the non-linear Reynolds equation for compressible fluids were compared. One based on an iterative Nl method, and one based on a SUR solution scheme. Both methods were found to have convergence rates close to 1. Even though the Nl method did not achieve a convergence rate of 2, i.e. second-order convergence, it had a lower convergence factor and converged nearly 10 times faster than the SUR method for a flexible bearing and more than 20 times faster for a rigid bearing.

Two different sets of boundary conditions which deal with the lack of foil deflection on the edges subjected to

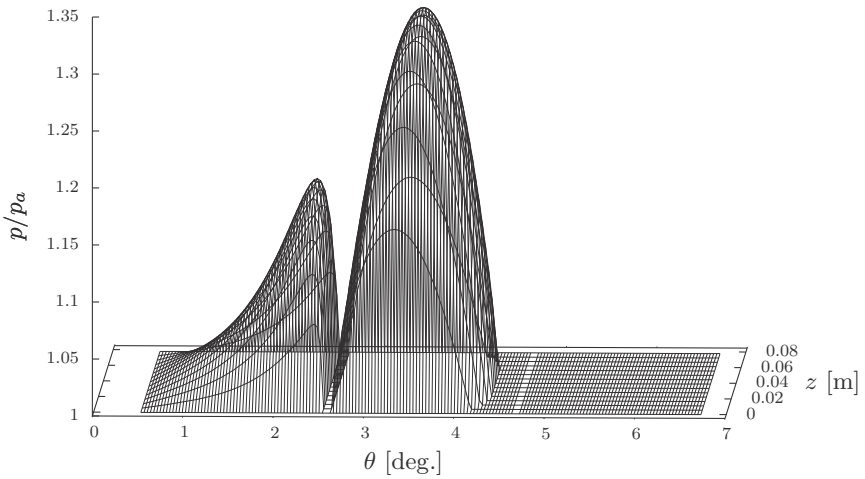

Fig. 5 Pressure field for the Siemens 3 pad foil bearing calculated for a bearing clearance and load of $C = 70\,\mu\text{m}$ and $W_x = 115\,\text{N}$. Sagging effect of top foil neglected (mesh size reduced for illustration purpose)

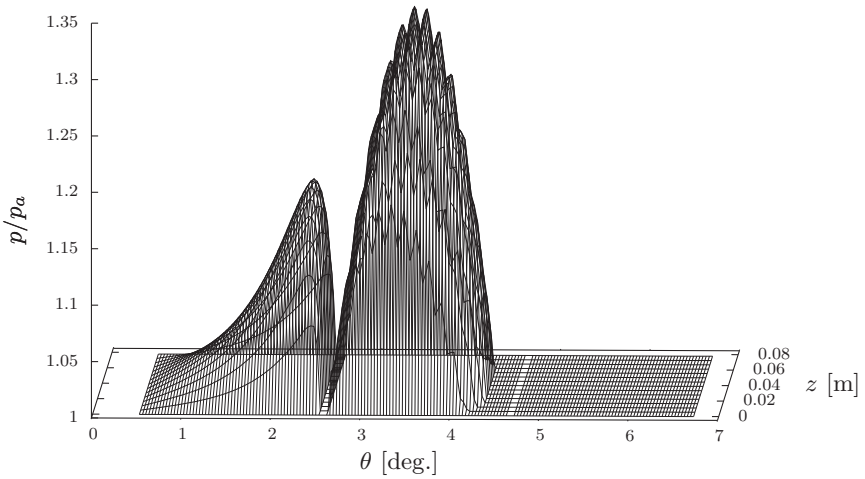

Fig. 6 Pressure field for the Siemens 3 pad foil bearing calculated for a bearing clearance and load of $C = 70\,\mu\text{m}$ and $W_x = 115\,\text{N}$. Sagging effect of top foil included (mesh size reduced for illustration purpose)

ambient pressure were investigated for a medium loaded bearing. Switching between the two different boundary conditions, BC1 and BC2, yields slightly different pressure profiles, but the shaft equilibrium position changes by less than 1 %. The influence on the dynamic stiffness and damping coefficients was found to be insignificant.

Finally, the inclusion of the top foil sagging effect was investigated. It was found that the foil sagging on a medium loaded bearing does not significantly affect the equilibrium position, which stays within 4 % of the value obtained without the sagging effect included. Furthermore, the dynamic stiffness and damping coefficients were not found to be significantly affected by the sagging effect.

The mathematical model (SEFM) and solution scheme outlined in this paper can easily be extended to incorporate tabulated experimental values of the foil flexibility and damping, considering them constant or frequency dependent. Furthermore, the scheme is suitable for simulating non-linear rotor bearing systems in time due to the improved convergence.

Appendix 1: Top foil deflection

To include the 'sagging' effect of the top foil, as illustrated in Fig. 8a, into the mathematical model of the foil bearing, a periodic expression for the top foil flexibility, dependant on the angle θ, is sought. If the top foil is assumed to have unit width, the uniform pressure P becomes a uniformly distributed load along x (Fig. 8b). The top foil is assumed in pure bending and the bump foil deflection is kept at zero. Requiring the infinitesimal element of the top foil, Fig. 8b, to be in static equilibrium one obtain:

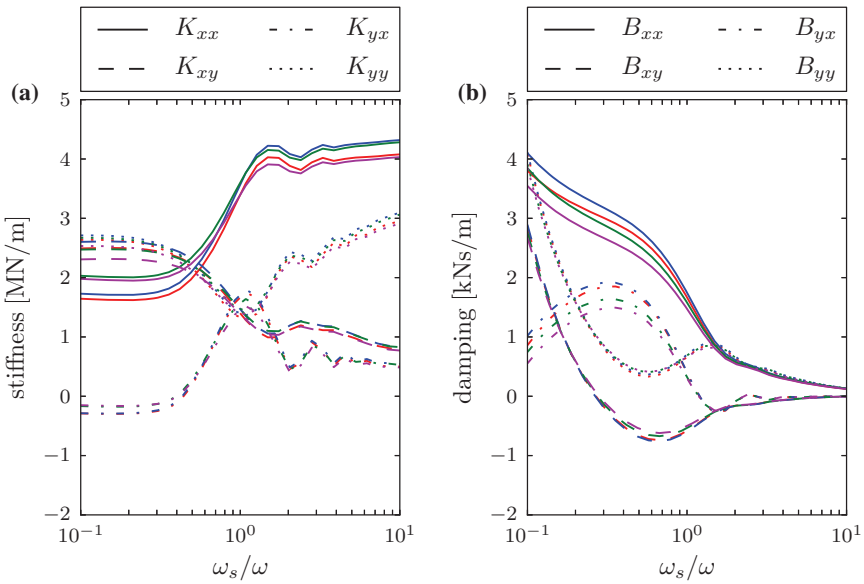

Fig. 7 Calculated stiffness and damping coefficients for the Siemens foil bearing. Case 1 *blue*, Case 2 *red*, Case 3 *green*, Case 4 *magenta*

$$M + \mathrm{d}M - M + \frac{1}{2}P\mathrm{d}\tilde{\theta}^2 + (T + \mathrm{d}T)\mathrm{d}\tilde{\theta} = 0 \quad \Rightarrow \quad \frac{\mathrm{d}M}{d\tilde{\theta}} = T$$
$$-N + N + \mathrm{d}N = 0 \quad \Rightarrow \mathrm{d}N = 0$$
$$T + \mathrm{d}T - T - P\mathrm{d}\tilde{\theta} = 0 \quad \Rightarrow \frac{\mathrm{d}T}{\mathrm{d}\tilde{\theta}} = P \tag{31}$$

rewriting and differentiating (31) yields

$$\frac{\mathrm{d}M}{\mathrm{d}\tilde{\theta}} = T \;\Rightarrow\; \frac{\mathrm{d}^2M}{\mathrm{d}\tilde{\theta}^2} = \frac{\mathrm{d}T}{\mathrm{d}\tilde{\theta}} = P. \tag{32}$$

If pure bending in one direction is assumed, then Kirchhoff–Love plate theory for isotropic plates, describes the relation between the bending moment M and the curvature $\frac{\mathrm{d}^2w_t}{\mathrm{d}\tilde{\theta}^2}$ as

$$M = D_t\frac{\mathrm{d}^2w_t}{\mathrm{d}\tilde{\theta}^2}, \quad D_t = \frac{Et_t^3}{12(1-\nu^2)} \tag{33}$$

where D_t is the flexural rigidity. Integrating (32) twice and inserting (33) leads to

$$D_\mathrm{t}\frac{\mathrm{d}^2w_t}{\mathrm{d}\tilde{\theta}^2} = \frac{P^2}{2}\tilde{\theta}^2 + c_1\tilde{\theta} + c_2 \tag{34}$$

which upon double integration yields

$$w_\mathrm{t}(\tilde{\theta}) = \frac{1}{D_\mathrm{t}}\left(\frac{P}{24}\tilde{\theta}^4 + \frac{c_1}{6}\tilde{\theta}^3 + \frac{c_2}{2}\tilde{\theta}^2 + c_3\tilde{\theta} + c_4\right). \tag{35}$$

Since the distributed load P is assumed uniform and the deflection of the bump foil is kept zero, the boundary conditions for a section of the top foil between two consecutive bump tops over the length S, as depicted in Fig. 8a, are

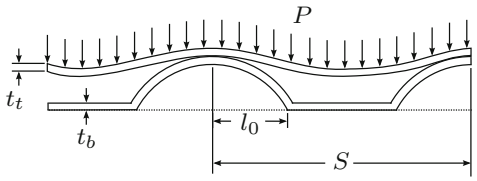

(a) Top foil 'sagging' between bumps

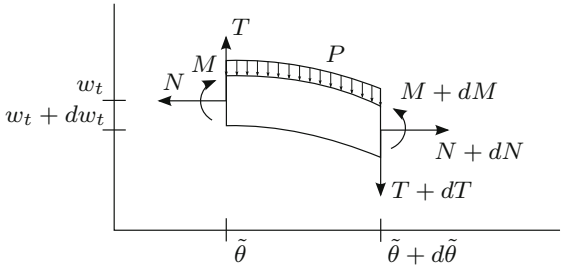

(b) Infinitesimal element of the deformed top foil

Fig. 8 Schematics and nomenclature of a the foil structure (bump foil and top foil) together with an infinitesimal element of the deformed top foil between two consecutive bump tops

$$w_\mathrm{t}(0) = w_\mathrm{t}'(0) = w_\mathrm{t}(S) = w_\mathrm{t}'(S) = 0. \tag{36}$$

Applying these boundary conditions leads to the integration constants $c_1 = -PS/2$, $c_2 = PS^3/12$ and $c_3 = c_4 = 0$ which by insertion in (35) leads to the foil deflection function

$$w_\mathrm{t}(\tilde{\theta}) = (p - p_\mathrm{a})K_\mathrm{t} \tag{37}$$

where $(p - p_a) = P$ and the top foil flexibility per unit width is

$$K_t(\tilde{\theta}) = \frac{(1-\nu^2)}{2Et_t^3}\left(\tilde{\theta}^4 - 2S\tilde{\theta}^3 + S^2\tilde{\theta}^2\right), \quad \tilde{\theta} \in [0:S]. \tag{38}$$

The top foil flexibility $K_t(\tilde{\theta})$ is defined over a section of the length S, i.e. in a closed interval between two bump tops. To develop an expression for the top foil flexibility over several bump tops, i.e. a periodic expression (38) is expanded into a Fourier series as

$$K_t(\tilde{\theta}) = \frac{(1-\nu^2)}{2Et_t^3}\left(\frac{a_0}{2} + a_1\cos\left(\frac{2\pi\tilde{\theta}}{S}\right) + \ldots\right) \tag{39}$$

where

$$a_0 = \frac{S^4}{15}, \quad a_1 = -3\left(\frac{S}{\pi}\right)^4, \quad \ldots \tag{40}$$

It can be shown, that the first two terms of (39) approximate the top foil flexibility with sufficient accuracy and thereby the top foil flexibility per unit width can be written as:

$$K_t(\tilde{\theta}) \approx \frac{S^4(1-\nu^2)}{Et_t^3}\left(\frac{1}{60} - \frac{3}{2\pi^4}\cos\left(\frac{2\pi\tilde{\theta}}{S}\right)\right) \tag{41}$$

Appendix 2: Iterative solution based on Nl method

The pressure p is found iteratively by trying to satisfy the non-linear equilibrium condition [16] which can be written in residual form as:

$$R(p) = R_{ext}(p) - R_{int}(p). \tag{42}$$

If p_i is an approximate solution to the exact solution p, then a first-order Taylor expansion gives an equilibrium equation for the next Nl step as

$$R(p_{i+1}) \approx R(p_i) + \frac{dR_{int}(p_i)}{dp}\Delta p_i = 0. \tag{43}$$

If we now define the tangent as

$$K_t \equiv \frac{dR_{int}(p_i)}{dp} \tag{44}$$

then the equilibrium equation (43) can be written as

$$K_t\Delta p_i = -R(p_i) \tag{45}$$

or inserting (42)

$$K_t\Delta p_i = -R_{ext}(p_i) + R_{int}(p_i). \tag{46}$$

When the equilibrium equation (46) has been solved the pressures are updated from

$$p_{i+1} = p_i + \Delta p_i. \tag{47}$$

The tangent is then updated with the new pressure $p_i = p_{i+1}$ and the procedure is repeated. We repeat until the norm of the residual is sufficiently small. Even though the Nl method, as shown above, was derived for a scalar problem, it is directly applicable to vector problems as well.

Appendix 3: Solution algorithm

Based on the iterative Nl method outlined in Appendix 2, a pseudo algorithm is given as:

Algorithm 1 Incremental Newton-Raphson scheme

```
{p_0} = {p_a}                                   ▷ Set {p_0} to ambient pressure (initial guess)
for i = 0 → i_max do
    {R_i} = {R_ext({p_i}) − {R_int({p_i})}}     ▷ Calculate the residual
    if ‖ {R_i} ‖< ε_stop then
        Stop iteration loop                     ▷ Stop at convergence
    end if
    Calculate [K_t({p_i})]
    Modify [K_t({p_i})] and {R_i} to account for BC   ▷ If non-zero only in
                                                ▷ first iteration
                                                ▷ then zero for all other
    {Δp_i} = [K_t({p_i})]^−1 {R_i}              ▷ Solve equilibrium equation
    if i = 0 then
        {p_i} = {0}
    end if
    {p_i+1} = {p_i} + α{Δp_i}                   ▷ Update the pressure (use α ∈ ]0, 1])
end for
```

References

1. Anderson E, Bai Z, Bischof C, Blackford S, Demmel J, Dongarra J, Du Croz J, Greenbaum A, Hammarling S, McKenney A, Sorensen D (1999) LAPACK Users' Guide, 3rd edn. Society for Industrial and Applied Mathematics, Philadelphia
2. Bhore SP, Darpe AK (2013) Nonlinear dynamics of flexible rotor supported on the gas foil journal bearings. J Sound Vib
3. Bruckner RJ (2004) Simulation and modeling of the hydrodynamic, thermal, and structural behavior of foil thrust bearings. PhD thesis, Case Western Reserve University
4. Carpino M, Talmage G (2006) Prediction of rotor dynamic coefficients in gas lubricated foil journal bearings with corrugated sub-foils. Tribol Trans 49(3):400–409
5. Cook RD, Malkus DS, Plesha ME, Witt JW (2002) Concepts and applications of finite element analysis, 4th edn. Wiley, New York
6. Hamrock BJ (1994) Fundamentals of fluid film lubrication. McGRAW-HILL Series in Mechanical Engineering. McGRAW-HILL Inc., New York
7. Hassini MA, Arghir M (2013) A new approach for the stability analysis of rotors supported by gas bearings. In: Proceedings of ASME turbo expo, pp 1–13
8. Heshmat H (1994) Advancements in the performance of aerodynamic foil journal bearings: high speed and load capability. J Tribol 116(2):287–294
9. Heshmat H, Walowit JA, Pinkus O (1983) Analysis of gas lubricated compliant thrust bearings. J Lub Technol 105(4):638–646
10. Heshmat H, Walowit JA, Pinkus O (1983) Analysis of gas-lubricated foil journal bearings. J Lub Technol 105(4):647–655
11. Inman DJ (2000) Engineering vibration. Prentice-Hall Inc., New Jersey
12. Kim D (2007) Parametric studies on static and dynamic performance of air foil bearings with different top foil geometries and bump stiffness distributions. J Tribol 129(2):354–364
13. Kim D, Lee AS, Choi BS (2013) Evaluation of foil bearing performance and nonlinear rotordynamics of 120 kw oil-free gas turbine generator. In: Proceedings of ASME turbo expo 2013, pp 1–8
14. Kim D, Park S (2009) Hydrostatic air foil bearings: analytical and experimental investigation. Tribol Int 42(3):413–425
15. Kim TH, San Andrés L (2005) Heavily loaded gas foil bearings: a model anchored to test data. In: ASME conference proceedings, vol 47276, pp 763–771
16. Krenk S (2009) Non-linear modeling and analysis of solids and structures. Cambridge University Press, Cambridge
17. Larsen JS, Santos IF (2013) Compliant foil journal bearings: investigation of dynamic properties. In: Proceedings of 10th international conference on Schwingungen in Rotierenden Maschinen (SIRM2013), pp 1–12, 25–27. ISBN 978-3-00-038602-2, Berlin, Germany
18. Larsen JS, Varela AC, Santos IF (2014) Numerical and experimental investigation of bump foil mechanical behaviour. Tribol Int 74:46–56
19. Le Lez S, Arghir M, Frene J (2007) A new bump-type foil bearing structure analytical model. J Eng Gas Turbines Power 129(4):1047–1057
20. Le Lez S, Arghir M, Frene J (2008) A dynamic model for dissipative structures used in bump-type foil bearings. Tribol Trans 52(1):36–46
21. Lee D, Kim D (2011) Design and performance prediction of hybrid air foil thrust bearings. J Eng Gas Turbines Power 133(4)
22. Lee D, Kim Y-C, Kim K-W (2009) The dynamic performance analysis of foil journal bearings considering coulomb friction: rotating unbalance response. Tribol Trans 52(2):146–156
23. Lund JW (1968) Calculation of stiffness and damping properties of gas bearings. J Lub Technol pp 793–804
24. Peng JP, Carpino M (1993) Calculation of stiffness and damping coefficients for elastically supported gas foil bearings. J Tribol 115(1):20–27
25. Peng JP, Carpino M (1997) Finite element approach to the prediction of foil bearing rotor dynamic coefficients. J Tribol 119(1):85–90
26. Peng ZC, Khonsari MM (2004) Hydrodynamic analysis of compliant foil bearings with compressible air flow. J Tribol 126(3):542–546
27. Ruscitto D, Cormick JM, Gray S (1978) Hydrodynamic air lubricated compliant surface bearing for an automotive gas turbine engine 1: journal bearing performance. Technical Report NASA CR-135368
28. San Andrés L, Kim TH (2007) Improvements to the analysis of gas foil bearings: integration of top foil 1d and 2d structural models
29. San Andrés L, Kim TH (2009) Analysis of gas foil bearings integrating fe top foil models. Tribol Int 42(1):111–120
30. San Andrés L, Kim TH (2010) Thermohydrodynamic analysis of bump type gas foil bearings: a model anchored to test data. J Eng Gas Turbines Power 132(4):042504
31. Walowit JA, Anno JN (1975) Modern developments in lubrication mechanics. Applied Science, London
32. Walton JF, Heshmat H, Tomaszewski MJ (2007) Design and test program in the developmen of a 100 hp oil-free high-speed blower. In: Proceedings of ASME turbo expo
33. Wang CC (2012) Bifurcation and nonlinear dynamic analysis of united gas-lubricated bearing system. Comput Math Appl 64(5):729–738
34. Xu F, Liu Z, Zhang G, Xie L (2011) Hydrodynamic analysis of compliant foil bearings with modified top foil model
35. Zhang XQ, Wang XL, Zhang YY (2013) Non-linear dynamic analysis of the ultra-short micro gas journal bearing-rotor systems considering viscous friction effects. Nonlinear Dyn pp 1–15
36. Zywica G (2013) The dynamic performance analysis of the foil bearing structure. Acta mechanica et automatica 7(1)

[P4] Experimental and theoretical analysis of a rigid rotor supported by air foil bearings

---

This paper was submitted to the Journal *Mechanics & Industry* in May 2014 and accepted for publication the 2 July, 2014.

Mechanics & Industry **16**, 106 (2015)
© AFM, EDP Sciences 2014
DOI: 10.1051/meca/2014066
www.mechanics-industry.org

Mechanics & Industry

Experimental and theoretical analysis of a rigid rotor supported by air foil bearings

Jon S. Larsen[1,2,a], Asger J. T. Hansen[2] and Ilmar F. Santos[1]

[1] Department of Mechanical Engineering, DTU-Technical University of Denmark, 2800 Kgs. Lyngby, Denmark
[2] Siemens A/S - Aeration Competence Center, 3000 Helsingør, Denmark

Received 26 May 2014, Accepted 8 July 2014

Abstract – The popularity of compressors utilizing foil bearings is increasing. Their mechanical design is challenging, and an accurate prediction of the bearing coefficients is important. A mathematical model taking into account the foil structure, and the detailed geometry of a three pad foil bearing are presented. The steady state solution and dynamic coefficients are obtained through zeroth and first order perturbed equations respectively. Analysis of the foil structure reveals the importance of distinguishing between a static foil stiffness for the zeroth order equation and a dynamic stiffness for the first order equation. Calculated bearing coefficients are compared to experimental results obtained from a dedicated test rig. Generally, good agreement is observed and minor discrepancies for the damping coefficients are discussed.

Key words: Air foil bearing / experimental identification / bearing coefficients / foil structural stiffness

1 Introduction

After five decades of research, compliant foil bearings are now gaining more popularity in the industry than ever before. The current trend is, that foil bearings are being implemented in larger and heavier machinery such as turbo compressors and turbo expanders. Turbo compressors with rotor weights up to 50 kg are available and now widely used. However, mathematical modelling of foil bearings are still associated with significant uncertainties which makes the design of rotor bearing systems difficult and sometimes very costly. Without more accurate mathematical models for prediction of the mechanical behaviour, the technology will continue to be associated with a limited amount of applications and its true potential will not be explored.

Heshmat [1, 2] was among the pioneers within this research field. He originally included the flexibility of the foil structure in the Reynolds equation by introducing a linear elastic displacement as function of the fluid film pressure, $h_c = K(p - p_a)$. The foil flexibility was based on the analytical expressions given by Walowit and Anno [3]. This model is commonly referred to as the simple elastic foundation model (SEFM). The model has later been extended by several authors. Iordanoff [4] developed a more detailed analytical model for the bump foil stiffness which took into account the fixation of the first bump. However, it did not account for the state (stick-slip) of the individual contact points and the resulting interaction between the bumps. Peng and Carpino [5] employed a perturbation method to the SEFM [6] to obtain a steady state solution and equations for the linearised bearing coefficients. Similar work was later performed by Kim [7] and extended with theoretical parametric stability studies. Both used the foil flexibility given by Walowit and Anno [3].

Several authors worked on coupled fluid and structure models as well as including the friction. San Andrés and Kim [8, 9] integrated finite element models of the top foil structure into the steady state solution and compared this result against experimental values [10]. The bump foils were modelled using the analytical mathematical expressions developed by Iordanoff [4]. Carpino et al. [11] developed a structural finite element model of the bump and top foils. Simultaneously, Peng and Carpino [12] investigated the effects of Coulomb friction on the linearised bearing coefficients by means of an equivalent viscous damping coefficient. Their joint effort resulted in the first fully coupled mathematical model [13] with a detailed foil finite element formulation and an equivalent viscous damping for the friction. Their work was of purely theoretical nature. Other authors have later introduced similar models e.g. Heshmat [14] who coupled the structural results obtained by a commercial FE program with the solution of the Reynolds equation for a thrust bearing, and Lee [15] who solved a fully coupled model of a journal foil bearing in the time domain. Lee et al. [16] coupled

[a] Corresponding author: jon@stadsen.dk

Nomenclature

C	Radial clearance	t_b	Thickness of bump foil
E	Modulus of elasticity of foils	t_t	Thickness of top foil
K	Foil flexibility	x, y, z	Cartesian coordinates
L	Bearing length	$\Delta e_{x,y}$	Perturbation of journal equilibrium position
N_p	Number of pads	μ	Dynamic viscosity
R	Bearing radius	μ_f	Coefficient of friction
S	Bump foil pitch	$\nabla\cdot$	Divergence
W	Load on bump foils	∇	Gradient, $\nabla = \left\{\frac{\partial}{\partial\theta},\ \frac{\partial}{\partial z}\right\}$
W_x	Journal load in x direction	ν	Poisson's ratio
W_y	Journal load in y direction	ω	Journal angular speed
f_γ	Trigonometric functions	ω_s	Excitation frequency of journal
$e_{x,y}$	Journal eccentricity components	θ	Circumferential coordinate
e_{x_0,y_0}	Journal equilibrium position	θ_l	First pad leading edge angle
h	Film height	θ_s	Slope extend
h_0	Steady state film height	θ_t	First pad trailing edge angle
h_b	Bump foil height	$\{U\}$	Speed, $\{U\} = \{\omega R/2,\ 0\}^T$
h_c	Film height (compliant)	$\{f_E\}$	Complex force vector
h_r	Film height (rigid)	$\{f_{b_0}\}$	Reaction force vector
h_s	Slope height	$\{f\}$	Complex force vector
h_{c_0}	Steady state film height (compliant)	$\{q_p\}$	Complex deflection vector
h_{r_0}	Steady state film height (rigid)	$\{q\}$	Complex deflection vector
k_d	Dynamic foil stiffness	$[C_b]$	Bearing damping matrix
k_s	Static foil stiffness	$[C]$	Shaft damping matrix
k_{eq}	Equivalent bump stiffness	$[H^r_{AB}]^{-1}$	Dynamic stiffness matrix of the rotor
l_0	Bump half length	$[H_{AB}]$	FRF matrix related to A and B
p	Film pressure	$[H_{EP}]$	FRF matrix related to E and P
p_0	Steady state film pressure	$[K_b]$	Bearing stiffness matrix
p_a	Ambient pressure	$[K]$	Shaft stiffness matrix
p_γ	Dynamic film pressure	$[M]$	Mass matrix
$p_{x,y}$	Perturbed pressures	$[T_1]$, $[T_2]$	Transformation matrices
t	Time		

a detailed three dimensional structural model with the steady state solution of the Reynolds equation but did not include friction.

The fully coupled models are computationally heavy. As a consequence, accurate equivalent structural models are desirable. Le Lez et al. [17, 18] developed equivalent structural models taking into account the Coulomb friction in the contact zones. The theoretical models were compared to experimental results with good agreement and underlined the importance of taking into account the bump interactions and their individual state (stick-slip). Feng and Kaneko [19] developed a similar equivalent foil model coupled with the fluid film equations and compared calculated film heights with experimental data [10].

While mathematical modelling of the gas film itself, using Reynolds equation, has proven to be very accurate compared to experiments [20, 21], accurate mathematical modelling of the foil structure is still a main research topic among tribologists, especially when coupling these models with the fluid film equations. A large amount of the work related to the foil structure modelling has been purely theoretical. However the structural models presented by Ku and Heshmat [22–24] were compared to experimental data [25, 26] showing reasonably good agreement. Theoretical and experimental investigations entirely focused on the bump foil mechanical behaviour were performed by Le Lez et al. [17, 18] and Larsen et al. [27]. Their theoretical bump foil models were able to accurately predict the steady state hysteresis loops, related to the friction in the sliding points which was previously identified by Ku and Heshmat [28] through isolated bump foil experiments. The experiments of Larsen et al. [27] indicated that the Coulomb friction model is insufficient to properly model the dynamic behaviour of the bump foil structure when subjected to loads at higher frequencies.

Overall experimental investigations of foil journal bearings were performed by several authors e.g. San Andrés et al. [29] who compared predicted unbalance response and critical speeds to experimental results. Dellacorte and Valco [30] experimentally investigated the load carrying capacity of foil bearings and derived a rule of thumb, and Howard [31] investigated the effect of misalignment on the bearing performance. However, the number of authors dealing with the experimental identification of the linearised dynamic stiffness and damping coefficients is limited. Howard et al. [32, 33] experimentally identified the dynamic coefficients of a foil journal bearing and investigated the temperature dependency. Matta et al. [34] identified the bearing coefficients of a rigid journal gas bearing. Ertas et al. [35] developed a floating bearing test rig for the identification of foil journal bearing coefficients, and presented experimental results,

and San Andrés [36] identified the dynamic coefficients for a hybrid flexural tilting pad gas bearing.

In this paper a theoretical model for obtaining the steady state solution and the linearised bearing coefficients of a journal foil bearing is presented. It takes into account the slope related to the leading edge fixation arrangement of the individual pads and is based on the SEFM which is perturbed in order to obtain a set of first order equations for the linearised bearing coefficients. The zeroth order equation is then coupled with a detailed structural model to obtain a more accurate steady state solution. The structural model has previously been described and compared to experimental results in [27]. Results of this model show a significant difference between the static and dynamic foil stiffness, and indicate the need to distinguish between them. The static stiffness should be used when solving for the steady state solution i.e. the zeroth order equation, and the dynamic stiffness should be used when solving the first order equation, which is obtained by assuming small harmonic pressure oscillations. Furthermore, a dedicated test rig has been designed and built to experimentally identify the linearised bearing coefficients of two identical three pad foil bearings supporting a nearly symmetrical rotor. The rotor mass is approximately 21 kg. Bearing coefficients obtained experimentally are presented and compared to the theoretical results of both the SEFM and the presented coupled model. The experimental identification of the bearing coefficients, the inclusion and investigation of the inlet slope and the calculation of the static and dynamic structural stiffness used in the coupled fluid structure model constitute the main original contributions of this work.

2 Theoretical model

The derivation of theoretical model is based on the SEFM originally presented by Heshmat [1, 2] and later extended by several authors [5,13,37,38]. Here the derivation of the mathematical model is kept brief but generally follows [39].

For a journal bearing with the nomenclature as given in Figures 1 and 2, the compressible Reynolds equation can be written in vector form [40] as

$$\nabla \cdot \left(\frac{ph^3}{12\mu} \nabla p \right) = \nabla \cdot (ph)\{U\} + \frac{\partial}{\partial t}(ph) \tag{1}$$

For a simple journal bearing, with the nomenclature as illustrated in Figure 1, the film height can be written as

$$h = h_r + h_c \tag{2}$$

where

$$h_r = \begin{cases} C + e_x \cos(\theta) + e_y \sin(\theta) - h_s \frac{\theta - \theta_i}{\theta_s}, & \theta_{li} \le \theta \le \theta_i \\ C + e_x \cos(\theta) + e_y \sin(\theta), & \theta_i < \theta \le \theta_{ti} \end{cases}$$

$$h_c = K(p - p_a) \tag{3}$$

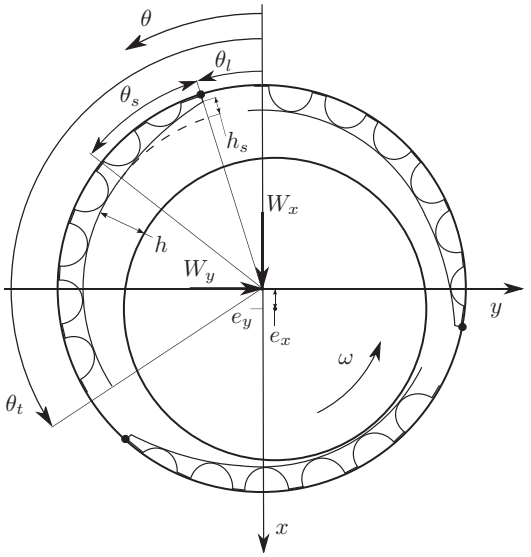

Fig. 1. Schematics and nomenclature of the foil journal bearing.

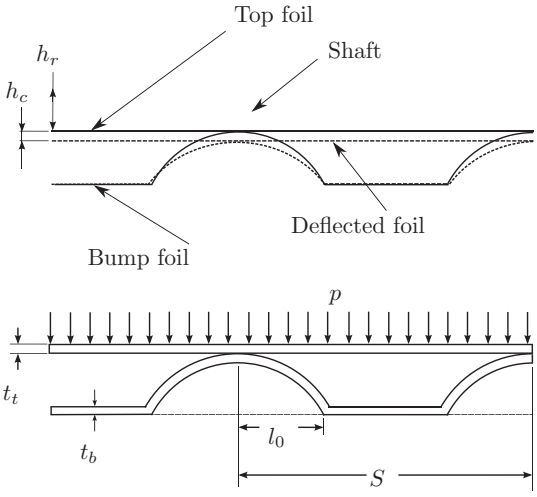

Fig. 2. Schematics and nomenclature of the top and bump foils comprising the compliant outer surface.

and

$$\theta_i = \theta_s + \theta_l + \frac{2\pi}{N_p}(i-1)$$

$$\theta_{li} = \theta_l + \frac{2\pi}{N_p}(i-1)$$

$$\theta_{ti} = \theta_t + \frac{2\pi}{N_p}(i-1) \tag{4}$$

with h_c being the foil deflection [1,2] and $i = 1, 2, \ldots, N_p$ the pad number.

A perturbation method is employed [6] by assuming that the shaft exhibits small harmonic oscillations around its equilibrium position in the bearing (e_{x_0}, e_{y_0}). The shaft motion is given by

$$e_x = e_{x_0} + \Delta e_x e^{i\omega_s t} \quad \text{and} \quad e_y = e_{y_0} + \Delta e_y e^{i\omega_s t}. \tag{5}$$

Assuming the amplitudes to be small $\Delta e_x \ll C$ and $\Delta e_y \ll C$, a first order Taylor expansion of the pressure can be written as

$$p = p_0 + (\Delta e_x p_x + \Delta e_y p_y) e^{i\omega_s t}. \tag{6}$$

Substituting (5), (6) into (1) and (2), discarding second and higher order terms yields, upon separation of variables, the zeroth and first order equations:
Zeroth order

$$\nabla \cdot \left(\frac{p_0 h_0^3}{12\mu} \nabla p_0 \right) - \nabla \cdot (p_0 h_0)\{U\} = \{0\} \tag{7}$$

First order

$$\nabla \cdot \left(\frac{p_0 h_0^3}{12\mu} \nabla p_\gamma \right) + \nabla \cdot \left(\frac{h_0^3 + 3h_0^2 p_0 K}{12\mu} \nabla p_0 p_\gamma \right) - \nabla \cdot ((h_0 + p_0 K) p_\gamma)\{U\} - i\omega_s (h_0 + p_0 K) p_\gamma = - \nabla \cdot \left(\frac{p_0 h_0^2 \mathrm{f}_\gamma}{4\mu} \nabla p_0 \right) + \nabla \cdot (p_0 f_\gamma)\{U\} + i\omega_s (p_0 f_\gamma) \tag{8}$$

where $\gamma = x, y$ and $f_x = \cos(\theta)$ and $f_y = \sin(\theta)$ and the film height h_0 is given by

$$h_0 = h_{r_0} + h_{c_0} \tag{9}$$

where

$$h_{r_0} = \begin{cases} C + e_{x_0} \cos(\theta) + e_{y_0} \sin(\theta) - h_s \frac{\theta - \theta_i}{\theta_s}, \\ \qquad \theta_{li} \le \theta \le \theta_i \\ C + e_{x_0} \cos(\theta) + e_{y_0} \sin(\theta), \\ \qquad \theta_i < \theta \le \theta_{ti} \end{cases}$$

$$h_{c_0} = K(p_0 - p_a). \tag{10}$$

Solving the zeroth order Equation (7) for an eccentricity (e_{x_0}, e_{y_0}) yields the static film pressure p_0. Then by solving the first order Equation (8), with respect to this pressure, the dynamic pressures p_x and p_y are obtained. Integrating these pressures over the bearing pad areas yields the linearised dynamic stiffness and damping coefficients. The Equations (7)–(9) constitute the SEFM. Solutions of these equations are obtained numerically by use of an FE approach [39].

2.1 Foil flexibility

In this paper, the foil flexibility is predicted using two methods. One is to treat the foils linearly having constant flexibility K based on the analytical expression given by Walowit and Anno [3]. The other is to model the entire foil structure using a non-linear finite element model. The development of the latter is thoroughly described in [27] and its derivation is only briefly introduced in the following.

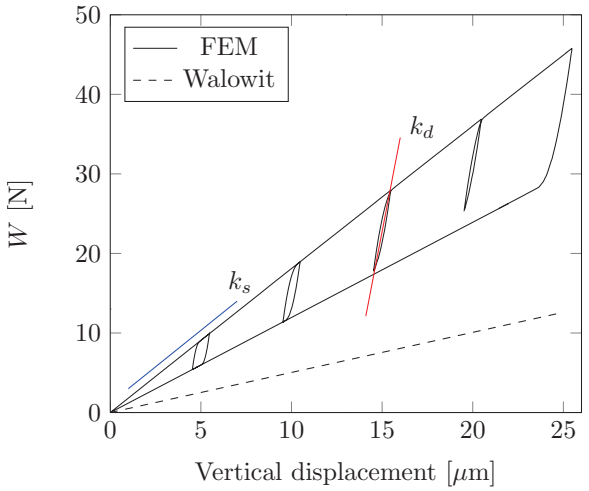

Fig. 3. Load displacement diagrams obtained using non-linear finite element model and the analytical expression of Walowit and Anno [3].

2.1.1 Simple elastic foundation model

The steady state foil deflection is given by $h_{c_0} = K(p_0 - p_a)$ and the foil flexibility K can be assumed to be constant, based on the analytical expressions given by Walowit and Anno [3] as

$$K \approx \frac{2S}{E} \left(\frac{l_0}{t_b} \right)^3 (1 - \nu^2), \tag{11}$$

or it can be a scalar field $K(\theta, z, p_0)$ based on a closed form expression e.g. [39] and a mechanical loss factor η can be included by making K complex [5, 37–39]. Here, (11) is used in complex form to include a loss factor.

2.1.2 Coupled fluid structure model

A more accurate prediction of h_{c_0} can be obtained numerically, using a non-linear FE model. Such a model taking into account the sliding friction in contact points between bump foils and top foils and bump foils and bearing housing is presented and compared to experiments in [27]. In Figure 3, load displacement diagrams obtained by (11) and this FE model for a strip of four bumps is compared.

It is clear that the flexibility obtained by (11) is overestimated [27]. It forms a straight line in the load displacement plot as opposed to the curve predicted by the FE model which forms closed hysteresis loops. From the FE result, it is seen that a monotonic loading will result in a near linear deflection line with a slope k_s. At 5, 10, 15 and 20 μm, the monotonic loading is substituted by small load oscillations which are seen to result in significantly higher slopes k_d. Due to the significant difference between the stiffness k_s and k_d it is necessary to distinguish between them. A foil flexibility based on the slope represented by

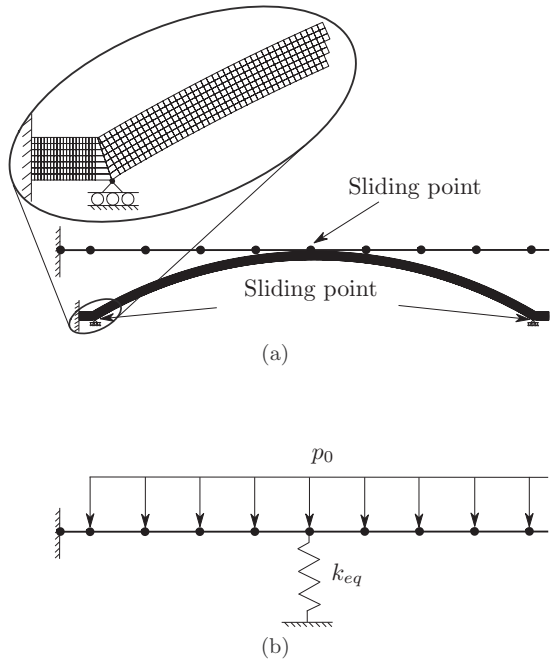

Fig. 4. (a) First bump segment (at leading edge) of the structural finite element model of top and bump foils with boundary conditions. (b) Equivalent linear model.

k_s should be used when solving for the steady state solution i.e. the zeroth order Equation (7). However, the first order Equation (8) which is obtained by assuming small harmonic pressure oscillations should be solved using a foil flexibility based on the slope represented by k_d.

The mesh and boundary conditions of the finite element model are illustrated in Figure 4a. The bump foils are modelled using iso-parametric plain strain elements based on the Green-Lagrange strain measure for large displacements and the top foil is modelled using a simple 2D-plate model with a nodal distribution equal to the fluid film mesh. In this work, the structural non-linear FE model is coupled with the fluid film FE model and solved iteratively in order to obtain a more accurate estimate of the steady state foil deflection h_{c_0}. The coupling of the structure and fluid film is straight forward as the solution of the zeroth order steady state Equation (7) follows an iterative Newton-Raphson scheme [39]. Between each iteration one may simply solve the structural model for the deflected height h_c. However this is computationally demanding so a faster approach, which is used here, is to linearise by a numerical perturbation, each bump stiffness and add these equivalent stiffness k_{eq} to the linear top foil model as shown in Figure 4b.

The equivalent foil structure model is then solved between each Newton-Raphson step until pressure convergence is obtained and the bump equivalent stiffness k_{eq} is updated between each shaft eccentricity step. This approach is valid only if the bump foil behaves linearly. However, as seen in Figure 3 this is the case under monotonic loading.

The coupled fluid-structure model (CFSM) is compared to the deflection obtained by the SEFM using the flexibility given by Walowit and Anno [3] as well as experimental data obtained from a dedicated test rig.

2.2 Assumptions

Both the SEFM and the CFSM are based on the assumption that the foil structure deflects evenly over the the axial length of the bearing. For both methods, the pressure applied on the foil structure is taken to be the arithmetic mean pressure along the length of the bearing. According to [1,2] sub-ambient pressures will lift the top foil of the bumps. Here the Gumbel boundary condition is used by simply setting any sub ambient pressures equal to p_a.

Solving for a steady state solution $(e_{x_0}, e_{y_0}, p_0, h_{c_0})$ using the CFSM with a coefficient of friction $\mu_f \neq 0$, may lead to several solutions dependant on the initial conditions and the loading path. With the CFSM it is not possible to know the loading path. The loading path for the CFSM is determined by the Newton-Raphson routine applied to solve for the steady state shaft equilibrium position. To overcome the problem of multiple solutions, the coefficient of friction is set to zero when solving for the steady state solution, thus eliminating the load path dependency.

3 Experimental setup

With the goal of identifying the linearised stiffness and damping coefficients of a foil bearing experimentally, under realistic loading and operation conditions, a dedicated test rig was constructed. The test rig is illustrated in Figure 5.

The test rig consists of a near symmetrical hollow shaft supported by two identical segmented foil journal bearings having 3 pads. Detailed data of the bearings is listed in Table 1.

A set of permanent magnets is press fit mounted in the centre of the shaft, and together with the stator windings this arrangement forms the electrical motor used for spinning the shaft. There are no axial bearings. High accuracy proximity sensors are mounted in horizontal and vertical directions close to each bearing location. In each shaft end a disk is mounted which has a stationary (non-rotating) inner part connected through high precision preloaded ball bearings. This stationary inner part is used in connection with an electromagnetic shaker to excite the shaft. The excitation force is measured using a piezoelectric force transducer mounted directly at the stationary inner part. The assembled shaft mass is approximately 21 kg and the operating speed range is 15 to 30 kRPM. The first free-free natural frequency (bending) of the assembled shaft is calculated to approximately 1050 Hz. This

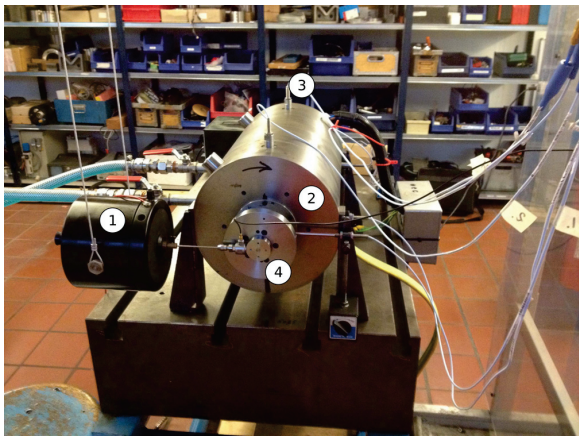

Fig. 5. Experimental test rig for identification of bearing coefficients. (1) Electro magnetic shaker. (2) Stator housing. (3) Proximity probe. (4) Rotor disk with stator inner part.

Table 1. Geometry, material properties and operating conditions of the Siemens air foil bearing.

Parameters	Values
Bearing radius, R	33.50 mm
Bearing length, L	53.00 mm
Bearing radial clearance, C	40 μm
Number of pads, N_p	3
First pad leading edge, θ_l	30 deg
First pad trailing edge, θ_t	145 deg
Slope extend, θ_s	30 deg
Slope, h_s	50 μm
Bump foil thickness, t_b	0.127 mm
Top foil thickness, t_t	0.254 mm
Bump foil pitch, S	7.00 mm
Bump foil half length, l_0	3.30 mm
Bump foil height, h_b	0.9 mm
Young's modulus of bump foil, E	2.07×10^{11} Pa
Poisson's ratio of bump foil, ν	0.3
Foil friction coefficient, μ_f	0.2
Ambient pressure, p_a	1×10^5 Pa
Air viscosity, μ	1.95×10^{-5} Pa·s

is more than twice the 1X excitation frequency at maximum speed, hence the shaft can be treated as rigid in the operational speed range. The entire rotor assembly is balanced to below ISO grade G2.5.

4 Identification procedure

The identification of the linearised bearing coefficients, of the two bearings A and B, is achieved using frequency domain techniques combined with the method of structural joint parameter identification procedure [41, 42]. Harmonic forcing excitation is applied in the individual excitation points AE, BE of the rotor, while simultaneously obtaining the vibrations in the position sensor locations AP, BP as illustrated in Figure 6. Values of all

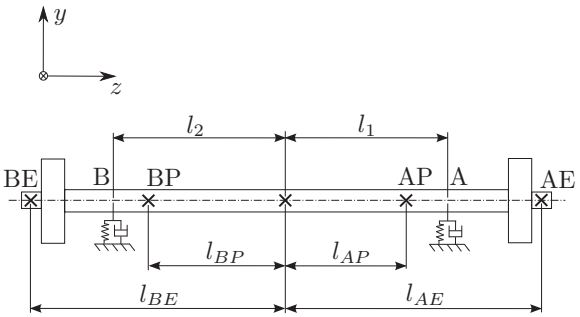

Fig. 6. Schematics and position nomenclature of the test shaft.

Table 2. Geometry and parameters for the identification.

Parameters	Values
l_1	201.1 mm
l_2	197.9 mm
l_{AP}	163.1 mm
l_{BP}	158.4 mm
l_{AE}	287.2 mm
l_{BE}	304.0 mm
$m = m_x = m_y$	21.1166 kg
$I_{xx} = I_{yy}$	525.166×10^{-3} kg.m^2
I_{zz}	30.079×10^{-3} kg.m^2

relevant parameters, for the identification, are listed in Table 2.

The relation between excitation forcing and the mechanical vibrations are

$$[H_{EP}]\{f_E\} = \{q_P\}, \tag{12}$$

where $[H_{EP}]$ is the FRF matrix which is determined experimentally (see Appendices A and B) and $\{f_E\} = \{f_{AEx}, f_{AEy}, f_{BEx}, f_{BEy}\}^T$ and $\{q_P\} = \{q_{APx}, q_{APy}, q_{BPx}, q_{BPy}\}^T$ are the complex force and deflection vectors respectively. The FRF matrix (12) can be transformed to relate the forcing and mechanical vibrations to the bearing locations A and B

$$[H_{AB}]\{f\} = \{q\} \tag{13}$$

where

$$\begin{aligned}[H_{AB}] &= [T_1][H_{EP}][T_2]^{-1} \\ \{f\} &= \{f_{Ax}, f_{Ay}, f_{Bx}, f_{By}\}^T \\ \{q\} &= \{q_{Ax}, q_{Ay}, q_{Bx}, q_{By}\}^T. \end{aligned} \tag{14}$$

The transformation matrices $[T_1]$ and $[T_2]$ are given in Appendix A. The equation of motion of the rotor-bearing system can be written as

$$[M]\{\ddot{q}\} + ([C] + [C_b])\{\dot{q}\} + ([K] + [K_b])\{q\} = \{f\} \tag{15}$$

where $[M]$, $[C]$ and $[K]$ are the mass, damping and stiffness matrices of the rotor alone, and $[C_b]$ and $[K_b]$ are

the damping and stiffness contributions from the bearings. The dynamic stiffness of the rotor-bearing system can then be stated as

$$[H_{AB}]^{-1} = -\omega^2 [M] + i\omega([C] + [C_b]) + ([K] + [K_b]). \quad (16)$$

Since $[H_{AB}]$ is obtained experimentally, the stiffness and damping of the bearings can be obtained as

$$[K_b] + i\omega [C_b] = [H_{AB}]^{-1} - [H^r_{AB}]^{-1} \quad (17)$$

where $[H^r_{AB}]^{-1}$ is the dynamic stiffness matrix of the rotor without bearings which can be obtained theoretically as shown in Appendix A.

4.1 Uncertainty analysis

If the values of the matrices $[H_{AB}]$ and $[H^r_{AB}]$ are exactly known, then from (17), the bearing coefficients can be exactly identified too, since no approximations have been introduced. However, both matrices are associated with uncertainties. The matrix $[H_{AB}]$ is associated with measurement uncertainties and the matrix $[H^r_{AB}]$ is associated with modelling uncertainties. The systematic uncertainties of both have been evaluated using standard statistical methods as described in [43,44]. Specifically, a computerized uncertainty analysis is imposed where the uncertainty of all variables, i.e. measurement transducers and geometrical properties like mass, inertia and lengths associated with the identification procedure is taken into account. The identified uncertainties are relatively small, generally below 25%. It should be kept in mind though, that this is under the assumption that the dynamics of the test rig can be precisely described by the mathematical model given in Appendix A i.e. the higher order (non-modelled) dynamics does not play a role in the frequency range of interest. Any mechanical effects not described by the mathematical model may result in significant uncertainties, higher than what has been estimated.

5 Results

The experimental results obtained from the test rig are compared to theoretical predictions based on the mathematical model represented by the zeroth and first order Equations (7) and (8), respectively. In this comparison, the compliant height h_c is based on both the compliance (11) given by Walowit and Anno [3] as well as the structural finite element model illustrated in Figure 4 and derived in [27].

5.1 Experimental results

The first four eigenfrequencies of the rotor-bearing system are identified between 90 and 210 Hz for the entire speed range. As mentioned, the test rig is operated below its first bending mode so the corresponding eigenmodes

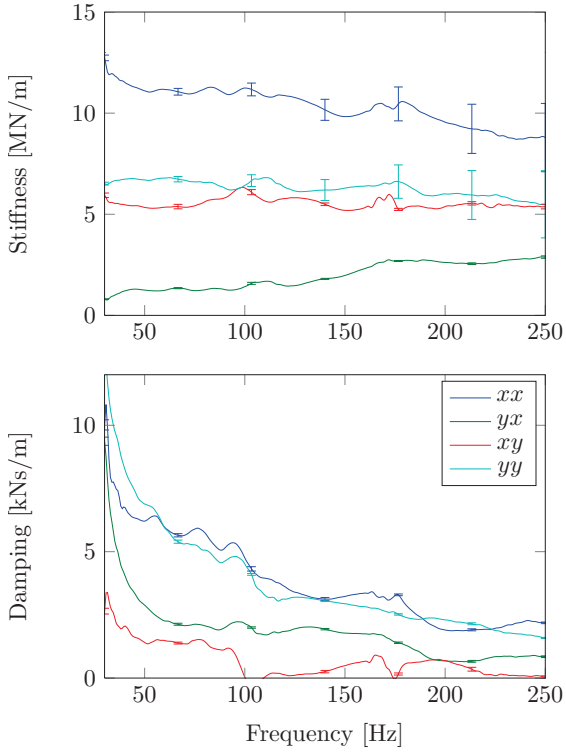

Fig. 7. Experimentally obtained linear bearing coefficients versus excitation frequency ω_s, and the associated uncertainties, experimentally obtained at 20 000 RPM for bearing B.

are a barrel and a conical mode with respectively backward and forward precession. Validation of the mathematical model is of particular interest around these modes, as they can potentially become unstable during operation. Therefore, the experimental identification of the bearing coefficients is carried out in the frequency range 25–250 Hz. Validation at the synchronous frequency is desirable too, but identification close to and at the synchronous frequency turned out difficult and even impossible with the current test setup. The shaft vibration amplitudes are below 5 μm 0-p meaning that the mechanical and magnetic run-out becomes significant. The frequency domain based method, described here, cannot compensate for the run-out or mass imbalance. They both results in fundamental vibration components at the synchronous frequency. This is the main reason for not identifying coefficients at synchronous frequency. In order to obtain the synchronous bearing coefficients with the current test rig, a very accurate run-out compensation, requiring additional instrumentation is necessary, and the knowledge of the exact rotor mass imbalance and the vibrations caused by the excitation bearing arrangement should be known. Hence it is decided to focus on the sub-synchronous frequency range around the rigid modes only. In Figure 7, the identified coefficients, at 20 kRPM for bearing B, are illustrated. Results for bearing A are very similar.

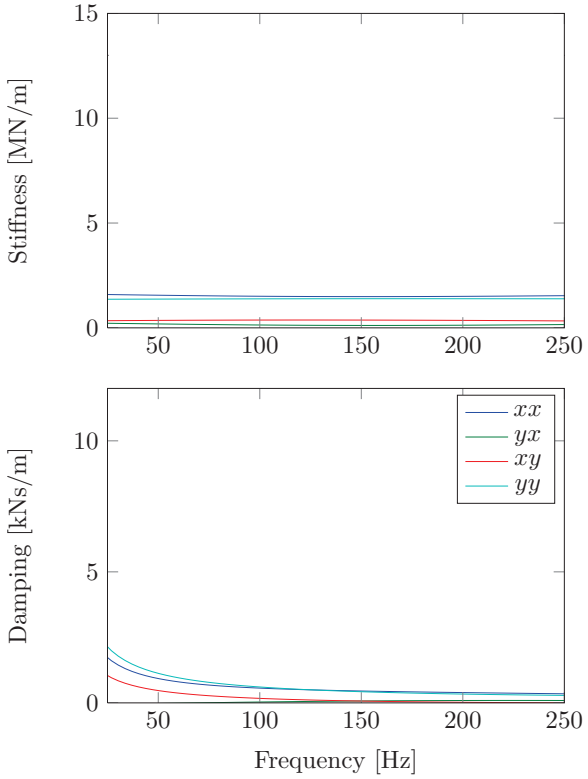

Fig. 8. Theoretically predicted linear bearing coefficients versus excitation frequency ω_s predicted at 20 000 RPM with the simple elastic foundation model ($\eta = 0.25$).

All cross coupled stiffness and damping coefficients are positive in this sub-synchronous frequency range which is likely a consequence of the segmented bearing geometry. The stiffness coefficients are flat over the frequency range, whereas the damping is found to decrease asymptotically towards low values as the excitation frequency approaches the rotational frequency. The systematic uncertainties are seen to be low for all coefficients except for the direct stiffness coefficients at higher speeds. As mentioned, these uncertainties exclude the effects of "un-modelled" dynamics in the identification procedure.

Coefficients are identified at rotor speeds from 16 kRPM up to 25 kRPM and only minor differences are observed. The focus in this paper is therefore limited to one operating speed only i.e. 20 kRPM.

5.2 Theoretical results

By using the SEFM, as given in (7) to (9), with a foil flexibility based on (11), a set of bearing coefficients is obtained. The coefficients are illustrated in Figure 8. Comparing these coefficients to those experimentally obtained, a qualitative similarity is seen. However, the quantitative discrepancies are large. The SEFM significantly under predicts the bearing coefficients.

Table 3. Predicted steady state eccentricity ratios using SEFM and CFSM, respectively.

Method	ε_{x_0}	ε_{y_0}
SEFM	1.8511	0.2884
CFSM	1.0625	0.2480

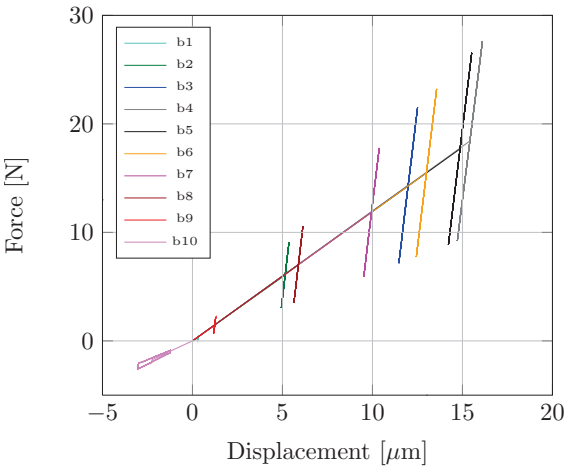

Fig. 9. Calculated load displacement diagram for each of the 10 bumps under the second pad. Low slope $\mu_f = 0$, high slope $\mu_f = 0.2$.

As mentioned in Section 2.2, solving for a steady state solution, using the CFSM with a coefficient of friction $\mu_f \neq 0$, may lead to several solutions. Therefore, the coefficient of friction is set to zero when solving for the steady state solution. The resulting shaft eccentricity ratios predicted by using the two different methods are listed in Table 3.

Though it is not possible to measure the shaft eccentricity ratios experimentally, it is assumed that the results of the CFSM are the most accurate since this model is more detailed. Furthermore, previous comparisons have proven that the bump foil stiffness is far under estimated by the SEFM [27], hence the large difference in the shaft eccentricity ratios as illustrated in Table 3.

Having a steady state solution of better accuracy, the first order equation is solved with a flexibility based on the slope represented by k_d, as illustrated in Figure 3, to yield the linearised coefficients. The steady state load on all pads and hence all bumps are then known, so a separate foil calculation can be performed in which the load is applied gradually with $\mu_f = 0$ until the steady state load is achieved. At this point, the foil deflection is equal to the results of the CFSM. Then by performing simultaneous load oscillations with an amplitude equal to a fraction of the steady state loads and with $\mu_f = 0.2$ [27], the flexibility for each bump is found. The resulting load displacement diagram for each of the bumps under the second bearing pad (the loaded pad) is illustrated in Figure 9. Here, the amplitudes of the individual load oscillations are given as $\{f_{b_0}\}/2$, where $\{f_{b_0}\}$ is the vector

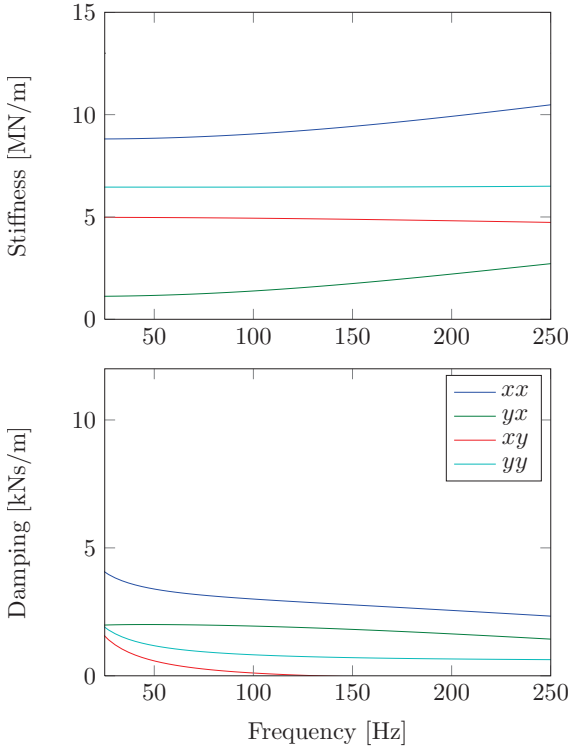

Fig. 10. Theoretically predicted linear bearing coefficients versus excitation frequency ω_s predicted at 20 000 RPM using the CFSM ($\eta = 0.25$).

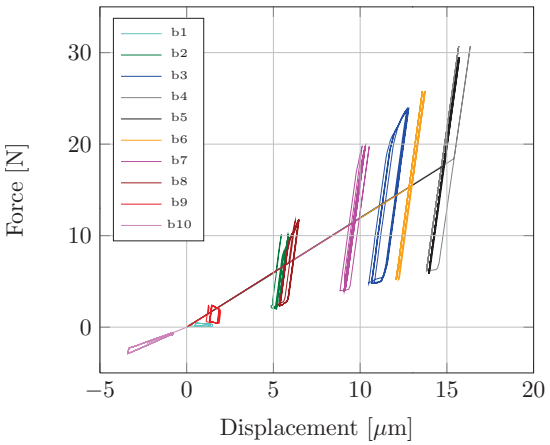

Fig. 11. Load displacement diagram for each of the 10 bumps under the second pad. Low slope $\mu_f = 0$, high slope $\mu_f = 0.2$.

containing the radial reaction forces at the top of the bumps (in the contact between bump and top foil). The slope related to the oscillations is found to be approximately a factor of 10 higher than the steady state slope. With the flexibility K, in the first order Equation (8), based on this, the bearing coefficients are recalculated. The result is illustrated in Figure 10. Comparing the stiffness coefficients obtained using the CFSM, against the coefficients experimentally obtained, presented in Figure 7, shows good agreement. However, discrepancies are seen when comparing the damping coefficients. Even though a loss factor of $\eta = 0.25$ is used when solving the first order equation, the experimentally identified damping coefficients are generally higher than the theoretically predicted. This is especially evident for the direct damping coefficient in the y direction, and generally at lower frequencies. It is important to highlight, that the choice of the structural loss factor $\eta = 0.25$ is based partly on a guess and partly on previous investigations [37, 45]. However, the equivalent structural loss factor is strongly dependant on both frequency and displacement amplitude. The latter is clearly seen in Figure 11 where the load/deflection amplitude is increased, compared to Figure 9.

It is clear that the area covered by the hysteresis loops increases leading to more energy dissipation. This increase in energy dissipation does not follow a linear relationship with the size of deflection amplitude [27]. In fact, a small increase in deflection amplitude can lead to a 10 times higher energy dissipation.

Choosing a higher structural loss factor $\eta = 0.8$ is found to increase the overall damping coefficients without significantly altering the calculated stiffness coefficients. This is illustrated in Figure 12. However, the direct damping coefficient in the horizontal direction is still under predicted.

Parametric studies indicates that the parameter h_s, which defines the slope height at the leading edge of each pad, is quite important (see Fig. 3). In the Siemens bearing design, this slope height is originally introduced to avoid rotor to stator contact. The leading edge of the pads is not flexible due to the foil fixation arrangement. Hence the leading edge needs to be detracted somewhat (h_s). In Figure 13, the stiffness and damping coefficients obtained theoretically using the nominal value $h_s = 50$ μm as well as a smaller value $h_s = 5$ μm are compared.

Both the stiffness and damping coefficients are clearly altered by the variations in h_s. In fact, discarding the slope in the theoretical model leads to large deviations in the bearing coefficients when compared to experimentally obtained results.

6 Conclusion

Experimentally obtained bearing coefficients of an air foil bearing are presented and compared to theoretical predictions. The theoretical predictions are based on the simple elastic foundation model as well as an improved model implementing a detailed foil structure finite element formulation [39] coupled with the zeroth order steady state equation. The finite element formulation takes into account large deflections and friction in the sliding contact points.

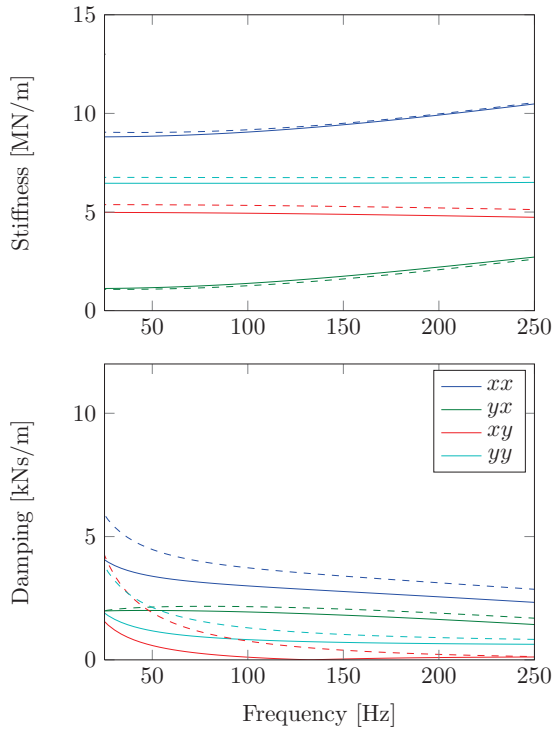

Fig. 12. Theoretically predicted linear bearing coefficients versus excitation frequency ω_s predicted at 20 000 RPM using the CFSM. Solid lines $\eta = 0.25$, dashed lines $\eta = 0.80$.

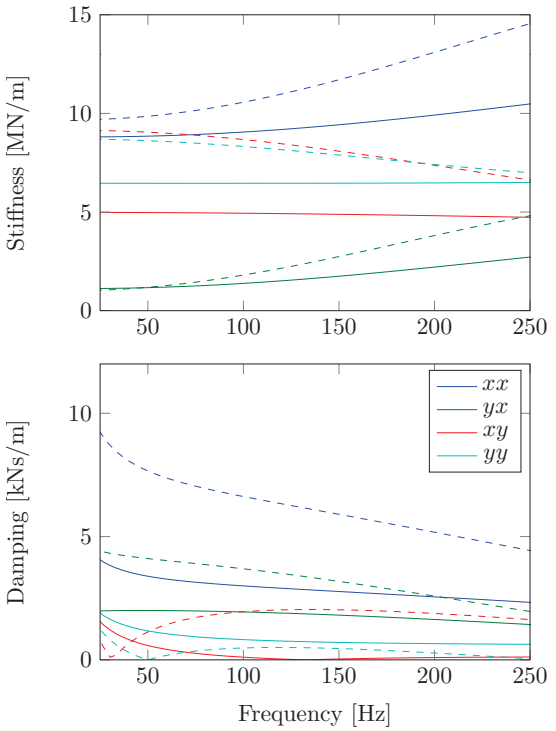

Fig. 13. Theoretically predicted linear bearing coefficients versus excitation frequency ω_s predicted at 20 000 RPM using the CFSM ($\eta = 0.25$). Solid lines $h_s = 50$ μm, dashed lines $h_s = 5$ μm.

Results of the structural foil model indicate the need to distinguish between the static and dynamic stiffness of the foil structure when solving the zeroth and first order equations respectively. Ignoring this, by using the simple elastic foundation model with a constant foil stiffness, a poor agreement between theoretical predictions and experimental results is observed. In contrast, by distinguishing between the static and dynamic foil stiffness, when solving the zeroth and first order equations respectively, the theoretically obtained coefficients show generally good agreement with the experimental results. However, a certain discrepancy related to the direct damping coefficient perpendicular to the loading direction is observed. This discrepancy cannot be explained by varying the equivalent loss factor alone. The loss factor is regarded constant for the entire foil structure. However, a lightly loaded pad can offer a significantly higher amount of damping than a heavily loaded pad since the sticking phase is less dominant [27]. This is also seen as the wider hysteresis loops occurring in the lower left of the load-displacement plot Figure 3. A more accurate method for predicting the damping should be established in future work.

Finally, the influence of the leading edge slope, related to the foil fixation arrangement, is investigated and found to affect the bearing coefficients significantly. Careful modelling of this part of the bearing geometry is therefore important.

Appendix A: Matrices

A.1 Transformation matrices

Relating the FRF matrix $[H_{EP}]$ to the bearings A and B can be achieved using the following transformation matrices:

$$[T_1] = \begin{bmatrix} a_1 & 0 & 1-a_1 & 0 \\ 0 & a_1 & 0 & 1-a_1 \\ a_2 & 0 & 1-a_2 & 0 \\ 0 & a_2 & 0 & 1-a_2 \end{bmatrix} \tag{A.1}$$

where $a_1 = \dfrac{l_2 + l_{AP}}{l}$, $a_2 = \dfrac{l_2 - l_{BP}}{l}$ and

$$[T_2] = \begin{bmatrix} a_3 & 0 & -a_5 & 0 \\ 0 & a_3 & 0 & -a_5 \\ -a_6 & 0 & a_4 & 0 \\ 0 & -a_6 & 0 & a_4 \end{bmatrix} \tag{A.2}$$

where $a_3 = \dfrac{l_{AE} + l_2}{l}$, $a_4 = \dfrac{l_{BE} + l_1}{l}$, $a_5 = \dfrac{l_{BE} - l_2}{l}$, $a_6 = \dfrac{l_{AE} - l_1}{l}$.

A.2 Rotor model matrices

The dynamic stiffness matrix of a rigid rotor without bearings can be written as:

$$[H^r_{AB}]^{-1} = -\omega^2 [M] - i\omega\Omega [G] \tag{A.3}$$

where

$$[M] = \frac{1}{l^2} \times \begin{bmatrix} l_2^2 m_x + I_{yy} & 0 & l_1 l_2 m_x - I_{yy} & 0 \\ 0 & l_2^2 m_y + I_{xx} & 0 & l_1 l_2 m_y - I_{xx} \\ l_1 l_2 m_x - I_{yy} & 0 & l_1^2 m_x + I_{yy} & 0 \\ 0 & l_1 l_2 m_y - I_{xx} & 0 & l_1^2 m_y + I_{xx} \end{bmatrix} \tag{A.4}$$

$$[G] = \frac{1}{l^2} \begin{bmatrix} 0 & -I_{zz} & 0 & I_{zz} \\ I_{zz} & 0 & -I_{zz} & 0 \\ 0 & I_{zz} & 0 & -I_{zz} \\ -I_{zz} & 0 & I_{zz} & 0 \end{bmatrix} \tag{A.5}$$

A.3 Experimental FRF matrix

The experimentally obtained FRF matrix $[H_{EP}]$ are defined as:

$$[H_{EP}] = \begin{bmatrix} f_{E_1 q_{P_1}} & f_{E_2 q_{P_1}} & f_{E_3 q_{P_1}} & f_{E_4 q_{P_1}} \\ f_{E_1 q_{P_2}} & f_{E_2 q_{P_2}} & f_{E_3 q_{P_2}} & f_{E_4 q_{P_2}} \\ f_{E_1 q_{P_3}} & f_{E_2 q_{P_3}} & f_{E_3 q_{P_3}} & f_{E_4 q_{P_3}} \\ f_{E_1 q_{P_4}} & f_{E_2 q_{P_4}} & f_{E_3 q_{P_4}} & f_{E_4 q_{P_4}} \end{bmatrix} \tag{A.6}$$

where each of the individual FRF's $f_{E_j q_{P_i}}$ are obtained experimentally and illustrated in Appendix B.

Appendix B: Experimental FRF

The experimental frequency response functions (FRF's) are obtained by linear 5–300 Hz chirp excitation with a duration of 9.5 s. All signals were simultaneously sampled at a frequency of 1706 Hz. To cancel out measurement noise, each FRF consists of an average of 50 measurements (individual chirps). 1024 points were used in the FFT and 512 overlaps when calculating the auto power and cross power spectrum for each FRF.

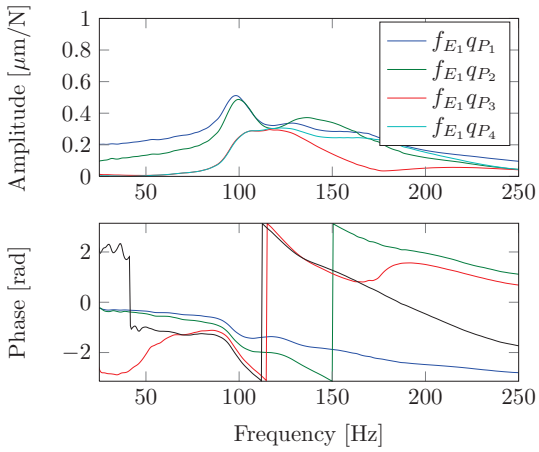

Fig. 14. Experimentally obtained FRF's (amplitude and phase). Excitation in point AE in horizontal (x) direction.

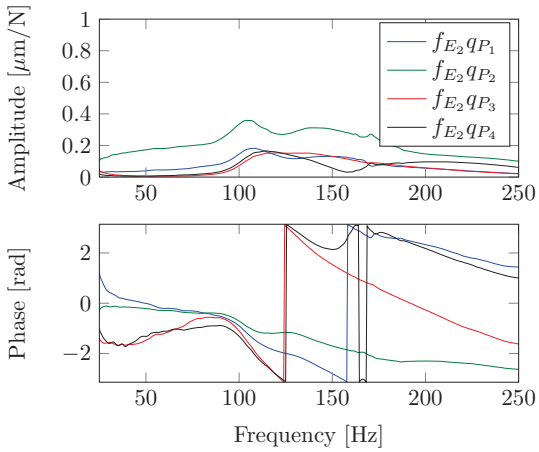

Fig. 15. Experimentally obtained FRF's (amplitude and phase). Excitation in point AE in vertical (y) direction.

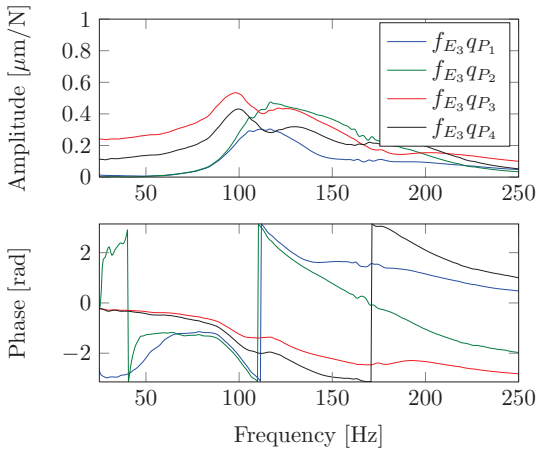

Fig. 16. Experimentally obtained FRF's (amplitude and phase). Excitation in point BE in horizontal (x) direction.

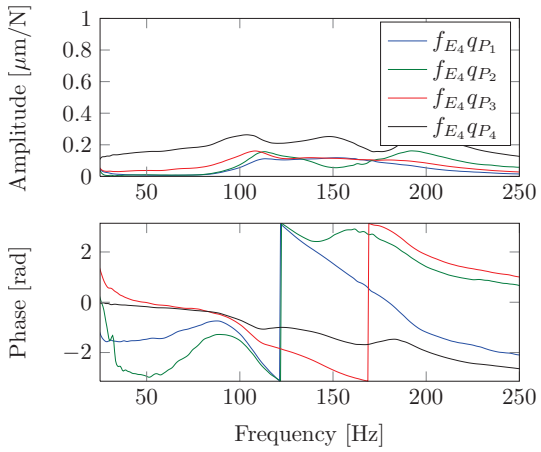

Fig. 17. Experimentally obtained FRF's (amplitude and phase). Excitation in point BE in vertical (y) direction.

References

[1] H. Heshmat, J.A. Walowit, O. Pinkus, Analysis of gas lubricated compliant thrust bearings, J. Lubrication Technol. 105 (1983) 638–646

[2] H. Heshmat, J.A. Walowit, O. Pinkus, Analysis of gas-lubricated foil journal bearings, J. Lubr. Technol. 105 (1983) 647–655

[3] J.A. Walowit, J.N. Anno, Modern developments in lubrication mechanics, Applied Science Publishers, London, 1975

[4] I. Iordanoff, Analysis of an aerodynamic compliant foil thrust bearing: method for a rapid design, J. Tribol. 121 (1999) 816–822

[5] J.P. Peng, M. Carpino, Calculation of stiffness and damping coefficients for elastically supported gas foil bearings, J. Tribol. 115 (1993) 20–27

[6] J.W. Lund, Calculation of stiffness and damping properties of gas bearings, J. Lubr. Technol. 1968, pp. 793–804

[7] T.H. Kim, L. San Andrés, Analysis of advanced gas foil bearings with piecewise linear elastic supports, Tribol. Int. 40 (2007) 1239–1245

[8] L. San Andrés, T.H. Kim, Improvements to the analysis of gas foil bearings: integration of top foil 1d and 2d structural models, 2007

[9] L San Andrés, T.H. Kim, Analysis of gas foil bearings integrating fe top foil models, Tribol. Int. 42 (2009) 111–120

[10] D. Ruscitto, J. Mc Cormick, S. Gray, Hydrodynamic air lubricated compliant surface bearing for an automotive gas turbine engine i - journal bearing performance, Technical Report NASA CR-135368, 1978

[11] M. Carpino, L.A. Medvetz, J.-P. Peng, Effects of membrane stresses in the prediction of foil bearing performance, Tribol. Trans. 37 (1994) 43–50

[12] J.P. Peng, M. Carpino, Coulomb friction damping effects in elastically supported gas foil bearings, Tribol. Trans. 37 (1994) 91–98

[13] J.P. Peng, M. Carpino, Finite element approach to the prediction of foil bearing rotor dynamic coefficients, J. Tribol. 119 (1997) 85–90

[14] C.A. Heshmat, D.S. Xu, H. Heshmat, Analysis of gas lubricated foil thrust bearings using coupled finite element and finite difference methods, J. Tribol. 122 (2000) 199–204

[15] D. Lee, Y.-C. Kim, K.-W. Kim, The dynamic performance analysis of foil journal bearings considering Coulomb friction: Rotating unbalance response, Tribol. Trans. 52 146–156 (2009)

[16] D.-H. Lee, Y.-C. Kim, K.-W. Kim, The static performance analysis of foil journal bearings considering three-dimensional shape of the foil structure, J. Tribol. 130 (2008) 031102

[17] S. Le Lez, M. Arghir, J. Frene, A new bump-type foil bearing structure analytical model, J. Eng. Gas Turbines Power 129 (2007) 1047–1057

[18] S. Le Lez, M. Arghir, J. Frene, A dynamic model for dissipative structures used in bump-type foil bearings, Tribol. Trans. 52 (2008) 36–46

[19] K. Feng, S. Kaneko, Analytical model of bump-type foil bearings using a link-spring structure and a finite-element shell model, J. Tribol. 132 (2010) 021706

[20] B.T. Paulsen, S. Morosi, I.F. Santos, Static, dynamic, and thermal properties of compressible fluid film journal bearings, Tribol. Trans. 54 (2011) 282–299

[21] J.S. Larsen, I.F. Santos, Compliant foil journal bearings – investigation of dynamic properties, In Proceedings of 10. International Conference on Schwingungen in Rotierenden Maschinen (SIRM2013), pages 1–12, ISBN 978–3–00–038602–2, Berlin, Germany, 25-27 February, 2013

[22] C.-P.R. Ku, H. Heshmat, Compliant foil bearing structural stiffness analysis: Part i-theoretical model including strip and variable bump foil geometry, J. Tribol. 114 (1992) 394–400

[23] C.-P.R. Ku, H. Heshmat, Structural stiffness and Coulomb damping in compliant foil journal bearings: theoretical considerations, Tribol. Trans. 37 (1994) 525–533

[24] C.-P.R. Ku, H. Heshmat, Structural stiffness and Coulomb damping in compliant foil journal bearings: parametric studies, Tribol. Trans. 37 (1994) 455–462

[25] H. Heshmat, C.P. Ku, Structural damping of self-acting compliant foil journal bearings, J. Tribol. 116 (1994) 76–82

[26] C.-P.R. Ku, H. Heshmat, Effects of static load on dynamic structural properties in a flexible supported foil journal bearing, ASME Trans. J. Vib. Acoust. 116 (1994) 257–262

[27] J.S. Larsen, A.C. Varela, I.F. Santos, Numerical and experimental investigation of bump foil mechanical behaviour, Tribol. Int. 74 (2014) 46–56

[28] C.-P.R. Ku, H. Heshmat, Compliant foil bearing structural stiffness analysis. ii: Experimental investigation, J. Tribol. 115 (1993) 364–369

[29] L. San Andrés, D. Rubio, T.H. Kim, Rotordynamic performance of a rotor supported on bump type foil gas bearings: experiments and predictions, J. Eng. Gas Turbines Power 129 (2007) 850–857

[30] C. DellaCorte, M.J. Valco, Load capacity estimation of foil air journal bearings for oil–free turbomachinery applications, Tribol. Trans. 43 (2000) 795–801

[31] S.A. Howard, Misalignment in gas foil journal bearings: An experimental study, J. Eng. Gas Turbines Power 131 (2009) 022501

[32] S.A. Howard, C. Dellacorte, M.J. Valco, J.M. Prahl, H. Heshmat, Steady-state stiffness of foil air journal bearings at elevated temperatures, Tribol. Trans. 44 (2001) 489–493

[33] S. Howard, C. Dellacorte, M.J. Valco, J.M. Prahl, H. Heshmat, Dynamic stiffness and damping characteristics of a high-temperature air foil journal bearing, Tribol. Trans. 44 (2001) 657–663

[34] P. Matta, M. Arghir, O. Bonneau, Experimental analysis of cylindrical air-bearing dynamic coefficients, Tribol. Trans. 53 (2010) 329–339

[35] B. Ertas, M. Drexel, J. Van Dam, D. Hallman, A general purpose test facility for evaluating gas lubricated journal bearings, J. Eng. Gas Turbines Power 131 (2009) 022502

[36] L. San Andrés, Hybrid flexure pivot-tilting pad gas bearings: analysis and experimental validation, J. Tribol. 128 (2006) 551–558

[37] D. Kim, Parametric studies on static and dynamic performance of air foil bearings with different top foil geometries and bump stiffness distributions, J. Tribol. 129 (2007) 354–364

[38] T.H. Kim, L. San Andrés, Heavily loaded gas foil bearings: A model anchored to test data, ASME Conference Proceedings 2005 (2005) 763–771

[39] J.S. Larsen, I.F. Santos, Efficient solution of the non-linear Reynolds equation for compressible fluid using the finite element method, J. Braz. Soc. Mecha. Sci. Eng., DOI: 10.1007/s40430-014-0220-5

[40] B.J. Hamrock, Fundamentals of Fluid Film Lubrication, McGRAW-HILL Series in Mechanical Engineering, McGRAW-HILL, Inc., New York, 1994

[41] P. Arumugam, S. Swarnamani, B.S. Prabhu, Experimental identification of linearized oil film coefficients of cylindrical and tilting pad bearings, J. Eng. Gas Turbines Power 117 (1995) 593–599

[42] J.X. Yuan, X.M. Wu, Identification of the joint structural parameters of machine tool by dds and fem, J. Eng. Ind. 107 (1985) 64–69

[43] R.J. Moffat, Describing the uncertainties in experimental results, Exp. Thermal Fluid Sci. 1 (1988) 3–17

[44] IEC BIPM, ILAC IFCC, IUPAP IUPAC, and OIML ISO. Evaluation of measurement data–guide for the expression of uncertainty in measurement, jcgm 100 (2008) 2008

[45] L. Rubio, D. San Andrés, Structural stiffness, dry friction coefficient, and equivalent viscous damping in a bump-type foil gas bearing, J. Eng. Gas Turbines Power 129 (2007) 494–502

[P5] On the Numerical Simulation of Nonlinear Transient Behavior of Compliant Air Foil Bearings

---

This paper has been submitted to and is going to be presented (by co-author) at the *11th International Conference on Schwingungen in Rotierenden Maschinen* (SIRM2015), Magdeburg, Germany, 23-25 February, 2015.

**SIRM 2015 – 11th International Conference on Vibrations in Rotating Machines,
Magdeburg, Deutschland, 23. – 25. February 2015**

On the Numerical Simulation of Nonlinear Transient Behavior of Compliant Air Foil Bearings

Jon S. Larsen [1,2], **Bo B. Nielsen** [2], **Ilmar F. Santos** [2]

[1] Siemens A/S - Aeration Competence Center, 3000 Helsingør, Denmark
[2] Department of Mechanical Engineering, Technical University of Denmark, 2900 Kgs. Lyngby, Denmark

Abstract

Compliant Air Foil Bearings (AFB) have fundamental importance in the development of high speed machines due to low friction and no need of an external lubrication system, leading to a more environmental-friendly design. Nevertheless, rotors supported by such a type of bearing are more sensitive to unbalance and nonlinear instabilities due to low level of damping.

The transient nonlinear behaviour of rotors supported by AFBs demands the solution of the Reynolds equation for compressible fluid coupled to the compliance of top/bump foil surfaces and the friction between parts of this complex flexible structure. The nonlinear transient simulation of rotors interacting with AFB is still a challenge and a very time-consuming task. In the particular case of assuming the variation of pressure in time dp/dt negligible, time simulations for predicting rotor-bearing transient behaviour can be carried out relatively safely and without numerical instability problems. Nevertheless, a precise and correct way of dealing with the nonlinear problem is taking into consideration the variation of pressure in time, i.e. dp/dt. In this framework, this paper gives an original contribution by implementing a method, as proposed in the literature, in which the variation of pressure in time dp/dt is included as part of the state space variable domain. It is extended to simulate the transient and nonlinear behaviour of an industrial AFB, built by three independent segments and coupled to a rigid rotor as used in a Siemens compressor. An efficient finite element model previously developed, is used for the discretisation of the pressure field and foil compliant structure.

The theoretical results are validated against the literature and the importance of the term dp/dt is carefully elucidated. A parameter study with focus on the transient nonlinear behavior of the rotor-bearing system is carried out and the efficiency of the method presented is discussed, highlighting advantages and drawbacks.

Nomenclature

$(\ddot{\cdot})$	Time derivative, $\frac{\partial^2}{\partial \tau^2}$
$(\dot{\cdot})$	Time derivative, $\frac{\partial}{\partial \tau}$
$(\,)^*$	Approximating field
A, B	Bearings
C	Radial clearance
E	Modulus of elasticity of foil
L, $\tilde{L}$	Bearing length, $\tilde{L} = L/R$
N_p	Number of pads
R	Journal radius
S	Bearing number, $S = \frac{6\mu\omega}{p_a}\left(\frac{R}{C}\right)^2$
S^e	Element surface
S_b	Bump foil pitch
V	Volume
W	Static load
b, $\tilde{b}$	Structural damping per unit area, $\tilde{b} = \frac{C}{p_a \omega} b$
e, ε	Journal eccentricity components, $\varepsilon = e/C$
h, $\tilde{h}$	Film height, $\tilde{h} = h/C$
$h_c, \tilde{h_c}$	Film height correction, $\tilde{h_c} = h_c/C$
$h_r, \tilde{h_r}$	Film height (rigid), $\tilde{h_r} = h_r/C$
$h_s, \tilde{h_s}$	Slope height, $\tilde{h_s} = h_s/C$
k, $\tilde{k}$	Structural stiffness per unit area, $\tilde{k} = \frac{C}{p_a} k$
l_1	Distance to Bearing A
l_2	Distance to Bearing B
p, $\tilde{p}$	Film pressure, $\tilde{p} = p/p_a$
p_a	Ambient pressure
t_b	Thickness of bump foil
t_t	Thickness of top foil
u	Unbalance kg·m
x, y, z	Cartesian coordinates
CG	Center of gravity
η	Structural loss factor of foils
μ	Dynamic viscosity
$\nabla\cdot$	Divergence
∇	Gradient, $\nabla = \left\{\frac{\partial}{\partial\theta},\ \frac{\partial}{\partial\tilde{z}}\right\}$

ν Poisson's ratio of foil
ω Angular speed of journal
ψ Film state variable
θ Circumferential angle
θ_l First pad leading edge angle
θ_s First pad slope extend
θ_t First pad trailing edge angle
$\tilde{\theta}$ Circumferential coordinate, $\tilde{\theta} = \theta R$
ξ, η Gauss points
t, τ Time, $\tau = \omega t$
$\{F_{ub}\}, \{\tilde{F_{ub}}\}$ Unbalance force vector, $\{\tilde{F_{ub}}\} = \frac{1}{p_a R^2}\{F_{ub}\}$
$\{F\}, \{\tilde{F}\}$ Bearing force vector, $\{\tilde{F}\} = \frac{1}{p_a R^2}\{F\}$
$\{R\}$ Residual vector
$\{S\}$ Advection vector, $\{S\} = \{S,\ 0\}^T$
$\{W\}, \{\tilde{W}\}$ Load vector, $\{\tilde{W}\} = \frac{1}{p_a R^2}\{W\}$
$\{\psi\}$ Film state vector
$\{\mathbf{n}\}$ Unit normal vector
$\{\tilde{h}_c\}$ Foil deformation vector
$\{\tilde{h}\}$ Height vector
$\{\tilde{p}\}$ Pressure vector
$\{\varepsilon\}$ Eccentricity vector
$\{y\}$ State vector
$\{z_1\}, \{z_2\}$ Rotor state vectors
$[A]$ Fluidity matrix
$[B]$ Shape function derivatives matrix
$[G]$, $[\tilde{G}]$ Gyroscopic matrix
$[M]$, $[\tilde{M}]$ Mass matrix
$[N]$ Shape function matrix

1 Introduction

Gas bearings have been intensively investigated, theoretically as well as experimentally, for over five decades [3, 20, 21] although some initial publications are dated already from the beginning of last century [7]. In order to deal with time consuming rotor-bearing dynamic analysis in time domain, linear damping and stiffness coefficients were introduced to predict rotor-bearing stability [16]. The rapid development of computer science and increasing computer power, later enabled the solution of the mathematical models in time, and allowed for the inclusion of gas compressibility and foil compliance in the models. Although almost a century has passed since the first publications about gas bearings, the accurate time simulation of gas bearings with compliant surfaces is still a challenging and very time consuming task.

Prior to the presented work, different approaches for solving the compressible Reynolds equation has been investigated. Among others Wang and Chen [22] who used finite difference for the spatial and temporal dimensions when solving the Reynolds equation. They simulated the steady-state response of a perfectly balanced rigid rotor supported by two identical bearings. The spatial discretisation was performed with a central-difference scheme, while the temporal discretisation was performed with an implicit-backward-difference scheme. Furthermore, Successive Over Relaxation (SOR) was used in order to reduce the number of unknowns in the iteration step. Their solution took advantages of the bearings being rigid, hence only the rotor movement contributed to dh/dt. This made an explicit solution of the transient compressible Reynolds equation possible since a movement of the rotor resulted in a change in the gap and then a change in pressure, which then again affected the rotor.

Arghir *et al.* [2] presented a finite volume solution, where the pressure was implicitly integrated for a prescribed gap perturbation to calculate linear stiffness and damping coefficients dependent on the perturbation amplitude. In the procedure, the rotor was stationary in one direction, while the other was perturbed by a sinusoidal displacement $A\sin(\omega t)$. At each time step, the reaction forces from the air film was calculated, including dp/dt, and based on the displacement/velocity and reaction force pairs, the least square method was used to calculate the linear stiffness and damping for a given amplitude A. This allowed a linear analysis of a rotor system to take into account the nonlinearities related to the vibration amplitude of the rotor in the air bearings. This method works well for calculating the linear coefficients in a bearing with gap discontinuities e.g. thrust bearing.

Song and Daejong [19] calculated the time dependent pressure in the next time step by explicit time integration, but by utilising the present and previous time step values for the gap size. As stated in the paper, this was done to reduce the computational time spend in each time step, but this also required very small time steps in order to minimize the error introduced when dp/dt and dh/dt are taken from different time steps. Le Lez *et al.* [14] used a similar method to [19]. This method was also used in [23] to solve the transient Reynolds equation, but with four-node planar finite elements for the spatial discretisation of the Reynolds equation and for a rigid gas journal bearing. Lee *et al.* [15] also used a four-node finite element to solve the compressible Reynolds equation in time and space and a backward-difference iterative procedure to solve the pressure in time. This solution was used in conjunction with a finite element model of the bump foil, affected by coulomb friction at the bump foils contact points, to investigate the performance of a rigid rotor symmetrically supported by two bearings under different bearing configurations.

More recently Bonello and Pham [4, 18] solved the nonlinear Reynolds equation by using an alternative state variable $\psi = ph$. Using this alternative state variable, it was possible to solve the Reynolds equation explicitly with

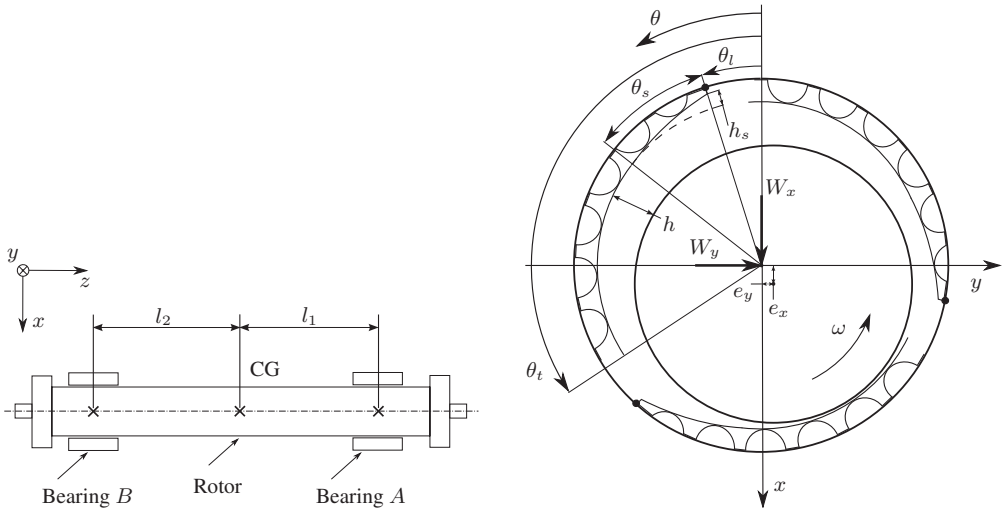

(a) Shaft and bearings.

(b) Detailed view of bearing geometry.

Figure 1: Schematics and nomenclature of a rigid rotor supported by foil journal bearings.

$d(ph)/dt$ calculated in the same time step. For spatial discretisation, a finite difference and Galerkin Reduction method were used. The solution for the transient compressible Reynolds equation was then coupled to the simple elastic foundation model, and the transient response of a rotor system was presented.

This paper is a continuation of the work done by the authors reported in [12], where the compressible Reynolds equation is solved for an equilibrium position and a perturbation method is used to obtain the linear stiffness and damping coefficients and perform rotor-bearing dynamic analyses. In this framework, this paper gives an original contribution to the time simulation of a rigid rotor supported by a set of industrial foil bearings. Bonello and Phams approach is used to properly solve the coupled equations of motion related to the time-dependent fluid film pressure and the rotor lateral movements. Instead of finite differences and Galerkin Reduction methods, the finite element method is used to evaluate the compressible Reynolds equation in time. The theoretical results are validated against the literature and the importance of the term dp/dt is carefully elucidated. A parameter study with focus on the transient nonlinear behaviour of the rotor-bearing system is carried out, and the efficiency of the method presented is discussed, highlighting advantages and drawbacks.

2 Mathematical model

In Fig. 1, the schematics of the rotor-bearing system is illustrated. With the nodal vector defined as $\{\varepsilon\} = \{\varepsilon_{Ax}, \varepsilon_{Ay}, \varepsilon_{Bx}, \varepsilon_{By}\}^T$ describing the instantaneous position of the shaft in the bearing locations A and B, and under the assumption; that the shaft is rigid and subjected to small rotations around x- and y-axis, its equations of motion can be written in dimensionless form as

$$[\tilde{M}]\{\ddot{\varepsilon}\} - [\tilde{G}]\{\dot{\varepsilon}\} = \{\tilde{W}\} - \{\tilde{F}\} + \{\tilde{F}_{ub}\}. \tag{1}$$

Here, the dimensionless mass and gyroscopic matrices, $[\tilde{M}]$ and $[\tilde{G}]$, are given in Appendix A, together with the mass unbalance vector $\{\tilde{F}_{ub}\}$. Furthermore, $\{\tilde{W}\}$ is the static load vector and $\{\tilde{F}\}^T = \{\{\tilde{F_A}\}^T, \{\tilde{F_B}\}^T\}^T$ is the reaction force vector stemming from the bearings. It is composed by the reactions from the bearings A and B, which are determined by integration of the fluid film pressure for each particular bearing as

$$\{\tilde{F}\} = \begin{Bmatrix} \tilde{F}_x \\ \tilde{F}_y \end{Bmatrix} = \int_0^{\tilde{L}} \int_0^{2\pi} (\tilde{p} - 1) \begin{Bmatrix} \cos(\theta) \\ \sin(\theta) \end{Bmatrix} d\theta d\tilde{z}. \tag{2}$$

The bearing pressures can be obtained by solving the Reynolds equation for compressible fluids for each bearing. This can be written dimensionless in vector form [6] as

$$\nabla \cdot \left(\tilde{p}\tilde{h}^3 \nabla \tilde{p}\right) = \nabla \cdot \left(\tilde{p}\tilde{h}\right) \{S\} + 2S \frac{\partial}{\partial \tau} \left(\tilde{p}\tilde{h}\right) \tag{3}$$

where the film height is defined as

$$\tilde{h}(\varepsilon_x, \varepsilon_y, \tilde{p}, \dot{\tilde{h}}_c) = \tilde{h}_r(\varepsilon_x, \varepsilon_y) + \tilde{h}_c(\tilde{p}, \dot{\tilde{h}}_c) \tag{4}$$

and $\tilde{h}_r(\varepsilon_x, \varepsilon_y)$ is the undeformed rigid height which depends of the rotor eccentricity and $\tilde{h}_c(\tilde{p}, \dot{\tilde{h}}_c)$ is a pressure dependent deformation in the foils referred to as the compliant height. For a bearing with the geometry as illustrated in Figure 1b and under the assumption of simple elastic foundation model [8, 9], expressions for these heights are given in Appendix B.

2.1 Solution strategy

The equations (1) through (4) constitutes the mathematical model for the rotor-bearing system. In order to simulate the nonlinear rotor response, a commonly used strategy is to rewrite (1) to a system of ODEs to be integrated while the bearing forces $\{\tilde{F}\}$ are updated at each time step. The bearing forces relates to the pressure, through (2), which is then obtained by solving (3). This can be accomplished by discretising the film PDE and substituting the time dependent terms by backward difference approximations as;

$$\frac{\partial\{\tilde{p}\}}{\partial\tau} \approx \frac{\{\tilde{p}\}_n - \{\tilde{p}\}_{n-1}}{\Delta\tau}, \quad \frac{\partial\{\tilde{h}\}}{\partial\tau} \approx \frac{\{\tilde{h}\}_n - \{\tilde{h}\}_{n-1}}{\Delta\tau}, \tag{5}$$

where n is the current time-step. The pressure can then be found by iteratively solving a set of nonlinear algebraic equations. Following the above described strategy, the time dependent terms are lagging behind in time since they are based on the previous time-step in the integration of the rotor ODEs. As pointed out by Bonello and Pham [4, 18], this method does not preserve the true simultaneously coupled nature of the state variables, $\varepsilon, \tilde{p}, \tilde{h}_c$, of the system. This means that very small time-steps are necessary in order to ensure an accurate solution. It makes the solution slow, and being strictly rigorous, each simulation should be accompanied by a convergence study on the time-step size to ensure an accurate solution.

Another problem with the above described solution strategy is the numerical stability. This is particularly related to the term $\partial\{\tilde{p}\}/\partial\tau$ which tends to become dominant and sensitive to the accuracy of $\{\tilde{p}\}_n - \{\tilde{p}\}_{n-1}$ due to the division by the very small number $\Delta\tau$. Assuming the term negligible is no option, simulations performed by Olsen [17] clearly showed that discarding this term leads to significant errors.

Bonello and Pham [4, 18] introduced a basic strategy to solve for all the state variables simultaneously and an efficient solution method based on a Gallerkin Reduction method to significantly limit the number of state-variables. Here, only the basic strategy is followed, which implies setting up one coupled system of nonlinear ODEs of the state variables $\varepsilon, \psi, \tilde{h}_c$, where $\psi = \tilde{p}\tilde{h}$.

2.2 Reynolds equation - discretisation

We discretise the PDE (3) using a standard Bubnov-Galerkin FE procedure with implementation of an isoparametric element formulation [5]. Firstly we perform a partial substitution with ψ to obtain

$$\nabla \cdot \left(\tilde{p}\tilde{h}^3 \nabla \tilde{p}\right) - \nabla \cdot \left(\tilde{p}\tilde{h}\right) \{S\} - 2S \frac{\partial \psi}{\partial \tau} = 0 \tag{6}$$

secondly, approximating fields $\tilde{p}^* = [N]\{\tilde{p}^e\}$ and $\dot{\psi}^* = [N]\{\dot{\psi}^e\}$ over the elements are introduced, where $\{\tilde{p}^e\}$ is the nodal pressures, $\{\dot{\psi}^e\}$ is the nodal film state variable and $[N]$ is the shape function matrix. Thus the Galerkin residual equation for (6), on the element level, is

$$\int_{V^e} [N]^T \nabla \cdot \left(\tilde{p}^* \tilde{h}^3 \nabla \tilde{p}^*\right) dV - \int_{V^e} [N]^T \nabla \cdot \left(\tilde{p}^* \tilde{h}\right) \{S\} dV - 2S \int_{V^e} [N]^T \dot{\psi}^* dV = \{0\} \tag{7}$$

where V^e is the element volume. Applying Greens theorem on (7) yields

$$\begin{aligned} -\int_{V^e}[B]^T\left(\tilde{p}^*\tilde{h}^3\nabla\tilde{p}^*\right)dV+\int_{V^e}[B]^T\left(\tilde{p}^*\tilde{h}\right)\{S\}dV-2S\int_{V^e}[N]^T\dot{\psi}^*dV \\ +\int_{S^e}[N]^T\left(\tilde{p}^*\tilde{h}^3\nabla\tilde{p}^*\right)\{\mathbf{n}\}dS-\int_{S^e}[N]^T\left(\tilde{p}^*\tilde{h}\right)\{S\}\{\mathbf{n}\}dS=\{0\} \end{aligned} \tag{8}$$

where matrix $[B]^T=\left[[N,_\theta]^T,\ [N,_{\tilde{z}}]^T\right]$ contains the spatial derivatives of the shape functions and $\{\mathbf{n}\}$ is the outward pointing unit normal vector of surface element dS. Due to continuity conditions, the boundary integrals vanishes and (8) reduces to

$$-\int_{V^e}[B]^T\left(\tilde{p}^*\tilde{h}^3\nabla\tilde{p}^*\right)dV+\int_{V^e}[B]^T\left(\tilde{p}^*\tilde{h}\right)\{S\}dV-2S\int_{V^e}[N]^T\dot{\psi}^*dV=\{0\}. \tag{9}$$

The spatial derivatives of the approximating pressure field are $\tilde{p}^*,_i=[N,_i]\{\tilde{p}^e\}$ with $i=\theta,\tilde{z}$ or in vector form, $\nabla\{\tilde{p}^*\}=[B]\{\tilde{p}^e\}$. Inserting this into (9) gives

$$[A^e]\{\dot{\psi}^e\}=\{R^e\} \tag{10}$$

where

$$\begin{aligned} [A^e]&=2S\int_{V^e}[N]^T[N]dV \\ \{R^e\}&=-\int_{V^e}[B]^T\tilde{p}^*\tilde{h}^3[B]dV\{\tilde{p}^e\}+\int_{V^e}[B]^T\{S\}\tilde{h}[N]dV\{\tilde{p}^e\}. \end{aligned} \tag{11}$$

The element vectors and matrices are expanded to structure size by the usual element summation:

$$\{R\}=\sum_e\{R^e\};\quad\{\tilde{p}\}=\sum_e\{\tilde{p}^e\};\quad\{\dot{\psi}\}=\sum_e\{\dot{\psi}^e\} \tag{12}$$

where the volume integrals are numerically integrated using a quadrature rule [5]. The scalar field quantities $\tilde{p}^*$, $\tilde{h}$, are calculated in the respective Gauss points (ξ_i,η_j) by use of the interpolation functions as:

$$q(\xi_i,\eta_j)=[N(\xi_i,\eta_j)]\{q^e\} \tag{13}$$

where q and $\{q^e\}$ are the scalar field quantities and nodal vectors respectively. Note that the right hand side of (10) is denoted $\{R^e\}$. In fact, $\{R^e\}$ is the residual that needs to be minimized in order to find the static equilibrium of the journal. When performing certain simulations in the time domain, it is very handy to start the simulations from this static equilibrium position. An efficient method for minimizing $\{R^e\}$ is given in [12].

2.3 Coupled system of ODEs

With the film PDE discretised, a system of ODEs of the form $\{\dot{y}\}=\mathbf{f}(\tau,\{y\})$ can be set up, and solved for all state variables simultaneously. The state-vector is defined as

$$\{y\}^T=\{\{\psi_A\}^T,\ \{\psi_B\}^T,\ \{\tilde{h}_{cA}\}^T,\ \{\tilde{h}_{cB}\}^T,\ \{z_1\}^T,\ \{z_2\}^T\}^T. \tag{14}$$

The right hand side $\mathbf{f}$ consists of three different equations. For each of the bearings A,B the film state is calculated by:

$$\{\dot{\psi}\}=[A]^{-1}\{R\}. \tag{15}$$

Vectorizing the pad deflection given in (26), the pad deflection for each of the bearings A, B is calculated by:

$$\{\dot{\tilde{h}}_c\} = \left(\frac{\{\tilde{p}\} - 1}{\tilde{k}} - \{\tilde{h}_c\} \right) \frac{1}{\eta} \tag{16}$$

and finally, the rotor state variables $\{z_1\} = \{\varepsilon\}$ and $\{z_2\} = \{\dot{\varepsilon}\}$ are calculated by:

$$\begin{Bmatrix} \{\dot{z}_1\} \\ \{\dot{z}_2\} \end{Bmatrix} = \begin{bmatrix} [0] & [I] \\ [0] & [\tilde{M}]^{-1}[\tilde{G}] \end{bmatrix} \begin{Bmatrix} \{z_1\} \\ \{z_2\} \end{Bmatrix} + \begin{Bmatrix} \{0\} \\ [\tilde{M}]^{-1}(\{\tilde{W}\} - \{\tilde{F}\} + \{\tilde{F_{ub}}\}) \end{Bmatrix}. \tag{17}$$

In this work, the system of ODEs are solved using the 'lsoda' solver from the Fortran library ODEPACK [10]. This solver has an automatic time-step control and switches between dedicated solvers for stiff and non-stiff systems. To efficiently solve the ODEs, a program for the discretisation and solution of (15) is implemented in C using the sparse solver DGBESV from the LaPack library [1]. However, the solution is still time consuming, and it should be highlighted, that Bonello and Pham [4, 18] significantly improved the solution efficiency by implementing a Galerkin reduction method.

2.4 Boundary conditions

In dimensionless form, the edge boundary conditions for the bearings, as depicted in Fig. 1b, are:

$$\begin{aligned} \tilde{p}(\theta_l, \tilde{z}) = \tilde{p}(\theta_t, \tilde{z}) = 1 \\ \tilde{p}(\theta, \tilde{L}/2) = \tilde{p}(\theta, -\tilde{L}/2) = 1. \end{aligned} \tag{18}$$

To obey these conditions, it is necessary to evaluate the film state variable $\dot{\psi} = \dot{\tilde{p}}h + \dot{\tilde{h}}p$. On the pad edges, we know that $\tilde{p} = 1$ and is constant so $\dot{\tilde{p}} = 0$. This means, that when solving (15) to obtain the film state variable, the following boundary conditions must be imposed:

$$\begin{aligned} \dot{\psi}(\theta_l, \tilde{z}) = \dot{\psi}(\theta_t, \tilde{z}) = \dot{\tilde{h}}(\dot{\varepsilon}_x, \dot{\varepsilon}_y, \dot{\tilde{h}}_c) \\ \dot{\psi}(\theta, \tilde{L}/2) = \dot{\psi}(\theta, -\tilde{L}/2) = \dot{\tilde{h}}(\dot{\varepsilon}_x, \dot{\varepsilon}_y, \dot{\tilde{h}}_c) \end{aligned} \tag{19}$$

which is achieved by using standard FE procedure. Symmetry conditions can be achieved by neglecting (19) on one side, e.g. on $(\theta, \tilde{L}/2)$. In this case, the reaction forces needs to be multiplied by two. A commonly used boundary condition [12], which is also used in this work, is to assume that the bearing foils deforms evenly over the length $\tilde{L}$ of the bearing. This condition is implemented by replacing $\{\tilde{p}\}$ in (16) by $\{\tilde{p}\}_m$, where $\{\tilde{p}\}_m$ is the arithmetic mean pressure over the length $\tilde{L}$.

In gas bearings, significant sub-ambient pressures may arise. These sub-ambient pressures can cause the top foil to separate from the bumps into a position in which the pressure on both sides of the pad are equalized. Heshmat [9] introduced a set of boundary conditions accounting for this separation effect. However, in this work, a simple Gümbel [6] boundary condition is imposed, which means that sub-ambient pressures are discarded when integrating the pressure (2) to obtain the bearing force components (W_x, W_y), essentially leaving the sub-ambient regions ineffective.

3 Results

As mentioned, the integration of (1) using a decoupled solution strategy, in which the time dependent terms of the Reynolds equation are approximated by backward difference approximations, can lead to numerical instability [17]. This problem is specifically related to the term dp/dt, hence it is interesting to investigate the significance of this term, in order to determine if it can be neglected in the simulations of the nonlinear rotor response.

Table 1: Geometry, material properties and operating conditions of a single pad foil bearing.

Parameters	Values	Parameters	Values
Bearing radius, R	19.05 mm	Young's modulus of bump foil, E	2.07×10^{11} Pa
Bearing length, L	38.10 mm	Poisson's ratio of bump foil, ν	0.3
Bearing clearance, C	32 μm	Loss factor, η	0.25
Bump foil thickness, t_b	0.1016 mm	Ambient pressure, P_a	1×10^5 Pa
Top foil thickness, t_t	0.2032 mm	Air viscosity, μ	1.95×10^{-5} Pa·s
Bump foil pitch, S_b	4.572 mm	Load, (W_x, W_y)	$(30, 0)$ N
Bump half length, l_0	1.778 mm	Speed, ω	$12,000$ RPM

Table 2: Geometry, material properties and operating conditions of the Siemens foil bearing test-rig

Parameters	Values	Parameters	Values
Bearing radius, R	33.50 mm	Bump foil height, h_b	0.9 mm
Bearing length, L	53.00 mm	Young's modulus of bump foil, E	2.07×10^{11} Pa
Bearing radial clearance, C	40 μm	Poisson's ratio of bump foil, ν	0.3
Number of pads, N_p	3	Foil friction coefficient, μ_f	0.2
First pad leading edge, θ_l	30 deg	Ambient pressure, p_a	1×10^5 Pa
First pad trailing edge, θ_t	145 deg	Air viscosity, μ	1.95×10^{-5} Pa·s
Slope extend, θ_s	30 deg	l_1	201.1 mm
Slope, h_s	50 μm	l_2	197.9 mm
Bump foil thickness, t_b	0.127 mm	$m = m_x = m_y$	21.1166 kg
Top foil thickness, t_t	0.254 mm	$I_{xx} = I_{yy}$	$525.166 \cdot 10^{-3}$ kgm^2
Bump foil pitch, S_b	7.00 mm	I_{zz}	$30.079 \cdot 10^{-3}$ kgm^2
Bump foil half length, l_0	3.30 mm		

3.1 Significance of dp/dt

To investigate the significance of the term dp/dt, a well known bearing geometry from the literature is simulated. Only a single bearing and a journal with two degrees of freedom are considered. The bearing geometry and operation conditions are listed in Tab. 1. The simulation is started at constant speed with the initial conditions $\{\varepsilon\} = \{\dot{\varepsilon}\} = \{0\}$, which in physical terms, corresponds to dropping the rotor from the center of the bearing. The result of this simulation is illustrated in Fig. 2. It is clear, that the two different solution strategies yields different results. Both yield the same equilibrium positions, but their transient trajectories toward this are different. Judging from the transient orbits, the journal-bearing system is less damped when including the term dp/dt. From Fig. 2, it is also seen that the calculations including the term dp/dt yields good agreement with similar results obtained by Pham and Bonello [4, 18]. The lower part of the trajectories coincide very well, but a slight discrepancy in the upper part is observed. This discrepancy could be due to different boundary conditions. For instance, a periodic boundary condition in the top of the bearing would cause the journal to lift higher on its way up, as found by Pham and Bonello [18].

3.2 Coupled rotor-bearing system

The rigid rotor-bearing system investigated in this paper (Fig. 1) is that of a test-rig designed for the identification of the linear bearing coefficients [11]. All parameters, operating conditions and dimensions are listed in Tab. 2. The authors wish to highlight, and reproduce by simulation, a phenomenon commonly seen when performing factory approval tests of compressors supported by AFBs. Specifically, the 'destabilizing effect' of rotor unbalance. First a perfectly balanced rotor, $\{F_{ub}\} = \{0\}$, is simulated at a variety of rotor speeds when dropped from the bearing centre i.e. $\{\varepsilon\} = \{\dot{\varepsilon}\} = \{0\}$. For these simulations, a foil stiffness of $k = 9.26$ GN/m^3 is used which is based on a structural finite element calculation of the foils [13] under the assumption of $\mu = 0.2$. At 30,000 RPM, the system is clearly unstable as illustrated in Fig. 3. At approximately 24,000 RPM, the system is marginally stable, and at 20,000 RPM the system is stable and quickly approaching its static equilibrium position as illustrated in Fig. 4. With the knowledge, that the perfectly balanced rotor-bearing system is stable at 20,000 RPM, a simulation with a different amount of unbalance applied is then performed. In Fig. 5, the orbit for bearing A and the associated frequency spectra for the two directions is illustrated with a rotor unbalance of $20\ \mathrm{g} \cdot \mathrm{mm}$ applied in each bearing 180 deg. out of phase. It is clear that the rotor-bearing system is still stable, moving in an almost circular orbit with the rotor running frequency (333 Hz).

Increasing the unbalance in each bearing to $40\ \mathrm{g} \cdot \mathrm{mm}$, an increase in the synchronous vibration components is

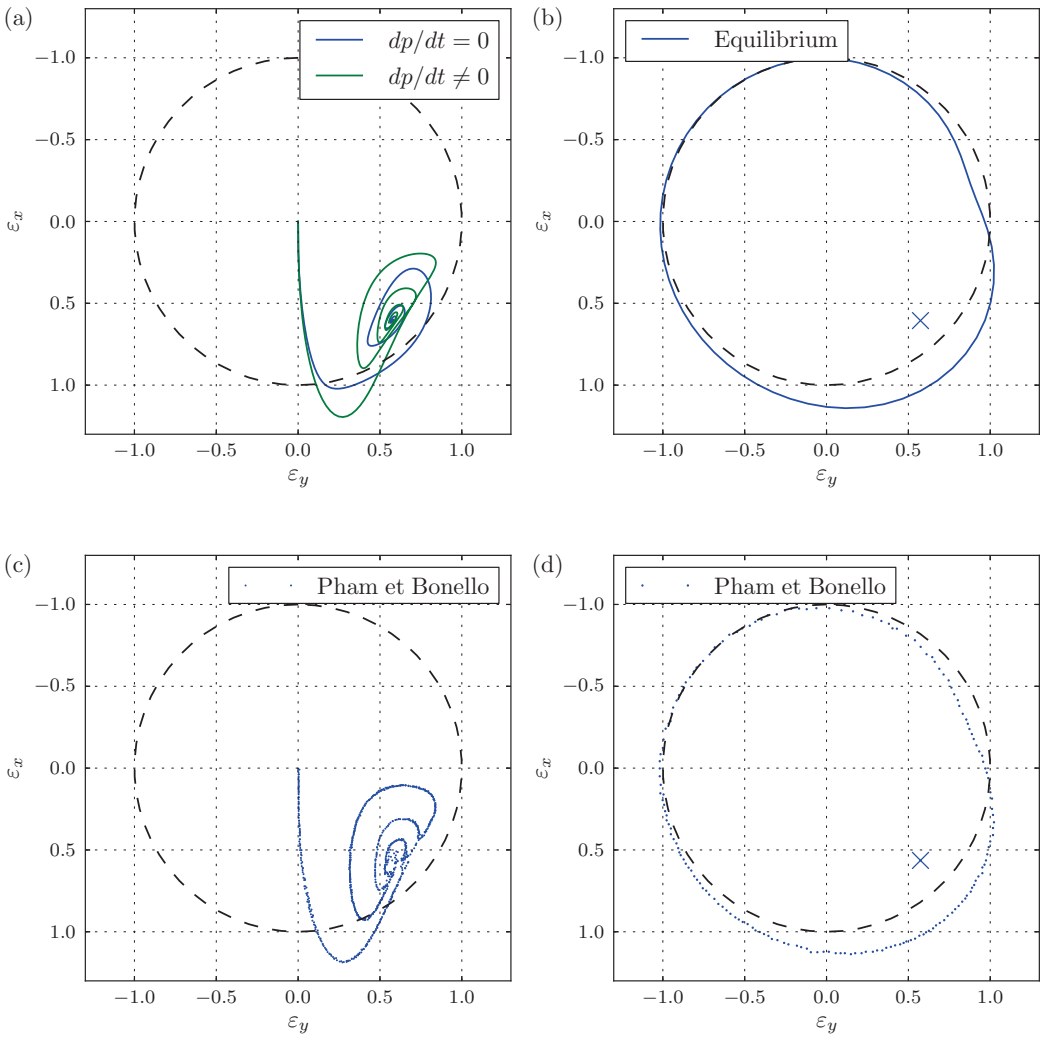

Figure 2: (a) Journal response when dropped from the bearing centre. The dashed line indicates the undeformed foil shape. (b) Deformed and undeformed foil shape at the static equilibrium. (c) and (d) Journal response results and foil deflection extracted from Pham and Bonello [4, 18].

observed, as illustrated in Fig. 6. Not unexpectedly, the synchronous vibrations amplitude grows to approximately twice the size, compared to the previous simulation, which had half the mass unbalance. What is less expected is the fact, that the rotor is now tracing a quasi-periodic orbit and as seen in the associated spectra, four sub-synchronous vibrations appears. With two of them having significant amplitudes at approximately 150 Hz and 195 Hz. Dependent on the general rotor and bearing geometry and the running conditions, these sub-synchronous vibrations can appear with very high amplitudes that can lead to bearing failures. In the simulated example the rotor unbalances are between ISO G2.5 and ISO G16 which are high unbalance levels for a rotor supported by foil bearings. A well designed rotor on foil bearings might be stable and trace an almost circular orbit, when the level of unbalance is within a safe range, usually ISO G2.5, but as shown, unstable when outside. Therefore, rotor balancing should be given great attention when mass-producing turbo machinery supported by AFBs.

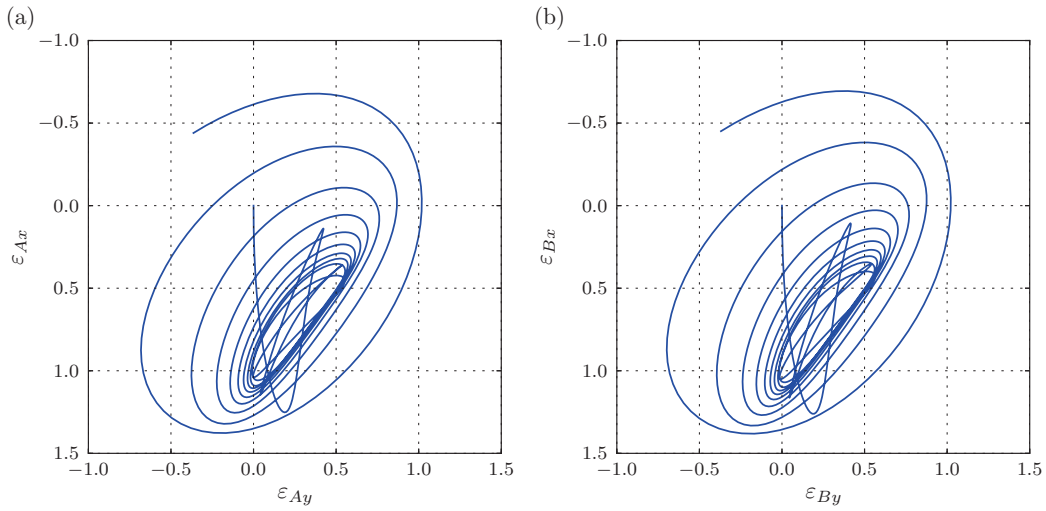

Figure 3: Journal response when dropped from the centre. (a) Bearing A. (b) Bearing B. $\omega = 30,000$ RPM.

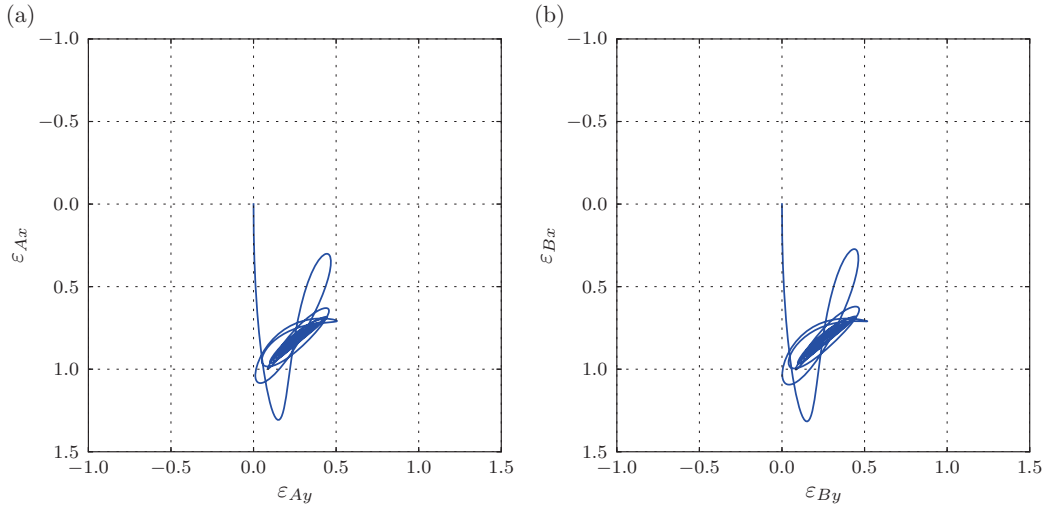

Figure 4: Journal response when dropped from the centre. (a) Bearing A. (b) Bearing B. $\omega = 20,000$ RPM.

4 Conclusion

A method [4, 18] for simulating the rotor response of a rigid rotor supported by AFBs were implemented and validated. The method, which solves for all state variables simultaneously, was compared to calculations in which the time dependent term dp/dt was neglected. The comparison clearly showed that neglecting dp/dt will lead to significant errors, and overestimation of the damping in the bearings.

The influence of rotor mass unbalance, on a rigid shaft supported by two identical AFBs, were investigated as well. This investigation highlighted the importance of balancing turbo machines to a high grade as unbalance can cause sub-synchronous vibrations to occur that can lead to bearing failures.

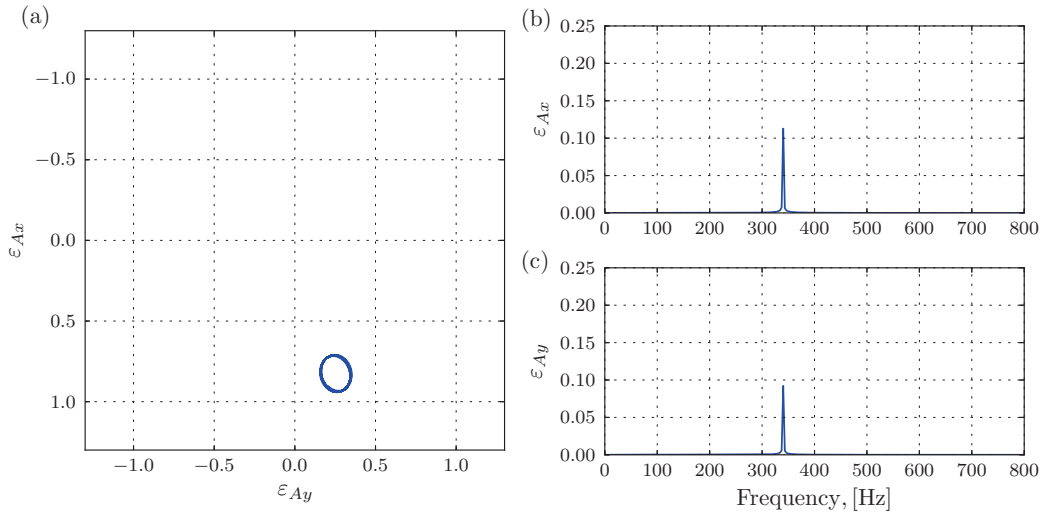

Figure 5: Journal steady state unbalance response after 1.5 s. (a) Bearing A. (b) Bearing B. $\omega = 20,000$ RPM.

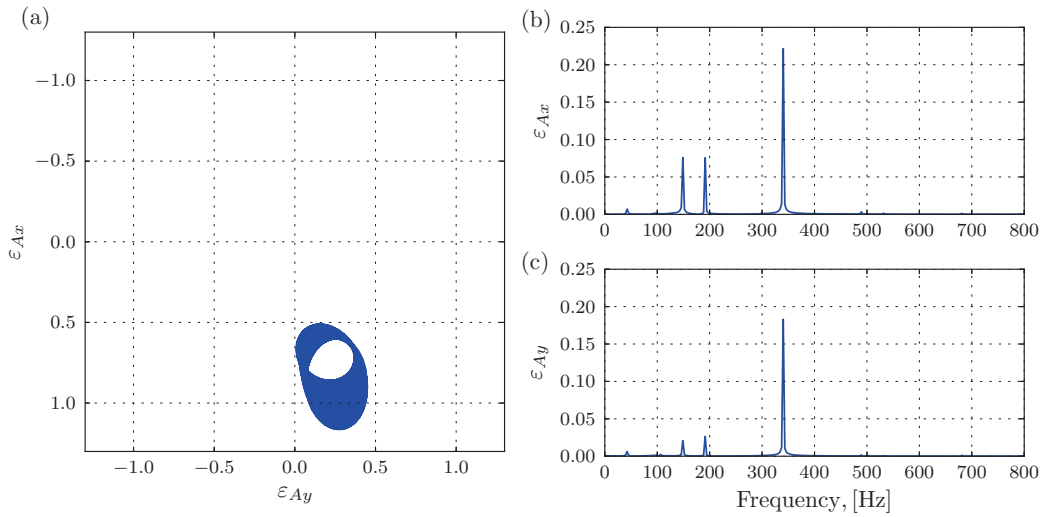

Figure 6: Journal steady state unbalance response after 1.5 s. (a) Bearing A. (b) Bearing B. $\omega = 20,000$ RPM.

A Rotor model matrices

The mass and gyroscopic matrices for a rigid rotor can be written as:

$$[M] = \frac{1}{l^2}\begin{bmatrix} l_2^2 m_x + I_{yy} & 0 & l_1 l_2 m_x - I_{yy} & 0 \\ 0 & l_2^2 m_y + I_{xx} & 0 & l_1 l_2 m_y - I_{xx} \\ l_1 l_2 m_x - I_{yy} & 0 & l_1^2 m_x + I_{yy} & 0 \\ 0 & l_1 l_2 m_y - I_{xx} & 0 & l_1^2 m_y + I_{xx} \end{bmatrix}, \quad [G] = \frac{1}{l^2}\begin{bmatrix} 0 & -I_{zz} & 0 & I_{zz} \\ I_{zz} & 0 & -I_{zz} & 0 \\ 0 & I_{zz} & 0 & -I_{zz} \\ -I_{zz} & 0 & I_{zz} & 0 \end{bmatrix} \tag{20}$$

The non-dimensional form of the mass and gyroscopic matrices and the mass unbalance vector are:

$$[\tilde{G}] = \frac{\omega^2 C}{p_a R^2}[G], \quad [\tilde{M}] = \frac{\omega^2 C}{p_a R^2}[M], \quad \{\tilde{F}_{ub}\} = \begin{Bmatrix} \frac{u_A \omega^2}{p_a R^2} \begin{Bmatrix} \cos(\tau) \\ \sin(\tau) \end{Bmatrix} \\ \frac{u_B \omega^2}{p_a R^2} \begin{Bmatrix} \cos(\tau) \\ \sin(\tau) \end{Bmatrix} \end{Bmatrix}. \tag{21}$$

B Film height

For a segmented journal bearing, with inlet slope and the nomenclature as illustrated in Fig. 1b, the dimensionless rigid film height can be written as:

$$\tilde{h}_r = \begin{cases} 1 + \varepsilon_x \cos(\theta) + \varepsilon_y \sin(\theta) - \tilde{h}_s \frac{\theta - \theta_i}{\theta_s}, & \theta_{li} \leq \theta \leq \theta_i \\ 1 + \varepsilon_x \cos(\theta) + \varepsilon_y \sin(\theta), & \theta_i < \theta \leq \theta_{ti} \end{cases} \tag{22}$$

where

$$\begin{aligned} \theta_i &= \theta_s + \theta_l + \frac{2\pi}{N_p}(i-1) \\ \theta_{li} &= \theta_l + \frac{2\pi}{N_p}(i-1) \\ \theta_{ti} &= \theta_t + \frac{2\pi}{N_p}(i-1) \end{aligned} \tag{23}$$

Discarding the mass of the foil structure, the equation of motion for the foil structure is:

$$\tilde{p} - 1 = \tilde{k}\tilde{h}_c + \tilde{b}\dot{\tilde{h}}_c \quad \text{or} \quad \tilde{h}_c(\tilde{p}, \dot{\tilde{h}}_c) = \frac{\tilde{p} - 1 - \tilde{b}\dot{\tilde{h}}_c}{\tilde{k}} \tag{24}$$

Introducing the mechanical loss factor

$$\eta = \frac{b\omega_s}{k} = \frac{\tilde{b}}{\tilde{k}}\frac{\omega_s}{\omega} \tag{25}$$

Inserting the loss factor into the foil equation of motion yields the first order ordinary differential equation:

$$\dot{\tilde{h}}_c = \left(\frac{\tilde{p} - 1}{\tilde{k}} - \tilde{h}_c\right)\frac{1}{\eta} \tag{26}$$

with $\omega_s/\omega = 1$ meaning the the vibrations in the foil are assumed synchronous.

REFERENCES

[1] E. Anderson, Z. Bai, C. Bischof, S. Blackford, J. Demmel, J. Dongarra, J. Du Croz, A. Greenbaum, S. Hammarling, A. McKenney, and D. Sorensen. *LAPACK Users' Guide*. Society for Industrial and Applied Mathematics, Philadelphia, PA, third edition, 1999.

[2] M. Arghir, S. Le Lez, and J. Frene. Finite-volume solution of the compressible reynolds equation: linear and non-linear analysis of gas bearings. *Proceedings of the Institution of Mechanical Engineers, Part J: Journal of Engineering Tribology*, 220(7):617–627, jan 2006.

[3] J. S. Ausman. An improved analytical solution for self-acting, gas-lubricated journal bearings of finite length. *Journal of Basic Engineering*, 83(2):188–192, 1961.

[4] P. Bonello and H. M. Pham. The efficient computation of the nonlinear dynamic response of a foil–air bearing rotor system. *Journal of Sound and Vibration*, 333(15):3459–3478, 2014.
[5] R. D. Cook, D. S. Malkus, M. E. Plesha, and J. W. Witt. *Concepts and applications of finite element analysis*. John Wiley, New York, 4 edition, 2002.
[6] B. J. Hamrock. *Fundamentals of Fluid Film Lubrication*. McGRAW-HILL Series in Mechanical Engineering. McGRAW-HILL, Inc., New York, 1994.
[7] W. J. Harrison. The hydrodynamical theory of lubrication with special reference to air as a lubricant. *Transactions Cambridge Philosophical Society*, 22:34–54, 1913.
[8] H. Heshmat, J. A. Walowit, and O. Pinkus. Analysis of gas lubricated compliant thrust bearings. *Journal of Lubrication Technology*, 105(4):638–646, 1983.
[9] H. Heshmat, J. A. Walowit, and O. Pinkus. Analysis of gas-lubricated foil journal bearings. *Journal of Lubrication Technology*, 105(4):647–655, 1983.
[10] A. C. Hindmarsh. Odepack, a systematized collection of ode solvers, stepleman rs, scientific computing, 55-64, 1983.
[11] J. S. Larsen, A. J.-T. Hansen, and I. F. Santos. Experimental and theoretical analysis of a rigid rotor supported by air foil bearings. *Mechanics & Industry*, 2014.
[12] J. S. Larsen and I. F. Santos. Efficient solution of the non-linear reynolds equation for compressible fluid using the finite element method. *Journal of the Brazilian Society of Mechanical Sciences and Engineering*, pages 1–13, 2014.
[13] J. S. Larsen, A. C. Varela, and I. F. Santos. Numerical and experimental investigation of bump foil mechanical behaviour. *Tribology International*, 74(Complete):46–56, 2014.
[14] S. Le Lez, M. Arghir, and J. Frêne. Nonlinear numerical prediction of gas foil bearing stability and unbalanced response. *Journal of Engineering for Gas Turbines and Power*, 131(1):012503, 2009.
[15] D. Lee, Y.-C. Kim, and K.-W. Kim. The dynamic performance analysis of foil journal bearings considering coulomb friction: Rotating unbalance response. *Tribology Transactions*, 52(2):146–156, 2009.
[16] J. W. Lund. Calculation of stiffness and damping properties of gas bearings. *Journal of Lubrication Technology*, pages 793–804, 1968.
[17] J. B. Olsen. Nonlinear dynamic behavior of rigid rotor foil bearing system. Master's thesis, Technical University of Denmark, 2014.
[18] H. M. Pham and P. Bonello. Efficient techniques for the computation of the nonlinear dynamics of a foil-air bearing rotor system. In *ASME Turbo Expo 2013: Turbine Technical Conference and Exposition*, pages –07, 2013.
[19] J.-H. Song and D. Kim. Foil gas bearing with compression springs: Analyses and experiments. *ASME Journal of Tribology*, 129(3):628–639, 2007.
[20] B. Sternlicht and R. C. Elwell. Theoretical and experimental analysis of hydrodynamic gas-lubricated journal bearings. *American Society of Mechanical Engineers – Papers*, (57), 1957.
[21] V. Stingelin. *Theoretische und experimentelle Untersuchungen an Gaslagern*. PhD thesis, Eidgenössischen Technischen Hochschule in Zürich, 1963.
[22] C.-C. Wang and C.-K. Chen. Bifurcation analysis of self-acting gas journal bearings. *Journal of Tribology*, 123(4):755, 2001.
[23] J. Zhang, W. Kang, and Y. Liu. Numerical method and bifurcation analysis of jeffcott rotor system supported in gas journal bearings. *Journal of Computational and Nonlinear Dynamics*, 4(1):011007, 2009.

[P6] On the non-linear steady state response of rigid rotors supported by air foil bearings - theory and experiments

---

This paper was submitted to the *Journal of Sound and Vibration* in September 2014 and was accepted February 2015.

ARTICLE IN PRESS

Journal of Sound and Vibration ▮ (▮▮▮▮) ▮▮▮–▮▮▮

Contents lists available at ScienceDirect

Journal of Sound and Vibration

journal homepage: www.elsevier.com/locate/jsvi

On the nonlinear steady-state response of rigid rotors supported by air foil bearings—Theory and experiments

Jon S. Larsen [a,b], Ilmar F. Santos [a]

[a] Department of Mechanical Engineering, Technical University of Denmark, 2800 Kgs. Lyngby, Denmark
[b] Siemens A/S – Aeration Competence Centre, 3000 Helsingør, Denmark

ARTICLE INFO

Article history:
Received 10 September 2014
Received in revised form
16 December 2014
Accepted 9 February 2015
Handling Editor: M.P. Cartmell

ABSTRACT

The demand for oil-free turbo compressors is increasing. Current trends are divided between active magnetic bearings and air foil bearings (AFB), the latter being important due to mechanical simplicity. AFB supported rotors are sensitive to unbalance due to low damping and nonlinear characteristics, hence accurate prediction of their response is important. This paper gives theoretical and experimental contributions by implementing and validating a new method to simulate the nonlinear steady-state response of a rotor supported by three pads segmented AFBs. The fluid film pressures, foil deflections and rotor movements are simultaneously solved, considering foil stiffness and damping coefficients estimated using a structural model, previously described and validated against experiments.

1. Introduction

Gas bearings have been intensively investigated, theoretically as well as experimentally, for nearly six decades [1–3] although some initial publications are dated already from the beginning of the last century [4]. In order to deal with computationally expensive rotor-bearing dynamic analysis in the time domain, linear damping and stiffness coefficients were calculated to predict rotor-bearing stability [5]. The rapid development of computer science and increasing computer power, later enabled the solution of the mathematical models in the time domain and allowed for the inclusion of gas compressibility and foil compliance in the models. Although almost a century has passed since the first publications about gas bearings, the accurate time simulation of gas bearings with compliant surfaces is still a challenging and very time-consuming task.

Prior to the presented work, different approaches for solving the compressible Reynolds equation have been investigated. Among others, Wang and Chen [6] who used finite difference for the spatial and temporal dimensions when solving the Reynolds equation. They simulated the steady-state response of a perfectly balanced rigid rotor supported by two identical bearings. The spatial discretisation was performed with a central-difference scheme, while the temporal discretisation was performed with an implicit-backward-difference scheme.

Arghir et al. [7] presented a finite volume solution where the pressure was implicitly integrated for a prescribed gap perturbation to calculate linear stiffness and damping coefficients dependent on the perturbation amplitude. In the procedure, the rotor was stationary in one direction, while the other was perturbed by a sinusoidal displacement, $A\sin(\omega t)$.

E-mail addresses: josla@mek.dtu.dk (J.S. Larsen), ifs@mek.dtu.dk (I.F. Santos).

http://dx.doi.org/10.1016/j.jsv.2015.02.017
0022-460X/

Nomenclature

$\dot{()}$	time derivative, $d/d\tau$
$\ddot{()}$	time derivative, $d^2/d\tau^2$
$\nabla\cdot$	divergence
∇	gradient, $\nabla = \{\partial/\partial\tilde{\theta}, \partial/\partial\tilde{z}\}$
A, B	bearings
C	radial clearance
E	modulus of elasticity of foil
F, D	force, displacement
I	mass moment of inertia
L, $\tilde{L}$	bearing length, $\tilde{L} = L/R$
N_p	number of pads
R	journal radius
S	compressibility number, $S = 6\mu\omega/p_a(R/C)^2$
S_b	bump foil pitch
V	volume
W	static load
b, $\tilde{b}$	structural damping per unit area, $\tilde{b} = (C/p_a\omega)b$
e, ε	journal eccentricity components, $\varepsilon = e/C$
h, $\tilde{h}$	film height, $\tilde{h} = h/C$
h_b	bump foil height
h_c, $\tilde{h}_c$	film height (flexible), $\tilde{h}_c = h_c/C$
h_r, $\tilde{h}_r$	film height (rigid), $\tilde{h}_r = h_r/C$
h_s, $\tilde{h}_s$	slope height, $\tilde{h}_s = h_s/C$
k, $\tilde{k}$	structural stiffness per unit area, $\tilde{k} = (C/p_a)k$
l_0	bump half-length
l_1, l_2	distance to bearings
m	mass
p, $\tilde{p}$	film pressure, $\tilde{p} = p/p_a$
p_a	ambient pressure
t	time
t_b	thickness of bump foil
t_t	thickness of top foil
u	unbalance kg m
$x, y, z, \tilde{z}$	Cartesian coordinates, $\tilde{z} = z/R$
CG	center of gravity
ODE	ordinary differential equations
η	structural loss factor of foils
μ	dynamic viscosity
ν	Poisson's ratio of foil
ω	angular speed of journal
ω_d	frequency of sub-synchronous vibration
ω_s	excitation frequency
ψ	film state variable, $\psi = ph$
τ	dimensionless time, $\tau = \omega t$
θ	circumferential angle
θ'	curve linear pad coordinate, $\theta' = \theta R$
θ_l	first pad leading edge angle
θ_s	first pad slope extend
θ_t	first pad trailing edge angle
$\tilde{\theta}$	dimensionless pad coordinate, $\tilde{\theta} = \theta'/R = \theta$
ξ, ζ	Gauss points
$\mathbf{f}$, $\tilde{\mathbf{f}}$	bearing force vector, $\tilde{\mathbf{f}} = (1/p_aR^2)\mathbf{f}$
$\mathbf{f}_{ub}$, $\tilde{\mathbf{f}}_{ub}$	unbalance force vector, $\tilde{\mathbf{f}}_{ub} = (1/p_aR^2)\mathbf{f}_{ub}$
$\mathbf{r}$	residual vector
$\mathbf{s}$	advection vector, $\mathbf{s} = \{S, 0\}^T$
$\mathbf{w}$, $\tilde{\mathbf{w}}$	load vector, $\tilde{\mathbf{w}} = (1/p_aR^2)\mathbf{w}$
$\tilde{\mathbf{h}}_c$	foil deformation vector
$\tilde{\mathbf{h}}$	height vector
$\tilde{\mathbf{p}}$	pressure vector
$\boldsymbol{\psi}$	film state vector
$\boldsymbol{\varepsilon}$	eccentricity vector
$\mathbf{g}()$	nonlinear vector function
$\mathbf{y}$	state vector
$\mathbf{z_1}, \mathbf{z_2}$	rotor state vectors
$\mathbf{A}$	fluidity matrix
$\mathbf{B}$	shape function derivatives matrix
$\mathbf{G}$, $\tilde{\mathbf{G}}$	gyroscopic matrix
$\mathbf{M}$, $\tilde{\mathbf{M}}$	mass matrix
$\mathbf{N}$	shape function matrix

At each time step, the reaction forces from the air film were calculated and based on the displacement/velocity and reaction force pairs, the least square method was used to calculate the linear stiffness and damping for a given amplitude A. This allowed a linear analysis of a rotor system to take into account the nonlinearities related to the vibration amplitude of the rotor in the air bearings.

A common method to solve the compressible Reynolds equation in time is to substitute the time derivatives $\mathrm{d}p/\mathrm{d}t$ and $\mathrm{d}h/\mathrm{d}t$ by backward-difference approximations [8,9]. In this case, these time derivatives will be lagging behind in time, and the time steps need to be very small in order to preserve the accuracy of the solution. This method was employed by e.g. Le Lez et al. [10] and Kim [11]. The method was also used by Zhang et al. [12] to solve the transient Reynolds equation, but with four-node planar finite elements for the spatial discretisation of the Reynolds equation and for a rigid gas journal bearing.

More recently, Bonello and Pham [13,14] solved the nonlinear Reynolds equation by using an alternative state variable $\psi = ph$. Using this alternative state variable, it was possible to set up a set of ordinary differential equations (ODE) to solve the Reynolds equation and other state variables simultaneously at each time step. For spatial discretisation, a finite difference and Galerkin reduction method were used. The solution for the transient compressible Reynolds equation was then coupled to the simple elastic foundation model (SEFM), and the transient response of a rotor system was presented.

In order to accelerate the time simulations, several authors have consistently and diligently been working on improving the numerical methods and developing new numerical strategies. A simplified method for evaluating the nonlinear fluid forces in air bearings was recently proposed by Hassini and Arghir [15–17]. The fundamental idea was based on approximating the frequency-dependent linearised dynamic coefficients at several eccentricities by second-order rational functions in the Laplace domain. By applying the inverse of the Laplace transform to the rational functions, a new set of ordinary differential equations was obtained, leading to an original way of linking the fluid forces components to the rotor displacements. The numerical results showed good agreement with the results obtained by solving the full nonlinear

Please cite this article as: J.S. Larsen, & I.F. Santos, On the nonlinear steady-state response of rigid rotors supported by air foil bearings—Theory and experiments, *Journal of Sound and Vibration* (2015), http://dx.doi.org/10.1016/j.jsv.2015.02.017

transient Reynolds equation coupled to the equation of motion of a point mass rotor. By ensuring the continuity of the values of the fluid forces and their first derivatives and imposing the same set of stable poles to the rational functions, simplified expressions of the fluid forces were found, avoiding the introduction of false poles into the rotor-bearing system. In [15], the authors showed that the new formulation may be applied to compute the nonlinear response of systems with multiple degrees of freedom such as a flexible rotor supported by two air bearings. On the other hand, working directly with the solution of the Reynolds equation for compressible fluids and compliant surfaces, Bonello and Pham [18,13] presented a generic technique for the transient nonlinear dynamic analysis and the static equilibrium stability analysis of rotating machines, using the finite-difference state equations of the air films with the state equations of the foil structures and the state equations of the rotating machine model. To accelerate the time simulations, the state Jacobian matrix was obtained using symbolic computing, and the equations were solved using a readily available implicit integrator and a predictor–corrector approach.

In this paper, an industrial rigid rotor supported by two identical segmented foil bearings is modelled and the effect of rotor unbalance is theoretically and experimentally investigated. In this framework, the main original contribution of the paper is related to the accurate, i.e. quantitatively and qualitatively, prediction of the nonlinear steady-state rotor response. The modelling of the segmented three pad foil bearings is carried out with high attention to the actual geometry by including the inlet slope, which has previously been found to influence both the static and dynamic results [19]. The foil structural model is based on the SEFM but with a stiffness k and loss factor η deduced from a previously described mathematical model [20]. This model takes into account the friction forces between the sliding surfaces and was validated against experiments. Consequently, the bump foil stiffness k used in this work differs significantly from results in the literature, in which the foil stiffness was based on analytical expressions not accounting for the stiffening effect generated by the friction forces, e.g. Walowit and Anno [21]. The discretisation of the Reynolds equation is performed using the finite element method [22] and the solution of the mathematical model is based on the strategy suggested in [13,14].

2. Mathematical model

In Fig. 1, the schematics of the rotor-bearing system is illustrated. With the nodal position vector defined as $\boldsymbol{\varepsilon}=\{\varepsilon_{Ax},\varepsilon_{Ay},\varepsilon_{Bx},\varepsilon_{By}\}^T$ describing the instantaneous position of the shaft in the bearing locations A and B, and under the assumption that the shaft is rigid and subjected to small rotations around the x- and the y-axis, its equations of motion can be written in the dimensionless form as

$$\tilde{\mathbf{M}}\ddot{\boldsymbol{\varepsilon}}-\tilde{\mathbf{G}}\dot{\boldsymbol{\varepsilon}}=\tilde{\mathbf{w}}-\tilde{\mathbf{f}}+\tilde{\mathbf{f}}_{ub}. \tag{1}$$

Here, the dimensionless mass- and gyroscopic-matrices, $\tilde{\mathbf{M}}$ and $\tilde{\mathbf{G}}$, are given in Appendix A together with the mass unbalance vector $\tilde{\mathbf{f}}_{ub}$. Furthermore, $\tilde{\mathbf{w}}$ is the static load vector and $\tilde{\mathbf{f}}^T=\{\tilde{\mathbf{f}}_A^T,\tilde{\mathbf{f}}_B^T\}^T$ is the reaction force vector stemming from the bearings. The reaction force $\mathbf{f}$ is composed by the reactions from the bearings A and B, which are determined by integrating the fluid film pressure for each particular bearing as

$$\tilde{\mathbf{f}}_\gamma=\begin{Bmatrix}\tilde{F}_x\\ \tilde{F}_y\end{Bmatrix}=\int_0^{\tilde{L}}\int_0^{2\pi}(\tilde{p}-1)\begin{Bmatrix}\cos(\tilde{\theta})\\ \sin(\tilde{\theta})\end{Bmatrix}\mathrm{d}\tilde{\theta}\,\mathrm{d}\tilde{z} \tag{2}$$

where $\gamma=A,B$. The bearing pressures can be obtained by solving the Reynolds equation for compressible fluids for each bearing. This equation can be written dimensionless in the vector form [23] as

$$\nabla\cdot\left(\tilde{p}\tilde{h}^3\nabla\tilde{p}\right)=\nabla\cdot\left(\tilde{p}\tilde{h}\right)\mathbf{s}+2S\frac{\partial}{\partial\tau}\left(\tilde{p}\tilde{h}\right) \tag{3}$$

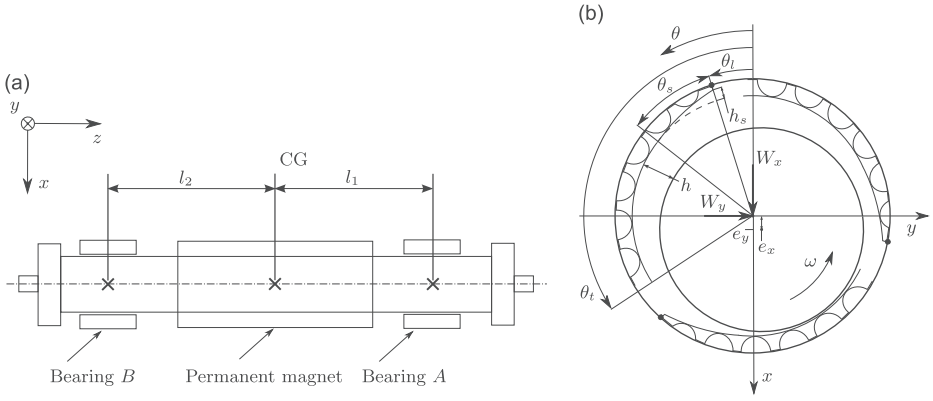

Fig. 1. Schematics and nomenclature of a rigid rotor supported by foil journal bearings: (a) Shaft and bearings; (b) Detailed view of bearing geometry.

Please cite this article as: J.S. Larsen, & I.F. Santos, On the nonlinear steady-state response of rigid rotors supported by air foil bearings—Theory and experiments, *Journal of Sound and Vibration* (2015), http://dx.doi.org/10.1016/j.jsv.2015.02.017

where the film height is defined as

$$\tilde{h}(\varepsilon_x, \varepsilon_y, \tilde{p}, \dot{\tilde{h}}_c) = \tilde{h}_r(\varepsilon_x, \varepsilon_y) + \tilde{h}_c(\tilde{p}, \dot{\tilde{h}}_c) \tag{4}$$

and $\tilde{h}_r(\varepsilon_x, \varepsilon_y)$ is the film height in the undeformed bearing that depends on the rotor eccentricity, and $\tilde{h}_c(\tilde{p}, \dot{\tilde{h}}_c)$ is a pressure-dependent deformation in the foils referred to as the compliant height. The compliant height can be related to the film pressure through $h_c = k(p - p_a)$ which, inserted in the Reynolds equation (Eq. (3)), forms the SEFM as originally proposed by Heshmat et al. [24,25]. For a bearing with the geometry as illustrated in Fig. 1b and under the assumption of the SEFM, expressions for h_r and h_c are given in Appendix B.

2.1. Solution strategy

Eqs. (1) through (4) constitute the mathematical model for the rotor-bearing system. In order to simulate the nonlinear rotor response, a commonly used strategy is to rewrite Eq. (1) to a system of ODEs to be integrated while the bearing forces $\tilde{\mathbf{f}}$ are updated at each time step. The bearing forces relate to the pressure, through Eq. (2), which is then obtained by solving Eq. (3). This can be accomplished by discretising the film PDE and substituting the time-dependent terms by backward-difference approximations as

$$\frac{\partial \tilde{\mathbf{p}}}{\partial \tau} \approx \frac{\tilde{\mathbf{p}}_n - \tilde{\mathbf{p}}_{n-1}}{\Delta \tau}, \quad \frac{\partial \tilde{\mathbf{h}}}{\partial \tau} \approx \frac{\tilde{\mathbf{h}}_n - \tilde{\mathbf{h}}_{n-1}}{\Delta \tau} \tag{5}$$

where n is the current time step. The pressure can then be found by iteratively solving a set of nonlinear algebraic equations. Following the above-mentioned strategy, the time-dependent terms are lagging behind in time since they are based on the previous time step in the integration of the rotor ODEs. As pointed out by Bonello and Pham [13,14], this method does not preserve the true simultaneously coupled nature of the state variables, $\varepsilon, \tilde{p}, \tilde{h}_c$, of the system. This means that very small time steps are necessary in order to ensure an accurate solution. It makes the solution slow, and being strictly rigorous, each simulation should be accompanied by a convergence study on the time step size to ensure an accurate solution.

Another problem with solution strategy described above is numerical stability. This is particularly related to the term $\partial \tilde{\mathbf{p}}/\partial \tau$, which tends to become dominant and sensitive to the accuracy of $\tilde{\mathbf{p}}_n - \tilde{\mathbf{p}}_{n-1}$ due to the division by the very small number $\Delta \tau$. Assuming the term negligible is not an option, simulations performed by Olsen [26] clearly showed that discarding this term leads to significant errors.

Bonello and Pham [13,14] introduced a basic strategy to solve all the state variables simultaneously and an efficient solution method based on a Galerkin reduction method to significantly limit the number of state variables. Here, only the basic strategy is followed, which implies setting up one coupled system of nonlinear ODEs of the state variables $\varepsilon, \psi, \tilde{h}_c$, where $\psi = \tilde{p}\tilde{h}$.

2.2. Reynolds equation – discretisation

We discretise the PDE equation (3) following a standard Bubnov–Galerkin FE procedure with the implementation of an isoparametric element formulation [27]. A partial substitution with ψ is performed to obtain

$$\nabla \cdot \left(\tilde{p}\tilde{h}^3 \nabla \tilde{p}\right) - \nabla \cdot \left(\tilde{p}\tilde{h}\right)\mathbf{s} - 2S\frac{\partial \psi}{\partial \tau} = 0 \tag{6}$$

which upon discretisation [28] yields a system of nonlinear equations on the element level

$$\mathbf{A}^e \boldsymbol{\psi}^e = \mathbf{r}^e \tag{7}$$

where

$$\mathbf{A}^e = 2S\int_{V^e} \mathbf{N}^T \mathbf{N}\, \mathrm{d}V, \quad \mathbf{r}^e = -\int_{V^e} \mathbf{B}^T \tilde{p}\tilde{h}^3 \mathbf{B}\, \mathrm{d}V \cdot \tilde{\mathbf{p}}^e + \int_{V^e} \mathbf{B}^T \mathbf{s}\tilde{h}\mathbf{N}\, \mathrm{d}V \cdot \tilde{\mathbf{p}}^e. \tag{8}$$

The element vectors and matrices are expanded to structure size by the usual element mapping symbolised by summations [27]

$$\mathbf{r} = \sum_e \mathbf{r}^e; \quad \tilde{\mathbf{p}} = \sum_e \tilde{\mathbf{p}}^e; \quad \boldsymbol{\psi} = \sum_e \boldsymbol{\psi}^e \tag{9}$$

where the volume integrals are numerically integrated using a quadrature rule [27]. The scalar field quantities, $\tilde{p}$, $\tilde{h}$, are calculated in the respective Gauss points (ξ_i, ζ_j) by use of the interpolation functions as

$$q(\xi_i, \zeta_j) = \mathbf{N}(\xi_i, \zeta_j)\mathbf{q}^e \tag{10}$$

where q and $\mathbf{q}^e$ are the scalar field quantities and nodal vectors respectively. Note that the right hand side of Eq. (7) is denoted $\mathbf{r}^e$. In fact, $\mathbf{r}^e$ is the residual that needs to be minimised in order to find the static equilibrium of the perfectly balanced journal. When performing certain simulations in the time domain, it is very handy to start the simulations from this static equilibrium position. An efficient method for minimising $\mathbf{r}^e$ using a Newton–Raphson procedure is explained in [22].

Please cite this article as: J.S. Larsen, & I.F. Santos, On the nonlinear steady-state response of rigid rotors supported by air foil bearings—Theory and experiments, *Journal of Sound and Vibration* (2015), http://dx.doi.org/10.1016/j.jsv.2015.02.017

2.3. Coupled system of ODEs

With the film PDE discretised, the mathematical model can be written as a system of ODEs, on the form $\dot{\mathbf{y}} = \mathbf{g}(\tau, \mathbf{y})$, and solved for all state variables simultaneously. The state-vector is defined as

$$\mathbf{y}^T = \{\boldsymbol{\psi}_A^T, \boldsymbol{\psi}_B^T, \tilde{\mathbf{h}}_{cA}^T, \tilde{\mathbf{h}}_{cB}^T, \mathbf{z}_1^T, \mathbf{z}_2^T\}^T \tag{11}$$

with $\mathbf{z}_1 = \varepsilon$ and $\mathbf{z}_2 = \dot{\varepsilon}$. For the particular case of a rigid rotor supported by two bearings, the system dimension of the coupled ODEs are $4N+8$ with N being the number of nodes in the fluid film finite element model of each individual bearing. The system of ODEs takes the form

$$\begin{Bmatrix} \dot{\boldsymbol{\psi}}_A \\ \dot{\boldsymbol{\psi}}_B \\ \dot{\tilde{\mathbf{h}}}_{cA} \\ \dot{\tilde{\mathbf{h}}}_{cB} \\ \dot{\mathbf{z}}_1 \\ \dot{\mathbf{z}}_2 \end{Bmatrix} = \begin{bmatrix} \mathbf{0} & \cdots & \mathbf{0} & \mathbf{0} \\ \vdots & \ddots & \vdots & \vdots \\ & & & \mathbf{0} \\ \mathbf{0} & \cdots & \mathbf{0} & \mathbf{I} \\ \mathbf{0} & \cdots & \mathbf{0} & \tilde{\mathbf{M}}^{-1}\tilde{\mathbf{G}} \end{bmatrix} \begin{Bmatrix} \boldsymbol{\psi}_A \\ \boldsymbol{\psi}_B \\ \tilde{\mathbf{h}}_{cA} \\ \tilde{\mathbf{h}}_{cB} \\ \mathbf{z}_1 \\ \mathbf{z}_2 \end{Bmatrix} + \begin{Bmatrix} \mathbf{g}_{\dot{\psi}A}(\boldsymbol{\psi}_A, \mathbf{z}_1, \mathbf{z}_2, \tilde{\mathbf{h}}_{cA}, \dot{\tilde{\mathbf{h}}}_{cA}) \\ \mathbf{g}_{\dot{\psi}B}(\boldsymbol{\psi}_B, \mathbf{z}_1, \mathbf{z}_2, \tilde{\mathbf{h}}_{cB}, \dot{\tilde{\mathbf{h}}}_{cB}) \\ \mathbf{g}_{\dot{\tilde{h}}_{cA}}(\boldsymbol{\psi}_A, \mathbf{z}_1, \mathbf{z}_2, \tilde{\mathbf{h}}_{cA}) \\ \mathbf{g}_{\dot{\tilde{h}}_{cB}}(\boldsymbol{\psi}_B, \mathbf{z}_1, \mathbf{z}_2, \tilde{\mathbf{h}}_{cB}) \\ \mathbf{0} \\ \tilde{\mathbf{M}}^{-1}(\tilde{\mathbf{w}} - \tilde{\mathbf{f}} + \tilde{\mathbf{f}}_{ub}) \end{Bmatrix}. \tag{12}$$

The nonlinear functions on the right hand side are defined as

$$\mathbf{g}_{\dot{\psi}\gamma}(\boldsymbol{\psi}_\gamma, \mathbf{z}_1, \mathbf{z}_2, \tilde{\mathbf{h}}_{c\gamma}, \dot{\tilde{\mathbf{h}}}_{c\gamma}) = \mathbf{A}_\gamma^{-1}\mathbf{r}_\gamma \tag{13}$$

and by vectorising the pad deflection given in Eq. (B.5)

$$\mathbf{g}_{\dot{\tilde{h}}_{c\gamma}}\left(\boldsymbol{\psi}_\gamma, \mathbf{z}_1, \mathbf{z}_2, \tilde{\mathbf{h}}_{c\gamma}\right) = \left(\frac{\tilde{\mathbf{p}}_\gamma - 1}{\tilde{k}_\gamma} - \tilde{\mathbf{h}}_{c\gamma}\right)\frac{1}{\eta_\gamma} \tag{14}$$

where $\gamma = A, B$ denotes the individual bearings. In this work, the system of ODEs are solved using the 'lsoda' solver from the Fortran library ODEPACK [29]. This solver has an automatic time step control and switches between dedicated solvers for stiff and non-stiff systems. To efficiently solve the ODEs, a program for the discretisation and solution of Eq. (13) is implemented in C using the sparse solver DGBESV from the LaPack library [30]. However, the solution is still time-consuming, and it should be highlighted that Bonello and Pham [13,14] significantly improved the speed of the solution by implementing a Galerkin reduction method.

2.4. Boundary conditions

In the dimensionless form, the edge boundary conditions for the bearings, as depicted in Fig. 1b, are

$$\begin{aligned} \tilde{p}(\tilde{\theta}_l, \tilde{z}) = \tilde{p}(\tilde{\theta}_t, \tilde{z}) = 1 \\ \tilde{p}(\tilde{\theta}, \tilde{L}/2) = \tilde{p}(\tilde{\theta}, -\tilde{L}/2) = 1. \end{aligned} \tag{15}$$

To obey these conditions, it is necessary to evaluate the film state variable $\dot{\psi} = \dot{\tilde{p}}h + \dot{\tilde{h}}p$. On the pad edges, we know that $\tilde{p} = 1$ and is constant, so $\dot{\tilde{p}} = 0$. This means that when solving Eq. (13) to obtain the film state variable, the following boundary conditions must be imposed:

$$\begin{aligned} \dot{\psi}(\tilde{\theta}_l, \tilde{z}) = \dot{\psi}(\tilde{\theta}_t, \tilde{z}) = \dot{\tilde{h}}(\dot{\varepsilon}_x, \dot{\varepsilon}_y, \dot{\tilde{h}}_c) \\ \dot{\psi}(\tilde{\theta}, \tilde{L}/2) = \dot{\psi}(\tilde{\theta}, -\tilde{L}/2) = \dot{\tilde{h}}(\dot{\varepsilon}_x, \dot{\varepsilon}_y, \dot{\tilde{h}}_c) \end{aligned} \tag{16}$$

which is achieved by using a standard FE procedure. Symmetry conditions can be achieved by neglecting Eq. (16) on one side, e.g. on $(\tilde{\theta}, \tilde{L}/2)$. In this case, the reaction forces need to be multiplied by two. A commonly used boundary condition [22], which is also used in this work, is to assume that the bearing foils deform evenly over the length $\tilde{L}$ of the bearing. This condition is implemented by replacing $\tilde{\mathbf{p}}_\gamma$ in Eq. (14) with $\tilde{\mathbf{p}}_{\gamma m}$, where $\tilde{\mathbf{p}}_{\gamma m}$ is the arithmetic mean pressure over the length $\tilde{L}$.

In gas bearings, significant sub-ambient pressures may arise. These sub-ambient pressures can cause the top foil to separate from the bumps into a position in which the pressure on both sides of the pad are equalised. Heshmat [25] introduced a set of boundary conditions accounting for this separation effect. In this work, a simple Gümbel [23] boundary condition is imposed, meaning that sub-ambient pressures are discarded when integrating the pressure Eq. (2) to obtain the bearing force components $(\tilde{F}_x, \tilde{F}_y)$, essentially leaving the sub-ambient regions ineffective. However, the foil deflection is still based on the unmodified pressure, i.e. including the sub-ambient part, but the error related to this is assumed to be small. As an example, the static steady state for the bearing with dimensions as given in Table 1 is obtained theoretically using the method as explained in e.g. [22]. The bearing is subjected to a load of 100 N when operating at 26,400 RPM. The predicted eccentricity becomes: $\varepsilon_x = 0.7176$ and $\varepsilon_y = 0.2632$ when using the Gümbel boundary condition as described above. If the analysis is repeated but this time with the foil deflection set to zero in the sub-ambient regions, the eccentricity becomes $\varepsilon_x = 0.7174$ and $\varepsilon_y = 0.2638$.

Please cite this article as: J.S. Larsen, & I.F. Santos, On the nonlinear steady-state response of rigid rotors supported by air foil bearings—Theory and experiments, *Journal of Sound and Vibration* (2015), http://dx.doi.org/10.1016/j.jsv.2015.02.017

Table 1
Geometry, material properties and operating conditions of the Siemens foil bearing test rig.

Parameters	Values	Parameters	Values
Bearing radius, R	33.50 mm	Bump foil height, h_b	0.9 mm
Bearing length, L	53.00 mm	Young's modulus of bump foil, E	2.07×10^{11} Pa
Bearing radial clearance, C	40 μm	Poisson's ratio of bump foil, ν	0.3
Number of pads, N_p	3	Foil friction coefficient, μ_f	0.2
First pad leading edge, θ_l	30°	Ambient pressure, p_a	1×10^5 Pa
First pad trailing edge, θ_t	145°	Air viscosity, μ	1.95×10^{-5} Pa s
Slope extend, θ_s	30°	l_1	201.1 mm
Slope, h_s	50 μm	l_2	197.9 mm
Bump foil thickness, t_b	0.127 mm	$m = m_x = m_y$	21.1166 kg
Top foil thickness, t_t	0.254 mm	$I_{xx} = I_{yy}$	525.166×10^{-3} kg m^2
Bump foil pitch, S_b	7.00 mm	I_{zz}	30.079×10^{-3} kg m^2
Bump foil half-length, l_0	3.30 mm		

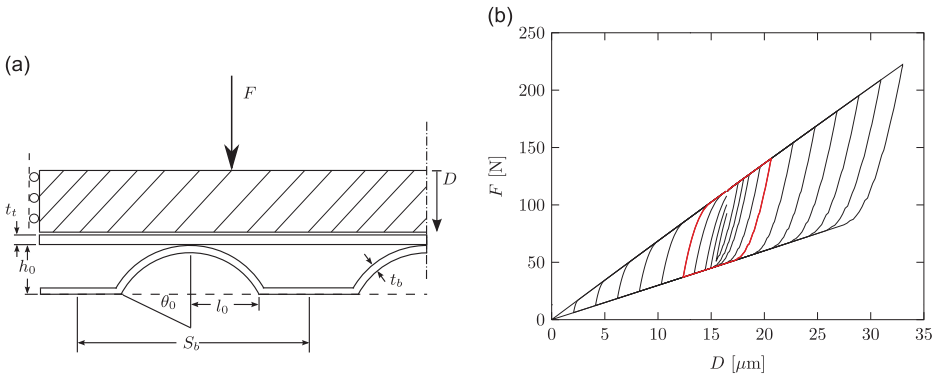

Fig. 2. Bump foil geometry and hysteresis loops obtained at varying deflection amplitudes: (a) uncompressed bump foil section; (b) hysteresis curves of a bump foil strip consisting of four bumps.

3. Theoretical results

The mathematical formulation for the foil deflection Eq. (14), derived in Appendix B is commonly referred to as the SEFM. This formulation assumes a linear stiffness and loss factor, k and η respectively, and discards local stiffness variations caused by friction effects in the contact points. A local point deflection of the foil surface is regarded to be independent of deflections in any neighbouring points. Depending on the fluid pressure profile and magnitude and the friction coefficient between the mating surfaces, these assumptions may lead to significant errors in the prediction of the foil deflection $\tilde{h}_c$. Several authors presented more advanced foil structure formulations incorporating the effect of friction coupled with the Reynolds equation, e.g. [31–33,9,34–36], though in this work only the SEFM is implemented. The test rig, bearing geometry and nomenclature are illustrated in Fig. 1, the foil geometry and nomenclature are illustrated in Fig. 2a, and all parameters and values are listed in Table 1.

3.1. Structural stiffness and energy dissipation

The SEFM is, due to its simplicity, often [24,25,11,37,38] implemented with the stiffness k estimated by the analytical expression derived by Walowit and Anno [21]. Detailed studies [20] of the bump foil structure, as illustrated in Fig. 2a, have proven this analytically obtained stiffness to be significantly underestimated. In this perspective, the stiffness and the loss factor used in this work are based on the bump foil FE model described in [20]. This FE model included the friction forces in the sliding contacts and the predicted results were compared to experiments with good agreement. Here, closed hysteresis loops of a bump foil strip using this FE model are simulated for compression cycles of different amplitudes as illustrated in Fig. 2b, and the stiffness and loss factor are extracted from this using standard methods [39]. In [20], the identified hysteresis loops were found to be frequency dependent. Though later experiments [40], using the same experimental setup, confirmed this rate dependency, it was found to be less prevalent for the given foil specimens. Based on these findings, the rate dependency is neglected in this work.

Certain assumptions are required when reducing a complex nonlinear structure, including friction, to two linear coefficients, k and η, by the method described above: (1) how many bumps should be included in the simulation and

Please cite this article as: J.S. Larsen, & I.F. Santos, On the nonlinear steady-state response of rigid rotors supported by air foil bearings—Theory and experiments, *Journal of Sound and Vibration* (2015), http://dx.doi.org/10.1016/j.jsv.2015.02.017

(2) which deflection amplitude should be employed. Here, the hysteresis loops are based on a strip of four bumps pinned in one end. This is a reasonable engineering assumption based on the shape of the film pressure profile forming a peak so that roughly 80 percent of the pad load is supported by these four bumps. Hence, the hysteresis loop simulation is based on the assumption that four bumps support a static load of approximately 80 N (the static bearing load is approximately 105 N) upon which a deflection oscillation is imposed. As illustrated in Fig. 2, the deflection amplitude is varied between 1 and 17 μm. The parameters, η and k, identified from the resulting hysteresis curves, are illustrated in Fig. 3. Assuming the actual shaft vibration amplitudes in the range 2–6 μm, which are values commonly found during factory testing, and the foil deflections are half that, the stiffness and the loss factor are estimated to be in the interval $k=[0.9;2.5]\times 10^{10}$ N/m^3 and $\eta=[0.15;0.3]$. If the rotor is initially assumed to run with small oscillations around a steady-state equilibrium, then the loss factor is at the low end of the interval $\eta=0.15$ and the stiffness is at the high end $k=2.5\times 10^{10}$ N/m^3. In other words, in the vicinity of a growing vibration, the loss factor should be low but increasing with the amplitude of the vibration. As this is not practically possible because the loss factor is kept constant in the present analysis, it is chosen to be low $\eta=0.15$. On the other hand, choosing the corresponding stiffness to be $k=2.5\times 10^{10}$ N/m^3 would result in an inaccurate prediction of the equilibrium position because the high stiffness reflects a stiffness for the preloaded foil i.e. from its static equilibrium position. Basically, the dilemma is the same as discussed in [19] where a static and a dynamic stiffness, k_s and k_d respectively, were introduced in the perturbation analysis. Since the stiffness k is constant in the present analysis, a compromise must be made, and the stiffness is chosen to be in the low end of the range, i.e. $k=0.9\times 10^{10}$ N/m^3.

3.2. Static equilibrium

In the theoretical analysis of the nonlinear steady-state response, the rotor is analysed at varying rotational speeds ranging from 5400 to 26,400 RPM. The static journal eccentricities (journal unbalance $u_A=u_B=0$) are illustrated in Fig. 4a from minimum to maximum rotor speed. The minimum and maximum static pad deflections, $\tilde{h}_c$, at maximum and minimum speed respectively, are also illustrated and the corresponding pressure profiles are given in Fig. 4b. As seen, the

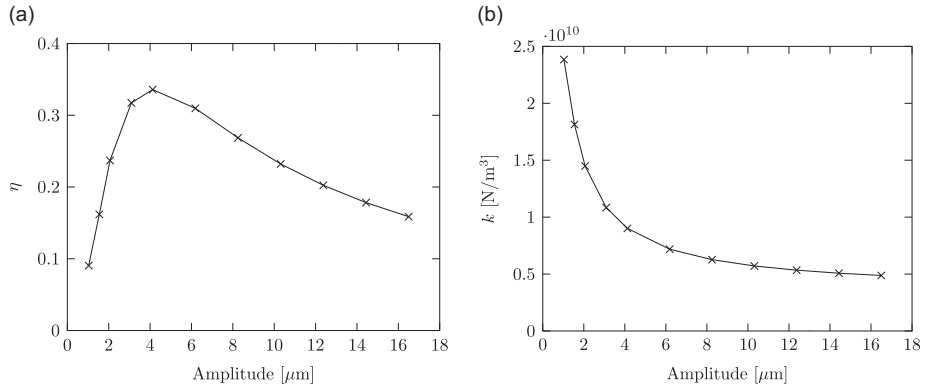

Fig. 3. Stiffness and loss factor obtained from a bump foil strip composed of four bumps at varying deflection amplitudes: (a) loss factor η at different deflection amplitudes; (b) stiffness k at different deflection amplitudes.

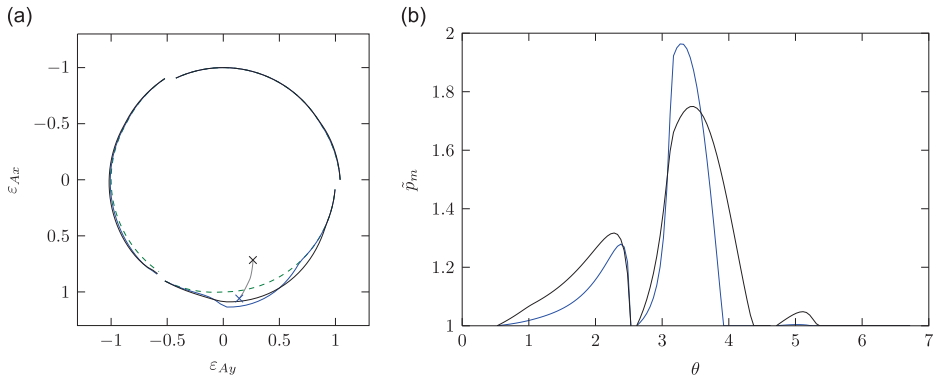

Fig. 4. Static equilibrium positions, foil deflections and pressure profiles (blue lines: 5400 RPM, black lines: 26,400 RPM): (a) pad deflections and journal eccentricity ratios for bearing A (blue line: 5400 RPM, black line: 26,400 RPM, green line: undeformed); (b) pressure profiles based on mean pressure along the z-direction for bearing A (blue line: 5400 RPM, black line: 26,400 RPM). (For interpretation of the references to color in this figure caption, the reader is referred to the web version of this paper.)

Please cite this article as: J.S. Larsen, & I.F. Santos, On the nonlinear steady-state response of rigid rotors supported by air foil bearings—Theory and experiments, *Journal of Sound and Vibration* (2015), http://dx.doi.org/10.1016/j.jsv.2015.02.017

maximum pressure occurs at minimum speed. The assumption of four bumps supporting approximately 80 percent of the weight is also seen to be valid when investigating these figures. Especially when evaluating the pad deflections in Fig. 4a, in which the pad deformation is stretching between 1/3 and 1/2 of the pad circumferential length, while keeping in mind that a pad is supported by nine bumps.

3.3. Nonlinear steady-state response

The following nonlinear steady-state results are obtained by simulating the rotor bearing system, from static steady-state initial conditions, until transient vibrations die out. At low unbalance levels, the rotor response is nearly linear, consisting mainly of the synchronous frequency components, and the rotor vibrations are unbalance driven. A steady-state simulation at $\omega = 11,400$ RPM, with an unbalance of $u_A = 10$ g mm, $u_B = -2.5$ gmm, which is approximately within ISO G2.5 range, are

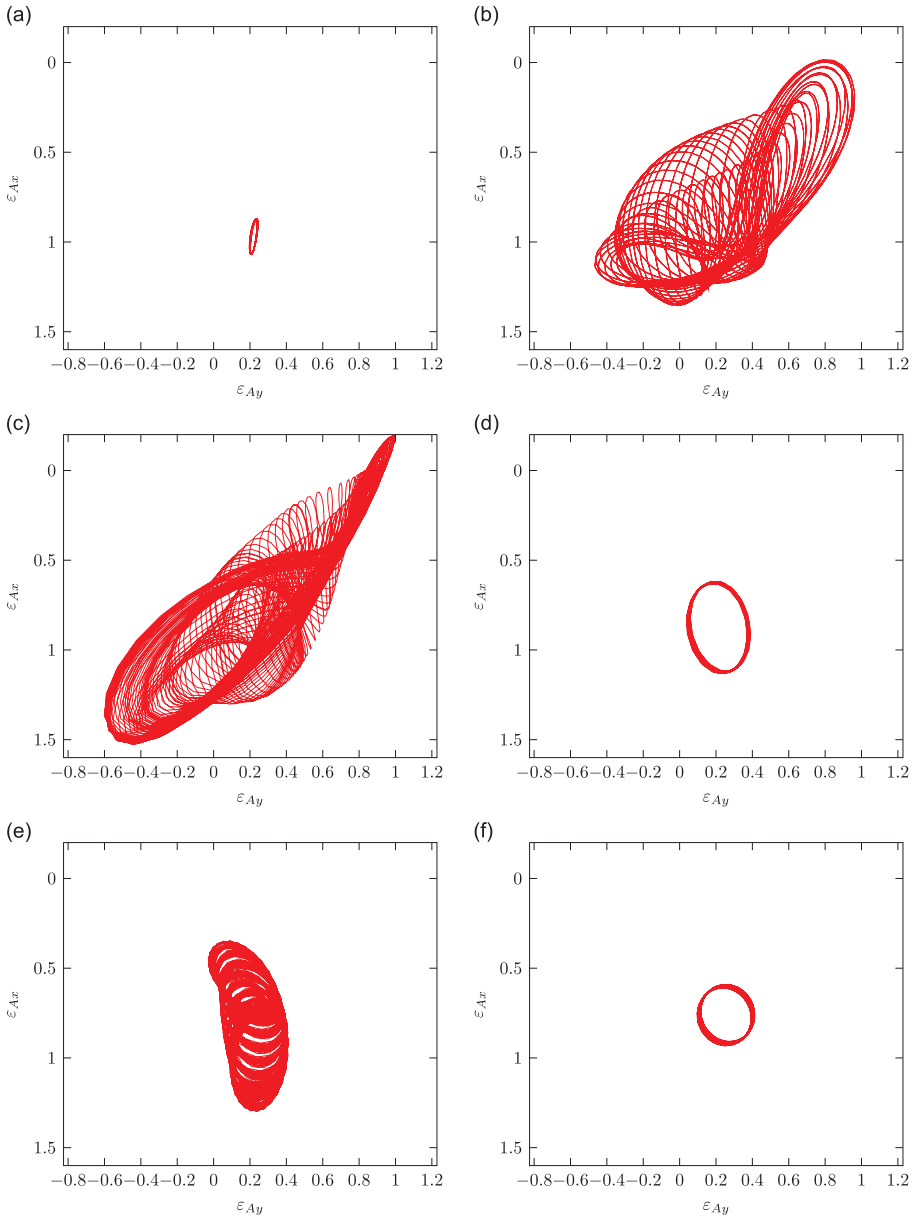

Fig. 5. Nonlinear steady-state rotor orbits in bearing A at varying rotor speeds and unbalance levels: (a) $u_A = 10$ g mm, $u_B = -2.5$ g mm and $\omega = 11,400$ RPM; (b) $u_A = 40$ g mm, $u_B = -2.5$ g mm and $\omega = 11,400$ RPM; (c) $u_A = 40$ g mm, $u_B = -2.5$ g mm and $\omega = 13,200$ RPM; (d) $u_A = 40$ g mm, $u_B = -2.5$ g mm and $\omega = 15,000$ RPM; (e) $u_A = 40$ g mm, $u_B = -2.5$ g mm and $\omega = 18,000$ RPM; (f) $u_A = 40$ g mm, $u_B = -2.5$ g mm. and $\omega = 25,200$ RPM.

Please cite this article as: J.S. Larsen, & I.F. Santos, On the nonlinear steady-state response of rigid rotors supported by air foil bearings—Theory and experiments, *Journal of Sound and Vibration* (2015), http://dx.doi.org/10.1016/j.jsv.2015.02.017

illustrated in Fig. 5a for bearing *A*. Note that the negative unbalance u_B is equivalent to a counterphase unbalance related to u_A. Clearly, the rotor is operated within the linear range and the result is an elliptical periodic orbit. Depending on the industrial application: corrosion, wear/erosion, accumulation of substances, it leads to the formation of residual unbalance. Changing the rotor unbalance to u_A=40 g mm and $u_B = -2.5$ g mm, which is roughly a factor of four and within the ISO G6.3 range, results in the birth of several sub-synchronous vibrations rendering orbits of complicated pattern. This is illustrated in Fig. 5b in which the rotor is now operated outside the linear range and the vibration is dominated by sub-synchronous vibrations. Ratios between the synchronous frequency and the frequencies of the sub-synchronous vibrations may be irrational resulting in quasi-periodic vibrations.

As illustrated in Fig. 5b–f, in which the rotor orbits in bearing *A* are illustrated at selected rotor speeds ω=11,400, 13,200, 15,000, 18,000, and 25,200 RPM, sub-synchronous vibrations appear and disappear, not only dependent on the level of rotor unbalance, but also the rotor speed. Similar rotor behaviour was found experimentally by San Andrés and Kim [41] and by Balducchi et al. [42]. The results can be examined in detail in the frequency domain by evaluating the two theoretically obtained waterfall diagrams, covering the range 90–440 Hz (5400–26,400 RPM), as illustrated in Figs. 6 and 7. The first waterfall diagram is based on a low level of unbalance (u_A=2.5 g mm and $u_B = -2.5$ g mm), and as seen, it is dominated by the synchronous vibration component. The simulated results indicate two critical speeds at approximately 110 and 210 Hz respectively. However, the most important detail to note is that there are no sub-synchronous vibration components in the waterfall apart from a vibration of very low amplitude and a frequency of 100 Hz that appears from approximately 22,000 RPM. In the next waterfall diagram, Fig. 6, the unbalance is u_A=40 g mm and $u_B = -2.5$ g mm. Now a sub-synchronous vibration is seen to appear at a rotor speed of approximately 9000 RPM. At approximately 11,000 RPM, it bifurcates into two sub-synchronous components tracking the synchronous component until both disappear again at 15,000 RPM. The spectra marked with red correspond to the orbits of Fig. 5 obtained at the rotor speeds ω=11,400, 13,200, 15,000, 18,000, and 25,200 RPM. As mentioned, theoretically simulated results are purely steady state. For each spectrum in the waterfalls in Figs. 6 and 7, a simulation started from static steady-state conditions, with a duration of 1 s, is performed. Transient vibrations die out after approximately 0.2 s, consequently leaving 0.8 s blocks for the FFT, yielding a frequency resolution of 1.25 Hz. Though the simulations are time-consuming, the results presented here are performed on a standard laptop computer with a computation time of approximately 120 h.

4. Experimental results

The experimentally obtained results presented in this work are obtained from a test rig originally designed for the identification of the linear bearing coefficients and it is thoroughly described in [19] and represented by the schematics of Fig. 1a. In short, the test rig consists of a near-symmetrical hollow shaft supported by two identical segmented foil journal bearings having three pads. A set of permanent magnets is press fit mounted in the centre of the shaft, and together with the stator windings, this arrangement forms the electrical motor used for spinning the shaft. There are no axial bearings. High accuracy proximity sensors are mounted both horizontally and vertically close to each bearing location. At each shaft end, a disk is mounted that accommodates for the introduction of rotor unbalance by adding calibrated masses.

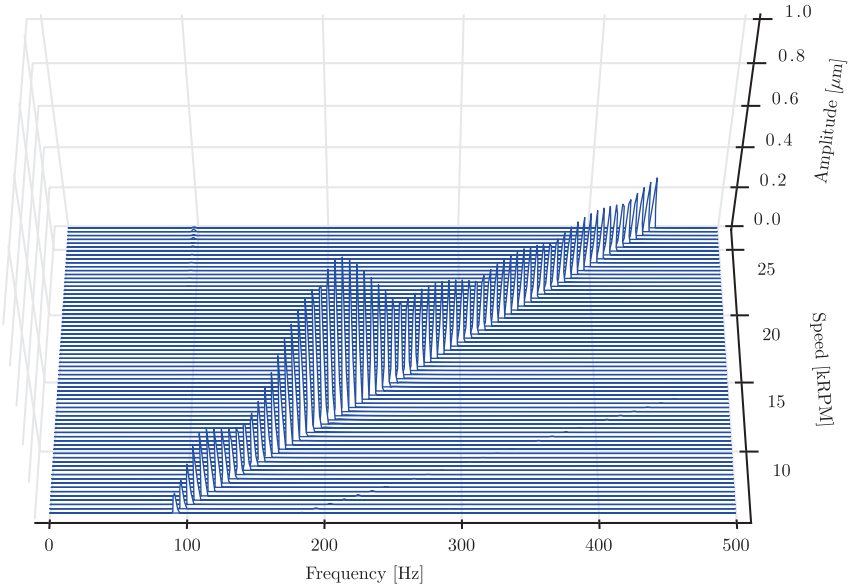

Fig. 6. Waterfall diagram theoretically obtained based on the vibrations simulated in Bearing *A* in the vertical direction (u_A=2.5 g mm and $u_B = -2.5$ g mm).

Please cite this article as: J.S. Larsen, & I.F. Santos, On the nonlinear steady-state response of rigid rotors supported by air foil bearings—Theory and experiments, *Journal of Sound and Vibration* (2015), http://dx.doi.org/10.1016/j.jsv.2015.02.017

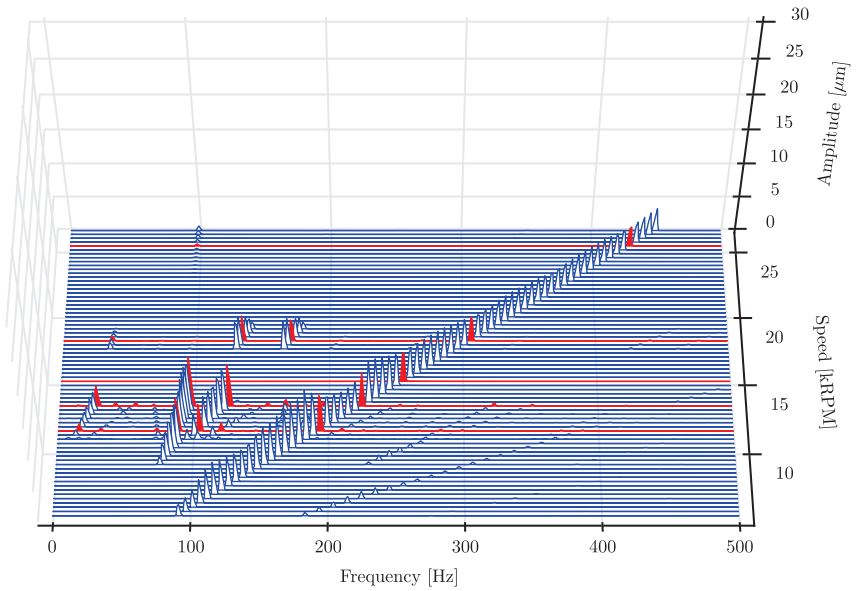

Fig. 7. Waterfall diagram theoretically obtained based on the vibrations simulated in Bearing *A* in the vertical direction (u_A=40 g mm and $u_B = -2.5$ g mm).

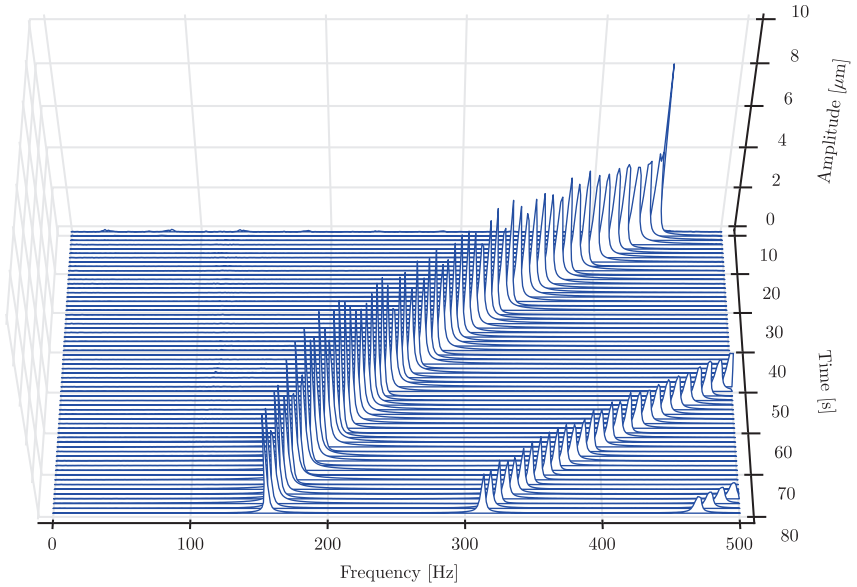

Fig. 8. Waterfall diagram experimentally obtained based on the vibrations measured in Bearing *A* in the vertical direction ($u_A \approx \pm 2.5$ g mm and $u_B \approx \pm 2.5$ g mm).

The assembled shaft mass is approximately 21 kg and the maximum speed is 30 kRPM. The first free-free natural frequency (bending) of the assembled shaft is calculated to approximately 1050 Hz. This is more than twice the synchronous frequency at maximum speed, hence the shaft can be treated as being rigid. The entire rotor assembly is balanced to below ISO grade G2.5.

Though this paper is on the nonlinear steady-state rotor response, the baseline experimental results are chosen to be the coast-down measurements obtained when switching of the drive motor at maximum speed. This is to eliminate the contamination of the measurements by force excitation and noise from the electrical drive (motor and VFD). Even though the coast-down time from 28,000 RPM to 0 is measured to approximately 140 s, which is a relatively long duration, it should be noted that the results are not steady state, and hence, divergence from the purely steady-state response may be expected.

The rotor vibrations measured during a coast-down with no unbalance mass applied are illustrated in the waterfall diagram Fig. 8. Here, the test rig rotor is balanced to the lowest practically obtainable level. It is clear that the rotor bearing

Please cite this article as: J.S. Larsen, & I.F. Santos, On the nonlinear steady-state response of rigid rotors supported by air foil bearings—Theory and experiments, *Journal of Sound and Vibration* (2015), http://dx.doi.org/10.1016/j.jsv.2015.02.017

system is healthy and the waterfall diagram is dominated by a clear synchronous vibration stretching from approximately 150 Hz to 450 Hz. The 2 and 3 × synchronous component, which is seen in the waterfall, is most likely a result of run out at the probe location. The run out might also explain the discrepancy related to the amplitude of the synchronous vibration component obtained theoretically and experimentally (Figs. 6 and 8).

Next, by adding a well-defined unbalance of $u_A = 40$ g mm and repeating the experiment, a completely different result is obtained as illustrated in the waterfall diagram in Fig. 9. The result is clear, and at different speeds sub-synchronous vibrations appear and disappear as the rotor speed approaches zero. Comparing the theoretically and experimentally obtained results, Figs. 7 and 9, the similarities are remarkable. In both figures, the sub-synchronous vibrations appear and disappear at nearly similar rotor speeds and their amplitudes are of the same order of magnitude. A comparison of the fundamental frequencies of the sub-synchronous vibrations observed experimentally and theoretically at 13,200 RPM is given in Table 2, and a very good correlation is found. The appearance of a 2 and 3 × synchronous component in the experimentally obtained result may as mentioned be explained by the presence of run out at the probe locations on the test rig rotor. Once again, it should be highlighted that even though the coast-down has a relatively long duration, there is a transient state of vibration in the experimentally obtained results.

As mentioned, San Andrés and Kim [41] and Balducchi et al. [42] presented experimental results showing a similar rotor behaviour. In [41], a mathematical model based on the Duffing oscillator was proposed. A cubic bearing stiffness function based on dry measurements were used in this model. It was obtained from a bearing subjected to monotonically increasing load when mounted on a non-rotating shaft. The mathematical model did predict subharmonic resonances at whirl speed ratios of 1/2 and 1/3; however, with significant discrepancies compared to the experiments. In [42], the experimental unbalance responses of two slightly different rigid rotors supported by two identical aerodynamic foil bearings were presented at rotation speeds between 50,000 RPM and 100,000 RPM. The displacements in the two foil bearings were also measured during coast-down and as waterfall diagrams. They showed a similar nonlinear behaviour, i.e. sub-synchronous vibrations accompanying the synchronous component. The sub-synchronous components bifurcate at typical rotation speeds, as was also illustrated in this work, Figs. 7 and 9. The nonlinear behaviour of the rotor-bearing system was also

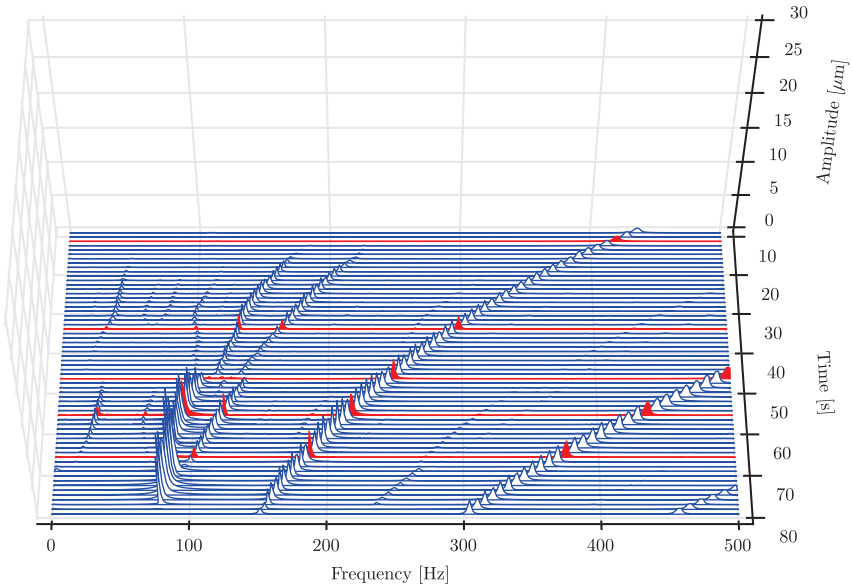

Fig. 9. Waterfall diagram experimentally obtained based on the vibrations measured in Bearing *A* in the vertical direction ($u_A \approx 40$ g mm and $u_B \approx \pm 2.5$ g mm).

Table 2
Frequency comparison of the three sub-synchronous vibrations observed experimentally and theoretically at 13,200 RPM. Data extracted from the red lines in the waterfall diagrams obtained theoretically and experimentally.

Sub-synchronous	1	2	3
Theoretical (Hz)	28	97	125
Experimental (Hz)	29	95	126
Difference (%)	3.5	−2	0.8

Please cite this article as: J.S. Larsen, & I.F. Santos, On the nonlinear steady-state response of rigid rotors supported by air foil bearings—Theory and experiments, *Journal of Sound and Vibration* (2015), http://dx.doi.org/10.1016/j.jsv.2015.02.017

underlined by increasing unbalance, leading to a vibration spectrum richer in new sub-synchronous vibrations. The experimental results were compared with a similar mathematical model based on the Duffing oscillator as in [41]. However, the experimentally obtained results could not be reproduced by the authors' simplified model.

From both Figs. 7 and 9, it is seen that at $\omega \approx 300$ Hz, four sub-synchronous vibrations are present at frequencies ranging from 45 to 200 Hz. The frequency ratio between these sub-synchronous vibrations and the rotational speed of the rotor is in the range $\omega_d/\omega \approx [0.13; 0.57]$ that does not correspond to a classical case of half-frequency whirl/whip instability. From the results illustrated in Figs. 6 and 8, it is clear that the sub-synchronous vibrations disappear at low unbalance levels. Therefore, the sub-synchronous vibrations are not caused by the typical self-excited instability phenomenon related to large bearing cross-coupled stiffness compared to direct damping. It is rather caused by nonlinearities forced by the unbalance i.e. a case of several sub-harmonic resonances. Hence, this kind of lateral rotor behaviour cannot be predicted by traditional linear analysis.

5. Conclusion

In this work, a mathematical approach for simulating a complete rotor-bearing system in the time domain was implemented, using the finite element method to discretise the Reynolds equation. The results of the mathematical model were compared to experimentally obtained results from a dedicated test rig. Though the mathematical model was based on the SEFM, the theoretical and experimental results showed very good agreement and it is concluded that the model is able to accurately predict the nonlinear steady-state response of rigid rotors supported by air foil bearings.

Both the experimentally and theoretically obtained results showed that the existence of sub-synchronous vibrations are dependent on rotational speed as well as the unbalance level. Based on results obtained at low unbalance levels, it is concluded that the sub-synchronous vibrations are not a case of classical rotor instability but rather a case of forced nonlinearities. Hence, this kind of lateral rotor behaviour cannot be predicted by traditional linear analysis.

The mathematical method was found to be computationally demanding. However, the results presented in this work were obtained from a standard laptop computer with a computation time of approximately 120 h, making the method directly applicable in an engineering design phase where knowledge of possible sub-synchronous vibrations are crucial. The sub-synchronous vibrations are often causing bearing failures or speed restrictions. Being able to predict these, the design of the rotor and bearing geometries, especially the bump foil geometry, can be optimised considerably at the design stage.

Though a good correlation between experimental and theoretical results was obtained, the accuracy of the method is dependent on a correct estimation of the foil stiffness and loss factor, k and η respectively. In this work, these foil parameters were estimated based on two main assumptions related to (1) the number of active load carrying bumps and (2) associated deflection amplitude. In order to eliminate the need for such assumptions, the mathematical model needs to be further expanded with a more detailed structural model taking the friction contacts e.g. [10] or [20] into account.

Appendix A. Rotor model matrices

The mass- and gyroscopic-matrices for a rigid rotor can be written as

$$\mathbf{M} = \frac{1}{l^2}\begin{bmatrix} l_2^2 m_x + I_{yy} & 0 & l_1 l_2 m_x - I_{yy} & 0 \\ 0 & l_2^2 m_y + I_{xx} & 0 & l_1 l_2 m_y - I_{xx} \\ l_1 l_2 m_x - I_{yy} & 0 & l_1^2 m_x + I_{yy} & 0 \\ 0 & l_1 l_2 m_y - I_{xx} & 0 & l_1^2 m_y + I_{xx} \end{bmatrix}, \quad \mathbf{G} = \frac{1}{l^2}\begin{bmatrix} 0 & -I_{zz} & 0 & I_{zz} \\ I_{zz} & 0 & -I_{zz} & 0 \\ 0 & I_{zz} & 0 & -I_{zz} \\ -I_{zz} & 0 & I_{zz} & 0 \end{bmatrix} \tag{A.1}$$

The non-dimensional form of the mass- and gyroscopic-matrices and the mass unbalance vector are

$$\tilde{\mathbf{G}} = \frac{\omega^2 C}{p_a R^2}\mathbf{G}, \quad \tilde{\mathbf{M}} = \frac{\omega^2 C}{p_a R^2}\mathbf{M}, \quad \tilde{\mathbf{f}}_{ub} = \begin{Bmatrix} \dfrac{u_A \omega^2}{p_a R^2}\begin{Bmatrix} \cos(\tau) \\ \sin(\tau) \end{Bmatrix} \\ \dfrac{u_B \omega^2}{p_a R^2}\begin{Bmatrix} \cos(\tau) \\ \sin(\tau) \end{Bmatrix} \end{Bmatrix}. \tag{A.2}$$

Appendix B. Film height

For a segmented journal bearing with inlet slope and the nomenclature as illustrated in Fig. 1b, the dimensionless rigid film height can be written as

$$\tilde{h}_r = \begin{cases} 1 + \varepsilon_x \cos(\theta) + \varepsilon_y \sin(\theta) - \tilde{h}_s \dfrac{\theta - \theta_i}{\theta_s}, & \theta_{li} \le \theta \le \theta_i \\ 1 + \varepsilon_x \cos(\theta) + \varepsilon_y \sin(\theta), & \theta_i < \theta \le \theta_{ti} \end{cases} \tag{B.1}$$

Please cite this article as: J.S. Larsen, & I.F. Santos, On the nonlinear steady-state response of rigid rotors supported by air foil bearings—Theory and experiments, *Journal of Sound and Vibration* (2015), http://dx.doi.org/10.1016/j.jsv.2015.02.017

where

$$\theta_i = \theta_s + \theta_l + \frac{2\pi}{N_p}(i-1)$$

$$\theta_{li} = \theta_l + \frac{2\pi}{N_p}(i-1)$$

$$\theta_{ti} = \theta_t + \frac{2\pi}{N_p}(i-1). \tag{B.2}$$

Discarding the mass of the foil structure, the equation of motion for the foil structure is

$$\tilde{p} - 1 = \tilde{k}\tilde{h}_c + \tilde{b}\dot{\tilde{h}}_c \quad \text{or} \quad \tilde{h}_c\left(\tilde{p}, \dot{\tilde{h}}_c\right) = \frac{\tilde{p} - 1 - \tilde{b}\dot{\tilde{h}}_c}{\tilde{k}} \tag{B.3}$$

Introducing the mechanical loss factor

$$\eta = \frac{b\omega_s}{k} = \frac{\tilde{b}}{\tilde{k}}\frac{\omega_s}{\omega} \tag{B.4}$$

Inserting the loss factor into the foil equation of motion yields the first-order ordinary differential equation

$$\dot{\tilde{h}}_c = \left(\frac{\tilde{p} - 1}{\tilde{k}} - \tilde{h}_c\right)\frac{1}{\eta} \tag{B.5}$$

with $\omega_s/\omega = 1$ meaning that the vibrations in the foil are assumed to be synchronous.

References

[1] B. Sternlicht, R.C. Elwell, Theoretical and experimental analysis of hydrodynamic gas-lubricated journal bearings, *American Society of Mechanical Engineers—Papers* (1957).
[2] J.S. Ausman, An improved analytical solution for self-acting, gas-lubricated journal bearings of finite length, *Journal of Basic Engineering* 83 (1961) 188–192.
[3] V. Stingelin, Theoretische und experimentelle Untersuchungen an Gaslagern, PhD Thesis, Eidgenössischen Technischen Hochschule in Zürich, 1963.
[4] W.J. Harrison, The hydrodynamical theory of lubrication with special reference to air as a lubricant, *Transactions Cambridge Philosophical Society* 22 (1913) 34–54.
[5] J.W. Lund, Calculation of stiffness and damping properties of gas bearings, *Journal of Lubrication Technology* (1968) 793–804.
[6] C.-C. Wang, C.-K. Chen, Bifurcation analysis of self-acting gas journal bearings, *Journal of Tribology* 123 (2001) 755.
[7] M. Arghir, S. Le Lez, J. Frene, Finite-volume solution of the compressible Reynolds equation: *linear and non-linear analysis of gas bearings*, *Proceedings of the Institution of Mechanical Engineers, Part J: Journal of Engineering Tribology* 220 (2006) 617–627.
[8] J.-H. Song, D. Kim, Foil gas bearing with compression springs: *analyses and experiments*, *ASME Journal of Tribology* 129 (2007) 628–639.
[9] D. Lee, Y.-C. Kim, K.-W. Kim, The dynamic performance analysis of foil journal bearings considering coulomb friction: *rotating unbalance response*, *Tribology Transactions* 52 (2009) 146–156.
[10] S. Le Lez, M. Arghir, J. Frêne, Nonlinear numerical prediction of gas foil bearing stability and unbalanced response, *Journal of Engineering for Gas Turbines and Power* 131 (2009) 012503.
[11] D. Kim, Parametric studies on static and dynamic performance of air foil bearings with different top foil geometries and bump stiffness distributions, *Journal of Tribology* 129 (2007) 354–364.
[12] J. Zhang, W. Kang, Y. Liu, Numerical method and bifurcation analysis of jeffcott rotor system supported in gas journal bearings, *Journal of Computational and Nonlinear Dynamics* 4 (2009) 011007.
[13] P. Bonello, H.M. Pham, The efficient computation of the nonlinear dynamic response of a foil–air bearing rotor system, *Journal of Sound and Vibration* 333 (2014) 3459–3478.
[14] H.M. Pham, P. Bonello, Efficient techniques for the computation of the nonlinear dynamics of a foil–air bearing rotor system, *ASME Turbo Expo 2013: Turbine Technical Conference and Exposition*, 2013, p. 7.
[15] M.A. Hassini, M. Arghir, *A Simplified and Consistent Nonlinear Transient Analysis Method for Gas Bearing: Extension to Flexible Rotors*, Düsseldorf, Germany, June 16–20, 2014. GT2014-25955.
[16] M.A. Hassini, M. Arghir, A new approach for the stability analysis of rotors supported by gas bearings, *Proceedings of ASME Turbo Expo 2013*, 2013, pp. 1–13.
[17] M.A. Hassini, M. Arghir, A simplified nonlinear transient analysis method for gas bearings, *Journal of Tribology* 134 (2012) 011704.
[18] P. Bonello, H. Pham, *Nonlinear Dynamic Analysis of a Turbocharger on Foil–Air Bearings with Focus on Stability and Self-Excited Vibration*, Düsseldorf, Germany, 2014. GT2014-25176.
[19] J.S. Larsen, A.J.-T. Hansen, I.F. Santos, Experimental and theoretical analysis of a rigid rotor supported by air foil bearings, *Mechanics & Industry* (2014).
[20] J.S. Larsen, A.C. Varela, I.F. Santos, Numerical and experimental investigation of bump foil mechanical behaviour, *Tribology International* 74 (2014) 46–56.
[21] J.A. Walowit, J.N. Anno, *Modern Developments in Lubrication Mechanics*, Applied Science Publishers, London, 1975.
[22] J.S. Larsen, I.F. Santos, Efficient solution of the non-linear Reynolds equation for compressible fluid using the finite element method, *Journal of the Brazilian Society of Mechanical Sciences and Engineering* (2014) 1–13.
[23] B.J. Hamrock, *Fundamentals of Fluid Film Lubrication, McGRAW-HILL Series in Mechanical Engineering*, McGRAW-HILL, Inc., New York, 1994.
[24] H. Heshmat, J.A. Walowit, O. Pinkus, Analysis of gas lubricated compliant thrust bearings, *Journal of Lubrication Technology* 105 (1983) 638–646.
[25] H. Heshmat, J.A. Walowit, O. Pinkus, Analysis of gas-lubricated foil journal bearings, *Journal of Lubrication Technology* 105 (1983) 647–655.
[26] J.B. Olsen, Nonlinear Dynamic Behavior of Rigid Rotor Foil Bearing System, Master's thesis, Technical University of Denmark, 2014.
[27] R.D. Cook, D.S. Malkus, M.E. Plesha, J.W. Witt, *Concepts and Applications of Finite Element Analysis*, 4th ed. John Wiley, New York, 2002.
[28] J.S. Larsen, B.B. Nielsen, I.F. Santos, On the numerical simulation of nonlinear transient behavior of compliant air foil bearings, *Proceedings of the 11th International Conference on Vibrations in Rotating Machines*, Magdeburg, Germany, 23–25 February, 2015, pp. 1–13.
[29] A.C. Hindmarsh, Odepack, A systematized collection of ode solvers, R.S. Stepleman (Ed.), *Scientific Computing*, 55-64, 1983.
[30] E. Anderson, Z. Bai, C. Bischof, S. Blackford, J. Demmel, J. Dongarra, J. Du Croz, A. Greenbaum, S. Hammarling, A. McKenney, D. Sorensen, *LAPACK Users' Guide*, 3rd ed. Society for Industrial and Applied Mathematics, Philadelphia, PA, 1999.

Please cite this article as: J.S. Larsen, & I.F. Santos, On the nonlinear steady-state response of rigid rotors supported by air foil bearings—Theory and experiments, *Journal of Sound and Vibration* (2015), http://dx.doi.org/10.1016/j.jsv.2015.02.017

[31] M. Carpino, G. Talmage, Prediction of rotor dynamic coefficients in gas lubricated foil journal bearings with corrugated sub-foils, *Tribology Transactions* 49 (2006) 400–409.
[32] K. Feng, S. Kaneko, Analytical model of bump-type foil bearings using a link-spring structure and a finite-element shell model, *Journal of Tribology* 132 (2010) 021706.
[33] D.-H. Lee, Y.-C. Kim, K.-W. Kim, The static performance analysis of foil journal bearings considering three-dimensional shape of the foil structure, *Journal of Tribology* 130 (2008) 031102.
[34] S. Le Lez, M. Arghir, J. Frene, A dynamic model for dissipative structures used in bump-type foil bearings, *Tribology Transactions* 52 (2008) 36–46.
[35] J.P. Peng, M. Carpino, Coulomb friction damping effects in elastically supported gas foil bearings, *Tribology Transactions* 37 (1994) 91–98.
[36] J.P. Peng, M. Carpino, Finite element approach to the prediction of foil bearing rotor dynamic coefficients, *Journal of Tribology* 119 (1997) 85–90.
[37] T.H. Kim, L. San Andrés, Heavily loaded gas foil bearings: *A model anchored to test data*, *ASME Conference Proceedings* 2005 (2005) 763–771.
[38] J.S. Larsen, I.F. Santos, Compliant foil journal bearings—investigation of dynamic properties, *Proceedings of the 10th International Conference on Schwingungen in Rotierenden Maschinen (SIRM2013)*, Berlin, Germany, 25–27 February, 2013, pp. 1–12, ISBN 978-3-00-038602-2.
[39] B.J. Lazan, Damping studies in materials science and materials engineering, *ASTM International* (1965).
[40] N.T. Christensen, Experimental Characterization of Dynamic Properties of Corrugated Structures, Master's thesis, Technical University of Denmark, 2014.
[41] L. San Andrés, T.H. Kim, Forced nonlinear response of gas foil bearing supported rotors, *Tribology International* 41 (2008) 704–715.
[42] F. Balducchi, M. Arghir, S. Gaudillere, *Experimental Analysis of the Unbalance Response of Rigid Rotors Supported on Aerodynamic Foil Bearings*, Düsseldorf, Germany, 2014. GT2014-25552.

Please cite this article as: J.S. Larsen, & I.F. Santos, On the nonlinear steady-state response of rigid rotors supported by air foil bearings—Theory and experiments, *Journal of Sound and Vibration* (2015), http://dx.doi.org/10.1016/j.jsv.2015.02.017

DTU Mechanical Engineering
Section of Solid Mechanics
Technical University of Denmark

Nils Koppels Allé, Bld. 404
DK- 2800 Kgs. Lyngby
Denmark
Phone (+45) 4525 4250
Fax (+45) 4593 1475
www.mek.dtu.dk
ISBN: 978-87-7475-402-2

DCAMM
Danish Center for Applied Mathematics and Mechanics

Nils Koppels Allé, Bld. 404
DK-2800 Kgs. Lyngby
Denmark
Phone (+45) 4525 4250
Fax (+45) 4593 1475
www.dcamm.dk
ISSN: 0903-1685